Design of Multiaxial Accelerometers with Simplicial Architectures for Rigid-Body Pose-and-Twist Estimation

Philippe Cardou

Design of Multiaxial Accelerometers with Simplicial Architectures for Rigid-Body Pose-and-Twist Estimation

by

Philippe Cardou

Department of Mechanical Engineering

McGill University

Montreal (QC) Canada

August 2007

A thesis submitted to McGill University
in partial fulfillment of the requirements for the degree of
Doctor of Philosophy

Abstract

Accelerometer arrays are used in biomechanics and other fields to estimate the rigid-body acceleration field and, thence, all kinematic variables describing the rigid-body displacements. However, the progress of this technology has been limited by that of micromachined gyroscopes, which turn out to be more accurate than accelerometer arrays in most applications. The work reported in this thesis aims at improving the accuracy of the angular velocity estimates provided by accelerometer arrays. The approach is twofold: A class of accelerometer mechanical architectures is proposed, with the goal of reducing the accelerometer cross-axis sensitivity, and robust algorithms are proposed to estimate the angular velocity from some or all components of the rigid-body acceleration field.

The novel class of accelerometers is inspired from parallel-kinematics-machine (PKM) architectures, taking the accelerometer proof mass to be the PKM moving platform, and the accelerometer frame the PKM base. A common characteristic of the proposed PKM architectures is that their moving platforms are connected to their bases by $n + 1$ legs each, $n = 1, 2, 3$ being their respective number of sensitive directions. For this reason, the resulting class of accelerometers is referred to as "Simplicial Multiaxial Accelerometers" (SMA). A micro-scale version of the Simplicial Biaxial Accelerometer (SBA) was devised, designed, fabricated, and tested.

Furthermore, the theory behind the estimation of the angular velocity from acceleration measurements is revisited. Hence, four algorithms are proposed, which allow for the estimation of the rigid-body angular velocity from

centripetal acceleration measurements alone. Based on Kalman filtering, another method is proposed in order to obtain a rigid-body angular-velocity estimate from both the centripetal and tangential components of the rigid-body acceleration field.

Résumé

Les assemblages d'accéléromètres sont utilisés entre autres en biomécanique afin d'estimer le champ des accélérations d'un corps rigide et, de là, les variables cinématiques décrivant les déplacements dudit corps rigide. On remarque toutefois que le progrès de cette technologie a été limité par celui des gyroscopes micro-usinés, lesquels sont plus précis que les assemblages d'accéléromètres dans la plupart des applications. Le but des recherches décrites dans cette thèse est d'améliorer la précision des estimés de vitesse angulaire produits par les assemblages d'accéléromètres. Les développements proposés portent sur deux aspects : une classe d'architectures mécaniques d'accéléromètres est proposée ayant pour but de réduire la sensibilité des capteurs aux accélérations transverses, des algorithmes robustes étant également proposés afin d'estimer la vitesse angulaire à partir de certaines ou de toutes les composantes du champ d'accélération du corps rigide.

La classe d'accéléromètres proposée est inspirée des architectures de machines à cinématique parallèle (MCP) en assimilant la masse d'épreuve et le support d'un accéléromètre à l'organe terminal et à la base d'une MCP, respectivement. Une caractéristique commune aux MCP proposées ici est que leurs organes terminaux et leurs bases sont reliées par $n + 1$ chaînes cinématiques simples, $n = 1, 2, 3$ étant leurs nombres de directions sensibles respectifs. Pour cette raison, on appelle accéléromètres simpliciaux multiaxiaux les capteurs résultant de ces MCP. Une version micro-usinée de l'accéléromètre simplicial biaxial est conçue, fabriquée et testée.

En outre, la théorie permettant l'estimation de la vitesse angulaire d'un corps rigide à partir de mesures d'accélérations est réexaminée. De cette

révision, quatre algorithmes permettant l'estimation de la vitesse angulaire à partir de mesures d'accélération centripète sont proposés. Enfin, un algorithme permettant l'estimation de la vitesse angulaire d'un corps rigide à partir de mesures d'accélérations centripète et tangentielle et reposant sur le filtrage de Kalman est proposé.

Acknowledgements

I would like to express my deepest gratitude to my two supervisors, Professors Jorge Angeles and Damiano Pasini. Their generous effort, patience, and dedication turned out to be keys in the completion of this thesis. I am thankful to the *Natural Sciences and Engineering Research Council* and the *Fonds Québécois de la Recherche sur la Nature et les Technologies*, which supported financially my studies and the project, respectively.

Let me express the great pleasure I had working at the Robotics Mechanical Systems Laboratory (RMSL) and the Multi-Scale Design Optimization Group (MDOG), which stemmed from the kindness and team spirit of all its members. I keep excellent memories of fascinating conversations with Zhongkai Qin, Sergio Hernandez, Geneviève Houde, Chao Chen, Alessio Salerno, Danielle Nasrallah, Waseem Ahmed Khan, Aya Amany, Simon Desrochers, Jean-François Gauthier, Vahid Mirjalili, Salim Ali, Irène Cartier, Shaoping Bai, Stéphane Caro—the "petit chef"—and Alexei Morozov.

Let me express my gratitude to Prof. Srikar Thattai Vengallatore, whose expertise and generous availability were necessary to the realization of the simplicial biaxial accelerometer. The invaluable help from the McGill Nanotools Microfab staff was another sine qua non condition to the microfabrication of the simplicial biaxial accelerometer. Special thanks are addressed to Don Berry and Neal Lemaire, who stood on the first front-line, and to Dr. Matthieu Nannini and Vito Logiudice for their advice and support.

I am greatly indebted to Prof. Michael P. Païdoussis, who responded positively to our call for help by lending us his sensing equipment, seeing that the delivery of ours was delayed beyond the time-frame of this thesis. I am also grateful to Jack Danieli and Mike Stone from Polytec, Hopkinton, MA,

USA, who helped me prepare and conduct the tests with a dedication that went far beyond the requirements of a regular sales operation.

I would also like to express my warmest feelings to all my friends in Montreal, who, each in his or her own way, aided during my studies. Here, I have special thoughts for François Deschênes, Véronique De Bellefeuille, Estelle Huard, Anne-Marie Huard, Frédéric Rioux, Raphaël Brochu, Laurence Blouin, Annie Therrien, Barnim Janta, Lionel Birglen, Valérie Houle, Sylvain Arnaud, Joël Robert, and Marie-Christine Denis. Finally, I thank my sister, Françoise, and my parents, Alain and Michèle, who are at the root of every effort embedded in this work.

Claim of Originality

To the knowledge of the author, the main ideas expressed in this thesis are original[1] . Those ideas that constitute the most significant contributions are listed below:

- Simplicial Multiaxial Accelerometers (SMAs) allowing measurements of 1, 2 or all 3 acceleration components of a single point of a rigid body, respectively;
- a microfabrication process for the fabrication of a Simplicial Biaxial Accelerometer;
- symbolic solutions to the problems of estimating the acceleration fields of rigid bodies moving in a plane and in space, respectively, from arrays of n uniaxial accelerometer measurements;
- conditions for an accelerometer array to be *feasible*, i.e., for it to allow the identification of the full rigid-body acceleration field;
- in the planar case, the generalization to n accelerometers of a graphical method already proposed for four accelerometers to assess the *feasibility* of a given accelerometer array;
- four algorithms to estimate the rigid-body angular velocity from centripetal acceleration measurements, all more robust than the existing ones, according to the simulation results included;
- an algorithm based on Kalman filtering to estimate the rigid-body angular velocity from centripetal and tangential acceleration measurements.

[1] Some of the reported results have in part been published in (Cardou and Angeles, 2005, 2006, 2007a,b, 2008b,a,c).

Contents

List of Tables

List of Figures

Chapter 1

Introduction

1.1 Background

Dating back to the 1920s, accelerometers consist essentially of a proof mass (or seismic mass) supported by a spring-acting force. This intrinsic simplicity has been critical to the propagation of these sensors to a broad spectrum of applications over the years. The early accelerometers were intended for acceleration measurement in airplane catapults, passenger elevators, aircraft shock absorbers, explosions, as well as vibration monitoring in turbines and underground pipes (Walter, 1996). According to Walter (1996), it was not before the Second World War that accelerometers were introduced in aircraft, to assist pilots in certain maneuvers.

Apparently, the advent of piezoelectricity, the field effect transistor (FET), and the charge amplifier were keys in the subsequent development of accelerometers. These technologies allowed for a first round of miniaturization in the 1950s and 1960s, and also for the broadening of the frequency bandwidth of the sensors. The higher sensor natural frequencies permitted the introduction of accelerometers in many shock applications such as crashworthiness. This was first reported by Mertz (1967), followed later by others such as Padgaonkar et al. (1975) and Mital and King (1979), and ended up as a standard in the

automotive industry.

In the 1980s and the 1990s, the advent of microelectromechanical systems (MEMS) gave rise to another round of miniaturization, allowing for the integration of the sensor and its associated circuitry. Apparently, this movement started with the work of Roylance (1978), pushing down the cost of accelerometers, and making them attractive to other applications, such as car crash detection, car navigation, unmanned vehicles, pedometers, camera stabilization, drop detection in consumer electronic devices, etc. One of the most promising advances came recently in the area of game controllers, and it may well be a precursor of a new paradigm in applications involving human-machine interaction. For example, Nintendo developed the Wii Remote, which allows the user to interact with the game on screen by shaking and tilting the remote. This device, which is shown in Fig. 1.1, is equipped with a triaxial MEMS accelerometer.

Figure 1.1: Nintendo's Wii Remote

1.2 Multiaxial Accelerometers

To this date, so much work has been reported on the development of accelerometers that it is impossible to do a comprehensive review in just a few

paragraphs. Indeed, there are as many types of accelerometers as there are methods for measuring the position of the proof mass; we will therefore restrict ourselves to the most important ones and to those that are related to the topic of this thesis.

Tunnelling-effect MEMS accelerometers are probably the most accurate instruments of the MEMS class, as they allow for resolutions in the ng—g symbolizing the gravitational constant of the Earth—range for a bandwidth of 100 Hz (Liu et al., 1998). These devices measure the tunnelling current to estimate the proof-mass displacements. This current flows between a sharp tunnelling tip and a flat surface separated by a small gap, usually in the orders of nanometres. The geometry of the electrodes allows for a simple accurate model of the tunnelling current in which appears the gap dimension, thereby allowing for its estimation. The main difficulty in this type of accelerometers is probably the micromachining of the tunnelling tip, which is detached of a few nanometers from the electrode.

Resonating MEMS accelerometers work on the same principle as the tuning of the string of a musical instrument. The beams supporting the proof mass are excited at high frequency, usually by means of piezoelectric elements. Any acceleration of the device along its sensitive direction induces an inertial force applied by the proof mass onto its supporting beams, causing a shift of their vibrating frequency. Similar to stringed instruments, the tension in the beams is determined by "listening" to this frequency shift, and, from there, the specific force on the proof mass is estimated. An example of this technology was developed by Le Traon et al. (1998), who etched the accelerometers in quartz substrates in one single step. The simplicity of the microfabrication

process and the reasonable accuracy of the device make it attractive. The main drawback lies in the associated oscillating circuitry, which is somewhat more complicated and sensitive than that of other types of accelerometers. The sensor consumes also more power than others working on different principles.

Notice that the two foregoing types of accelerometers have received extensive attention from researchers, and yet, until proven otherwise, none of them allows for the measurement of all three components of the acceleration from the same proof mass. In this thesis we are interested in multiaxial accelerometers, i.e., those accelerometers that can yield several components of the acceleration of one single point, and, therefore, from the same proof mass. Such accelerometers should offer four main advantages:

(*i*) They are likely to be smaller than the usual stacks of uniaxial accelerometer—accelerometers that measure only one component of the acceleration.

(*ii*) They are likely to eliminate or reduce the sensitivity to cross-axis accelerations, since these accelerations are measured.

(*iii*) They allow for isotropic mechanical architectures, which, if properly chosen, are less sensitive to uniform expansion of the material under a change of temperature.

(*iv*) In an accelerometer array, these multiaxial accelerometers simplify the associated set of equations.

The analysis of multiaxial accelerometers involves further work, but this is not insurmountable. In fact, the main difficulty with these devices is their lack of micromachinability, which explains why only a few are commercially available. In order to relieve the problem from some of the machining difficulty, the focus of this thesis will be on quasi-static accelerometers (a.k.a. pendulous-mass

accelerometers), which often present less machining difficulties than the foregoing classes of accelerometers. Quasi-static accelerometers may be defined as those accelerometers that are meant to measure acceleration signals with frequencies *much lower* than their natural frequency. From the literature, *much lower* would mean here that the measured frequencies are at most twenty times smaller than the accelerometer natural frequency.

Thanks to the planar nature of most existing micromachining techniques, the microfabrication of a quasi-static biaxial accelerometer is not much more difficult than that of a uniaxial accelerometer with its sensitive direction in the wafer plane. As a result, some biaxial accelerometers are available on the market (Analog Devices, 2004a), with ongoing research on the topic (Liu et al., 2007).

On the other hand, the fabrication of a triaxial accelerometer is a more challenging task. To the knowledge of the authors, the only commercially-available quasi-static triaxial accelerometer is the DeltaTron, developed by Brüel & Kjær (Hansen, 1997). This sensor relies on piezoelectricity to estimate the proof-mass displacements in all directions. As a result, this accelerometer does not measure DC accelerations, its lower frequency limit being in the orders of a fraction of a Hertz. If this is not a real issue for measuring vibration, it may pose problems when one wants to estimate the acceleration in an arbitrary rigid-body motion that encompasses very low frequencies. Notice also that the manufacturing of the DeltaTron does not rely on conventional MEMS fabrication techniques, which does not prevent it from being as small as 1 cm^3.

As a general rule, existing triaxial accelerometers may be filed into two categories: the ones that are MEMS-fabricated, and the others. Alike the DeltaTron, the accelerometer proposed by Chapsky et al. (2007) pertains to this category. However, this sensor allows for the estimation of both the point-acceleration and the angular-acceleration of the rigid body to which it is attached. Moreover, its proof mass is a cube, and is supported by eight triplets of mutually orthogonal linear springs located respectively at the eight vertices of the proof mass. Therefore, such a design is completely isotropic, and, for this reason, is referred to as the six-degree-of-freedom isotropic accelerometer. The main difference between the mechanical architecture proposed by Chapsky et al. (2007) and the ones proposed in this thesis is that the former allows for proof-mass rotations, whereas the latter allow only for translations.

Some parallel mechanical architectures for triaxial accelerometers were proposed by Shaad and Paros (2004), which are very similar to the cubic parallel architecture of Chapsky et al. (2007). The main difference between the two concepts is that Shaad and Paros (2004) used six linear springs instead of 24. The six springs are distributed by pairs on three of the six faces of the cubic proof mass. The main drawback of the design of Shaad and Paros (2004) is that the accelerometer allows also for rotations of the proof mass, which the authors neglect to mention. For this reason, it is somewhat different from the architectures proposed in this work. To the knowledge of the author, Shaad and Paros (2004) did not report any implementation of these architectures.

Another triaxial accelerometer that is not MEMS-fabricated is the Three-Axis Electrostatic Accelerometer (TEA) developed by Bernard et al. (1985). Unlike the devices of Chapsky et al. (2007) and Shaad and Paros (2004),

the TEA does not rely on any flexures to support the proof mass, which is rather electrostatically levitated by six electrodes forming a cube. Apparently, the TEA achieved a good resolution for the time when it was produced, its drawbacks coming mainly from the high voltages (± 1000 V) required at the electrodes in order to sustain the proof mass.

The foregoing design leads us to existing MEMS-fabricated triaxial accelerometers, among which we find another accelerometer working on the principle of electrostatic levitation. This accelerometer was developed by Toda et al. (2002); the small size of its spherical proof mass appears to solve the high-voltage problem of the TEA. Indeed, Toda et al. (2002) were able to fabricate this accelerometer with a 1-mm-diameter proof mass, which could be suspended using a reasonable 15-V potential difference between the electrodes, for a measurement range of $\pm 2g$. This beautiful design can only be criticized on the complexity of its underlying fabrication process, which is so innovative and elaborate, that it is explained in a series of different works—(Takeda, 2000; Ishikawa, 1999), for example. The micromachining of small balls requires very specialized equipment, and, even though the authors were able to produce a prototype of the accelerometer, it may not be well suited for mass production.

Another interesting unique MEMS-fabricated triaxial accelerometer was proposed by Xie et al. (2004). In fact, the accelerometer proposed by these researchers is very similar to the biaxial accelerometers already on the market (Analog Devices, 2004a), except for the presence of a second uniaxial accelerometer built in the proof mass of the biaxial accelerometer. Hence, the biaxial accelerometer picks up the motions in the wafer plane, whereas the uniaxial accelerometer picks up those that are normal to the wafer plane. From

a mechanical perspective, this architecture is hybrid, in that it is made of a serial arrangement of two parallel kinematic architectures. This hybrid architecture results in relatively high cross-axis sensitivities of 2.1% and 4.7% of the out-of-wafer plane sensitive direction to accelerations in the two in-plane sensitive directions, respectively, as acknowledged by the authors (Qu et al., 2006).

To the knowledge of the author, all other quasi-static MEMS-fabricated triaxial accelerometers that have been reported rely on the same mechanical architecture, which is illustrated in Fig. 1.2. In these accelerometers—(Mineta et al., 1996; Puers and Reyntjens, 1998; Li et al., 2001; Kim et al., 2005), for example—the proof-mass centre of mass is lower than the beam anchors. Therefore, any acceleration a_X in the X-axis direction results in a proof-mass angular displacement γ_X. Conversely, accelerations a_Z directed along the Z-axis induce a proof-mass displacement δ_Z in the same direction. The proof-mass displacements can be estimated by means of either piezoresistive sensors on the flexible beams or capacitance variations between the bottom surface of the proof-mass and the handle wafer displayed in black in Fig. 1.2. However, due to the unidirectional nature of the etching processes used in micromachining, all of these accelerometers have anisotropic mechanical structures, which make them sensitive to parasitic angular acceleration effects.

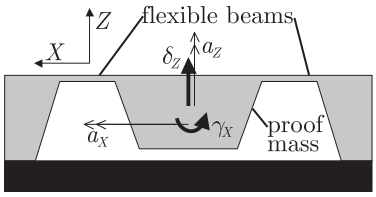

Figure 1.2: Working principle of many existing triaxial accelerometers

This review was intended just to give a glimpse of the vast body of research that has been dedicated to the development of novel techniques for the measurement of proof-mass displacements. On the other hand, few efforts have been devoted to the development of accelerometer mechanical architectures that exhibit a good isotropy among their sensitive directions, while remaining insensitive to cross-axis accelerations. Following this idea, Chapter 2 is concerned with the synthesis of novel isotropic parallel mechanical architectures for multiaxial accelerometers, which are inspired from those of parallel kinematic machines that are based on lower kinematic pairs. The following Chapters 3–5 are concerned with the fabrication and testing of one of these mechanical architectures, which lends itself to MEMS microfabrication techniques. The balance of the thesis is a sequel of the review provided in the section below.

1.3 Accelerometer Arrays

The use of accelerometers to estimate not only the translation of a landmark point on a rigid body but also the body angular acceleration field is an idea that can be traced back to 1965. On that year, Krishnan (1965) proposed the use of accelerometers mounted onto three rotating discs having their three axes mutually orthogonal and fixed to the rigid body. This would allow the estimation of both the acceleration of a point on the rigid body and its angular velocity vector. However, we may note that the proposed concept was relatively cumbersome and potentially required more power than the traditional gyroscopes, which may explain why no reports of its implementation have been found.

In the same year, "strapped" accelerometers were proposed by Grammatikos (1965) and Schuler (1965) to estimate the acceleration field of a rigid body and, thence, extract the kinematic variables of interest. To the knowledge of the author, these extensive works include the first instances of "accelerometer arrays," as they are referred to in this text, that is, rigid assemblies of spatially distributed accelerometers. This type of device has received different names throughout the literature: accelerometer-only inertial measurement unit (IMU), all-accelerometer IMU, nongyroscopic IMU, gyro-free IMU, for example. The main contribution of Grammatikos (1965) and Schuler (1965) was to propose and analyze seven different accelerometer array geometries, each being made-up of six to 12 accelerometers. They also provided error analyses of the resulting angular-acceleration and angular-velocity estimates. A criticism that may be levelled at these works is that all the solutions reported by these researchers are specific to the accelerometer-array geometries they proposed. In the opinion of the author, solving the general problem, and then applying its general solution to each of the accelerometer-array geometries would have been more useful to the researchers that followed on their trail.

1.3.1 Applications

Crashworthiness

Mertz (1967) studied the planar kinematics of the head when the neck is subjected to whiplash. In his work, Mertz resorted to two pairs of orthogonal uniaxial accelerometers mounted in opposition on the head of a dummy in order to estimate its angular acceleration after impact. Hence, this accelerometer array allowed the detection of the rigid-body acceleration field of a planar motion only, and turned out to be the first proof of concept for this class of IMUs.

This work was later followed by that of Padgaonkar et al. (1975), which may be regarded as a landmark in impact biomechanics, since it is the first proof of concept of spatial accelerometer arrays, and also because its nine-accelerometer scheme was later used by several other researchers—see (Chou and Sinha, 1976; Linder et al., 2002; Anderson et al., 2003; Yoganandan et al., 2006), for example. It should also be mentioned that the work of Padgaonkar et al. (1975) was further analyzed by Liu (1976), who showed that the six-accelerometer scheme was bound to yield unstable angular-velocity estimates. Mital and King (1979) were among those who later used the nine-accelerometer array; they showed by both simulation and experiments that this array could be used to estimate the attitude of the head of a dummy subjected to impact.

Shea and Viano (1994) reported on the use of planar seven-accelerometer arrays to estimate the complete in-plane kinematics of the head of the popular Hybrid III Dummies. As can be seen from this review, accelerometer arrays have been used extensively in crash tests, and, in most instances, as the primary or only source of information on the head kinematics. Therefore, any improvement of this measurement technique would be valuable to the impact biomechanics research community.

Other Biomechanics Applications

Accelerometer arrays have also proven to be useful in other biomechanics applications, such as gait analysis. Morris (1973) and Hayes et al. (1983) used accelerometers to track the motions of the human shank. We may also cite (Kane et al., 1974) as an example, since the authors used an accelerometer array mounted onto a tennis racket in order to estimate its acceleration field

during play. Hence, they were able to estimate and compare the forces exerted on the racket by both a novice and an expert player.

Other Applications

Several other simulations or implementations involving accelerometer arrays may be found in the literature on a wide variety of applications. In the interest of the circulation of ideas, some publications stemming from these somewhat disconnected fields are listed below:

1. projectile guidance (Costello, 2000; Ohlmeyer and Pepitone, 2002; Pamadi et al., 2004);
2. vibration control (Ang et al., 2001, 2003, 2004; Parsa, 2003; Algrain and Quinn, 1993);
3. vehicle navigation (Miles, 1986; Subramanian and Vendhan, 1993; Mostov et al., 1997; Peng and Golnaraghi, 2004; Cardou and Angeles, 2005);
4. gravity gradiometry (Zorn, 2002).

1.3.2 Acceleration Field of a Rigid Body

Let us now turn our attention towards the advances that have been reported on the theory behind accelerometer arrays. For a deeper understanding of the quantity that is to be measured, one may be interested in the work of Mohamed (1997), who gave a simple geometric interpretation of the acceleration field. Notice that the planar and spatial acceleration fields are also depicted in Fig. 6.1. The more advanced readers may also be interested in the acceleration field analysis based on screw differentiation—see Bokelberg et al. (1992); Ridley et al. (1992), for example. Despite the elegance and soundness of this method, due to space constraints, it will be left aside in this dissertation. We will opt instead for the more direct method of Mohamed (1997), which relies instead on linear algebra.

1.3.3 Accelerometer-Array Geometries

Several accelerometer-array geometries have been proposed over the years (Grammatikos, 1965; Schuler, 1965; Padgaonkar et al., 1975; Huijser, 1992; Chen et al., 1994; Genin et al., 1997; Parsa, 2003; Parsa et al., 2005). Apparently, all but the one studied by Parsa (2003) were drawn from mere intuition. Moreover, their associated analyses were carried out free of any common methodology, allowing for the estimation of only some components of the acceleration field in some cases, and all of them in others. From these observations, we see that it is desirable to have a more coherent approach to accelerometer-array synthesis and analysis. This would allow sound comparisons between the concepts, and a clearer understanding of their limitations with respect to the estimation of the rigid-body acceleration field.

Perhaps because he had perceived that need, Parsa (2003) proposed an explicit linear symbolic formulation that allowed for the estimation of the acceleration field of an accelerometer array made up of n triaxial accelerometers located at n arbitrary points. He then used the conditioning of the linear relation between the accelerometer readouts and the acceleration field parameters as a performance index for the synthesis of an accelerometer array. By means of that index, Parsa showed that the accelerometer array *Plato* allows for the linear operator between the accelerometer measurements and the acceleration field parameters to be isotropic. Plato is composed of four triaxial accelerometers located at the vertices of a tetrahedron; it was devised and prototyped at McGill University's Robotic Mechanical Systems Laboratory.

The only criticism that can be made regarding this nice and broad development in the field of accelerometer arrays is that Parsa (2003) assumed, for

simplicity, that all accelerometers were triaxial, i.e., that the sensors measured all three components of the acceleration of one given point. As mentioned in Section 1.2, the author has knowledge of only one commercially-available "real" triaxial accelerometer. Furthermore, most, if not all of the accelerometer arrays that were previously proposed involved uniaxial or biaxial accelerometers, and, therefore, fall outside the analysis reported by Parsa (2003). Hence, there may still be room for improvement in this aspect, as will be described in Chapter 6.

If Parsa (2003) used the condition number to assess the robustness of *Plato*, Williams and Fyfe (2004) directed their attention towards the other end of the spectrum: those accelerometer arrays that are close to being singular. Indeed, these authors analyzed planar accelerometer arrays of two, three, and four uniaxial accelerometers, and found the conditions under which these arrays allow for the estimation of some or all the components of the planar acceleration field. The main contribution of Williams and Fyfe (2004) lies in the guidelines provided to accelerometer-array designers regarding the location and orientation accelerometers so that the resulting array allows for the identification of *any* planar rigid-body acceleration field. This method is revisited in Chapter 7, generalizing it to planar arrays of $n \geq 4$ accelerometers. Moreover, in this Chapter, the introduction of the accelerometer pole to the solution of Williams and Fyfe (2004) is thought to bring deeper insight, as it turns the problem into a purely geometric one.

Some other researchers (Schuler, 1965; Mostov, 2000; Giansanti et al., 2003, see, for example) performed symbolic error analyses on specific accelerometer arrays to evaluate the effects of accelerometer measurement errors

and accelerometer misalignments. The merit of these studies would probably be the possibility of estimating the performance of accelerometer-only solutions with respect to other IMUs for researchers working in fields outside the main biomechanics applications of accelerometer arrays.

Apparently, accelerometer arrays have drawn some interest over the past decades and in various fields of engineering. However, few researchers have attempted general analyses, focusing rather on specific, simple geometries of accelerometer arrays. Chapters 6 and 7 of this work are dedicated to the analysis of accelerometer arrays, with the objective of remaining as general as possible. This analysis yields an expression that permits the extraction of the parameters of the rigid-body acceleration field from the readouts of a generic accelerometer array. In general, the rigid-body acceleration field estimate includes estimates of the acceleration of any of its points, its angular acceleration, and the quadratic powers of the components its angular velocity. Hence, it is possible to estimate the rigid-body angular velocity from its acceleration field. For this purpose, several methods are available, which are reviewed in the following section.

1.4 Rigid-Body Angular-Velocity Estimation from the Acceleration Field

The principle behind rigid-body angular velocity estimation from point-acceleration measurements is explained in Section 6.2, and is summarized here for quick reference. Assume that points A and B pertain to the same rigid

body, and that their positions in a fixed reference frame[1] are given by vectors $\mathbf{p}_A$ and $\mathbf{p}_B$, respectively. Then, the acceleration of point A with respect to that of point B may be expressed as

$$\ddot{\mathbf{p}}_A = \ddot{\mathbf{p}}_B + \mathbf{W}(\mathbf{p}_A - \mathbf{p}_B), \tag{1.1}$$

where $\mathbf{W} \equiv \dot{\mathbf{\Omega}} + \mathbf{\Omega}^2$ is the angular acceleration matrix (Angeles, 1999), $\boldsymbol{\omega} \in \mathbb{R}^3$ is the rigid-body angular velocity, $\mathbf{\Omega} \equiv \mathrm{CPM}(\boldsymbol{\omega})$, and $\mathrm{CPM}(\cdot)$ denotes the cross-product matrix[2] . Upon noticing that, in a rigid body, the difference $\mathbf{p}_A - \mathbf{p}_B$ is constant in a fixed reference frame, and measuring the accelerations of a sufficient number of pairs of points of the rigid body, one may infer the angular acceleration matrix $\mathbf{W}$. Hence, one may estimate the angular acceleration and the angular velocity, up to a sign indeterminacy.

1.4.1 Tangential Acceleration (TA) Methods

The first group of methods uses the time-integration of the angular acceleration, which is obtained, in turn, from tangential acceleration measurements. Hence, we label this class the TA methods. From the literature, these methods are most popular, since they are preferred to others for impact tests. Notice that they have also been used by researchers in other fields—see (Chen et al., 1994; Mostov et al., 1997; Tan et al., 2001), for example. In the TA methods, $\boldsymbol{\omega}$ is estimated from the skew-symmetric component of the angular acceleration

[1] As the discussion here is of a kinematic nature, the reference frame need not be inertial.

[2] $\mathrm{CPM}(\mathbf{a})$ is defined as $\partial(\mathbf{a} \times \mathbf{b})/\partial\mathbf{b}$, for any $\mathbf{a}, \mathbf{b} \in \mathbb{R}^3$.

matrix, which can be summarized symbolically as

$$\hat{\boldsymbol{\omega}} = \text{vect}(\hat{\mathbf{W}}) \tag{1.2a}$$

$$\hat{\boldsymbol{\omega}}_{TA}(t) = \int_0^t \hat{\boldsymbol{\omega}}(\tau)d\tau, \tag{1.2b}$$

where $\hat{\boldsymbol{\omega}}$ is the axial vector[3] of $\hat{\mathbf{W}}$, and $\hat{(\cdot)}$ is an estimate of $(\cdot)$. Several specific methods may be drawn from eq. (1.2a) by changing the numerical integration method, but, apart from that, the algorithm being linear, it is difficult to imagine that there would be any room for improvement here. Hence, for the sake of conciseness, we choose to use only one integration method, namely, the trapezoidal rule. We will refer to this method by the acronym TA, indiscriminately from the class to which it pertains.

1.4.2 Centripetal Acceleration (CA) Methods

The second class includes all methods that consist in taking the square-root of the centripetal acceleration, that is represented by the symmetric component $\mathbf{W}_S$ of $\mathbf{W}$. This class will therefore be referred to as the CA methods. In this category, the customary approach is to combine linearly the diagonal terms of $\mathbf{W}$ in order to obtain the squares of the components of $\boldsymbol{\omega}$. The ensuing square-root operation yields the absolute values of the components of $\boldsymbol{\omega}$. One must thus cope with sign-ambiguity. Schuler (1965) and Grammatikos (1965) suggested that low-cost extra sensors be added to resolve the sign-ambiguity. Another solution, proposed by Parsa (2003), and which seems more reasonable to the author, is to simply use the signs of the TA estimate. As a result, we

[3] The axial vector $\text{vect}(\mathbf{A})$ of matrix $\mathbf{A} \in \mathbb{R}^{3\times3}$ is defined such that $\text{vect}(\mathbf{A})\times \mathbf{u} = (1/2)(\mathbf{A} - \mathbf{A}^T)\mathbf{u}$, for any vector $\mathbf{u} \in \mathbb{R}^3$.

obtain

$$
\begin{aligned}
&\texttt{if } \operatorname{tr}(\hat{\mathbf{W}}) < 0 \texttt{ and } \hat{\boldsymbol{\omega}}_{TA} \neq \mathbf{0}_3 \\
&\quad \hat{\zeta}_i = \hat{w}_{i,i} - (1/2)\operatorname{tr}(\hat{\mathbf{W}}), \quad i = 1,2,3, \\
&\quad \hat{\omega}_{CAD,i} = \operatorname{sgn}(\hat{\omega}_{TA,i})\mathrm{u}(\hat{\zeta}_i)\sqrt{\hat{\zeta}_i}, \quad i = 1,2,3, \\
&\texttt{else} \\
&\quad \hat{\boldsymbol{\omega}}_{CAD} = \mathbf{0}_3, \\
&\texttt{end}
\end{aligned} \tag{1.3}
$$

where $\hat{w}_{i,j}$ is the (i,j) entry of $\hat{\mathbf{W}}_S$, $\operatorname{sgn}(\cdot)$ is the signum function, and $\mathrm{u}(\cdot)$ is the Heaviside (step) function. As it uses only the diagonal entries of $\mathbf{W}$, this estimation algorithm will be referred to as the CAD method.

An alternative method, which also pertains to the CA category was reported by Peng and Golnaraghi (2004); the authors nonetheless point out that this algorithm is prone to singularity problems. This approach uses the off-diagonal entries of $\mathbf{W}_S$ to estimate the square of the components of the angular velocity. For this reason, we choose the label CAOD for this method. The sign ambiguity may be resolved by resorting, again, to the TA estimate of the angular velocity. This yields the algorithm

$$
\begin{aligned}
&\texttt{for } i,j,k = 1,2,3, \quad i \neq j \neq k \neq i, \\
&\quad \hat{\xi}_i = \hat{w}_{i,j}\hat{w}_{k,i}/\hat{w}_{j,k}, \\
&\quad \hat{\omega}_{CAOD,i} = \operatorname{sgn}(\hat{\omega}_{TA,i})\mathrm{u}(\hat{\xi}_i)\sqrt{\hat{\xi}_i}, \\
&\texttt{end}
\end{aligned} \tag{1.4}
$$

where one notices that ξ_i becomes undetermined whenever $w_{j,k} = 0$, that is, when $\omega_j = 0$ or $\omega_k = 0$. In fact, these last equalities imply also that $w_{i,j}$ or $w_{i,k}$ be null, respectively. Hence, whenever any of the components of $\boldsymbol{\omega}$ goes

to zero, the other two components experience indeterminacies of the type 0/0, thereby making the algorithm unstable. This problem may be circumvented or attenuated by resorting to a different estimation method over certain ranges of angular velocity values.

Because the estimation of the angular velocity from centripetal acceleration measurement is a nonlinear problem, there may still be room for improvement of the robustness of its solutions. Following this idea, in Chapter 8, we propose four novel CA methods.

1.4.3 Tangential and Centripetal Acceleration (TCA) Methods

A third class of estimation methods may be identified by observing that the TA and the CA methods can be combined in order to provide more robust angular-velocity estimates. Let us call this the class of TCA methods. Obviously, the existing CA methods detailed above make use of the TA method, but since it is only for the purpose of determining the signs of the angular-velocity components, we will not include them in the TCA category. Indeed, it is reasonable to think that only a small piece of the information contained in the TA estimate is used in the CA methods, and that, therefore, their recombination with the TA estimate may yield more accurate results. Accordingly, all methods that use both the skew-symmetric and the symmetric components of $\mathbf{W}$, the former being used to change not only the signs of the square-roots of the latter, but also their magnitudes, will be considered as pertaining to the TCA class.

A first member of this class, which was proposed by Peng and Golnaraghi (2004), will be called the TCAQ method, the letter Q standing for quadratic.

Indeed, these authors remarked that the quadratic equations

$$\hat{\omega}_{TCAQ,i}^2 + \hat{\omega}_{TCAQ,i}\hat{\omega}_{TA,j} + (1/2)\mathrm{tr}(\hat{\mathbf{W}}) - \hat{w}_{i,i} - \hat{w}_{i,j} = 0, \quad i,j = 1,2,3, \quad i \neq j, \tag{1.5}$$

hold whenever the estimates are accurate. Angular velocity estimates may then be computed as

$$\begin{aligned}
&\texttt{for } \; i,j = 1,2,3, \quad i \neq j \\
&\quad \hat{\eta}_{i,j} = \hat{\omega}_{TA,j}^2 + 4\hat{w}_{i,i} + 4\hat{w}_{i,j} - 2\mathrm{tr}(\hat{\mathbf{W}}) \\
&\quad \hat{\omega}_{TCAQ,i} = -(1/2)\hat{\omega}_{TA,j} + (1/2)\mathrm{sgn}(2\hat{\omega}_{TA,i} + \hat{\omega}_{TA,j})\mathrm{u}(\hat{\eta}_{i,j})\sqrt{\hat{\eta}_{i,j}} \\
&\texttt{end}
\end{aligned} \tag{1.6}$$

where it is apparent that two possible values of j exist for a given i and, therefore, two estimates of ω_i are available. In the subsequent simulations, we choose the estimate that corresponds to the maximum value of $\hat{\eta}_{i,j}$.

A second method, which was proposed by Parsa et al. (2005), falls within the TCA category. The authors define a function $\mathbf{f}$ mapping the angular velocity onto the six-dimensional array $\mathbf{w}$ of the distinct entries of $\mathbf{W}_S$, that is,

$$\begin{aligned}
\mathbf{f}(\boldsymbol{\omega}) &\equiv \begin{bmatrix} -\omega_2^2 - \omega_3^2 & -\omega_3^2 - \omega_1^2 & -\omega_1^2 - \omega_2^2 & \omega_1\omega_2 & \omega_2\omega_3 & \omega_3\omega_1 \end{bmatrix}^T \\
&= \begin{bmatrix} w_{1,1} & w_{2,2} & w_{3,3} & w_{1,2} & w_{2,3} & w_{3,1} \end{bmatrix}^T \equiv \mathbf{w},
\end{aligned} \tag{1.7}$$

Notice that $\mathbf{f}$ is neither injective nor surjective and, hence, it is not invertible. Nevertheless, one may still compute its gradient, which allows for its Taylor series expansion:

$$\mathbf{f}(\boldsymbol{\omega}) = \mathbf{f}(\hat{\boldsymbol{\omega}}_{TA}) + \frac{\partial \mathbf{f}(\boldsymbol{\omega})}{\partial \boldsymbol{\omega}} \Delta\hat{\boldsymbol{\omega}} + O(2), \tag{1.8}$$

where $\Delta\hat{\boldsymbol{\omega}}$ will be the correction on the angular velocity estimate $\hat{\boldsymbol{\omega}}_{TA}$ obtained from the TA method, and where the gradient can be verified to be

$$\frac{\partial \mathbf{f}(\boldsymbol{\omega})}{\partial \boldsymbol{\omega}} = \begin{bmatrix} 0 & -2\omega_1 & -2\omega_1 & \omega_2 & 0 & \omega_3 \\ -2\omega_2 & 0 & -2\omega_2 & \omega_1 & \omega_3 & 0 \\ -2\omega_3 & -2\omega_3 & 0 & 0 & \omega_2 & \omega_1 \end{bmatrix}^T . \tag{1.9}$$

One may also verify that $\partial \mathbf{f}(\boldsymbol{\omega})/\partial \boldsymbol{\omega}$ is of rank 3 if and only if $\|\boldsymbol{\omega}\|_2 \neq 0$, which allows the computation of its left Moore-Penrose generalized inverse (Golub and Van Loan, 1996) $[\partial \mathbf{f}(\boldsymbol{\omega})/\partial \boldsymbol{\omega}]^\dagger$. Upon estimating the left-hand side of eq. (1.8) from $\hat{\mathbf{W}}_S$ and using $\hat{\boldsymbol{\omega}}_{TA}$ to estimate the gradient of $\mathbf{f}$, we obtain

$$\Delta\hat{\boldsymbol{\omega}} = (\partial \mathbf{f}(\boldsymbol{\omega})/\partial \boldsymbol{\omega})|^\dagger_{\boldsymbol{\omega}=\hat{\boldsymbol{\omega}}_{TA}} [\hat{\mathbf{w}} - \mathbf{f}(\hat{\boldsymbol{\omega}}_{TA})]. \tag{1.10}$$

The resulting estimate may be labelled $\hat{\boldsymbol{\omega}}_{TCAT}$, with T standing for the Taylor series expansion; it may be computed from eq. (1.10) as $\hat{\boldsymbol{\omega}}_{TCAT} = \hat{\boldsymbol{\omega}} + \Delta\hat{\boldsymbol{\omega}}$. In summary, its associated algorithm is

```
if  ω̂_TA ≠ 0_3
   Q, R ← Householder( (∂f(ω)/∂ω)|_{ω=ω̂_TA} ),
   Δω̂ ← Backsubstitution(R, Q^T(ŵ − f(ω̂_TA))),
   ω̂_TCAT = ω̂_TA + Δω̂,
else
   ω̂_TCAT = 0_3,
end
```
(1.11)

where `Householder` uses Householder reflections (see Golub and Van Loan, 1996) to return a QR factorization of its matrix argument, while `Backsubstitution` returns the solution of the linear system associated with its upper-triangular matrix and vector arguments through a back substitution. The TCA class is the topic of Chapter 9, where a TCA method based on extended

Kalman filtering is proposed.

1.5 Objectives

The main goal of this work is the improvement of the robustness of accelerometer arrays. To this end, we proceed by analysis. Hence, the constitutive accelerometers are the focus of Chapters 2-5. In Chapter 2, a new class of mechanical architectures for multiaxial accelerometers is proposed, with the aim of reducing the accelerometer sensitivity to cross-axis accelerations and rotations. Chapters 3-5 are dedicated to the design, microfabrication, and testing of a biaxial accelerometer based on one of the proposed mechanical architectures. Arrays of accelerometers are studied in Chapters 6 and 7. In the former, the input-output equations of a generic accelerometer array are given; in the latter, the conditions for an accelerometer array to allow the identification of the complete rigid-body acceleration field are stated. Finally, Chapters 8 and 9 are concerned with the estimation of the angular velocity from the rigid-body acceleration field. In particular, Chapter 8 includes algorithms for the estimation of the angular velocity from the centripetal component of the rigid-body acceleration field, while Chapter 9 includes similar algorithms that rely on both the centripetal and the tangential components of the rigid-body acceleration field.

Chapter 2

Parallel-Kinematics Machine Architectures for Multiaxial Accelerometers

In general, an accelerometer comprises a *proof-mass* $\mathcal{M}$ and a *suspension* coupling the mass with the *accelerometer frame*. The latter is rigidly mounted onto the moving body whose position, velocity and acceleration are to be estimated.

The novelty of the accelerometers introduced here lies in their versatile architecture. Versatility means that, with a common feature of their architecture, the accelerometers allow for the measurement of one, two or three acceleration components of the same body-point. The novel architecture can be termed *simplicial* in that the suspension consists of $n + 1$ *legs*, where n is the number of acceleration components that the accelerometer is capable of measuring. Here, we recall that a *simplex*, in the realm of mathematical programming (Hillier and Lieberman, 1995), is a polyhedron with the minimum number of vertices embedded in $\mathbb{R}^n$. Therefore, in one-dimensional space, the simplex is a line segment, its two "vertices" being its two end-points; in two-dimensional space, the simplex is a triangle; in three-dimensional space, a tetrahedron. While the shapes of the triangle and the tetrahedron can,

in principle, be arbitrary, one common feature of our accelerometer class is that the the simplexes used have faces of equal dimensions. The outcome is that the accelerometer is equally sensitive in all directions of motion, which makes these architectures *isotropic*. Here, we prefer to speak of *isotropy* rather than *symmetry*, as the latter, including the former as special instance, is more general. In the case of accelerometers, having an isotropic architecture implies that the dynamic properties of the sensor are the same in all directions. Moreover, the $n+1$ legs provide *redundancy* in the measurements, and hence, *robustness* against measurement errors. On the other hand, using more legs adds to the complexity of the device. In particular, it affects the fabrication by leaving less space for each leg around the proof-mass, which forces shorter legs with thinner compliant joints, for the same stiffness requirements. Hence, from mere intuition, having one more leg than the number of accelerometer sensitive directions appears as a reasonable trade-off between robustness and fabrication costs. We describe below the three types of accelerometers, for $n = 1, 2$ and 3, in this order.

The rationale behind the design principle used in all three accelerometer types lies in the mobility analysis of kinematic chains, as first proposed in Hervé (1978) and then applied systematically in Angeles (2005) to the design of parallel manipulators. Furthermore, the building block of the three accelerometer types is the Π-joint[1], as described in detail in Angeles (2005), and recalled in Section 2.4. This choice was motivated by two main reasons: (*i*) the Π-joint lends itself to compliant, micromachined implementation; (*ii*) in general, the kinetostatics behaviour of the compliant Π-joint is close to the

[1] Π stands for "Pi"-joint, as termed by Hervé and Sparacino (1992).

kinematics behaviour of its rigid counterpart (Derderian et al., 1996), which is not the case with all compliant joints. Hence, the Π-joint is especially well suited for implementation as a purely compliant mechanism, whereby the links and joints of the proposed multiaxial accelerometers are all fabricated of one single piece, as proposed in Arai et al. (1996).

2.1 The Simplicial Uniaxial Accelerometer (SUA) Architecture

The one-dimensional accelerometer is intended to measure the acceleration of a point constrained to move along a line. This is achieved by means of a ΠΠ leg-architecture. A Π joint is, essentially, a parallelogram linkage. In order to obtain a one-dimensional design, we use two opposing ΠΠ legs lying in perpendicular planes to sustain the proof-mass, as shown in Fig. 2.1.This

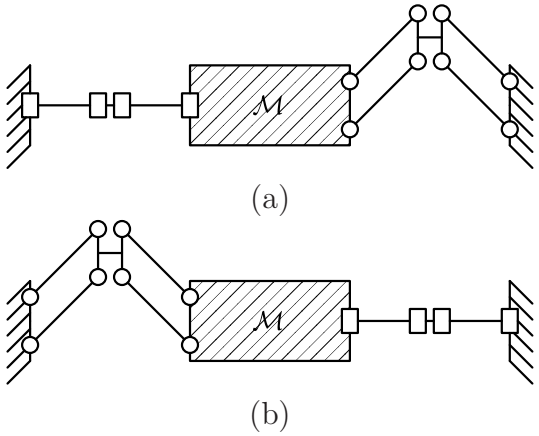

Figure 2.1: The SUA made-up of two ΠΠ chains: (a) top view; (b) front view.

architecture allows only motion along the line of intersection of the two planes containing the Π joints, while providing a high stiffness in a plane normal to this direction. For Earth-bound applications, the accelerometer may be oriented so that each of the two orthogonal planes containing the legs forms a 45° angle with respect to the vertical, thereby eliminating virtually any parasitical displacements produced by gravity.

2.2 The Simplicial Biaxial Accelerometer (SBA) Architecture

Other compliant planar parallel mechanisms have been proposed in the past, among which we may cite the one proposed by Yi et al. (2002). These researchers produced a compliant version of the planar 3RRR[2] parallel mechanism. In our case, however, we are to achieve translations in the plane only; hence, we start from a linkage which constrains any proof-mass rotation. By laying out the three ΠΠ legs in a common plane at 120° from one another, that is, along the three medians of an equilateral triangle, we obtain the mechanism shown in Fig. 2.2. This mechanism allows translation in the common plane, while providing a high stiffness in a direction normal to the plane, which includes in-plane rotations.

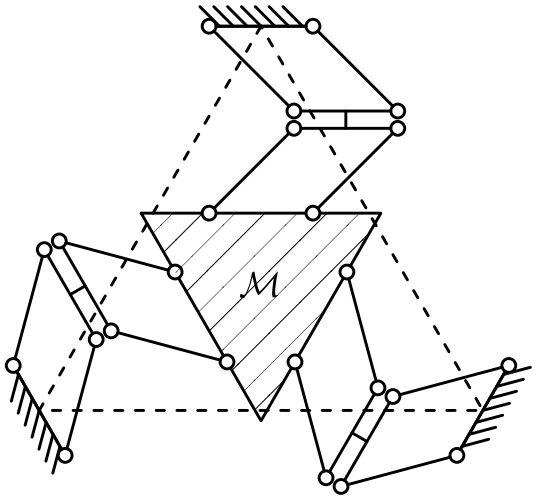

Figure 2.2: The SBA made-up of three ΠΠ chains

2.3 The Simplicial Triaxial Accelerometer (STA) Architecture

Many a parallel-robot architecture is available to generate pure translations of the moving platform with respect to the base (Clavel, 1988; Kong and Gosselin, 2007). We may also cite the compliant parallel mechanism of Pham

[2] R stands for *revolute joint*.

et al. (2005), which allows for pure translations of its moving platform in space. The proposed device is based on a novel architecture made up of the "legs" of the Japan Mechanical Engineering Laboratory (MEL) Micro Finger (Arai et al., 1996).

The proposed architecture is shown in Fig. 2.3, with a regular, heavy tetrahedron $\mathcal{M}$ playing the role of the moving platform, used as the proof-mass of the accelerometer. The four "legs" of the device are attached, at one end, to

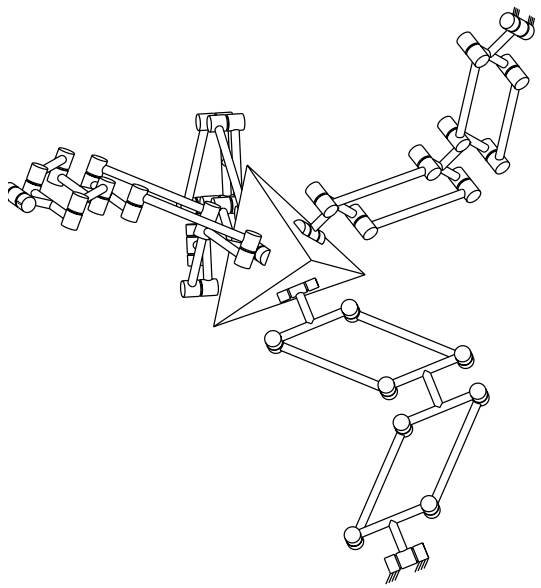

Figure 2.3: The STA made-up of four $R\Pi\Pi\Pi R$ chains

the tetrahedron-shaped proof-mass $\mathcal{M}$, at the other end to the moving body on which the accelerometer is mounted. This body is the accelerometer frame. Each leg is a $R\Pi\Pi\Pi R$ chain, where R stands for revolute, or pin joint. The $R\Pi\Pi\Pi R$ chain includes two revolute joints, one at each of its two ends, coupling

the leg to the tetrahedron and to the body[3] . This kinematic chain lies in a plane that contains the axes of its revolute joints and its two Π joints. This plane may be identified by means of its normal unit vector $\mathbf{n}_J$, as in Fig. 2.4, which, in turn, can be estimated from an angular measurement at the revolute joint that couples the leg to the moving body. Notice that the mechanism thus resulting comprises 40 flexures distributed onto four legs, whereas the architecture proposed in Pham et al. (2005) was made up of 51 flexures in three legs.

From mere intuition, it is preferable to have each leg of the parallel-kinematics machine lying in a plane that is orthogonal to its corresponding face of the tetrahedron proof-mass. This implies that the vector $\mathbf{n}_J$ associated with the J^{th} leg be parallel to the corresponding face of the tetrahedron. On the other hand, the direction of $\mathbf{n}_J$ within that plane remains to be determined. For this purpose, we examine the condition number of the forward Jacobian matrix of the parallel kinematic machine. Indeed, in the case of an accelerometer with body-fixed sensors that provide estimates of the angular displacements of the revolute joints coupling the accelerometer frame to the legs, the forward Jacobian matrix represents the sensitivity of the angular sensors to proof-mass translational displacements $\mathbf{p}$. Therefore, in order to distribute the sensor errors and the compliant joint stresses evenly, an isotropic forward Jacobian matrix is desirable.

[3] In the sequel, the R joints of the $R\Pi\Pi\Pi R$ chain are not to be confused with those of the parallelograms. We need not refer to the latter as stand-alone joints in this thesis.

As shown by Cardou and Angeles (2007a), the forward Jacobian matrix may be taken to be the left Moore-Penrose generalized inverse of $\mathbf{N} \equiv [\mathbf{n}_I \quad \mathbf{n}_{II} \quad \mathbf{n}_{III} \quad \mathbf{n}_{IV}]^T \in \mathbb{R}^{4\times 3}$. Therefore, the forward Jacobian matrix is isotropic if and only if unit-vectors $\mathbf{n}_J$, $J = I, II, III, IV$, form an isotropic set. This, in turn, is achieved if and only if these vectors represent the positions of the vertices of a regular tetrahedron with respect to its centroid.

On the other hand, let P be the centroid of the tetrahedral proof-mass, and F_J the centroid of the tetrahedron face that corresponds to the J^{th} leg of the parallel-kinematics machine, as depicted in Fig. 2.4. In the sequel, we define vector $\mathbf{f}_J$, which has its tail at P, and its head at F_J. Notice that points F_J, $J = I, II, III, IV$, are themselves located at the vertices of a tetrahedron inscribed into the proof-mass.

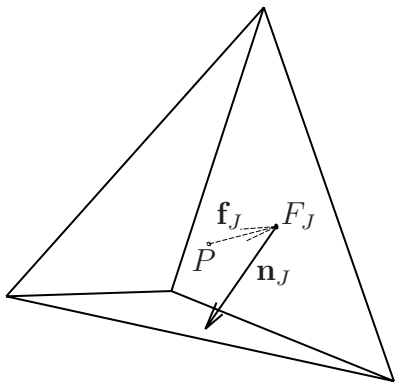

Figure 2.4: Orientation of the J^{th} leg with respect to the tetrahedral proof-mass

The foregoing array allows us to write any isotropic set of unit-vectors $\mathbf{n}_J$, $J = I, II, III, IV$, as

$$\mathbf{n}_J = \mathbf{Q}\mathbf{f}_J/\|\mathbf{f}_J\|_2, \quad J = I, II, III, IV, \tag{2.1}$$

where $\mathbf{Q} \in \mathbb{R}^{3\times 3}$ is a proper orthogonal matrix, and, hence, rotates vector $\mathbf{f}_J/\|\mathbf{f}_J\|_2$ onto $\mathbf{n}_J$, $J = I, II, III, IV$. Since we also require that $\mathbf{n}_J$ lie in its corresponding tetrahedron face, we may add the constraints

$$\mathbf{n}_J^T \mathbf{f}_J = 0, \quad J = I, II, III, IV. \tag{2.2}$$

Equations (2.1) and (2.2) may be combined in order to eliminate vectors $\mathbf{n}_J$, which yields,

$$\mathbf{f}_J^T \mathbf{Q} \mathbf{f}_J = 0, \quad J = I, II, III, IV. \tag{2.3}$$

Let us now parameterize the rotation matrix $\mathbf{Q}$ with the array $\mathbf{q} \equiv [r_0 \quad \mathbf{r}^T]^T \in \mathbb{R}^4$ of Euler-Rodrigues parameters. From Angeles (2007), we have the relation

$$\mathbf{Q} = (r_0^2 - \mathbf{r}^T\mathbf{r})\mathbf{1}_{3\times 3} + 2\mathbf{r}\mathbf{r}^T + 2r_0\mathbf{R}, \tag{2.4}$$

where $\mathbf{R} \equiv \mathrm{CPM}(\mathbf{r})$. Substituting eq. (2.4) into eq. (2.3) leads to

$$(r_0^2 - \mathbf{r}^T\mathbf{r})\mathbf{f}_J^T\mathbf{f}_J + 2(\mathbf{f}_J^T\mathbf{r})^2 = 0, \quad J = I, II, III, IV. \tag{2.5}$$

Upon recalling that the Euler-Rodrigues parameters obey the constraint

$$\mathbf{q}^T\mathbf{q} = r_0^2 + \mathbf{r}^T\mathbf{r} = 1, \tag{2.6}$$

we can rewrite eq. (2.5) as

$$(2r_0^2 - 1)f^2 + 2(\mathbf{f}_J^T\mathbf{r})^2 = 0, \tag{2.7a}$$

whence,

$$\mathbf{r}^T\mathbf{f}_J = \pm f\sqrt{1/2 - r_0^2}, \quad J = I, II, III, IV, \tag{2.7b}$$

or, in compact form,

$$\mathbf{r}^T\mathbf{F}^T = f\sqrt{1/2 - r_0^2}\,[\pm 1 \quad \pm 1 \quad \pm 1 \quad \pm 1], \tag{2.7c}$$

where $f \equiv \|\mathbf{f}_J\|_2$, $J = I, II, III, IV$, and $\mathbf{F} \equiv [\mathbf{f}_I \quad \mathbf{f}_{II} \quad \mathbf{f}_{III} \quad \mathbf{f}_{IV}]^T$. Equation (2.7a) represents $2^4 = 16$ different linear systems of equations to solve for $\mathbf{r}$. However, only six of these overdetermined systems allow for exact solutions, and, for that reason, we drop the other 10. There does not seem to be any good reason to choose one of the remaining six linear systems rather than the others. For the purpose of this analysis, we select arbitrarily the linear system

$$\mathbf{F}\mathbf{r} = f\sqrt{1/2 - r_0^2}\mathbf{t}, \tag{2.8}$$

where $\mathbf{t} \equiv [1 \quad 1 \quad -1 \quad -1]^T$. The corresponding exact solution may be hence written as

$$\mathbf{r} = f\sqrt{1/2 - r_0^2}(\mathbf{F}^T\mathbf{F})^{-1}\mathbf{F}^T\mathbf{t}, \tag{2.9}$$

thereby obtaining, upon substituting this result into eq. (2.6),

$$f^2(1/2 - r_0^2)\mathbf{t}^T\mathbf{F}(\mathbf{F}^T\mathbf{F})^{-2}\mathbf{F}^T\mathbf{t} + r_0^2 = 1. \tag{2.10}$$

One may verify that this last equation is frame-invariant, and, furthermore, independent from the scale of the regular tetrahedron. Hence, one may compute one of its two general solutions to be $r_0 = 1/2$, which yields $\mathbf{r}$ after its substitution into eq. (2.9). If r_0 is frame-invariant, $\mathbf{r}$ depends on the frame in which $\mathbf{f}_J$, $J = I, II, III, IV$, is expressed. For example, upon choosing the representation

$$\mathbf{f}_I = \begin{bmatrix} -\sqrt{2/3} \\ \sqrt{2}/3 \\ 1/3 \end{bmatrix}, \; \mathbf{f}_{II} = \begin{bmatrix} \sqrt{2/3} \\ \sqrt{2}/3 \\ 1/3 \end{bmatrix}, \; \mathbf{f}_{III} = \begin{bmatrix} 0 \\ -2\sqrt{2}/3 \\ 1/3 \end{bmatrix}, \; \mathbf{f}_{IV} = \begin{bmatrix} 0 \\ 0 \\ -1 \end{bmatrix}, \tag{2.11}$$

we obtain

$$\mathbf{q} = \begin{bmatrix} 1/2 & 0 & 1/\sqrt{2} & 1/2 \end{bmatrix}^T. \tag{2.12}$$

The rotation matrix $\mathbf{Q}$ is then found from eq. (2.4), namely,

$$\mathbf{Q} = \begin{bmatrix} -1/2 & -1/2 & 1/\sqrt{2} \\ 1/2 & 1/2 & 1/\sqrt{2} \\ -1/\sqrt{2} & 1/\sqrt{2} & 0 \end{bmatrix}, \tag{2.13}$$

which finally allows for the computation of $\mathbf{n}_J$, $J = I, II, III, IV$, from eq. (2.1). This yields the vectors

$$\mathbf{n}_I = \begin{bmatrix} 1/\sqrt{6} \\ \sqrt{2}/3 - 1/\sqrt{6} \\ 1/3 + 1/\sqrt{3} \end{bmatrix}, \ \mathbf{n}_{II} = \begin{bmatrix} -1/\sqrt{6} \\ \sqrt{2}/3 + 1/\sqrt{6} \\ 1/3 - 1/\sqrt{3} \end{bmatrix}, \tag{2.14}$$

$$\mathbf{n}_{III} = \begin{bmatrix} 1/\sqrt{2} \\ -1/(3\sqrt{2}) \\ -2/3 \end{bmatrix}, \text{ and } \mathbf{n}_{IV} = \begin{bmatrix} -1/\sqrt{2} \\ -1/\sqrt{2} \\ 0 \end{bmatrix}, \tag{2.15}$$

which are represented with gray arrows in Fig. 2.5 against the tetrahedral proof mass of the STA.

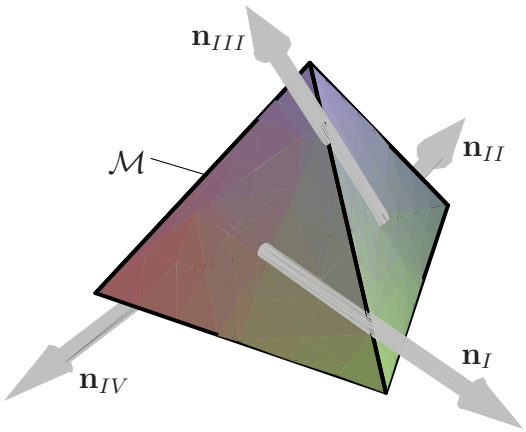

Figure 2.5: Orientation of vectors $\mathbf{n}_J$, $J = I, II, III, IV$, with respect to the tetrahedral proof mass

2.4 Compliant Realization of the Simplicial Biaxial Accelerometer

The common compliant approximation of a revolute joint is a straight flexible beam cast at both ends. If two such beams are identical and connected to the same two rigid bodies in such a way that their flexible directions given by the (parallel) axes about which the rigid cross-sections rotate are parallel, then the resulting mechanism can be called a compliant Π joint, parallel-guiding mechanism (Derderian et al., 1996), or parallelogram. Indeed, the flexible mechanism has the shape of a parallelogram, as can be seen from Fig. 2.6(a), and allows only for translation of the upper with respect to the lower beam along a circle. Arai et al. (1996) proposed a slightly different version of the compliant Π-joint—see Fig. 2.6(b), which uses *notched* beams rather than beams with constant cross-sections. The advantage of the notched Π-joint is higher ratios between the stiffness in the flexible direction and the stiffness in the other directions. The main drawback of this solution, as pointed out in Trease et al. (2005), is smaller beam minimum thickness—thereby rendering machining costlier, while giving rise to higher stress concentrations, and leading to a limited range of motion.

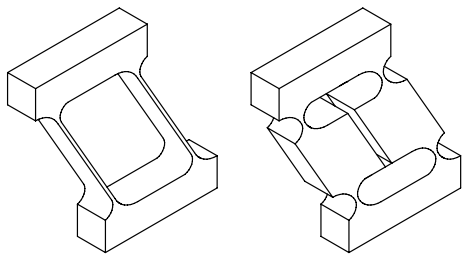

(a) (b)

Figure 2.6: Compliant realization of the Π-joint (a) with a pair of constant cross-section beams; and (b) with four notched beams

Because of its planar nature, the 2D-3ΠΠ architecture can be realized by means of microfabrication techniques. Here, the type of Π joint could be any of

the two proposed in Fig. 2.6. However, in order to minimize the cross-axis sensitivity, we must keep the out-of-plane thickness as high as possible. There are not many ways, in micromachining, to achieve high thickness-to-width ratios, that is, etch deeper than wide in the substrate. Deep Reactive Ion Etching (DRIE) is probably the most reliable technique, as it allows for trenches of a few microns wide by several hundred microns deep. As a general rule, the etch depth is increased at the expense of the in-plane accuracy, and, for that reason, it is preferable to keep the flexible beams as thick as possible. This leads to the use of constant cross-section beams in the Π joints instead of notched beams.

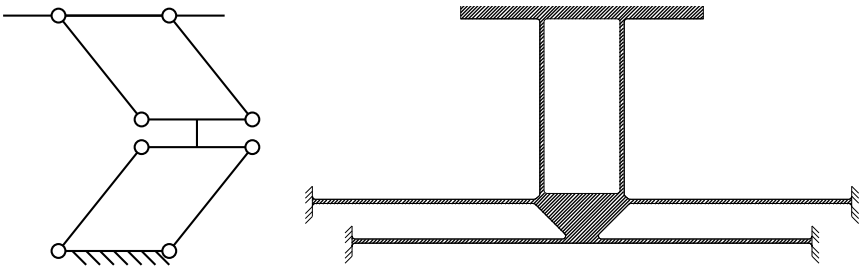

Figure 2.7: One leg of the 2D-3ΠΠ architecture: (a) rigid and (b) compliant realizations

As a result, the rigid-link ΠΠ leg of the 2D-3ΠΠ architecture, which is reproduced in Fig. 2.7(a), takes the compliant form shown in Fig. 2.7(b). In this compliant realization, notice that two Π joints replace the proximal Π joint of the rigid ΠΠ leg. This preserves the symmetry of the leg.

A CAD model of the corresponding compliant realization of the SBA is shown in Fig. 2.8. One may notice that the first Π joint of each leg, that is, the Π joint attached to the accelerometer frame, was mirrored in order to achieve

symmetry in each leg. Also, the proof-mass displacements are sensed by measuring the capacitance variations between the electrodes and the proof-mass.

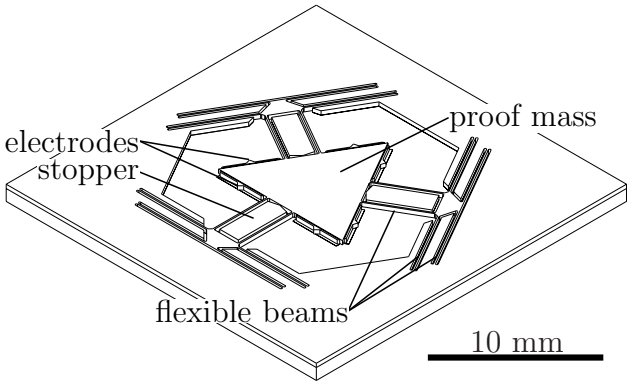

Figure 2.8: CAD model of a micromachined compliant realization of the 2D-3ΠΠΠ mechanism

Nevertheless, the proposed architecture lends itself to other types of displacement-measurement techniques, such as piezoresistive and piezoelectric sensing. In those cases, the sensors have to be installed on some of the flexible elements of the mechanism in order to track their angular displacements, and, through a direct kinematics solution, the motion of the proof-mass. An important advantage of the SBA architecture is that this problem is linear, provided that the lengths of the intermediate links of the Π joints attached to the proof-mass are known (Cardou and Angeles, 2007a).

In this Chapter, a novel class of multiaxial accelerometers was proposed. Apparently, from Fig. 2.8, the compliant realization of the SBA is well suited for micromachining techniques. For that reason, its detailed design is the topic of the following Chapter.

Chapter 3

Simplicial Biaxial Accelerometer Design

The SBA proposed in Section 2.4 is dimensioned in Section 3.3, the underlying synthesis procedure being based on the dynamics model proposed in Section 3.1, in order to reduce the proof-mass sensitivity to cross-axis accelerations. Even though it was not later tested, a capacitive measurement method is also devised in Section 3.5. We begin by setting up the dynamics model used in this synthesis problem. In order to allow for the evaluation of the proof-mass parasitic motions, this model is developped for general, six-degree-of-freedom proof-mass displacements in space.

3.1 Dynamics Model of Lumped Compliant Mechanisms Undergoing Small Displacements

Since this is a lumped-parameter model, each component of the flexible mechanism falls into one of two categories. The first category gathers the m *compliant links*, which are assumed to have no inertia and a given non-null compliance in all directions. The second category contains the n *rigid links*, which are attributed a given inertia and no compliance.

Moreover, the compliant links are modelled as straight Euler-Bernoulli straight beams, and all the rigid-link displacements are considered to be *small*.

From this last assumption, the mass and stiffness properties of the links are assumed to be constant, that is, independent from the mechanism posture.

3.1.1 The System Posture

Let us first define the fixed frame $\mathcal{F}$, and frames $\mathcal{R}'_j$, $j = 1, \ldots, n$, respectively, attached to each of the rigid links, as shown in Fig. 3.1. Moreover, we define frame $\mathcal{R}_j$, which coincides with frame $\mathcal{R}'_j$ whenever the j^{th} rigid-body lies in its equilibrium pose; this is designated the reference pose of the j^{th} body. The origins of frames $\mathcal{F}$, $\mathcal{R}_j$, and $\mathcal{R}'_j$, are labelled O, R_j, and R'_j, $j = 1, \ldots, n$, respectively, where R_j is chosen to lie at the mass centre of its corresponding rigid link.

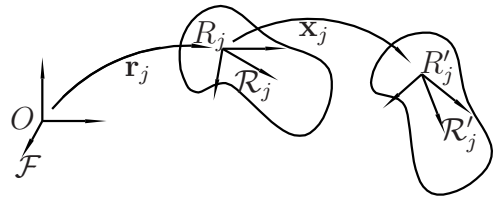

Figure 3.1: The j^{th} rigid link at both its equilibrium pose and its displaced pose

The displacement taking $\mathcal{F}$ into $\mathcal{R}_j$ is described by the pose array $\mathbf{r}_j \equiv [\boldsymbol{\theta}_j^T \quad \boldsymbol{\rho}_j^T]^T$, where $\boldsymbol{\theta}_j \in \mathbb{R}^3$ is defined as the product $\theta_j \mathbf{d}_j$, pertaining to the associated rotation, and $\boldsymbol{\rho}_j \equiv \overrightarrow{OR_j} \in \mathbb{R}^3$. The natural invariants of a rotation are the unit-vector $\mathbf{d}_j$ pointing in the direction of its associated axis, and its angle of rotation θ_j. In order to avoid ambiguities, we use the right-hand rule in order to determine the direction of the rotation around the screw axis, and we constrain $\boldsymbol{\theta}_j$ within a ball of radius π, that is, $0 \leq \|\boldsymbol{\theta}_j\|_2 \leq \pi$. Notice that this leaves an ambiguity at $\|\boldsymbol{\theta}_j\|_2 = \pi$ since, in that case, $\boldsymbol{\theta}_j$ and $-\boldsymbol{\theta}_j$ yield the same rotation. However, since we are using these parameters to describe postures of the mechanism that are close to its static equilibrium posture, this

ambiguity may be resolved a priori by the good judgment of the designer.

Similarly, we define the pose of the j^{th} rigid body with respect to its equilibrium pose as

$$\mathbf{x}_j \equiv [\boldsymbol{\nu}_j^T \quad \boldsymbol{\xi}_j^T]^T, \tag{3.1}$$

where $\boldsymbol{\nu}_j \in \mathbb{R}^3$ is the array of products of the natural invariants for the rotation taking $\mathcal{R}_j$ into $\mathcal{R}'_j$ and following the same convention as that used for $\boldsymbol{\theta}_j$, while $\boldsymbol{\xi}_j \equiv \overrightarrow{R_j R'_j} \in \mathbb{R}^3$. Since the posture of the mechanism is fully described by the poses of all the rigid links, we will regard the set of pose arrays $\mathbf{x}_j$, $j = 1, \ldots, n$, as the system posture. This results in the $6n$-dimensional *posture* vector

$$\mathbf{x} \equiv \begin{bmatrix} \mathbf{x}_1^T & \mathbf{x}_2^T & \cdots & \mathbf{x}_n^T \end{bmatrix}^T. \tag{3.2}$$

3.1.2 The System Kinetic Energy

The angular velocity $\boldsymbol{\omega}_j$ and the time-derivative of the pose array of the j^{th} rigid link obey the relation (Angeles, 2007)

$$\begin{aligned} \boldsymbol{\Omega}_j &= \text{CPM}(\boldsymbol{\omega}_j) = \left[\frac{d}{dt}\left(e^{\text{CPM}(\boldsymbol{\nu}_j)}\right)\right]\left(e^{\text{CPM}(\boldsymbol{\nu}_j)}\right)^T, \\ &= [\text{CPM}(\dot{\boldsymbol{\nu}}_j) + (1/2)\text{CPM}(\dot{\boldsymbol{\nu}}_j)\text{CPM}(\boldsymbol{\nu}_j) \\ &\qquad +(1/2)\text{CPM}(\boldsymbol{\nu}_j)\text{CPM}(\dot{\boldsymbol{\nu}}_j) + O(2)]\, e^{\text{CPM}(-\boldsymbol{\nu}_j)}, \end{aligned} \tag{3.3}$$

i.e.,

$$\boldsymbol{\Omega}_j = \text{CPM}(\dot{\boldsymbol{\nu}}_j) + \frac{1}{2}[\text{CPM}(\boldsymbol{\nu}_j)\text{CPM}(\dot{\boldsymbol{\nu}}_j) - \text{CPM}(\dot{\boldsymbol{\nu}}_j)\text{CPM}(\boldsymbol{\nu}_j] + O(2), \tag{3.4}$$

where $O(2)$ represents the terms that contain products of order two or higher of the natural invariants $\boldsymbol{\nu}_j$. As we are considering only small displacements of the rigid links, we drop any term containing the natural invariants, that is,

all terms of order one and higher, which leads to the approximation

$$\boldsymbol{\omega}_j \approx \dot{\boldsymbol{\nu}}_j, \quad j = 1, \ldots, n. \tag{3.5}$$

On the other hand, the velocity of point R'_j is exactly given by vector $\dot{\boldsymbol{\xi}}_j$.

Let us store the mass properties of the j^{th} rigid link into its associated *inertia dyad*, as defined in (Angeles, 2007):

$$\mathbf{M}_j \equiv \begin{bmatrix} \mathbf{I}_j & \mathbf{O}_{3\times 3} \\ \mathbf{O}_{3\times 3} & m_j \mathbf{1}_{3\times 3} \end{bmatrix}, \tag{3.6}$$

where m_j is the mass of the j^{th} rigid link, $\mathbf{I}_j$ is its inertia matrix about point R_j, its mass centre, and $\mathbf{O}_{3\times 3}$ is the 3×3 zero-matrix. As a result, the kinetic energy T of the system is computed as

$$T = (1/2) \sum_{j=1}^{n} \dot{\mathbf{x}}_j^T \mathbf{M}_j \dot{\mathbf{x}}_j = (1/2) \dot{\mathbf{x}}^T \mathbf{M} \dot{\mathbf{x}}, \tag{3.7}$$

where

$$\mathbf{M} \equiv \begin{bmatrix} \mathbf{M}_1 & \mathbf{O}_{6\times 6} & \cdots & \mathbf{O}_{6\times 6} \\ \mathbf{O}_{6\times 6} & \mathbf{M}_2 & \cdots & \mathbf{O}_{6\times 6} \\ \vdots & \vdots & \ddots & \vdots \\ \mathbf{O}_{6\times 6} & \mathbf{O}_{6\times 6} & \cdots & \mathbf{M}_n \end{bmatrix}$$

will be referred to as the mass matrix of the mechanism.

3.1.3 The System Potential Energy

Consider the i^{th} compliant link that is clamped, at one end, to the j^{th} rigid link, and, at the other end, to the k^{th} rigid link, with $j < k$. From the free-body diagram of the i^{th} compliant link shown in Fig. 3.2(a), we see that the wrench $\mathbf{v}_i \in \mathbb{R}^6$ applied at the mass centre R_j by the j^{th} rigid link onto the i^{th} compliant link has to be balanced by wrench $\mathbf{u}_i(s_i) \in \mathbb{R}^6$ applied at point $S_i(s_i)$, where s_i is a linear coordinate along the straight beam neutral

axis. The wrenches are defined so that their reciprocal product with the small-displacement screws defined in eq. (3.1) be dimensionally meaningful. Therefore, the first three components of the wrench represent a moment, whereas the last three represent a force, the latter applied at the corresponding mass centre, where the wrench is defined. Let us attach frame $\mathcal{S}_i(s_i)$ with axes $X_{\mathcal{S},i}$,

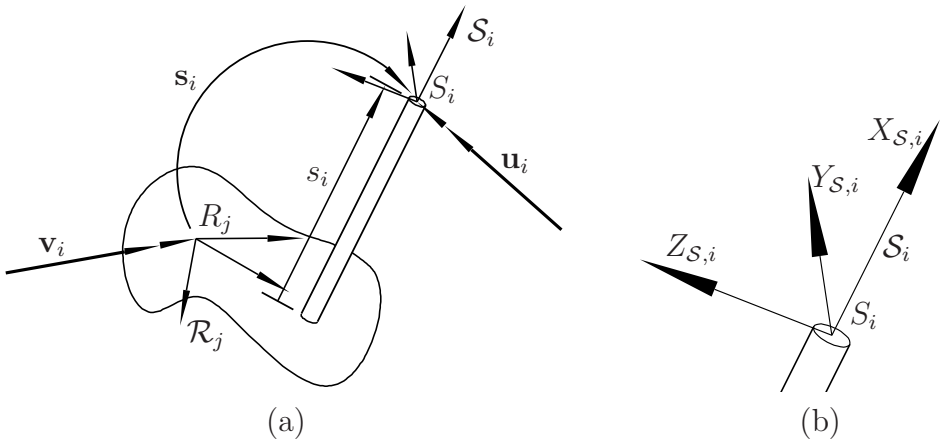

Figure 3.2: The i^{th} compliant link attached to the j^{th} rigid link: (a) layout; (b) detail of the definition of $\mathcal{S}_i(s_i)$

$Y_{\mathcal{S},i}$, and $Z_{\mathcal{S},i}$, to the beam cross-section at S_i, as shown in Fig. 3.2(b). Frame $\mathcal{S}_i(s_i)$ is defined so as to have its $X_{\mathcal{S},i}$-axis tangent to the beam neutral axis and pointing in the positive direction of s_i, and its $Y_{\mathcal{S},i}$- and $Z_{\mathcal{S},i}$-axes along the principal directions of the cross-section. Let $\boldsymbol{\tau}_i$ be the array of products of the natural invariants of the rotation taking frame $\mathcal{R}_j$ into frame $\mathcal{S}_i(s_i)$, following the same convention as that used for $\boldsymbol{\theta}_j$, and $\boldsymbol{\sigma}_i(s_i) \in \mathbb{R}^3$ be the vector directed from point R_j to point $S_i(s_i)$. We regroup these two arrays in the *cross-section pose array*

$$\mathbf{s}_i(s_i) \equiv [\boldsymbol{\tau}_i^T \quad \boldsymbol{\sigma}_i(s_i)^T]^T \in \mathbb{R}^6. \tag{3.8}$$

The strain energy in a beam element of length ds_i, starting at coordinate s_i and ending at coordinate $s_i + ds_i$, is computed as

$$dU_i(s_i) = (1/2)[\mathbf{u}_i(s_i)]^T_{\mathcal{S},i}\mathbf{H}_i(s_i)[\mathbf{u}_i(s_i)]_{\mathcal{S},i}ds_i, \tag{3.9}$$

where $[\,\cdot\,]_{\mathcal{S},i}$ indicates that the quantity $(\,\cdot\,)$ is expressed in frame $\mathcal{S}_i$, which has its origin at S_i. Matrix $\mathbf{H}_i(s_i) \in \mathbb{R}^{6\times6}$, in turn, contains the properties of the cross-section. This matrix is defined according to the strain energy formulas for beams (Roark and Young, 1975), namely,

$$\mathbf{H}_i(s_i) \equiv \text{diag}\left(\frac{1}{G_iJ_i}, \frac{1}{E_iI_{Y,i}}, \frac{1}{E_iI_{Z,i}}, \frac{1}{E_iA_i}, \frac{\alpha_{Y,i}}{G_iA_i}, \frac{\alpha_{Z,i}}{G_iA_i}\right), \tag{3.10}$$

where E and G are the Young and the shear moduli, respectively; $I_{Y,i}$, $I_{Z,i}$ and J_i are the $Y_{\mathcal{S},i}$-axis moment of inertia, the $Z_{\mathcal{S},i}$-axis moment of inertia and the torsional modulus of the beam cross section, respectively[1]; A_i is the area of the cross-section; and $\alpha_{Y,i}$ and $\alpha_{Z,i}$ are the shearing effect coefficients for the $Y_{\mathcal{S},i}$ and $Z_{\mathcal{S},i}$ directions, respectively. Notice that all these parameters are functions of the curvilinear coordinate s_i.

Let us now define the adjoint $\mathbf{S}_i(s_i)$ of the small-displacement screw $\mathbf{s}_i(s_i)$ as

$$\mathbf{S}_i(s_i) \equiv \begin{bmatrix} e^{\mathbf{\Psi}_i} & \mathbf{O}_{3\times3} \\ \mathbf{\Sigma}_i(s_i)e^{\mathbf{\Psi}_i} & e^{\mathbf{\Psi}_i} \end{bmatrix}, \tag{3.11}$$

where $\mathbf{\Psi}_i \equiv \text{CPM}(\boldsymbol{\tau}_i)$ and $\mathbf{\Sigma}_i(s_i) \equiv \text{CPM}(\boldsymbol{\sigma}_i(s_i))$. This leads to the following expression of wrench $[\mathbf{v}_i]_{\mathcal{R},j}$ in frame $\mathcal{S}_i$. This gives

$$[\mathbf{u}_i(s_i)]_{\mathcal{S},i} = -[\mathbf{v}_i]_{\mathcal{S},i} = -\mathbf{S}_i^T[\mathbf{v}_i]_{\mathcal{R},j}, \tag{3.12}$$

[1] $I_{Y,i}$, $I_{Z,i}$ and J are taken with respect to the centroid of the cross-section.

where the first equality was obtained from the equilibrium in the free-body diagram of Fig. 3.2. Upon substituting eq. (3.12) into eq. (3.9) and summing over the length of the i^{th} compliant link, we obtain the strain energy as

$$U_i = \frac{1}{2}[\mathbf{v}_i]^T_{\mathcal{R},j}\mathbf{B}_i[\mathbf{v}_i]_{\mathcal{R},j}, \quad \text{where} \quad \mathbf{B}_i \equiv \int_0^{l_i} \mathbf{S}_i(s_i)\mathbf{H}_i(s_i)\mathbf{S}_i(s_i)^T ds_i, \tag{3.13}$$

and l_i is the length of the i^{th} compliant link. It will prove useful to express all wrenches $\mathbf{v}_i$ in the same reference frame $\mathcal{F}$. For that purpose, we define $\boldsymbol{\Theta}_i \equiv \text{CPM}(\boldsymbol{\theta}_i)$, $\boldsymbol{\Upsilon}_i \equiv \text{CPM}(\boldsymbol{\rho}_i)$, and

$$\mathbf{R}_j \equiv \begin{bmatrix} e^{\boldsymbol{\Theta}_i} & \mathbf{O}_{3\times 3} \\ \boldsymbol{\Upsilon}_i e^{\boldsymbol{\Theta}_i} & e^{\boldsymbol{\Theta}_i} \end{bmatrix}, \tag{3.14}$$

with $\mathbf{R}_j$ denoting the *adjoint* of the small-displacement screw $\mathbf{r}_j$, which represents the rigid-body motion taking frame $\mathcal{F}$ into frame $\mathcal{R}_j$. Hence, we have the relation

$$[\mathbf{v}_i]_{\mathcal{R},j} = \mathbf{R}_j^T[\mathbf{v}_i]_{\mathcal{F}}, \tag{3.15}$$

and the total strain energy of the system becomes

$$U = \sum_{i=1}^{m} U_i = \sum_{i=1}^{m} \frac{1}{2}[\mathbf{v}_i]^T_{\mathcal{F}}\mathbf{R}_j\mathbf{B}_i\mathbf{R}_j^T[\mathbf{v}_i]_{\mathcal{F}}. \tag{3.16}$$

For the sake of conciseness, let us rewrite this expression as

$$U = (1/2)[\mathbf{v}]^T_{\mathcal{F}}\mathbf{B}[\mathbf{v}]_{\mathcal{F}}, \tag{3.17}$$

where

$$\mathbf{B} \equiv \begin{bmatrix} \mathbf{R}_{j_1}\mathbf{B}_1\mathbf{R}_{j_1}^T & \mathbf{O}_{6\times 6} & \cdots & \mathbf{O}_{6\times 6} \\ \mathbf{O}_{6\times 6} & \mathbf{R}_{j_2}\mathbf{B}_2\mathbf{R}_{j_2}^T & \cdots & \mathbf{O}_{6\times 6} \\ \vdots & \vdots & \ddots & \vdots \\ \mathbf{O}_{6\times 6} & \mathbf{O}_{6\times 6} & \cdots & \mathbf{R}_{j_m}\mathbf{B}_m\mathbf{R}_{j_m}^T \end{bmatrix}, \tag{3.18}$$

with j_i taking the value of the smallest index among those of the two rigid links that are connected to the i^{th} compliant link, and

$$[\mathbf{v}]_{\mathcal{F}} \equiv [[\mathbf{v}_1]_{\mathcal{F}}^T \quad [\mathbf{v}_2]_{\mathcal{F}}^T \quad \cdots \quad [\mathbf{v}_m]_{\mathcal{F}}^T]^T.$$

Upon writing the static equilibrium of the wrenches acting on the j^{th} rigid link, we obtain

$$[\mathbf{w}_j]_{\mathcal{R}_j} - \sum_{i \in \mathcal{C}_j^+} [\mathbf{v}_i]_{\mathcal{R}_j} + \sum_{i \in \mathcal{C}_j^-} [\mathbf{v}_i]_{\mathcal{R}_j} = \mathbf{0}_6, \tag{3.19}$$

where $\mathbf{0}_6$ is the six-dimensional zero-vector, $\mathcal{C}_j^+$ is the set of the indices of the compliant links that are connected to the j^{th} rigid link and to another rigid link that has an index greater than j, while $\mathcal{C}_j^-$ is the set of the indices of the compliant links that are connected to the j^{th} rigid link and to another rigid link that has an index smaller than j. We substitute eq. (3.15) into eq. (3.19), and solve for $[\mathbf{w}_j]_{\mathcal{R}_j}$, which leads to

$$[\mathbf{w}_j]_{\mathcal{R}_j} = \mathbf{R}_j^T \left(\sum_{i \in \mathcal{C}_j^+} [\mathbf{v}_i]_{\mathcal{F}} - \sum_{i \in \mathcal{C}_j^-} [\mathbf{v}_i]_{\mathcal{F}} \right). \tag{3.20}$$

In order to simplify the notation, let us define the arrays $\mathbf{v}$ and $\mathbf{w}$ of compliant- and rigid-link wrenches, respectively, that is,

$$[\mathbf{v}]_{\mathcal{F}} \equiv \begin{bmatrix} [\mathbf{v}_1]_{\mathcal{F}} \\ [\mathbf{v}_2]_{\mathcal{F}} \\ \vdots \\ [\mathbf{v}_m]_{\mathcal{F}} \end{bmatrix} \quad \text{and} \quad [\mathbf{w}]_{\mathcal{R}} \equiv \begin{bmatrix} [\mathbf{w}_1]_{\mathcal{R},1} \\ [\mathbf{w}_2]_{\mathcal{R},2} \\ \vdots \\ [\mathbf{w}_n]_{\mathcal{R},n} \end{bmatrix}. \tag{3.21}$$

Accordingly, we may rewrite eq. (3.20) in the more convenient form

$$[\mathbf{w}]_{\mathcal{R}} = \mathbf{R}^T \mathbf{A} [\mathbf{v}]_{\mathcal{F}}, \tag{3.22}$$

where $\mathbf{R} \equiv \mathrm{diag}(\mathbf{R}_1, \mathbf{R}_2, \ldots, \mathbf{R}_n) \in \mathbb{R}^{6n\times 6n}$,

$$\mathbf{A} \equiv \begin{bmatrix} \mathbf{A}_{11} & \mathbf{A}_{12} & \cdots & \mathbf{A}_{1m} \\ \mathbf{A}_{21} & \mathbf{A}_{22} & \cdots & \mathbf{A}_{2m} \\ \vdots & \vdots & \ddots & \vdots \\ \mathbf{A}_{n1} & \mathbf{A}_{n2} & \cdots & \mathbf{A}_{nm} \end{bmatrix} \in \mathbb{R}^{6n\times 6m}, \tag{3.23}$$

and

$$\mathbf{A}_{ji} = \begin{cases} \mathbf{O}_{6\times 6} & \text{if compliant link } i \text{ is not connected to rigid link } j, \\ \mathbf{1}_{6\times 6} & \text{if compliant link } i \text{ is connected to rigid links } j \text{ and } k, \text{ with } j < k, \\ -\mathbf{1}_{6\times 6} & \text{if compliant link } i \text{ is connected to rigid links } j \text{ and } k, \text{ with } j > k. \end{cases}$$

This allows the introduction of the potential energy of the external wrenches as a function of the internal wrenches, namely,

$$\Pi = -[\mathbf{w}]_{\mathcal{R}}^T [\mathbf{x}]_{\mathcal{R}} = -[\mathbf{v}]_{\mathcal{F}}^T \mathbf{A}^T \mathbf{R} [\mathbf{x}]_{\mathcal{R}}. \tag{3.24}$$

For a linearly elastic system, the potential energy V and the complementary potential energy[2] $\bar{V}$ take the same value, which is the sum of the strain energy and the potential energy; symbolically,

$$\bar{V} = V = U + \Pi = (1/2)[\mathbf{v}]_{\mathcal{F}}^T \mathbf{B} [\mathbf{v}]_{\mathcal{F}} - [\mathbf{v}]_{\mathcal{F}}^T \mathbf{A}^T \mathbf{R} [\mathbf{x}]_{\mathcal{R}}. \tag{3.25}$$

[2] The complementary energy density may be viewed as the area above the stress-strain curve of a tensile test, the complementary energy being the sum of the complementary energy density over a given volume of material (Dym and Shames, 1973).

From eq. (3.25), the problem may now be regarded as that of finding the internal wrenches $\mathbf{v}$ that minimize the complementary potential energy $\bar{V}$ for given displacements $\mathbf{x}$ of the rigid links. This follows from the second theorem of Castigliano. The partial derivative of $\bar{V}$ with respect to the internal wrenches yields

$$\frac{\partial \bar{V}}{\partial [\mathbf{v}]_{\mathcal{F}}} = \mathbf{B}[\mathbf{v}]_{\mathcal{F}} - \mathbf{A}^T \mathbf{R}[\mathbf{x}]_{\mathcal{R}}, \tag{3.26}$$

the Hessian of $\bar{V}$ being

$$\frac{\partial^2 \bar{V}}{\partial [\mathbf{v}]_{\mathcal{F}}^2} = \mathbf{B}. \tag{3.27}$$

One may readily verify, from eq. (3.17), that $\mathbf{B}$ is symmetric, positive-definite and, therefore, all stationary points $\mathbf{v}$ of $\bar{V}$ are minima. Matrix $\mathbf{B}$ being nonsingular, $\partial \bar{V}/\partial [\mathbf{v}]_{\mathcal{F}}$ of eq. (3.26) admits one single root, namely,

$$[\mathbf{v}]_{\mathcal{F}} = \mathbf{B}^{-1} \mathbf{A}^T \mathbf{R}[\mathbf{x}]_{\mathcal{R}}. \tag{3.28}$$

Upon substituting eq. (3.22) into the foregoing equation, we obtain

$$[\mathbf{w}]_{\mathcal{R}} = \mathbf{K}[\mathbf{x}]_{\mathcal{R}}, \quad \text{where} \quad \mathbf{K} \equiv \mathbf{R}^T \mathbf{A} \mathbf{B}^{-1} \mathbf{A}^T \mathbf{R}. \tag{3.29}$$

The potential energy can now be written as a function of the system posture $\mathbf{x}$, namely,

$$V = (1/2) \mathbf{x}^T \mathbf{K} \mathbf{x}. \tag{3.30}$$

3.1.4 Dissipated Energy

Assuming linear damping only on the rigid links allows us to define the Rayleigh dissipation function

$$P = -(1/2) \dot{\mathbf{x}}^T \mathbf{C} \dot{\mathbf{x}}, \tag{3.31}$$

where $\mathbf{C} \in \mathbb{R}^{n \times n}$ is at least positive semi-definite, and contains the system damping factors.

3.1.5 Dynamics Model of the Compliant Mechanism

The Lagrangian of the mechanism is readily computed as

$$L \equiv T - V = (1/2)\dot{\mathbf{x}}^T\mathbf{M}\dot{\mathbf{x}} - (1/2)\mathbf{x}^T\mathbf{K}\mathbf{x}, \tag{3.32}$$

and its associated Lagrange equations are

$$\frac{d}{dt}\left(\frac{\partial L}{\partial \dot{\mathbf{x}}}\right) - \frac{\partial L}{\partial \mathbf{x}} = \frac{\partial P}{\partial \dot{\mathbf{x}}} + \mathbf{w} \tag{3.33}$$

whence,

$$\mathbf{M}\ddot{\mathbf{x}} + \mathbf{K}\mathbf{x} = -\mathbf{C}\dot{\mathbf{x}} + \mathbf{w}, \tag{3.34}$$

which is the dynamics model sought. As the mass matrix is bound to be symmetric and positive definite, we can compute its Cholesky decomposition as $\mathbf{M} = \mathbf{L}\mathbf{L}^T$. This allows us to rewrite eq. (3.34) in its monic representation (Angeles et al., 1999) by performing the change of variable $\mathbf{z} = \mathbf{L}^T\mathbf{x}$, namely,

$$\ddot{\mathbf{z}} + \boldsymbol{\Delta}\dot{\mathbf{z}} + \boldsymbol{\Omega}^2\mathbf{z} = \mathbf{L}^{-1}\mathbf{w}, \tag{3.35}$$

where $\boldsymbol{\Delta} \equiv \mathbf{L}^{-1}\mathbf{C}\mathbf{L}^{-T}$ is the *dissipation matrix*, and $\boldsymbol{\Omega}^2 \equiv \mathbf{L}^{-1}\mathbf{K}\mathbf{L}^{-T}$ is the *frequency matrix* of the compliant mechanism.

Let μ_i and $\boldsymbol{\mu}_i$, $i = 1, \ldots, n$, be the eigenvalues and eigenvectors of $\boldsymbol{\Omega}^2$, respectively, the former being identical to the natural frequencies-squared, the latter linear transformations of the modal vectors of the undamped, non-excited system of eq. (3.35). That is, if we let λ_i and $\boldsymbol{\lambda}_i$ be the natural frequencies and the modal vectors of the undamped, non-excited system (3.34), then

$$\begin{aligned} \lambda_i &= \sqrt{\mu_i}, \quad \text{and} \\ \boldsymbol{\lambda}_i &= \mathbf{L}^{-T}\boldsymbol{\mu}_i, \quad i = 1, \ldots, n. \end{aligned} \tag{3.36}$$

Let us pursue this analysis by computing the Laplace-domain transfer function $\mathbf{H}(s)$, which maps the input wrenches $\mathbf{w}$ acting on the rigid bodies onto the system states $\mathbf{x}$, and where s is the variable of the Laplace domain. From eq. (3.34), we have

$$\mathbf{H}(s) = \mathbf{L}^{-T}(\mathbf{1}_{6n\times 6n}s^2 + \mathbf{\Delta}s + \mathbf{\Omega}^2)^{-1}\mathbf{L}^{-1}. \tag{3.37}$$

3.2 Case Study: the ADXL150 Accelerometer from Analog Devices

Even though it has now been replaced by the ADXL78, the ADXL150 accelerometer from Analog Devices has been a reference for accelerometer designers (see Senturia, 2001, for example). Because of that, its properties are known, and it is thus a good starting point to validate the proposed dynamics model. The ADXL150 has a range of action of $\pm 50g$. It is fabricated using surface-micromachining techniques, which allows a size as small as $753\,\mu\text{m} \times 657\,\mu\text{m}$, which can be appreciated from Fig. 3.3, where the white horizontal bar is a reference scale of 100 μm long. The ADXL150 is a uniaxial accelerometer, and

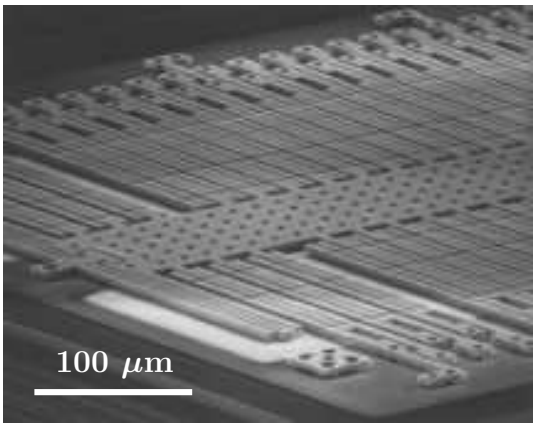

Figure 3.3: Analog Devices ADXL150

hence, its stiffness should be much lower along its sensitive axis than along any other direction. To verify this, we analyze the mechanical structure of the device, which is sketched in Fig. 3.4. In this sketch, the thickness t of the compliant mechanism is measured in the orthogonal direction to the plane of the

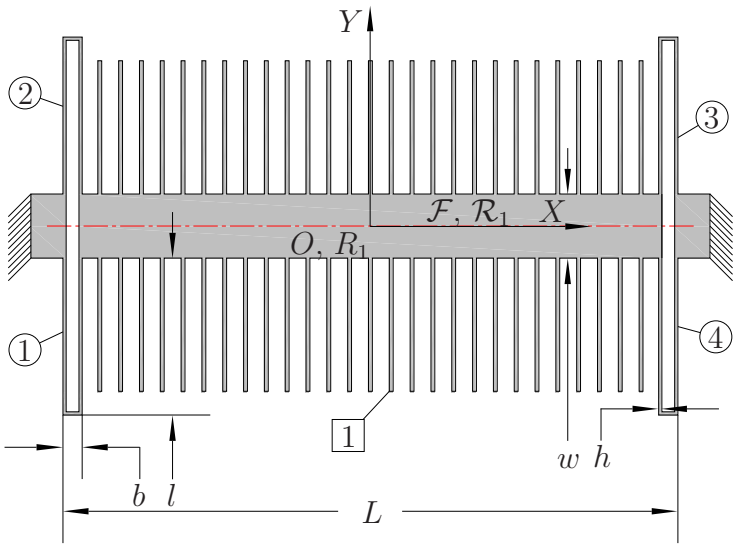

Figure 3.4: The mechanical structure of the ADXL150

figure. The compliant legs are numbered in balloons from 1 to 4, whereas the only rigid link of this mechanism is the proof mass itself, which is thus labelled with number 1, in a square. The dimensions are recorded in Table 3.1, as they were taken from the work of Senturia (2001), except for b, which was estimated directly from Fig. 3.3. Frames $\mathcal{F}$ and $\mathcal{R}_1$ are defined as displayed in Fig. 3.4, with their X axes along the accelerometer sensitive axis—represented here by a dashed line, and with their Y axes in the plane of the wafer surface. We take those frames to be right-handed, and so their Z axes stem out of the plane of the wafer surface. Moreover, the origins O and R_1 of these two frames are located at the proof-mass centroid. Hence, apparently, frames $\mathcal{F}$ and $\mathcal{R}_j$ are chosen to be identical, which simplifies subsequent calculations. The material

Table 3.1: Dimensions of the ADXL150 accelerometer

L	l	w	b	h	t
500 μm	120 μm	50 μm	10 μm	2.5 μm	2 μm

of the flexible mechanism is polysilicon, which has a Young modulus $E = 160$ GPa, a Poisson ratio $\nu \approx 0.2$, and a density $\rho = 2331\,\mathrm{kg/m^3}$. The mass matrix $\mathbf{M}$ of the mechanism is the mass matrix of the proof mass as defined in

eq. (3.6). The corresponding inertia matrix and mass were estimated to be

$$[\mathbf{I}_1]_{\mathcal{F}} = [\mathbf{I}_1]_{\mathcal{R},1} = \begin{bmatrix} 0.5586 & 0 & 0 \\ 0 & 3.088 & 0 \\ 0 & 0 & 3.647 \end{bmatrix} \times 10^{-18} \quad \text{kg·m}^2 \tag{3.38}$$

and $m_1 = 1.846 \times 10^{-10}$ kg from a CAD model of the proof mass that included its 54 electrodes. This allows the evaluation of the kinetic energy from eq. (3.7).

On the other hand, calculating the potential energy requires the definition of the additional frames $\mathcal{S}_i(s_i)$, $i = 1, 2, 3, 4$. This can be done through the definition of their associated screws $\mathbf{s}_i(s_i)$, $i = 1, 2, 3, 4$, which take frame $\mathcal{R}_1$ into their respective frames $\mathcal{S}_i(s_i)$, $i = 1, 2, 3, 4$. Because of the discontinuous nature of the compliant links, these screws are defined as piecewise functions, as detailed in Table 3.2. Although the neutral axes are located at the centre of the thin beams, the half widths $h/2$ were omitted in the expressions of $\mathbf{s}_i(s_i)$, $i = 1, 2, 3, 4$. Their effects are thought to be negligible with respect to the overall model accuracy.

Table 3.2: Screws $\mathbf{s}_i(s_i)$, $i = 1, 2, 3, 4$

$s_i \in$	i	$\mathbf{s}_i^T(s_i)$
[0,l[	1	$[0 \quad 0 \quad 3\pi/2 \quad -L/2 \quad -w/2 - s_1 \quad 0]$
	2	$[0 \quad 0 \quad \pi/2 \quad -L/2 \quad w/2 + s_2 \quad 0]$
	3	$[0 \quad 0 \quad \pi/2 \quad L/2 \quad w/2 + s_3 \quad 0]$
	4	$[0 \quad 0 \quad 3\pi/2 \quad L/2 \quad -w/2 - s_4 \quad 0]$
[l,l+b[	1	$[0 \quad 0 \quad 0 \quad s_1 - l - L/2 \quad b - L/2 \quad 0]$
	2	$[0 \quad 0 \quad 0 \quad s_2 - l - L/2 \quad w/2 + l \quad 0]$
	3	$[0 \quad 0 \quad \pi \quad L/2 + l - s_3 \quad w/2 + l \quad 0]$
	4	$[0 \quad 0 \quad \pi \quad L/2 + l - s_4 \quad -w/2 - l \quad 0]$
[l+b,2l+b]	1	$[0 \quad 0 \quad \pi/2 \quad b - L/2 \quad s_1 - 2l - b - w/2 \quad 0]$
	2	$[0 \quad 0 \quad 3\pi/2 \quad b - L/2 \quad 2l + b + w/2 - s_2 \quad 0]$
	3	$[0 \quad 0 \quad 3\pi/2 \quad L/2 - b \quad 2l + b + w/2 - s_3 \quad 0]$
	4	$[0 \quad 0 \quad \pi/2 \quad L/2 - b \quad s_4 - 2l - b - w/2 \quad 0]$

The beam cross-section remains constant in all the compliant links, and, therefore, from the numerical data of Table 3.2, we obtain,

$$\begin{aligned} J_i &= \beta h t^3 = 3.37 \times 10^{-24}\ \mathrm{m}^4, \\ I_{Y,i} &= t^3 h/12 = 1.67 \times 10^{-24}\ \mathrm{m}^4, \\ I_{Z,i} &= h^3 t/12 = 2.60 \times 10^{-24}\ \mathrm{m}^4, \\ A_i &= ht = 5.00 \times 10^{-12}\ \mathrm{m}^2, \\ \alpha_{Y,i} &= \alpha_{Z,i} = 6/5, \end{aligned} \tag{3.39}$$

and where $\beta = 0.1685$ (Roark and Young, 1975) is a correction factor that depends upon the cross-section geometry. Since frames $\mathcal{F}$ and $\mathcal{R}_1$ are coincident, we have

$$\mathbf{R} = \mathbf{R}_1 = \mathbf{1}_{6\times 6}, \tag{3.40}$$

and, because the four compliant links connect the fixed rigid link to the only mobile rigid link, we may assign

$$\mathbf{A} = \begin{bmatrix} -\mathbf{1}_{6\times 6} & -\mathbf{1}_{6\times 6} & -\mathbf{1}_{6\times 6} & -\mathbf{1}_{6\times 6} \end{bmatrix}, \tag{3.41}$$

where the minus sign comes from the assumption that the fixed rigid link corresponds to the index $j = 0$. From eq. (3.29), we obtain directly

$$\begin{aligned} \mathbf{K} = \mathrm{diag}\big(&2.87 \times 10^{-8}\ \mathrm{N\ m/rad},\ 1.94 \times 10^{-7}\ \mathrm{N\ m/rad}, \\ &1.61 \times 10^{-5}\ \mathrm{N\ m/rad},\ 5.16\ \mathrm{N/m},\ 268\ \mathrm{N/m},\ 3.17\ \mathrm{N/m}\big). \end{aligned} \tag{3.42}$$

The fourth diagonal term in eq. (3.42) represents the stiffness of the mechanism along the accelerometer sensitive axis. The value obtained by Senturia (2001) from the same dimensions was 5.6 N/m, but this did neither take into account the deflection of the shorter intermediate straight beams in each leg nor the shear strain in any of the beams. According to Senturia (2001), the

Table 3.3: Modal analysis of the ADXL150 accelerometer

i	1	2	3	4	5	6
f_i (kHz)	20.87	26.61	36.08	39.90	191.70	334.62
$\boldsymbol{\lambda}_i$	0.000	0.000	1.000	0.000	0.000	0.000
	0.000	0.000	0.000	1.000	0.000	0.000
	0.000	0.000	0.000	0.000	0.000	1.000
	0.000	1.000	0.000	0.000	0.000	0.000
	0.000	0.000	0.000	0.000	1.000	0.000
	1.000	0.000	0.000	0.000	0.000	0.000

actual value measured by Analog Devices is 5.4 N/m. Hence, the proposed model appears to be accurate enough for engineering work.

The frequency matrix can thus be computed from its definition, in eq. (3.35), which yields

$$\begin{aligned} \boldsymbol{\Omega} &= \operatorname{diag}(2.27 \quad 2.51 \quad 21.0 \quad 1.67 \quad 12.0 \quad 1.31) \times 10^5 \quad \text{rad/s}, \\ &= \operatorname{diag}(36.1 \quad 39.9 \quad 335 \quad 26.6 \quad 192 \quad 20.9) \quad \text{kHz}. \end{aligned}$$

Apparently, the frequency matrix is diagonal, which allows for the extraction of its eigenvalues and eigenvectors by simple inspection. For the sake of clarity, these values are listed in Table 3.3, in ascending order.

A natural frequency of 24.7 kHz was obtained by Senturia (2001) in the direction of the accelerometer sensitive axis, which is somewhat smaller than the 26.6 kHz obtained here. The reason behind is the different stiffness and proof mass estimates. In our model, the proof mass was estimated as 1.846×10^{-10} kg from a CAD model, whereas Senturia (2001) used a value of 2.2×10^{-10} kg that had been provided by Analog Devices. There is a relatively large difference between the fundamental frequency and that of the mode in the direction of

the accelerometer sensitive axis, as compared to the small difference of the former with that of a translational out-of-plane motion of the proof mass, which may surprise anyone who is not familiar with MEMS design. Indeed, at this scale, the damping due to the squeezed film of air between the proof mass and the substrate is very important in that direction, and prevents this parasitic motion from becoming significant at high frequencies.

To substantiate this claim, let us estimate the damping in the system by assigning some values to matrix $\mathbf{C}$ defined in eq. (3.31). Here, we consider only the damping that is due to air friction beneath the proof mass and between the electrodes. Moreover, even though it may be just as high as the damping due to proof-mass translations, we neglect air damping due to proof mass rotations. This choice is mainly justified by virtue of correspondence of the lowest frequencies of the system to those of the translational proof-mass motions; the choice can also be justified by the level of complication associated with the modelling of the air flow around a rotating plate close to a flat surface. Indeed, the air flow beneath the proof mass induced by in-wafer-plane translations may be modelled as a simple Couette flow, whereas the air flow produced by out-of-wafer-plane translations may be assimilated to a Poiseuille[3] flow (Senturia, 2001). Moreover, as a rough approximation, we consider the flow between the electrodes as well as when the proof mass translates in the X-axis direction to be of the Poiseuille type; we consider a Couette[4] flow when the proof mass

[3] A Poiseuille flow is a laminar flow of an incompressible Newtonian fluid in a pipe (Munson et al., 2006).

[4] A Couette flow is a laminar flow of an incompressible Newtonian fluid induced by the relative motion of the two surfaces that contain the fluid (Munson et al., 2006).

translates in the Y-axis direction. As a result, we have

$$\begin{aligned}\mathbf{C} \;=\; \mathrm{diag}\{0,\, 0,\, 0,\, &\eta(L-2b)w/c + 108\times 96\eta l t^3/(\pi^4 d^3),\\ &\eta(L-2b)w/c + 108\eta l t/d,\, 96\eta(L-2b)w^3/(\pi^4 c^3)\},\end{aligned} \tag{3.43}$$

i.e.,

$$\begin{aligned}\mathbf{C} \;=\; \mathrm{diag}\{0,\, 0,\, 0,\, &1.107\times 10^{-6}\,\mathrm{N\,s/m},\\ &0.629\times 10^{-6}\,\mathrm{N\,s/m},\, 259.858\times 10^{-6}\,\mathrm{N\,s/m}\},\end{aligned} \tag{3.44}$$

where $c = 1.6\,\mu$m is the gap between the proof mass and the chip, $d = 1.3\,\mu$m is the gap between two electrodes, and $\eta = 18\times 10^{-6}\,\mathrm{Pa\cdot s}$ is the dynamic viscosity of air.

The associated matrix transfer function is computed from eq. (3.37). In the case of an accelerometer, the array of rigid-link external wrenches $\mathbf{w}$ defined in eq. (3.21) may be regarded, from d'Alembert's principle, as an array of *inertial wrenches*. Moreover, if we assume that the instant screw axis of any motion of the accelerometer frame lies at infinity, which is reasonable for a small mechanical system, we can neglect the angular velocity and write $\mathbf{w}$ as a linear function of the twist time-derivative $\mathbf{a}$ of the accelerometer frame. Hence, the acceleration field of the accelerometer frame is approximated by a helical field represented by screw $\mathbf{a}$, which is formed with the angular acceleration of frame $\mathcal{F}$ with respect to an inertial frame, and the acceleration of its origin O with respect to a fixed reference point, both expressed in the accelerated frame $\mathcal{F}$. Symbolically, we obtain

$$\mathbf{w} = -\mathbf{M}\mathbf{R}^T\mathbf{T}\mathbf{a}, \tag{3.45}$$

where $\mathbf{T} \equiv [\mathbf{1}_{6\times6} \quad \mathbf{1}_{6\times6} \quad \cdots \quad \mathbf{1}_{6\times6}]^T$.

Let us now label ξ_X, ξ_Y, and ξ_Z the components of the position of the proof-mass position vector $\boldsymbol{\xi}_1$, and a_X, a_Y, and a_Z the components of $\mathbf{a}$. We also define unit vectors $\mathbf{e}_4 \equiv [\mathbf{0}_3^T \quad 1 \quad \mathbf{0}_2^T]^T$, $\mathbf{e}_5 \equiv [\mathbf{0}_4^T \quad 1 \quad 0]^T$, and $\mathbf{e}_6 \equiv [\mathbf{0}_5^T \quad 1]^T$, which lets us write the input-output relationships

$$\begin{aligned} h_X(s) &\equiv \xi_X(s)/a_X(s) = -\mathbf{e}_4^T\mathbf{H}(s)\mathbf{M}\mathbf{R}^T\mathbf{T}\mathbf{e}_4\mathbf{e}_4^T, \\ h_Y(s) &\equiv \xi_Y(s)/a_Y(s) = -\mathbf{e}_5^T\mathbf{H}(s)\mathbf{M}\mathbf{R}^T\mathbf{T}\mathbf{e}_5\mathbf{e}_5^T, \\ h_Z(s) &\equiv \xi_Z(s)/a_Z(s) = -\mathbf{e}_6^T\mathbf{H}(s)\mathbf{M}\mathbf{R}^T\mathbf{T}\mathbf{e}_6\mathbf{e}_6^T. \end{aligned} \tag{3.46}$$

We compute the complex frequency responses $h_X(\omega)$, $h_Y(\omega)$, and $h_Z(\omega)$ of the proof mass to transverse accelerations by evaluating the corresponding transfer functions at $\omega\sqrt{-1}$, where ω is the input frequency. Upon computing the magnitudes and phase angles of these complex functions, we obtain the Bode plots of Fig. 3.5.

From the magnitude-vs.-frequency plot of Fig. 3.5(a), we see that the accelerometer response to Z-axis accelerations is overdamped, whereas the responses to in-wafer plane accelerations are underdamped. Nevertheless, the out-of-wafer-plane motion can still pose problems when the proof mass is subjected to low-frequency accelerations (e.g. gravitational or centripetal) along the Z-direction of frame $\mathcal{F}$. Indeed, cross-axis sensitivity is the highest source of errors ($\pm2\%$ of the full-scale range, i.e., $1g$) for the ADXL150 accelerometer.

Hence, increasing the cross-axis natural frequencies with respect to the sensitive-axis natural frequencies generally improves the accelerometer accuracy. Of course, the effects of the relative sensitivities to vibration are also

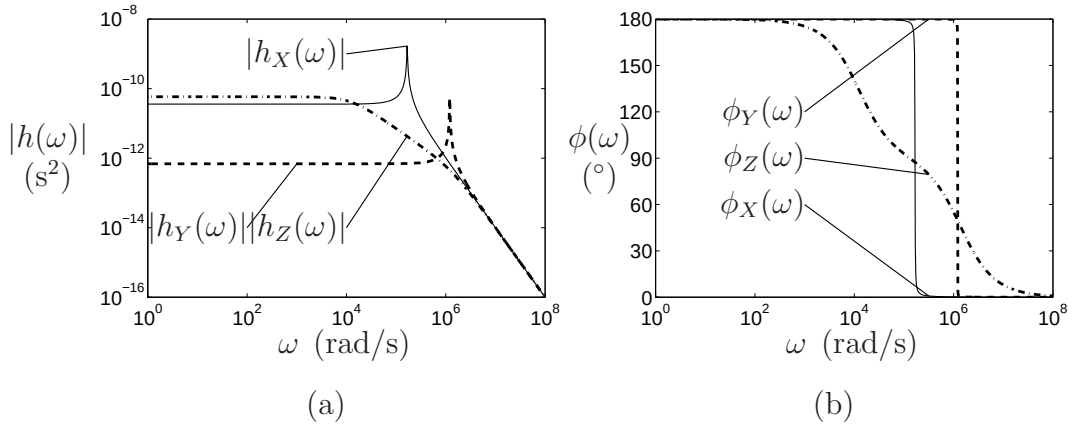

Figure 3.5: Frequency response of the ADXL150: (a) magnitude and (b) phase

influenced by the proof mass displacement sensing method. Notice, however, that choosing the right mechanical architecture solves the problem at its root, and, therefore, constitutes an essential part of the sensor design. This is what the novel SBA architecture aims at improving.

3.3 Dynamics Model of the Simplicial Biaxial Accelerometer

Let us now turn our attention towards the SBA of Fig. 2.8, a top view of which is shown in Fig. 3.6. In this drawing, each link is labelled with a number appearing in a circle for a compliant link, and in a box for a rigid link. Table 3.4 lists the numerical values of the dimensions appearing in Fig. 3.6 as well as the numerical value of the device-wafer thickness t. These dimensions were obtained by considering the SBA frequency response from the model developed in Section 3.1 and the micromachinability of the resulting silicon structure. As a general rule, since this is intended to be a proof of concept, it was decided to aim at a slightly larger size than most existing micromachined accelerometers.

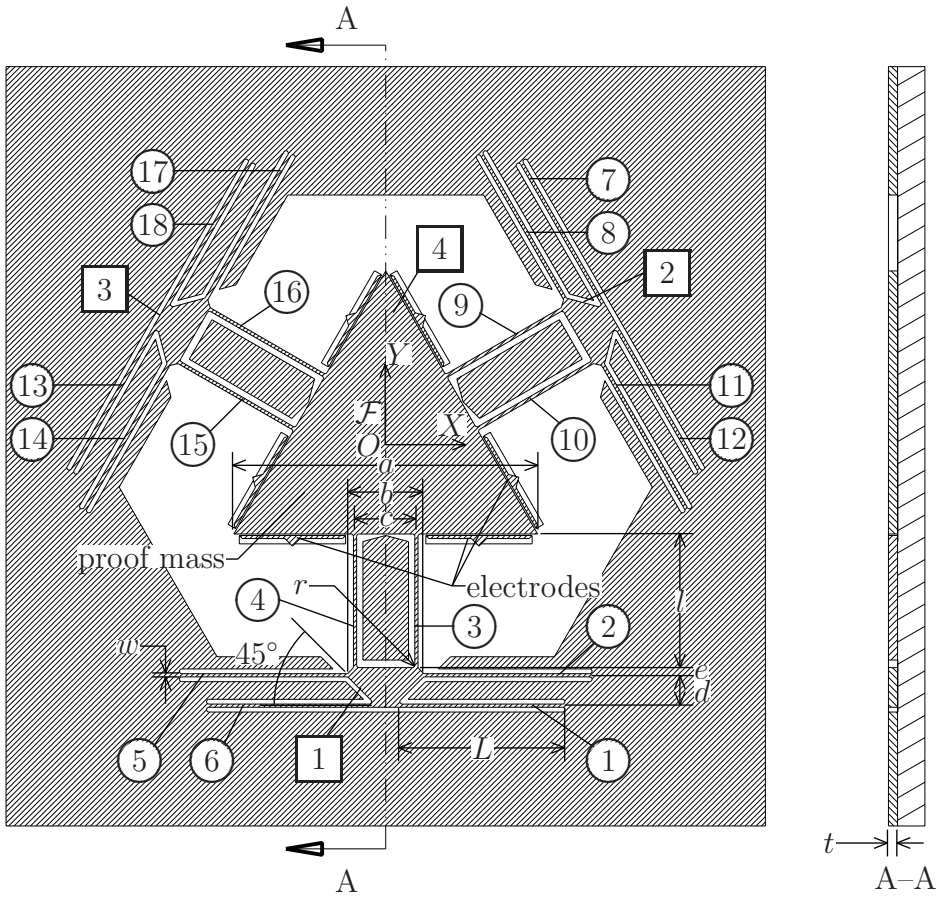

Figure 3.6: Dimensions of the 2D-3ΠΠ Simplicial Accelerometer

Table 3.4: Dimensions of the Simplicial Biaxial Accelerometer

L	l	w	t	r
5544 μm	4400 μm	105 μm	300 μm	78.7 μm
a	b	c	d	e
10000 μm	2500 μm	2020 μm	1000 μm	200 μm

3.3.1 Kinetic Energy

Frames $\mathcal{R}_j$, $j = 1, \ldots, n$, $n = 4$, are located at the mass centres of their corresponding rigid links, and oriented so that screws $\mathbf{r}_j$, $j = 1, \ldots, n$, take

the values

$$\begin{aligned}
\mathbf{r}_1 &= \begin{bmatrix} \mathbf{0}_4^T & -\sqrt{3}a/6 - l - f & 0 \end{bmatrix}^T, \\
\mathbf{r}_2 &= \begin{bmatrix} \mathbf{0}_2^T & 2\pi/3 & (a/2 + \sqrt{3}l + \sqrt{3}f)/2 & (\sqrt{3}a/6 + l + f)/2 & 0 \end{bmatrix}^T, \\
\mathbf{r}_3 &= \begin{bmatrix} \mathbf{0}_2^T & -2\pi/3 & -(a/2 + \sqrt{3}l + \sqrt{3}f)/2 & (\sqrt{3}a/6 + l + f)/2 & 0 \end{bmatrix}^T,
\end{aligned} \tag{3.47}$$

and $\mathbf{r}_4 = \mathbf{0}_6$, where

$$f \equiv \frac{be^2(b+c) - 2d^3(b+c) - 2e^2c^2 + 3bd^2(b+c) + 6bde(b+c) - 6de^2(b+c)}{3(e(b-c) + 2d(b-d))(b+c)}.$$

The mass properties of the rigid links are computed from a CAD model, which yields

$$\begin{aligned}
m_1 &= 1.387 \times 10^{-3}\,\mathrm{kg} = m_2 = m_3,\ m_4 = 30.25 \times 10^{-3}\,\mathrm{kg}, \\
[\mathbf{I}_1]_{\mathcal{R},1} &= \mathrm{diag}\,(0.1456 \quad 0.4656 \quad 0.5904) \times 10^{-9}\,\mathrm{kg\,m^2}, \\
&= [\mathbf{I}_2]_{\mathcal{R},2} = [\mathbf{I}_3]_{\mathcal{R},3},\ \text{and} \\
[\mathbf{I}_4]_{\mathcal{R},4} &= \mathrm{diag}\,(12.63 \quad 12.63 \quad 252.1) \times 10^{-9}\,\mathrm{kg\,m^2}.
\end{aligned}$$

The mass matrix is evaluated directly from these numerical values and the definition of eq. (3.7).

3.3.2 Potential Energy

Upon defining the lengths $g \equiv b/2 + L$ and $h \equiv \sqrt{3}a/6 + l + e$, screws $\mathbf{s}_i$, $i = 1, \ldots, m$, $m = 18$, are evaluated as

$$\mathbf{s}_1 = [0 \quad 0 \quad \pi \quad g - d - s_1 \quad -h - d \quad 0]^T,$$

$$\mathbf{s}_2 = [0 \quad 0 \quad \pi \quad g - s_2 \quad -h \quad 0]^T,$$

$$\mathbf{s}_3 = \begin{bmatrix} 0 & 0 & \pi/2 & c/2 & s_3 - \sqrt{3}a/6 - l & 0 \end{bmatrix}^T = \mathbf{s}_9 = \mathbf{s}_{15},$$

$$\mathbf{s}_4 = \begin{bmatrix} 0 & 0 & \pi/2 & -c/2 & s_4 - \sqrt{3}a/6 - l & 0 \end{bmatrix}^T = \mathbf{s}_{10} = \mathbf{s}_{16},$$

$$\mathbf{s}_5 = [0 \quad 0 \quad 0 \quad s_5 - g \quad -h \quad 0]^T,$$

$$\mathbf{s}_6 = [0 \quad 0 \quad 0 \quad s_6 + d - g \quad -h - d \quad 0]^T,$$

$$\mathbf{s}_7 = \begin{bmatrix} 0 & 0 & -\pi/3 & \sqrt{3}(h+d)/2 - (g - d - s_7)/2 \\ & & & (h+d)/2 + \sqrt{3}(g - d - s_7)/2 & 0 \end{bmatrix}^T,$$

$$\mathbf{s}_8 = \begin{bmatrix} 0 & 0 & -\pi/3 & \sqrt{3}h/2 - (g - s_8)/2 & h/2 + \sqrt{3}(g - s_8)/2 & 0 \end{bmatrix}^T,$$

$$\mathbf{s}_{11} = \begin{bmatrix} 0 & 0 & 2\pi/3 & \sqrt{3}h/2 + (g - s_{11})/2 & h/2 - \sqrt{3}(g - s_{11})/2 & 0 \end{bmatrix}^T,$$

$$\mathbf{s}_{12} = \begin{bmatrix} 0 & 0 & 2\pi/3 & \sqrt{3}(h+d)/2 + (g - d - s_{12})/2 \\ & & & (h+d)/2 - \sqrt{3}(g - d - s_{12})/2 & 0 \end{bmatrix}^T,$$

$$\mathbf{s}_{13} = \begin{bmatrix} 0 & 0 & \pi/3 & -\sqrt{3}(h+d)/2 - (g - d - s_{13})/2 \\ & & & (h+d)/2 - \sqrt{3}(g - d - s_{13})/2 & 0 \end{bmatrix}^T,$$

$$\mathbf{s}_{14} = \begin{bmatrix} 0 & 0 & \pi/3 & -\sqrt{3}h/2 - (g - s_{14})/2 & h/2 - \sqrt{3}(g - s_{14})/2 & 0 \end{bmatrix}^T,$$

$$\mathbf{s}_{17} = \begin{bmatrix} 0 & 0 & -2\pi/3 & -\sqrt{3}h/2 + (g - s_{17})/2 \\ & & & h/2 + \sqrt{3}(g - s_{17})/2 & 0 \end{bmatrix}^T, \text{ and}$$

$$\mathbf{s}_{18} = \begin{bmatrix} 0 & 0 & -2\pi/3 & -\sqrt{3}(h+d)/2 + (g - d - s_{18})/2 \\ & & & (h+d)/2 + \sqrt{3}(g - d - s_{18})/2 & 0 \end{bmatrix}^T.$$

Turning our attention to the elastostatic properties of the compliant links, we realize that the beams are not all identical in that respect, since silicon crystal is an anisotropic material. The axes of the cubic crystal correspond to the axes of frame $\mathcal{F}$ shown in Fig. 3.6. As a result, the Young moduli E_i and the shear moduli G_i, $i = 1, \ldots, m$, are not all equal, depending on the orientation of their corresponding compliant link with respect to the crystal axes. Because of the symmetry in the crystal, we have

$$\mathbf{H}_i = \text{diag}\left(\frac{1}{G_\perp J}, \frac{1}{E_\perp I_Y}, \frac{1}{E_\perp I_Z}, \frac{1}{E_\perp A}, \frac{\alpha_Y}{G_\perp A}, \frac{\alpha_Z}{G_\perp A}\right), \tag{3.48}$$

for $i = 1, \ldots, 6$, and

$$\mathbf{H}_i = \text{diag}\left(\frac{1}{G_{\angle,T} J}, \frac{1}{E_\angle I_Y}, \frac{1}{E_\angle I_Z}, \frac{1}{E_\angle A}, \frac{\alpha_Y}{G_{\angle,Y} A}, \frac{\alpha_Z}{G_{\angle,Z} A}\right), \tag{3.49}$$

for $i = 7, \ldots, 18$, where the $\perp$ superscript refers to the beams that are at 0° or 90° from a crystal axis, and the $\angle$ superscript refers to the beams that are at 30° or 60° from a crystal axis. Because of material anisotropy, two distinct shear moduli are associated with the cross-sections that are not orthogonal to one of the crystallographic axes. These moduli, which we label $G_{\angle,Y}$ and $G_{\angle,Z}$, correspond, respectively, to the directions of the $Y_{\mathcal{S},i}$ and $Z_{\mathcal{S},i}$ axes of the cross-section frames $\mathcal{S}_i(s_i)$, $i = 7, \ldots, 18$. Moreover, in this model, we neglect any coupling between torsion and bending due to the distinct shear moduli in compliant links $i = 7, \ldots, 18$. In fact, to avoid overcomplicating the problem, we define the section shear modulus in torsion as the average of the two real shear moduli of the section, that is,

$$G_{\angle,T} \equiv (G_{\angle,Y} + G_{\angle,Z})/2. \tag{3.50}$$

This saves us from resorting to a modified Saint-Venant method, which would require the solution of a partial differential equation of the form

$$G_{\angle,Y}\frac{\partial^2\phi(y,z)}{\partial y^2}+G_{\angle,Z}\frac{\partial^2\phi(y,z)}{\partial z^2}=0, \tag{3.51}$$

and where $\phi(y,z)$ represents the warping of the beam cross-sections. Hence, in the case of pure torsion, we consider the material to be isotropic with a shear modulus of $G_{\angle,T}$. In the present case, as the objective is to compute an order of magnitude of the accelerometer cross-axis sensitivity, this rough approximation is sufficient.

Table 3.5: Cross-section properties of the compliant links of the SBA

$E_\perp$	130.2 GPa	$G_\perp$	79.4 GPa
$E_{\angle,X}$	157.2 GPa	$G_{\angle,Y}$	79.4 GPa
$G_{\angle,Z}$	55.9 GPa	$G_{\angle,T}$	67.6 GPa
J	$0.8965\times10^{-16}\,\mathrm{m}^4$	I_Y	$0.2363\times10^{-15}\,\mathrm{m}^4$
I_Z	$0.2894\times10^{-16}\,\mathrm{m}^4$	A	$0.3150\times10^{-7}\,\mathrm{m}^2$
α_Y	1.2	α_Z	1.2

The numerical values of the foregoing elastic properties are given in Table 3.5, as reported by Wortman and Evans (1965). The geometric properties of the beam cross-sections, also gathered in Table 3.5, were computed from the formulae $J=\beta wt^3$, with $\beta=0.258$, $I_Y=wt^3/12$, $I_Z=w^3t/12$, and $A=wt$, whereas the shear correction factors are $\alpha_Y=\alpha_Z=6/5$ for rectangular cross-sections (see Pilkey, 2005). This permits the computation of the stiffness matrix as defined in eq. (3.29).

3.3.3 Dissipated Energy

It is assumed that all energy dissipation comes from air friction within the 2.5 μm gap between the proof mass and the handle wafer. Following the same method as in Section 3.2, a Couette flow is assumed for in-wafer-plane

proof-mass translations, while the air flow produced by proof-mass rotations and other rigid-link displacements are neglected. As in Section 3.2, we may yet assume that an out-of-wafer-plane proof-mass translation generates a Poiseuille flow beneath it, but the triangular geometry of the proof mass prevents us from using the solution for rectangular plates. In order to obtain a rough estimate of the dissipated energy, let us assume a Poiseuille air flow beneath the proof mass that is orthogonal to the closest triangle edges, as sketched in Fig. 3.7. Consider now the small element of area underneath the proof mass that has a width dq and a total length of $a/\sqrt{3} - y$, where y is the coordinate of its intersection with the Y-axis. We may assume that the damping due to this small element is given by the formula for rectangular plates that have one side much larger than the other (Senturia, 2001), that is,

$$dc_Z = 96\eta(dq)(a/\sqrt{3} - y)^3/(\pi^4 p^3), \tag{3.52}$$

where $p = 2.5\ \mu$m is the gap between the proof mass and the handle wafer. Projecting the element width dq onto the Y-axis yields the relation $dq = \sqrt{3}dy/2$, which, upon substitution in eq. (3.52), allows for a summation over the upper branch of the triangular proof mass, we obtain

$$c_Z/3 = \frac{48\sqrt{3}\eta}{\pi^4 p^3}\int_0^{a/\sqrt{3}} (a/\sqrt{3} - y)^3 dy = \frac{48\sqrt{3}\eta}{\pi^4 p^3}\int_0^{a/\sqrt{3}} y^3 dy$$

whence,

$$c_Z = \frac{4\sqrt{3}\eta a^4}{\pi^4 p^3}, \tag{3.53}$$

thereby obtaining the result sought.

Hence, matrix $\mathbf{C}$ of eq. (3.31) takes the symbolic and numeric values

$$\begin{aligned}\mathbf{C} &= \text{diag}\left([\mathbf{0}_{21}^T \quad \eta A_4/p \quad \eta A_4/p \quad 4\sqrt{3}\eta a^4/(\pi^4 p^3)]^T\right), \quad \text{and} \\ &= \text{diag}\left([\mathbf{0}_{21}^T \quad 3.12\times 10^{-4} \quad 3.12\times 10^{-4} \quad 8.19\times 10^{2}]^T\right) \ \text{N s/m},\end{aligned}$$

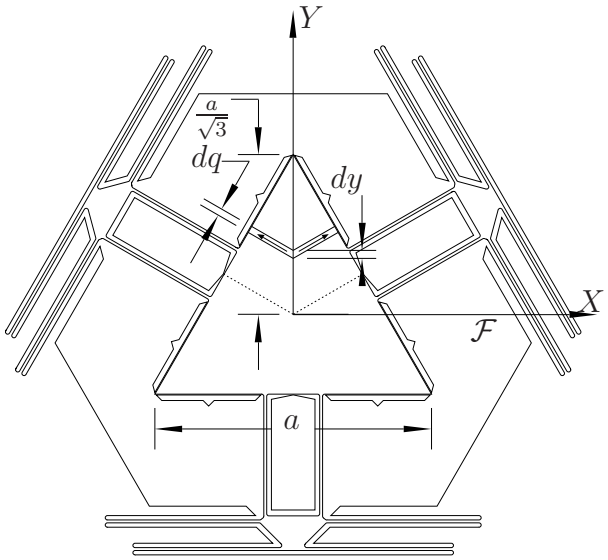

Figure 3.7: Squeezed-film damping of the SBA proof mass

respectively.

The first modes of the SBA are computed from eq. (3.36), which yields the results of Table 3.6. Because of the 24 degrees of freedom of the compliant mechanism, these results are somewhat more intricate. The first two frequencies differ only by round-off error, their associated modes involving motions of all four rigid links. For acceleration measurement, we are interested only in proof-mass motions, which are represented here by vector $\boldsymbol{\lambda}_{i,4}$. Apparently, from Table 3.6, the first two modes correspond to in-wafer-plane motions of the proof mass, with, in one case, a parasitic in-wafer-plane rotation. This parasitic motion is not due to round-off errors, but rather to silicon anisotropy. One must bear in mind, however, that the rotational component of $\boldsymbol{\lambda}_{i,4}$ is expressed in radians, whereas the translational component is expressed in meters. Hence, for instance, a 100 μm displacement of the proof mass along the direction of the first mode results in a parasitic rotation of 7.88 rad, or to relative position errors of the vertices of the proof mass of 0.788 μm. This

result is thought to be acceptable; we may safely say that the fundamental frequency corresponds now to the two sensitive directions. Moreover, we see that the orthotropic behaviour of silicon does not affect the isotropic property of the triangular mechanical architecture, since these two modes correspond to the same natural frequency. In turn, the third natural frequency appears to be dominated by rotations, except for a small non-null value at the Z-axis translational direction of the proof-mass. In fact, mode $\boldsymbol{\lambda}_3$ may be visualized as a rotation of the proximal rigid links about their associated X_i axes—which are parallel to their corresponding edge of the triangular proof mass—and a translation—for the most part—of the proof mass along the Z-axis. Hence, we see that the natural frequency of the parasitic out-of-wafer-plane motion is now higher than that of the sensitive axes, which is, apparently, an advantage of the SBA over the ADXL150 accelerometer.

In order to evaluate the effect of damping over the accelerometer, matrix $\mathbf{H}(s)$ is computed according to eq. (3.37). As in Section 3.2, we apply d'Alembert's principle of inertia forces to the dynamic system, taking the inertia forces acting on the rigid links as input forces of eq. (3.34), the outputs being the proof mass displacements. In particular, upon applying successively pure accelerations along the X, Y, and Z-axis directions, we obtain the complex frequency responses $h_X(\omega)$, $h_Y(\omega)$, and $h_Z(\omega)$, respectively, of translations of the proof mass in each of these directions. The magnitudes and phase angles of these frequency responses are shown in the Bode plots of Fig. 3.8. The lower sensitivity of the proof-mass displacements to Z-axis accelerations than to the X- and Y-axis accelerations is confirmed from Fig. 3.8(a). One may also observe a good isotropy for in-wafer-plane accelerations, and a bandwidth of approximately 100 rad/s.

Table 3.6: Modal analysis of the simplicial biaxial accelerometer

i	1	2	3	4	5	6
f_i (Hz)	53.21	53.21	66.04	171.45	179.46	418.86
$\boldsymbol{\lambda}_{i,1}$	0.000	-0.000	0.601	-0.557	0.000	-0.998
	-0.000	0.000	0.000	-0.000	0.059	-0.000
	0.244	0.000	0.000	-0.000	0.000	0.000
	-0.000	-0.000	-0.000	0.000	-0.000	0.000
	-0.000	0.472	0.000	0.000	0.000	0.000
	0.000	-0.000	0.000	-0.001	0.000	0.003
$\boldsymbol{\lambda}_{i,2}$	-0.000	-0.000	0.564	0.305	-0.502	-0.020
	0.000	0.000	0.003	-0.048	-0.027	-0.003
	-0.460	-0.471	-0.000	-0.000	0.000	0.000
	-0.000	0.000	-0.000	0.000	-0.000	-0.000
	0.353	-0.236	-0.000	-0.000	-0.000	-0.000
	0.000	-0.000	0.000	0.000	-0.001	0.000
$\boldsymbol{\lambda}_{i,3}$	0.000	-0.000	0.564	0.305	0.502	-0.020
	0.000	0.000	-0.003	0.048	-0.027	0.003
	-0.460	0.471	0.000	0.000	0.000	0.000
	-0.000	-0.000	0.000	0.000	0.000	0.000
	-0.353	-0.236	-0.000	-0.000	-0.000	0.000
	-0.000	-0.000	0.000	0.000	0.001	0.000
$\boldsymbol{\lambda}_{i,4}$	-0.000	-0.000	0.040	-0.707	0.000	-0.047
	0.000	0.000	0.000	0.000	-0.700	-0.000
	0.319	0.000	-0.000	0.000	-0.000	-0.000
	0.408	0.000	-0.000	0.000	0.000	0.000
	0.000	-0.472	-0.000	-0.000	-0.000	0.000
	-0.000	0.000	-0.003	-0.000	0.000	0.000

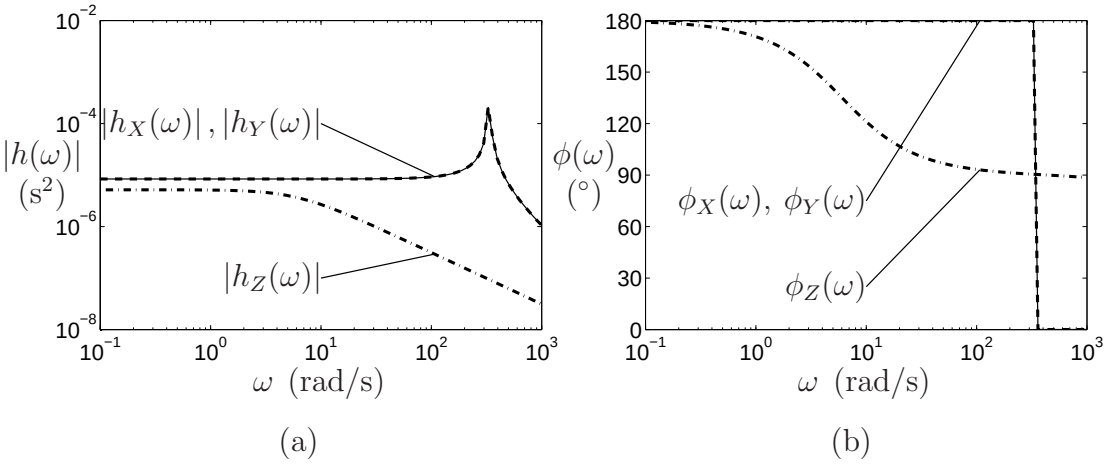

Figure 3.8: Frequency response of the SBA: (a) magnitude and (b) phase angle

3.4 Comparison of the SBA Model with a Finite Element Analysis

In this Section, the in-wafer-plane stiffness of the accelerometer obtained in Section 3.1.3 is compared against that estimated through a finite element analysis. For that purpose, the SBA is modeled in the CAD modelling software Pro/ENGINEER Wildfire 1.0 and its FEA module, Pro/MECHANICA. The resulting SBA model is illustrated in Fig. 3.9, along with the mesh of shell elements that was used for the FEA. The material used for this model is orthotropic single-crystal silicon with the same mechanical properties as those recorded in Table 3.5.

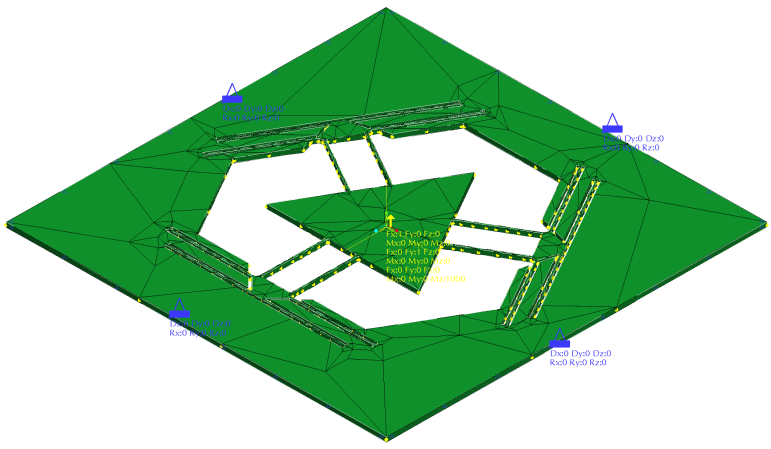

Figure 3.9: CAD model of the SBA and its associated mesh for FEA

Here, we are interested in estimating the stiffness of the structure for pure proof-mass translations along the X and Y directions, and for pure proof-mass rotations about the Z axis. Hence, three static analyses were performed corresponding to the three loading conditions:

(i) A 1 N force applied at point O in the X-axis direction;

(ii) A 1 N force applied at point O in the Y-axis direction;

(iii) A $1 \cdot 10^{-3}$ N m moment applied at point O in the Z-axis direction.

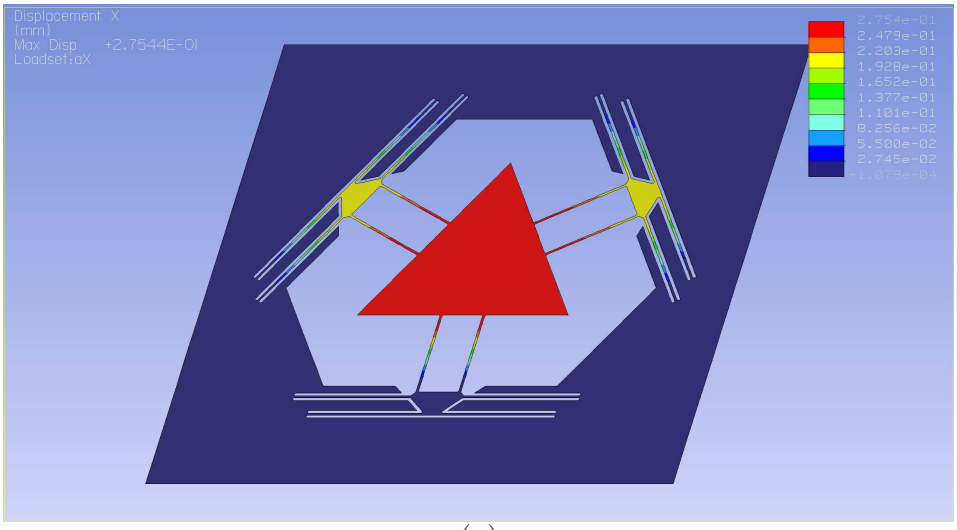

(a)

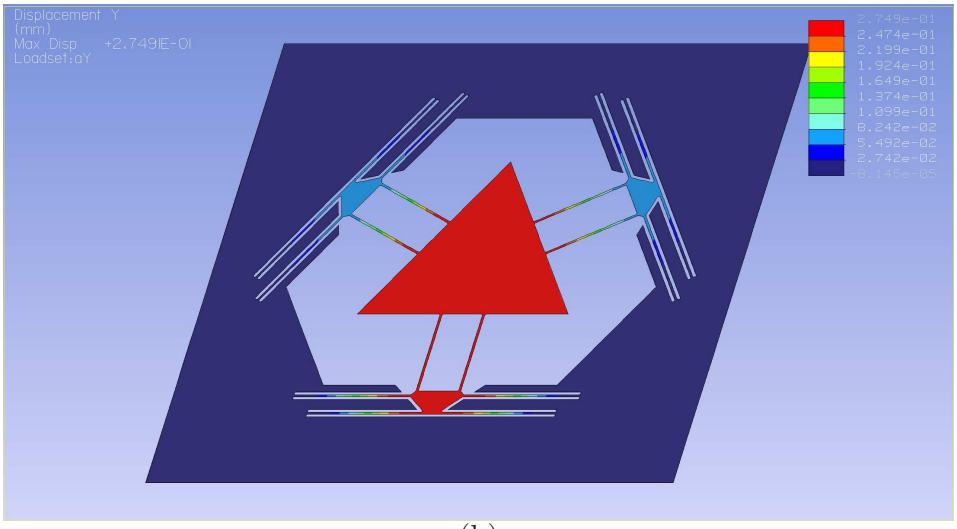

(b)

Figure 3.10: FEA results: (a) displacements in the X-axis direction due to a 1 N force in the same direction; (b) displacements in the Y-axis direction due to a 1 N force in the same direction

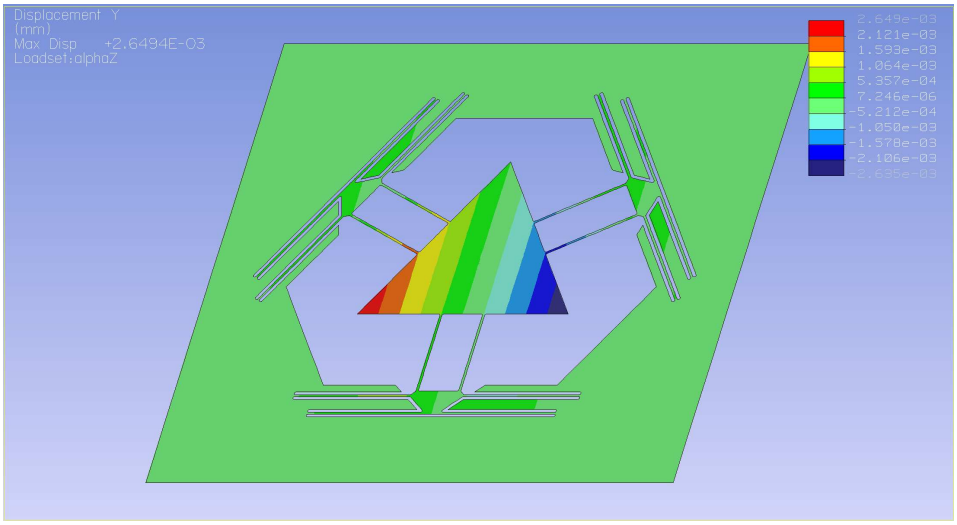

Figure 3.11: FEA results: displacements in the Y-axis direction due to a $1 \cdot 10^{-3}$ N m moment in the Z-axis direction

The resulting displacement fields are displayed in Figs. 3.10 and 3.11. In the case of the unit forces, we are interested in the displacements $\xi_{4,X}$ and $\xi_{4,Y}$ of point R_4' along the X and Y directions, respectively. From Fig. 3.10, we have

$$\begin{aligned} \xi_{4,X} &= 275.4\ \mu\text{m}, \\ \xi_{4,Y} &= 274.9\ \mu\text{m}. \end{aligned}$$

In the case of the $1 \cdot 10^{-3}$ N m moment, we are interested in the third component $\nu_{4,Z}$ of $\boldsymbol{\nu}_4$, which represents the proof-mass rotation about the Z axis. This angle can be estimated from Fig. 3.11, by first extracting the Y-axis displacements of two points of the proof mass that have the same Y-coordinate. Upon choosing the two bottom vertices of the proof mass, we have the Y-axis displacements $\xi_{4,Y,-} = -2.649\ \mu$m and $\xi_{4,Y,+} = 2.635\ \mu$m. As a result, the angular displacement is estimated to be

$$\nu_{4,Z} = \arctan\left(\frac{\xi_{4,Y,+} - \xi_{4,Y,-}}{a}\right) = 5.284 \cdot 10^{-4}\ \text{rad}.$$

The stiffness coefficients $k_{\xi,X}$, $k_{xi,Y}$ and $k_{\nu,Z}$, which correspond, respectively, to the translational stiffness in the X-axis direction, translational stiffness in the Y-axis direction, and rotational stiffness about the Z axis, are computed as

$$\begin{aligned} k_{\xi,X} &= \frac{1\ \text{N}}{\xi_{4,X}} = 3631\ \text{N/m}, \\ k_{\xi,Y} &= \frac{1\ \text{N}}{\xi_{4,Y}} = 3638\ \text{N/m}, \\ k_{\nu,Z} &= \frac{1 \cdot 10^{-3}\ \text{N m}}{\nu_{4,Z}} = 1.893\ \text{N m/rad}. \end{aligned} \tag{3.54}$$

On the other hand, these stiffness coefficients may be estimated from the stiffness matrix $\mathbf{K}$ computed in Subection 3.3.2 as

$$\begin{aligned} k_{\xi,X} &= \frac{1}{\mathbf{e}_{22}^T \mathbf{K}^{-1} \mathbf{e}_{22}} = 3613\ \text{N/m}, \\ k_{\xi,Y} &= \frac{1}{\mathbf{e}_{23}^T \mathbf{K}^{-1} \mathbf{e}_{23}} = 3614\ \text{N/m}, \\ k_{\nu,Z} &= \frac{1}{\mathbf{e}_{21}^T \mathbf{K}^{-1} \mathbf{e}_{21}} = 2.032\ \text{N m/rad}. \end{aligned} \tag{3.55}$$

Hence, from a quick inspection of eqs. (3.54) and (3.55), we see that the FEA corroborates the results obtained with the symbolic model proposed in Section 3.1.

3.5 Proof-Mass Displacement Measurement

Even though the development of a measurement technique for the estimation of proof-mass displacements was not accomplished in this work, the author would like to express a few thoughts on this issue. Three measurement methods were considered in the design: piezoelectricity; piezoresistivity; and capacitance.

Apparently, piezoelectricity is used mainly in *dynamic* accelerometers (Gautschi, 2002), i.e., accelerometers intended for the measurement of vibrations, and not uniform motions. Notice, however, that this does not mean that they cannot be used to track quasistatic signals. According to Gautschi (2002), the use of charge amplifiers in replacements of electrometers reduces the effect of leakage currents, and renders possible the measurement close-to-DC signals. As the implementation of this technique may turn out to be challenging, and because piezoelectric materials pose serious difficulties for their insertion in the fabrication process developed by the author, this technique does not appear as the most attractive.

On the other hand, piezoresistivity is a far more common technique to produce quasistatic accelerometers (see Wilson, 2005, for example). However, in most instances, the piezoresistive accelerometers have their sensitive direction normal to the wafer plane, so that the compliant beams bend in and out of the wafer plane, i.e., so that the maximum strain takes place at the top and bottom surfaces of the compliant beams. This is important, because the piezoresistors are to be implanted on these surfaces of maximum sensitivity. In the case of the SBA, all compliant beams are intended to bend in the plane, which makes the maximum sensitivity surfaces normal to the wafer plane. Nevertheless, due to the large width of the beams, it would be possible to implant piezoresistors on the top surfaces of the compliant beams, close to their lateral edges, where the strains are close to maximum. The implantation of piezoresistors could fit well in the fabrication process of Section 4, between the wafer bonding step and the aluminum deposition step.

Finally, capacitance is probably the most widely used physical prniciple for the determination of proof-mass displacements in accelerometers that offer a good accuracy at low frequencies (Analog Devices, 2004a; Freescale Semiconductor, 2007). In our case, since the sensor natural frequency is very low, the proof-mass motions are relatively large. Indeed, with a natural frequency of $\omega_0 = 334.33\,\mathrm{rad/s}$, we obtain, for accelerations of $2g$, proof-mass displacements of

$$\delta x = 2g/\omega_0^2 = 2 \cdot 9.81/334.33^2\ \mu\mathrm{m} = 176\ \mu\mathrm{m}, \tag{3.56}$$

which, for the electrode areas and air permittivity involved, is too wide a range to be picked up by capacitance variations. Hence, as a conclusion, in the opinion of the author, the capacitance variation method would be implementable only after increasing the accelerometer natural frequency, in order to reduce the proof-mass displacements.

In this Chapter, a dynamic model was proposed for elastically-articulated multibody systems undergoing small displacements. This model was applied to the aldready-existing ADXL150 accelerometer, and the estimated dynamic properties of the device were compared to those obtained by other authors, which confirmed the accuracy of the proposed model. The dynamic model was then applied to the SBA, from which we could dimension the device and estimate its dynamic performance. The following step consists in the microfabrication of the SBA according to the specified dimensions.

Chapter 4

Microfabrication of the Simplicial Biaxial Accelerometer

The microfabrication process developed for the realization of the SBA may be broken down into five main steps, as described in Sections 4.2 to 4.6. These steps are also illustrated in Fig. 4.1, for quick reference. The SBA was fabricated at the McGill Nanotools Microfab,[1] except for the DRIE step, which was conducted at the Nanofabrication and Nanocharacterization Research Centre[2] of Université de Sherbrooke.

The specifications of the two substrates used in the fabrication process are listed in Table 4.1. One may notice the difference in resistivity between the two wafers, which comes from their different functions. Indeed, the device wafer contains the electrodes, the accelerometer proof mass, and the compliant beams, which all need to allow for current to flow. On the other hand, the

[1] McGill Nanotools Microfab, McGill Institute for Advanced Materials, Ernest Rutherford Building, 3600 University St. Montreal, QC, H3A 2T8, Canada.

[2] Nanofabrication and Nanocharacterization Research Centre, Department of Electrical and Computer Engineering, Faculty of Engineering, Université de Sherbrooke, Sherbrooke, QC, J1K 2R1, Canada.

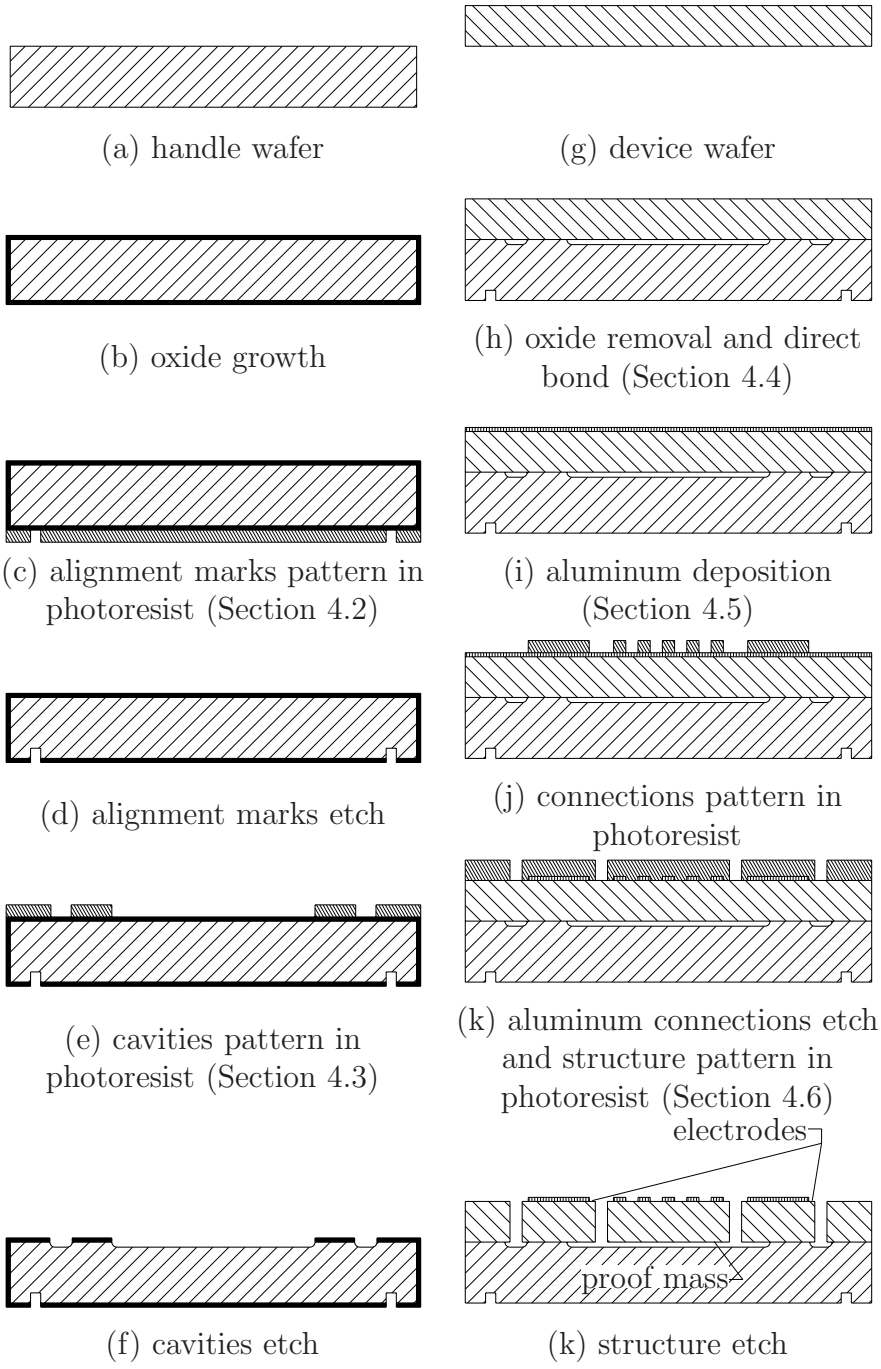

Figure 4.1: SBA fabrication process

role of the handle wafer is to support the device wafer without allowing any short circuit between its components. As a result of the high resistivity of the handle wafer, each electrode is electrically isolated from the proof mass and the rest of the device wafer, since the DRIE step etches all the surrounding

conductive silicon down to the handle wafer. This can be appreciated from the cross-section shown in Fig. 4.1(k).

Notice also the polished surface finish of both sides of each wafer. The top side of the device wafer has to be polished because it is where the device is etched. The bottom side of the device wafer and the top side of the handle wafer need to be polished as well, for they are to be bonded together. Finally, the alignment marks etched on an unpolished silicon surface turned out to be either blurry in the aligner or inaccurate, when deep-etched into the silicon using TMAH[3]. An example of the difference in visibility is shown in the pictures of Fig. 4.2, which were taken by a microscope that gives even a much better contrast between the etched and intact surfaces than do the objectives of the EVG620 aligner. From this, it was decided to require that the bottom surface of the handle wafer be polished as well.

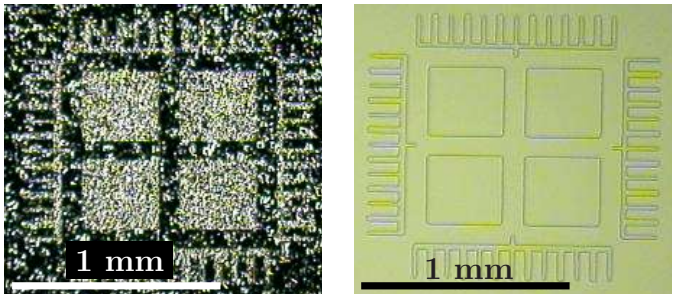

(a) (b)

Figure 4.2: Microphotographs of the alignment marks etched using RIE on: (a) unpolished; and (b) polished silicon surfaces

Finally, the aluminum metallization is illustrated in Fig. 4.3, where it is seen to serve primarily as a connection from the proof mass to the bonding

[3] Tetra-methyl ammonium hydroxide

Table 4.1: Substrates for the SBA fabrication

specification	**handle wafer**	**device wafer**
material	single-crystal silicon	single-crystal silicon
crystal orientation	100	100
dopant	boron (P)	boron (P)
resistivity	$1000\,\Omega\,\mathrm{cm}$	$\leq 5\,\Omega\,\mathrm{cm}$
front surface	polished	polished
back surface	polished	polished
diameter	150 mm	150 mm
thickness	$1000\,\mu\mathrm{m}$	$300\,\mu\mathrm{m}$

pads. These connections run along the compliant links of the SBA up to the proof mass. On top of each electrode is a bonding pad, which allows for an external connection to the electrode, without any short circuit with the proof mass. The stripe patterns on the proof mass were initially intended to allow for the measurement of interference patterns produced by light reflected on the proof mass. This method was first envisionned to measure proof-mass displacements, but we finally opted for a scanning vibrometer, which does not require these patterns. Notice that none of the on-chip circuitry was used nor tested, since proof-mass displacements were measured using an external non-contact displacement sensor.

4.1 Handle Wafer Preparation

In anticipation of the bonding step of Section 4.4, the handle wafer bow is measured using the *Tencor Flexus 5200 Film Stress Measurement System*. The convex side is recorded, so that it becomes the top side of the handle wafer.

Trials and errors showed that growing a silicon dioxide (SiO_2) layer over the handle wafer increases the success rate of the bonding step. As silicon dioxide is harder than silicon, it can be selectively removed by dipping the wafer into hydrofluoric (HF) acid. For these reasons, SiO_2 forms a protection

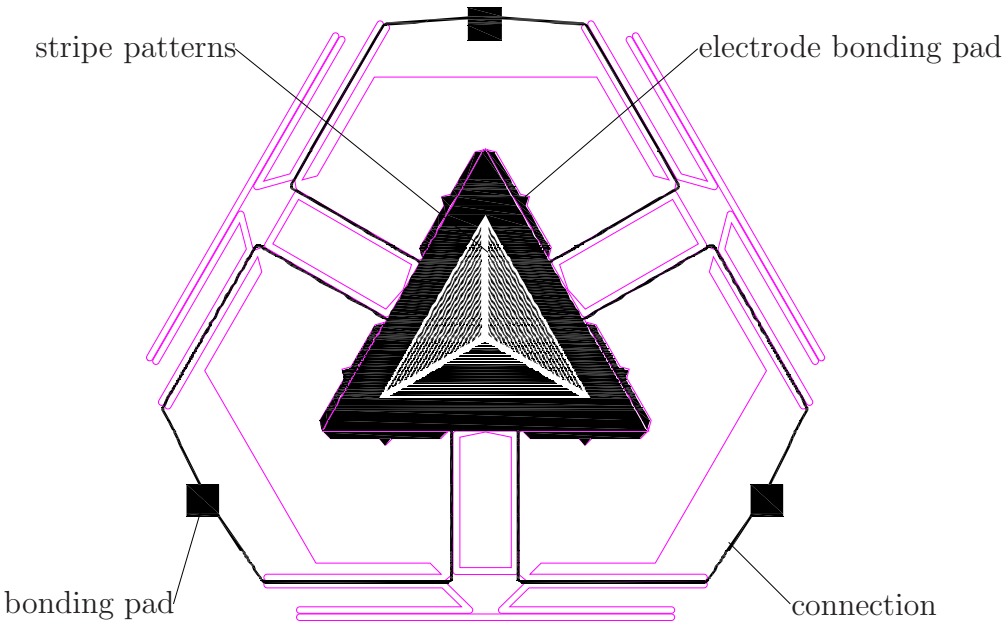

Figure 4.3: SBA aluminum metallization

against dust or scratches that threaten to alter the surface of the wafer during the pre-bonding manipulations. Hence, in this process, the oxide growth is the first step after measuring the wafer bow, whereas oxide removal takes place in the last step prior to bonding. The recipe of Table A.1, which is based on the model of Deal and Grove (1965), is followed, as it proved to result in a layer of approximately 0.5 μm of SiO_2.

4.2 Alignment Marks

The recipe of Table A.2 is used to coat the handle wafer with a layer of Shipley-1813 photoresist. The pattern is transferred from mask #1 of Fig. B.2(a) to the wafer by means of the recipe of Table A.3. The wafer is developed according to the recipe of Table A.4. The alignment marks are written by first etching the silicon oxide layer with the Reactive Ion Etching (RIE) process of Table A.5, and then etching the silicon down to approximately

2.5 μm by means of the RIE process of Table A.6.

In preparing the handle wafer for the next step, a plasma is used in order to remove the photoresist mask. A suggested set of parameters is displayed in Table A.7.

4.3 Interfacial Cavities

Since the top side of the handle wafer has been in contact with various wafer chucks in the previous alignment-mark etch step, it needs cleaning prior to coating it with photoresist. For that reason, the handle wafer undergoes a standard RCA clean without HF dip—we do not want to remove the silicon dioxide layer—according to the recipe given in Table A.8. The pattern of mask #2 shown in Fig. B.2(b) is transferred to a resist layer as per the recipes of Tables A.2, A.3, and A.4, in which the photoresist is, again, Shipley-1813, with a resulting thickness of 1.4 μm.

Notice the transparent horizontal and vertical stripes in mask #2, which were added in order to fix a problem that occurred at the later step of the aluminum deposition (see Section 4.5). These white stripes are absent in the previous version of mask #2, the rest of the layout being identical. In fact, these white stripes produce trenches at the interface of the two wafers so that the inner cavities be connected to the outside air. The problem in the aluminum deposition of Section 4.5 is that the sputtering process requires the bonded wafer pair to be held under vacuum throughout the operation. In the case where the interfacial cavities are hermetically sealed, there is an inevitable pressure difference between them and the outside vacuum. As a result,

the thinner device wafer is subjected to stresses which turned out to be sufficiently high to produce cracks that clearly ran across all of the nine interfacial cavities. Of course, these cracks are enough to spoil the bonded pair, which commands the use of interfacial trenches in order to avoid any pressure difference between the interfacial cavities and the outside air.

The cavities are etched into the silicon, as described in Section 4.2, that is, by applying successively the reactive ion etching recipes of Tables A.5 and A.6. Finally, the photoresist layer is removed through the application of the recipe of Table A.7.

A SEM micrographe of the cross-section of a typical interfacial cavity is shown on Fig. 4.4(a). A similar cross-section where the two surfaces are in contact is shown on Fig. 4.4(b), as a reference. Those micrographs were taken on a cleaved bonded wafer-pair.

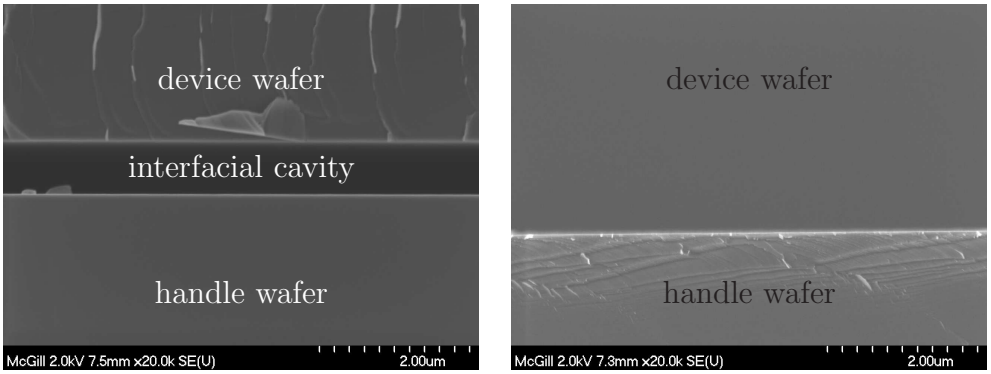

(a) (b)

Figure 4.4: SEM micrographs of the cross section of a bonded wafer pair: (a) the interfacial cavity and (b) the bonded surfaces

4.4 Bonding

The bonding step is probably the most critical one, as its repeatability is relatively low. Besides being dependent upon the curvature of the wafers, the process was found to be highly sensitive to the cleanliness of the interfacial surfaces. Therefore, the curvature of the device wafer should be measured using the *Tencor Flexus 5200 Film Stress Measurement System* prior to bonding. The orientation of that wafer should be recorded so that its convex face be mated with the top face of the handle wafer at the bonding step.

A special cleaning procedure was also devised in order to reduce the number and size of particles at the interface of two wafers prior to bonding. This cleaning procedure should be executed after taking the curvature measurements in order to minimize the risk of contamination of the wafers. The process is detailed in Table A.9, where apparently the silicon dioxide protective layer is removed by an HF-etch just before the RCA clean, so as to reduce the exposition of the silicon surface of the handle wafer to a minimum. Notice also the addition of a *piranha etch* as a precaution against organic residues that may come from the photoresist. The whole cleaning process is executed in approximately one afternoon.

Once the wafers are clean, one can proceed with the bonding recipe shown in Table A.10. In this process, we may highlight the relatively high applied force of 1 kN, and the four-hour annealing step. Every bonding is followed by an inspection of the bonded wafer pair under an infrared lamp and using a digital camera. Setting the focus of the digital camera at the interface reveals any separation region between the two wafers. A sample picture of the wafer interface is shown in Fig. 4.5, where the concentric interference fringes show

the local separation of the two wafers. Figures 4.5(a) and (b) show a successful and an unsuccessful bond, respectively.

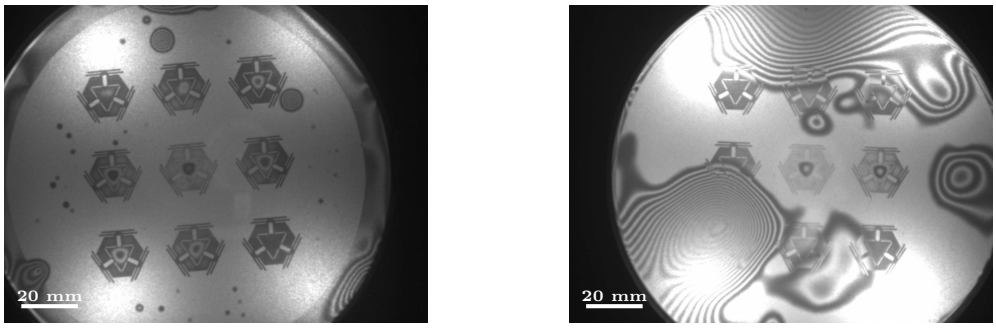

(a) wafer pair #9: a successful bond (b) wafer pair #11: an unsuccessful bond

Figure 4.5: Sample bonded pairs (photographs taken with an infrared camera)

Performing an additional annealing step proved to extend the bonded surface, in some instances. A typical set of parameters for such an annealing process is shown in Table A.11, which resulted in the bonds shown in Figs. 4.6, in the case of wafer pairs #9 and #11. Comparing these pictures with those of Fig. 4.5, one sees that the annealing had very little effect on wafer pair #9, although some very slight changes on the wafer periphery may be observed. On the other hand, the annealing is seen to have a clearly positive effect on wafer pair #11. Notice, however, that in the case of wafer pair #11, all potential samples have been affected by some flaws, and, therefore, none of them can be later used as accelerometers. Table A.11 reports an annealing temperature of 300°C, which is smaller than the annealing temperatures commonly used in silicon-to-silicon bonding. This is due to the limitations of the available Isotemp Programmable Oven, which can only go as high as 350°C. Because this annealing step was generally performed overnight, it was decided to operate slightly below the oven temperature limit.

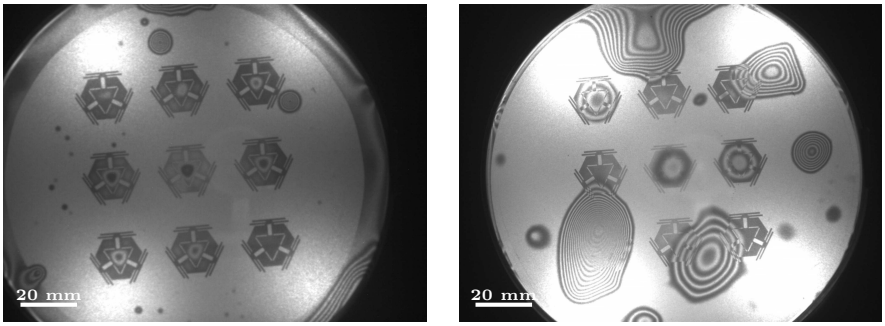

(a) wafer pair #9 (b) wafer pair #11

Figure 4.6: Sample bonded pairs after annealing step (pictures taken with an infrared camera)

Another interesting observation is that the introduction of horizontal and vertical trenches, discussed in Section 4.3, may have improved the bonding success rate. Indeed, three out of the four wafer pairs that were bonded using the new mask #2 of Fig. B.2 were completely successful, whereas the success rate with the older version of mask #2 was approximately 50%. More tests are required to confirm this claim, but it seems plausible that these trenches help evacuate the air trapped in the voids occurring during the bonding process.

4.5 Aluminum Deposition

The aluminum deposition step is preceded by a standard RCA clean just as that of Table A.8. This step is motivated by the contact between the exposed surface of the device wafer and the bonder piston, and also by the possible exposition of the wafer to dust particles during inspection.

The recipe used to deposit a layer of 0.32 μm of aluminum is explained in Table A.12. Notice the `pause` steps that allow for the wafer to cool down in between the sputtering steps. This is a precaution that was taken in order to ensure a better surface finish of the aluminum layer. The cooling time may be exaggerated, but this step is conducted overnight, and, in this case, time is

not an issue.

The aluminum layer is patterned by etching, that is, by covering it with a patterned photoresist mask, and then removing the exposed regions. The photoresist is spun, exposed, and developed as described in the recipes of Tables A.2, A.3, and A.4, respectively. In the exposition step, the pattern of mask #3 shown in Fig. B.2(c) is transferred to the photoresist layer. After the photoresist mask has been developed, we resort to the reactive ion-etching process of Table A.13 to selectively remove the aluminum.

Finally, the photoresist mask is dissolved in acetone according to the recipe of Table A.14. Notice that a removal method different from that of Table A.7 is required, since heating the bonded pair was found to cause the device wafer to break. The proposed removal method uses acetone to dissolve the photoresist, isopropyl alcohol to remove the acetone residues, and a low heating to force the evaporation of the remaining alcohol trapped at the interface of the bonded wafers.

4.6 Structure Etch

The carving of the mechanical structure of the SBA takes place in one single DRIE step, which is performed on an *Advanced Silicon Etch (ASE) Plasma Etching System*. In this case, the etch depth is 300 μm, which is more than 100 times the depths of the etches of Sections 4.2 and 4.3. As a result, the 1.4 μm Shipley-1813 photoresist mask used in these steps is not able to sustain such deep etch, and a different type of resist is needed. In order to remain in the same family of photoresist, the thicker Shipley-1818 was tested without success: the maximum thickness of 2.8 μm allowed by that polymer was etched

away before the depth of 300 μm could be reached in the silicon. To fix this problem, a photoresist from a different manufacturer is used: the AZ9260.

The wafers are coated, patterned and developed according to the recipe of Tables A.15 and A.16, which yields thicknesses ranging between 6 μm and 7 μm, and a uniformity of approximately ± 0.25 μm. They are then diced according to the dimensions shown in Fig. A.1. Notice that the dicing operation may produce some silicon dust that sticks to the photoresist layer. This proved to have no effect on the etch rate of the photoresist layer during the DRIE step.

The samples are etched one by one at *Université de Sherbrooke*, according to the recipe shown in Table A.17. Notice that the resulting etch depth is greater than 300 μm, which corresponds to the device wafer thickness. The reason behind is the lower etch rate within the small gap that separates the electrodes from the proof mass. Indeed, it was found that, after reaching the handle wafer by etching, these electrodes were still attached to the proof mass. Since no microscope could give a clear image of the bottom of the trench that separates the two components, the only way to verify this was to destroy a sample by taking apart the proof mass, which is photographed in Fig. 4.7(a). In that picture, one may verify that the electrodes are still attached to the proof mass, and hence, some overetching is necessary in order to achieve the 300 μm depth on the whole surface. A typical result of this overetching is shown in Fig. 4.8(a), where the handle wafer was etched over a depth of 87 μm.

Another means of determining whether the accelerometer proof mass is released is to press gently on it in order to displace it by a few microns without breaking it. To this end, a small contraption, shown in Fig. 4.7(b), was

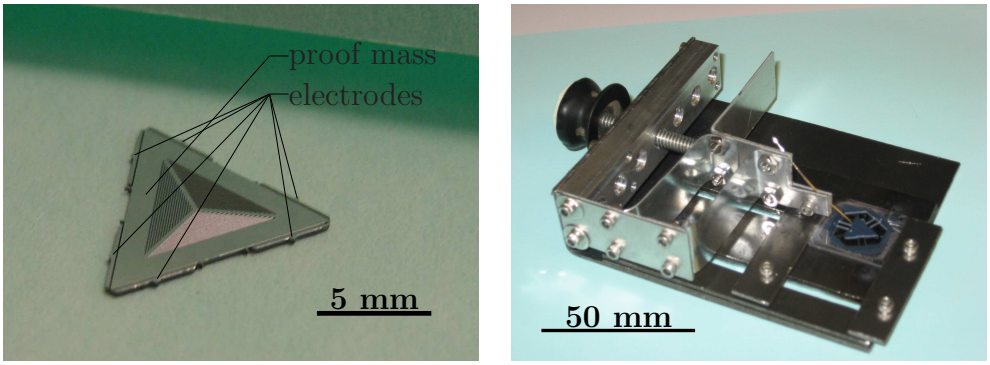

(a) (b)

Figure 4.7: (a) Broken SBA proof mass and (b) the releasing assessment testbed (RAT)

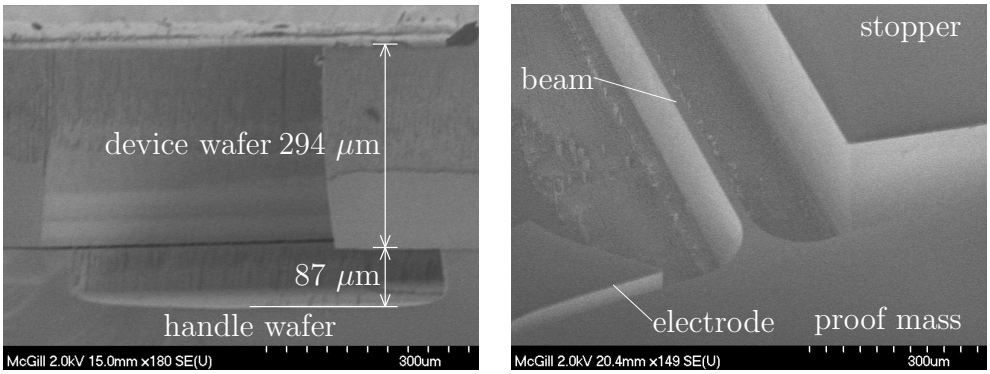

(a) (b)

Figure 4.8: SEM micrographs of the SBA: (a) typical wall profiles obtained with DRIE and (b) a closeup on a beam and its surrounding components

devised, which will be referred to as the *Releasing Assessment Testbed (RAT)*. RAT is, in fact, a compliant mechanism actuated by means of a screw, in order to reduce the mechanical advantage, and able to displace the proof mass over a small distance. A threading needle is used to make contact with the proof mass. Figure 4.9 shows the resulting small proof mass displacement under the microscope.

Once the mobility of the proof mass is verified, the remaining resist layer is dissolved in acetone, as explained in Table A.14.

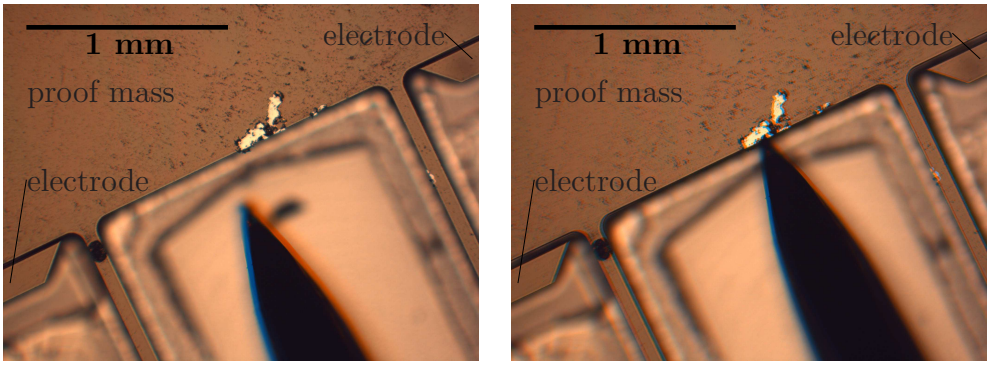

(a) (b)

Figure 4.9: Releasing assessment test: (a) proof mass in its equilibrium state and (b) in its displaced state

A SEM micrograph of some components of the resulting device is shown in Fig. 4.8(b), where the electrode is seen to stand off the proof mass by 40 μm. The gap between the electrodes and the proof mass is best seen by looking at one of the three vertices of the latter component, a top view of which is shown in Fig. 4.10. On this micrograph, which was taken using an optical microscope, only the bottom of the etched surface is in focus. Although this blurs the top surfaces of the electrodes and proof mass, it reveals the bases of the electrodes, which were left intact by the interfacial cavities etch. These bases connect the electrodes to the handle wafer, while the proof mass remains suspended over the handle wafer. This can be appreciated from the SEM micrographs of Fig. 4.11, where the gap between the proof mass and the handle wafer is apparent, while the electrodes remain connected to the handle wafer through their base. Fig. 4.11(a) also allows for a look into the gap that separates the proof mass and two of the six electrodes.

A better view of this gap was obtained from a sample that was destroyed by breaking the beams that suspend its proof mass. Some of the electrodes were removed while the proof mass left standing a few hundred microns away

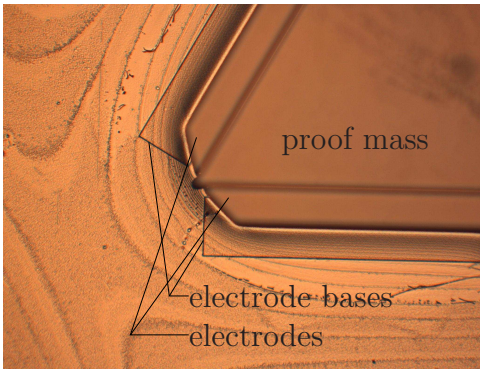

Figure 4.10: Optical micrograph of a vertex of the SBA proof mass

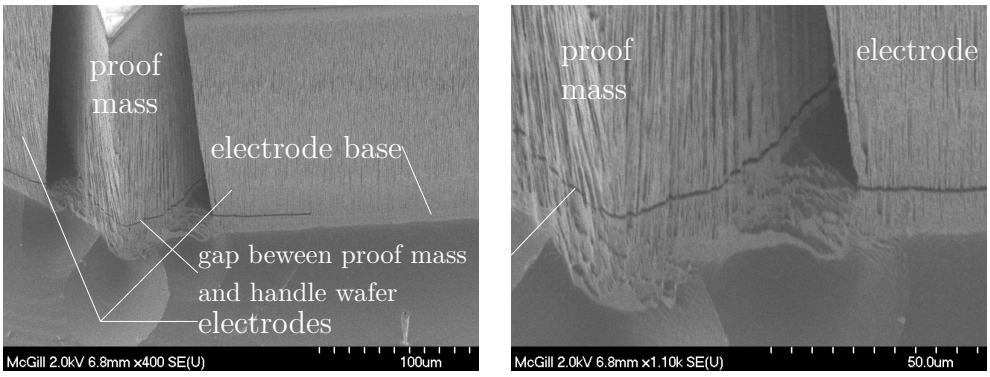

(a) (b)

Figure 4.11: SEM micrographs of a vertex of the SBA proof mass attached to its supporting structure and released from below: (a) 400× (b) 1100× closeup on the gap beween the proof mass and the handle wafer.

from its original position, as can be seen on the SEM micrographs of Fig. 4.12. Hence, one can see that the proof mass was completely separated from its surrounding electrodes. Also visible on these pictures, the trace of the electrode base that is left even after the overetch included in the DRIE step.

4.7 Packaging

It was difficult to find a package large enough to contain the SBA samples. The chosen package comes from Spectrum Semiconductor Materials, of San Jose, CA, and is made of ASTM F-15 alloy, which is constituted of cobalt, iron, and nickel. This package is clamped between an aluminum mount and an acrylic glass cover. The resulting package assembly is displayed in Fig. 4.13.

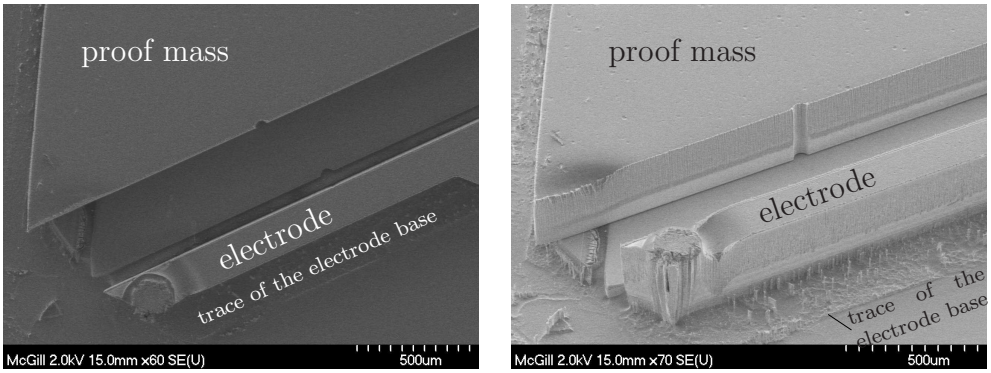

(a) (b)

Figure 4.12: SEM micrographs of a vertex of the SBA proof mass detached from its supporting structure: (a) top view and (b) 3D view

Notice that the resulting package is by no means hermetic, but it prevents dust from reaching the silicon chip; it also prevents the accelerometer from being affected by aerodynamic effects when shaken, while allowing for interferometric measurements through the clear acrylic cover. Although none of the on-chip circuitry was used, some of the packaged devices were connected to the metallic package by 1 μm-diameter gold wires. The wire bonding was performed on an ultrasonic wire bonder.

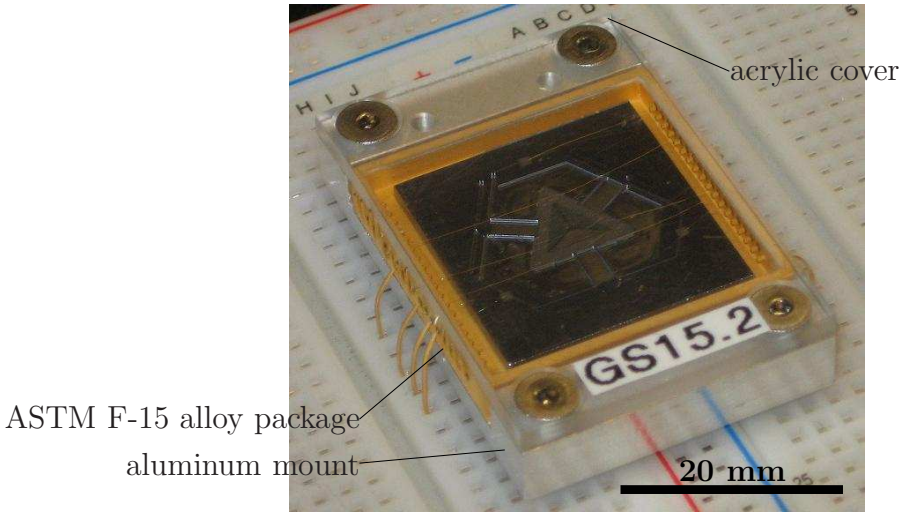

Figure 4.13: SBA package

Chapter 5

Testing the Simplicial Biaxial Accelerometer

The mechanical structure of the SBA was tested by applying to it short impulse accelerations in the negative direction of its Z axis, which is normal to the plane of Fig. 3.6, illustrating the SBA. The "free" resonances of the structure were then recorded using a vibrometer. A schematic and a picture of the test bench are shown in Fig. 5.1. In this setup, the shaker (Brüel & Kjær Mini-Shaker 4810) is driven by a regular power amplifier (Harman Kardon HK3300), which itself takes its input from a signal generator. A typical time-evolution of the shaker impulse input voltage is displayed in Fig. 5.2. The resulting motions of the SBA rigid-links are recorded by the vibrometer (Polytec PSV-400), which sheds a laser beam vertically down on the sample. The laser beam is programmed to scan 382 points on the SBA, according to the mesh shown in Fig. 5.3. Point-velocities are measured by the vibrometer, and, thence, a frequency-domain distribution of the point-velocities of the accelerometer architecture is computed and recorded by the controller (Polytec OFV–5000).

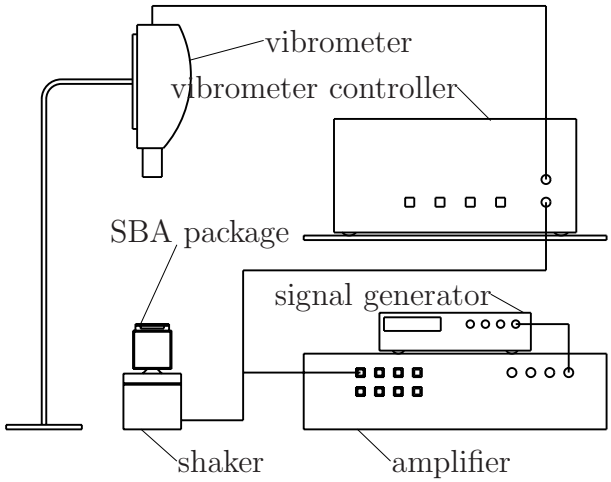

(a)

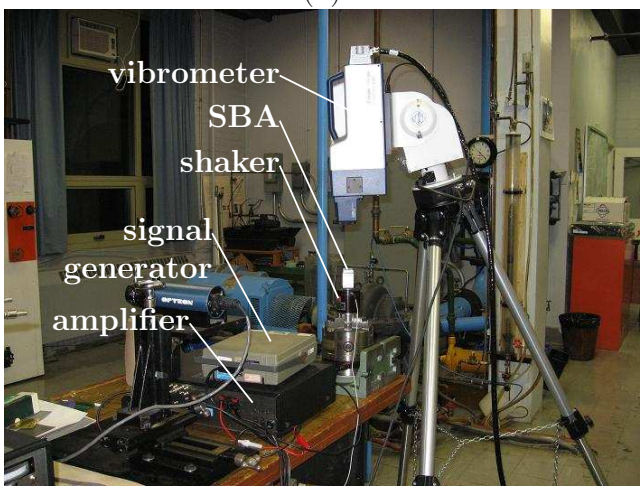

(b)

Figure 5.1: SBA test bench: (a) schematic representation; and (b) photograph

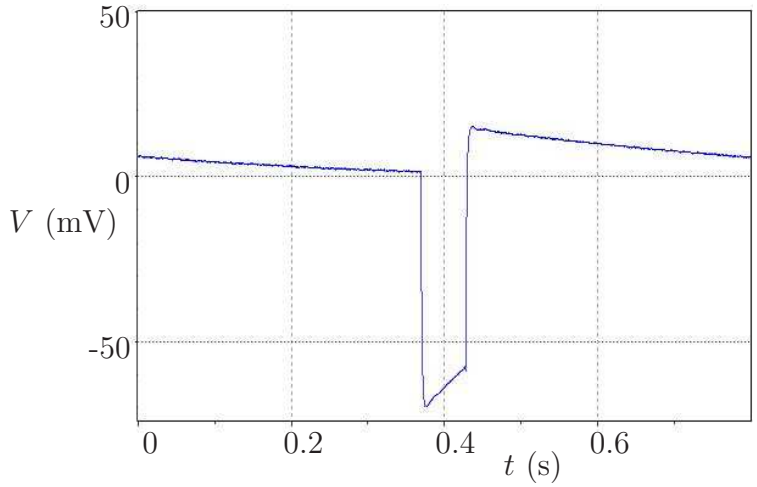

Figure 5.2: Typical voltage impulse applied at the shaker input

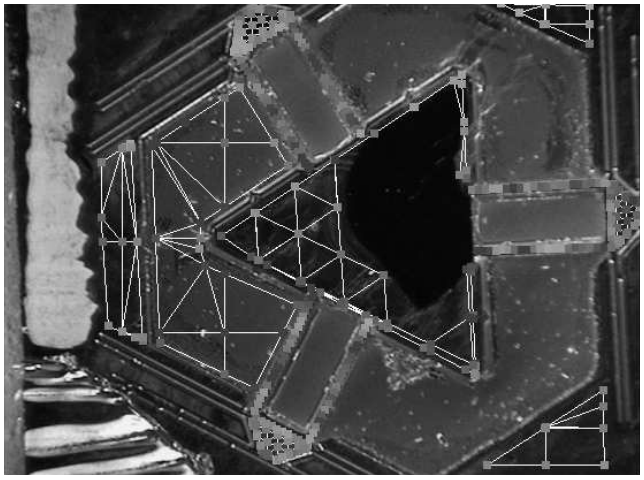

Figure 5.3: Points scanned by the vibrometer

The Polytec controller returns a frequency-domain distribution of the out-of-plane velocities of the scanned points $\{S_j\}_{j=1}^{382}$, along with their phase correspondance with a reference signal. As can be seen from Fig. 5.1(a), in the test bench, the shaker input voltage was used as the reference signal. From these results, the complex velocity frequency response $v_j(\omega)$ of each point may be computed.

The out-of-plane point-displacement frequency response $d_j(\omega)$ may then be obtained as

$$d_j(\omega) = v_j/(\omega i), \tag{5.1}$$

where $i \equiv \sqrt{-1}$. On the other hand, the out-of-plane point-acceleration frequency response $a_j(\omega)$ is given by

$$a_j(\omega) = \omega v_j i. \tag{5.2}$$

Let us now define the sets $\mathcal{F}$ and $\mathcal{P}$ of the indices of the points pertaining to the accelerometer frame and proof mass, respectively. From this, we may reference the proof mass point-displacement response magnitudes with the rms-value of the frame point-acceleration response magnitudes. This yields the normalized

displacements

$$\bar{d}_j(\omega) = \frac{d_j(\omega)}{\sqrt{(1/n)\sum_{k\in\mathcal{F}} |a_k(\omega)|^2}}, \quad j \in \mathcal{P}, \tag{5.3}$$

where n is the cardinality of $\mathcal{F}$. Finally, we obtain an overall magnitude response of the proof-mass by taking the rms-value of the displacements of its 60 scanned points. Symbolically, we have

$$\bar{d}_{rms}(\omega) = \sqrt{\frac{1}{m}\sum_{j\in\mathcal{P}} |\bar{d}_j(\omega)|^2}, \tag{5.4}$$

where $m = 60$ is the cardinality of $\mathcal{P}$. On the other hand, the meaning of an overall phase diagram of the proof-mass point-displacements is less apparent; it was thus decided to leave it aside. Hence, the phase angle $\bar{\phi}_j(\omega)$ of point $j \in \mathcal{P}$ is readily computed as

$$\bar{\phi}_j = \arctan\left(\frac{\Im(\bar{d}_j(\omega))}{\Re(\bar{d}_j(\omega))}\right). \tag{5.5}$$

The resulting frequency response is shown in Figs. 5.4(a) and (b), along with the modelled frequency response, which was already shown in Fig. 3.8. Notice that the 60 phase angles $\bar{\phi}_j$, $j \in \mathcal{P}$ are displayed in Fig. 5.4(b).

As can be seen from these figures, the measured frequency response is fairly close to the ones given by the transfer functions $h_X(\omega)$ and $h_Y(\omega)$ of the accelerometer along its sensitive directions. This is surprising, since the vibrometer is meant to measure out-of-plane motions, which should correspond rather to the transfer function $h_Z(\omega)$. However, the vibrometer is not completely insensitive to transverse motion. Indeed, when scanning a fixed point on a surface that undergoes in-plane motions, the vibrometer also detects the changes in depth of the surface over this fixed point. Hence, a rough surface moving in the plane only still generates a signal at the vibrometer

output. Because of the close resemblance between the modelled and measured responses (the peak frequencies are 53.2 Hz and 46.3 Hz, respectively) it is highly probable that the motion detected here corresponds to in-plane proof-mass translations. In order to be conclusive on this issue, one could use, for example, the Polytec PSV-400-3D, which allows the estimation of the three components of the point velocities and displacements. This test could not be performed because of lack of resources. If this assertion were to be verified, one could conclude safely that the Z-axis magnitude response of the accelerometer is indeed below those of the sensitive axes.

Hence, it is seen that accelerometer mechanical architectures inspired from PKM architectures can reduce the device sensitivity to cross-axis accelerations, angular velocities, and angular accelerations. The balance of this work is dedicated to the study of a generic array of accelerometers mounted on a rigid body to estimate its acceleration field, and, from there, its angular velocity. The cornerstone of this analysis is the accelerometer model, in which it is assumed that accelerometers are only sensitive to the acceleration components parallel to their sensitive directions, i.e., that their cross-axis sensitivity is null. Therefore, the preceding and following Chapters are linked by the same common thread: improving the robustness of accelerometer arrays.

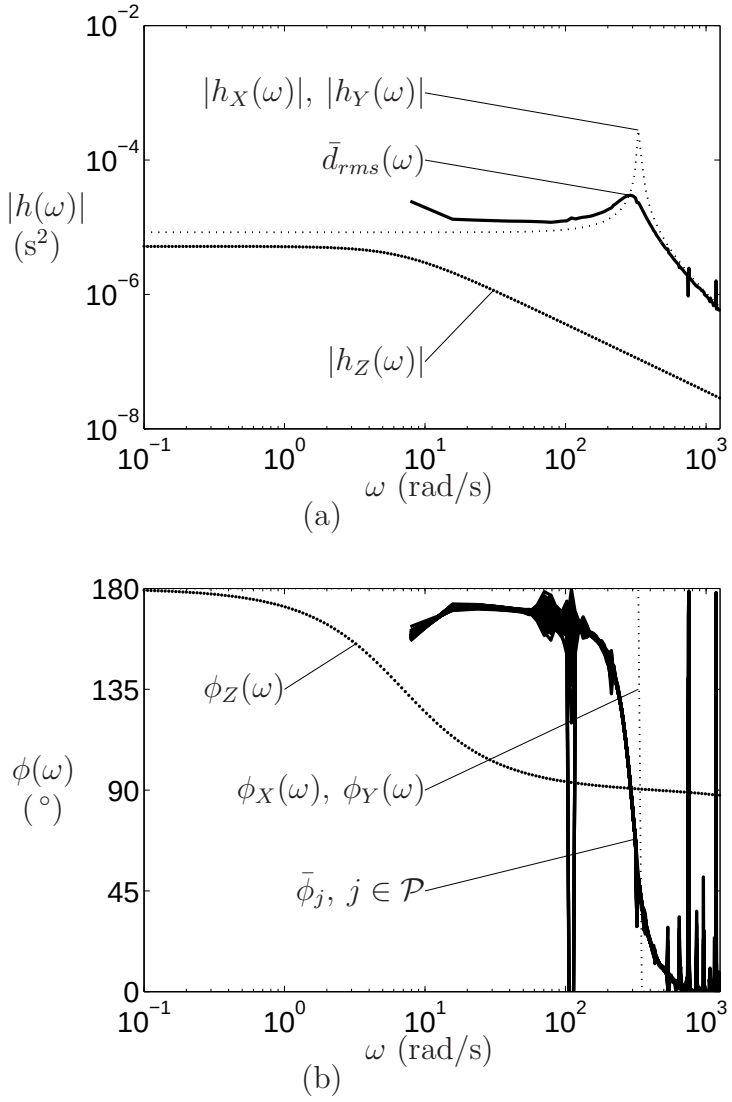

Figure 5.4: Comparison between the SBA model and the experimental results: (a) magnitudes; and (b) phase angles

Chapter 6

Mathematical Model of an Accelerometer Array

In this chapter, we address the problem of estimating the full acceleration field of a rigid body equipped with n accelerometers. For starters, let us recall the nature of the acceleration field of a rigid body, that is, the map that associates an acceleration vector to each point of a rigid body.

6.1 The Acceleration Field of a Rigid Body Moving in the Plane

We begin with the simpler case of a rigid body moving in the plane. Let O be a fixed point, i.e., a point attached to an inertial frame—which need not be specified—and B be a landmark point on the rigid body.

The superscript $(')$ will be used throughout the balance of this work to distinguish the planar case from the spatial case. Following this rule, we label $\mathbf{b}' \in \mathbb{R}^2$, the position vector of B, and $\mathbf{p}'_i \in \mathbb{R}^2$ the position vector of an arbitrary point P_i pertaining to the rigid body. Moreover, we define $\mathbf{r}'_i \equiv \mathbf{p}'_i - \mathbf{b}'$, the vector pointing to P_i from B, and ω, the time-rate of change of the angle between a reference line attached to the rigid body and a line of

the inertial frame, respectively. Hence, the time derivative of $\mathbf{p}'_i$ is

$$\dot{\mathbf{p}}'_i = \dot{\mathbf{b}}' + \dot{\mathbf{r}}'_i = \dot{\mathbf{b}}' + \omega \mathbf{S} \mathbf{r}_i, \quad \text{where} \quad \mathbf{S} \equiv \begin{bmatrix} 0 & -1 \\ 1 & 0 \end{bmatrix}, \tag{6.1}$$

and ω is defined positive when the rigid body rotates in the counterclockwise (CCW) direction, which is the rule observed throughout this thesis. This leads to the expression of the acceleration of the generic point P_i:

$$\ddot{\mathbf{p}}'_i = \ddot{\mathbf{b}}' + \mathbf{W}' \mathbf{r}'_i \tag{6.2}$$

where $\mathbf{W}' \equiv \dot{\omega}\mathbf{S} - \omega^2 \mathbf{1}_{2\times 2}$, and $\mathbf{1}_{2\times 2}$ is the 2×2 identity matrix. The vector field is best visualized by replacing the acceleration of point B with the position of the acceleration centre—see (Ridley et al., 1992), for example—A of the rigid body. Analogous to the instant centre of rotation, the *acceleration centre*, or *acceleration pole* (Veldkamp, 1969), is the point of the rigid body that has zero acceleration instantaneously. If the choice of B is arbitrary, A, in turn, depends solely on the rigid-body motion. Upon defining $\mathbf{p}'_A$, the position vector of A with respect to O, we may express the acceleration centre A as the point for which $\ddot{\mathbf{p}}'_A = \mathbf{0}_2$, where $\mathbf{0}_2$ is the two-dimensional zero vector. The introduction of the foregoing condition in eq. (6.2) leads to

$$\ddot{\mathbf{p}}'_A = \mathbf{0}_2 = \ddot{\mathbf{b}}' + \mathbf{W}' \mathbf{r}'_A, \tag{6.3}$$

where $\mathbf{r}'_A$ is the vector pointing to A from B. The determinant of $\mathbf{W}'$ may readily be calculated to be $\omega^4 + \dot{\omega}^2$, which leads to the conclusion that $\mathbf{W}'$ is nonsingular, except when the rigid body undergoes pure translation to the

second order[1]. In that case, the acceleration centre lies at infinity, whereas, in all other situations, the position vector of A is given by

$$\mathbf{r}'_A = -\mathbf{W}'^{-1}\ddot{\mathbf{b}}' = \frac{1}{\omega^4 + \dot{\omega}^2}\left(\omega^2 \mathbf{1}_{2\times 2} + \dot{\omega}\mathbf{S}\right)\ddot{\mathbf{b}}. \tag{6.4}$$

Hence, the vector field of eq. (6.2) may be rewritten as a function of $\mathbf{r}'_A$, namely,

$$\ddot{\mathbf{p}}'_i = \mathbf{W}'(\mathbf{r}'_i - \mathbf{r}'_A), \tag{6.5}$$

which leads to the geometric representation of Fig. 6.1(a), where the concentric circles are isocontours of points undergoing accelerations of the same magnitude. It is often useful to decompose the point acceleration $\ddot{\mathbf{p}}'_i$ of point P_i into two orthogonal components, tangent and radial to its corresponding circle. These components are called tangential and centripetal acceleration, respectively. From eq. (6.5), the magnitudes of these two components are proportional to the distance from A to P_i, and, therefore, the resulting acceleration $\ddot{\mathbf{p}}'_i$ makes an angle α with its corresponding tangential acceleration component that is constant for a given planar acceleration field.

It is now apparent that the planar acceleration field is a function of four independent scalar kinematic variables: the rigid body instant centre of acceleration, given by the position vector $\mathbf{r}'_A \in \mathbb{R}^2$; the angular velocity ω; and the angular acceleration $\dot{\omega}$. For this reason, a minimum of four accelerometer readouts is required for the definition of the complete acceleration field. Moreover, notice that the two angular velocities ω and $-\omega$ produce the same

[1] Pure translation is defined by $\omega = 0$; we term *pure translation to the second order* the motion under which $\omega = 0$ and $\dot{\omega} = 0$.

acceleration field. Consequently, it is impossible to identify unambiguously the angular velocity time history of the rigid body without prior knowledge of one of the previous values—e.g., the initial angular velocity of the rigid body.

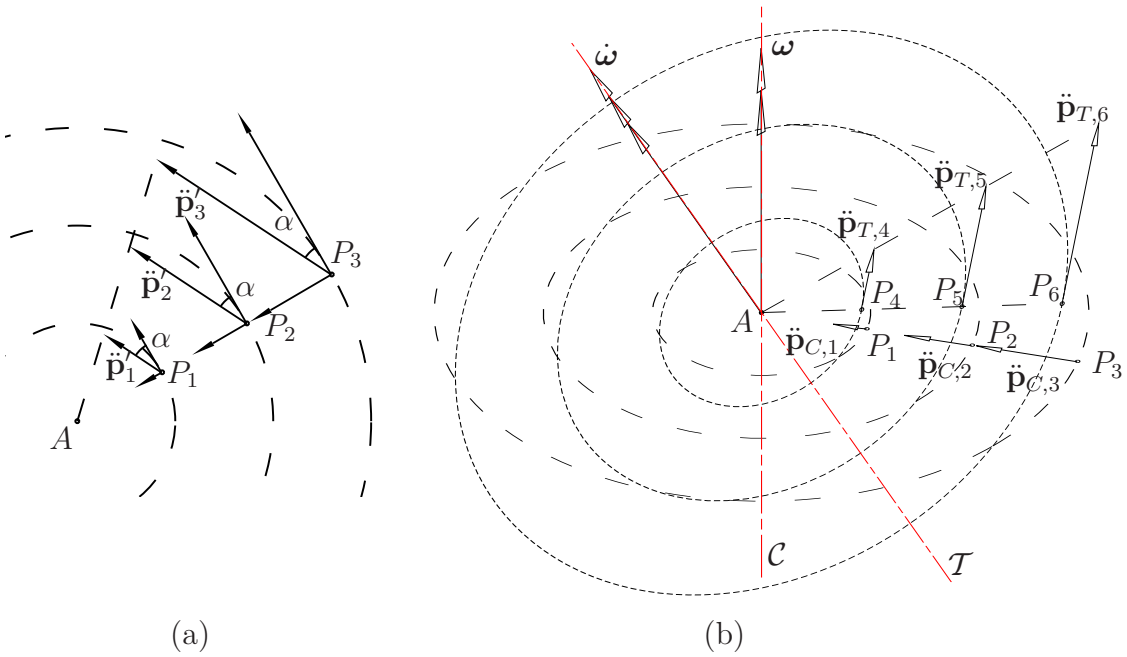

Figure 6.1: The acceleration field of a rigid body moving (a) in the plane and (b) in space

6.2 The Acceleration Field of a Rigid Body Moving in Space

The acceleration field of a rigid body moving in space is slightly more complicated than that of a rigid body moving in the plane. Let us assume that point O is attached to an inertial frame, whereas points B and P_i pertain to the moving rigid body. Observing the notation introduced for the planar case, we choose $\mathbf{b} \in \mathbb{R}^3$ to be the position vector of B, $\mathbf{p}_i \in \mathbb{R}^3$, the position vector of P_i, and $\mathbf{r}_i \in \mathbb{R}^3$, the vector pointing to P_i from B. As a result, we

obtain the equations of a rigid-body moving in space, namely,

$$\mathbf{p}_i = \mathbf{b} + \mathbf{r}_i, \tag{6.6}$$

$$\dot{\mathbf{p}}_i = \dot{\mathbf{b}} + \boldsymbol{\omega} \times \mathbf{r}_i, \tag{6.7}$$

$$\ddot{\mathbf{p}}_i = \ddot{\mathbf{b}} + \dot{\boldsymbol{\omega}} \times \mathbf{r}_i + \boldsymbol{\omega} \times \boldsymbol{\omega} \times \mathbf{r}_i = \ddot{\mathbf{b}} + \mathbf{W}\mathbf{r}_i, \tag{6.8}$$

where $\mathbf{W} \equiv \dot{\boldsymbol{\Omega}} + \boldsymbol{\Omega}^2$ is the angular acceleration matrix (Angeles, 1999), $\boldsymbol{\Omega} \equiv \mathrm{CPM}(\boldsymbol{\omega})$, and $\boldsymbol{\omega}$ is the rigid-body angular-velocity vector. As in Section 6.1, replacing $\ddot{\mathbf{b}}$ with the acceleration centre $\mathbf{r}_A \in \mathbb{R}^3$ eases the geometric representation of the acceleration field. Hence, we write

$$\mathbf{0}_3 = \ddot{\mathbf{b}} + \mathbf{W}\mathbf{r}_A, \tag{6.9}$$

where $\mathbf{W}$ is generally nonsingular. In fact, Angeles (1999) provided the relation $\det(\mathbf{W}) = -\|\boldsymbol{\omega} \times \dot{\boldsymbol{\omega}}\|_2^2$, which shows that $\mathbf{W}$ is singular if and only if $\boldsymbol{\omega} \parallel \dot{\boldsymbol{\omega}}$. This case is equivalent to having a rigid body moving in a plane orthogonal to $\boldsymbol{\omega}$ (and $\dot{\boldsymbol{\omega}}$), the plane itself undergoing a purely translational acceleration in the direction of $\boldsymbol{\omega}$ (and $\dot{\boldsymbol{\omega}}$). Hence, in that case, the acceleration field may be described by the superposition of the planar acceleration field of Fig. 6.1(b) and a uniform acceleration normal to it. An instance of this situation is a rigid body moving in a plane and subjected to a constant gravitational acceleration. In such a case, no acceleration centre will be found unless $\ddot{\mathbf{b}}$ is normal to $\boldsymbol{\omega}$ (and $\dot{\boldsymbol{\omega}}$), in which case we will not have one acceleration centre, but rather a line of acceleration centres. However, in general, $\det(\mathbf{W}) \neq 0$, and we have one single acceleration centre with position vector

$$\mathbf{r}_A = -\mathbf{W}^{-1}\ddot{\mathbf{b}} = \frac{-1}{\|\boldsymbol{\omega} \times \dot{\boldsymbol{\omega}}\|_2^2} \left[\|\boldsymbol{\omega}\|_2^2 \boldsymbol{\omega}\boldsymbol{\omega}^T + \dot{\boldsymbol{\omega}}\dot{\boldsymbol{\omega}}^T + \|\boldsymbol{\omega}\|_2^2 \dot{\boldsymbol{\Omega}} - (\boldsymbol{\omega}^T \dot{\boldsymbol{\omega}}) \boldsymbol{\Omega} \right] \ddot{\mathbf{b}}, \tag{6.10}$$

where $\mathbf{W}^{-1}$ was obtained by Angeles (1999). Hence, we may write

$$\ddot{\mathbf{p}}_i = \mathbf{W}(\mathbf{r}_i - \mathbf{r}_A), \tag{6.11}$$

which corresponds to the vector field schematized in Fig. 6.1(b). In this figure, the rigid-body acceleration field was divided into two components, the tangential and centripetal acceleration fields, which are given by the expressions $\ddot{\mathbf{p}}_{T,i} = \dot{\mathbf{\Omega}}(\mathbf{r}_i - \mathbf{r}_A)$ and $\ddot{\mathbf{p}}_{C,i} = \mathbf{\Omega}^2(\mathbf{r}_i - \mathbf{r}_A)$, respectively. As a result, the tangential acceleration field is a helical field with zero pitch and with axis $\mathcal{T}$ parallel to $\dot{\boldsymbol{\omega}}$ and passing through the acceleration centre A. On the other hand, from (Angeles, 2007), matrix $\mathbf{\Omega}^2$ may be decomposed into

$$\mathbf{\Omega}^2 = \boldsymbol{\omega}\boldsymbol{\omega}^T - \|\boldsymbol{\omega}\|_2^2\mathbf{1}_{3\times 3} = -\|\boldsymbol{\omega}\|_2^2\left(\mathbf{1}_{3\times 3} - \frac{\boldsymbol{\omega}\boldsymbol{\omega}^T}{\|\boldsymbol{\omega}\|_2^2}\right), \tag{6.12}$$

from which it is apparent that $\mathbf{\Omega}^2$ is proportional to an orthogonal projector onto a plane normal to $\boldsymbol{\omega}$, or, equivalently, normal to the instant screw axis (ISA). Hence, the centripetal acceleration vectors are directed normally and towards line $\mathcal{C}$, which is parallel to the ISA and passes through the acceleration centre A. Notice that, unlike the planar tangential and centripetal acceleration fields, the spatial tangential and centripetal acceleration fields are not necessarily orthogonal.

Apparently, from eq. (6.11), the spatial acceleration field is a function of the nine independent kinematic parameters contained in $\mathbf{r}_A$, $\boldsymbol{\omega}$, and $\dot{\boldsymbol{\omega}}$. Consequently, a minimum of nine accelerometer readouts are required to estimate the full acceleration field at a given instant. Moreover, similar to the planar acceleration field, the spatial field at a single instant alone does not allow for a univocal estimation of the angular velocity. Indeed, one may readily verify

that the angular velocities $\boldsymbol{\omega}$ and $-\boldsymbol{\omega}$ produce the very same acceleration field.

6.3 The Accelerometer Model

For the purpose of the analysis below, we may assume without loss of generality that all accelerometers used on the rigid body to measure the point accelerations are uniaxial. Indeed, biaxial and triaxial accelerometers may be modelled, respectively, as dyads and triads of uniaxial accelerometers located at the same point of the rigid body. In this vein, we associate a *sensitive direction* $\mathbf{e}_i$ to the i^{th} accelerometer located at point P_i, where $\mathbf{e}_i$ is a unit vector in $\mathbb{R}^3$. It is assumed that the readout a_i of the i^{th} accelerometer is equal to the magnitude of the component of $\ddot{\mathbf{p}}_i$ that is parallel to $\mathbf{e}_i$, whereas the accelerometer is completely insensitive to the components of the acceleration $\ddot{\mathbf{p}}_i$ that are orthogonal to $\mathbf{e}_i$. In the industry, the sensitivity of an accelerometer to acceleration components orthogonal to its sensitive direction is called the *cross-axis sensitivity*, and it amounts at most to a few percentage points of the accelerometer sensitivity to acceleration components parallel to its sensitive direction. Hence, upon neglecting these cross-axis effects, we obtain the simple expression

$$a_i = \mathbf{e}_i^T \ddot{\mathbf{p}}_i. \tag{6.13}$$

As a result, in the analysis that follows, an accelerometer i will be completely characterized by its position $\mathbf{r}_i$ with respect to a reference point B attached to the rigid body and its sensitive direction $\mathbf{e}_i$.

6.4 An Accelerometer Array Moving in the Plane

We start from the general case where n accelerometers are attached at n points $\{P_i\}_1^n$ of a rigid body moving in the plane, $n \geq 4$, as shown in Fig. 6.2. Unit-vectors $\mathbf{e}_i'$, $i = 1, \ldots, n$, yield the corresponding accelerometer sensitive directions. As before, point O is attached to an inertial frame and point B is

attached to the rigid body. Vectors $\mathbf{p}'_i \equiv \overrightarrow{OP_i}$, $\mathbf{b}' \equiv \overrightarrow{OB}$, and $\mathbf{r}'_i \equiv \overrightarrow{BP_i}$ are also defined as before.

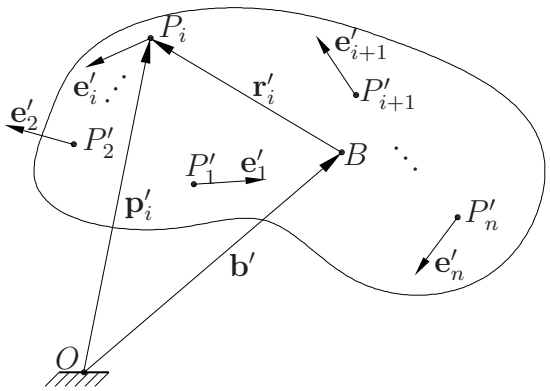

Figure 6.2: A rigid body equipped with n accelerometers moving in the plane

Upon pre-multiplying eq. (6.2) by the rank-one matrix $\mathbf{e}'_j\mathbf{e}'^T_j$, we obtain

$$\mathbf{e}'_j\mathbf{e}'^T_j\ddot{\mathbf{b}}' = \mathbf{e}'_j\mathbf{e}'^T_j\ddot{\mathbf{p}}'_j - \mathbf{e}'_j\mathbf{e}'^T_j\left(-\omega^2\mathbf{r}'_j + \dot{\omega}\mathbf{S}\mathbf{r}'_j\right) = a_j\mathbf{e}'_j - \mathbf{e}'_j\mathbf{e}'^T_j\mathbf{R}'_j\mathbf{w}', \qquad (6.14)$$

for $j = 1, \ldots, n$, where $a_j \equiv \mathbf{e}'^T_j\ddot{\mathbf{p}}'_j$ is the planar version of eq. (6.13), $\mathbf{R}'_j \equiv [-\mathbf{r}'_j \quad \mathbf{S}\mathbf{r}'_j]$, and $\mathbf{w}' \equiv [\omega^2 \quad \dot{\omega}]^T$. Let us sum both sides of eq. (6.14) over $j = 1, \ldots, n$, which yields

$$\mathbf{E}'\mathbf{E}'^T\ddot{\mathbf{b}}' = \mathbf{E}'\mathbf{a}' - \sum_{j=1}^{n}\mathbf{e}'_j\mathbf{e}'^T_j\mathbf{R}'_j\mathbf{w}' = \mathbf{E}'\mathbf{a}' - \mathbf{E}'\mathbf{F}'\mathbf{R}', \qquad (6.15)$$

where $\mathbf{E}' \equiv [\mathbf{e}'_1 \quad \mathbf{e}'_2 \quad \cdots \quad \mathbf{e}'_n]$, $\mathbf{a}' \equiv [a_1 \quad a_2 \quad \cdots \quad a_n]^T$,

$$\mathbf{F}' \equiv \begin{bmatrix} \mathbf{e}'^T_1 & \mathbf{0}_2^T & \cdots & \mathbf{0}_2^T \\ \mathbf{0}_2^T & \mathbf{e}'^T_2 & \cdots & \mathbf{0}_2^T \\ \vdots & \vdots & \ddots & \vdots \\ \mathbf{0}_2^T & \mathbf{0}_2^T & \cdots & \mathbf{e}'^T_n \end{bmatrix} \quad \text{and} \quad \mathbf{R}' \equiv \begin{bmatrix} \mathbf{R}'_1 \\ \mathbf{R}'_2 \\ \vdots \\ \mathbf{R}'_n \end{bmatrix}.$$

At this point, let us assume that the sensitive directions $\{\mathbf{e}'_j\}_{j=1}^n$ span the whole plane of rigid body motions. Should this condition not be fulfilled, unit vectors

$\mathbf{e}'_j$, $j = 1, \ldots, n$, would all be parallel, and it would be impossible to detect any translational rigid-body acceleration perpendicular to them. As it is not of practical interest, we rule out this case, and, since $\mathbf{E}'\mathbf{E}'^T = \sum_{j=1}^{n} \mathbf{e}'_j \mathbf{e}'^T_j$ is a sum of symmetric positive-semidefinite matrices, we may write its range as the sum of the ranges of $\mathbf{e}'_j \mathbf{e}'^T_j$, $j = 1, \ldots, n$. As a result, we obtain

$$\text{span}\{\mathbf{E}'\mathbf{E}'^T\} = \text{span}\{\mathbf{e}'_1(\mathbf{e}'_1)^T\} + \text{span}\{\mathbf{e}'_2(\mathbf{e}'_2)^T\} + \cdots + \text{span}\{\mathbf{e}'_n(\mathbf{e}'_n)^T\} = \mathbb{R}^2, \tag{6.16}$$

the last equality following from the assumption that the direction vectors $\mathbf{e}'_j$, $j = 1, \ldots, n$, span $\mathbb{R}^2$. Hence, $\mathbf{E}'\mathbf{E}'^T$ is nonsingular and we may safely calculate $\ddot{\mathbf{b}}'$ as

$$\ddot{\mathbf{b}}' = (\mathbf{E}'\mathbf{E}'^T)^{-1}\mathbf{E}'\mathbf{a}' - (\mathbf{E}'\mathbf{E}'^T)^{-1}\mathbf{E}'\mathbf{F}'\mathbf{R}'\mathbf{w}'. \tag{6.17}$$

Upon substituting eq. (6.17) into eq. (6.2) and projecting $\ddot{\mathbf{p}}'_i$ onto the sensitive direction of the corresponding accelerometers, we obtain,

$$a_i = \mathbf{e}'^T_i \ddot{\mathbf{p}}'_i = \mathbf{e}'^T_i (\mathbf{E}'\mathbf{E}'^T)^{-1}\mathbf{E}'\mathbf{a}' - \mathbf{e}'^T_i (\mathbf{E}'\mathbf{E}'^T)^{-1} \sum_{j=1}^{n} \mathbf{e}'_j \mathbf{e}'^T_j \mathbf{R}'_j \mathbf{w}' + \mathbf{e}'^T_i \mathbf{R}'_i \mathbf{w}', \tag{6.18}$$

whence,

$$a_i - \mathbf{e}'^T_i (\mathbf{E}'\mathbf{E}'^T)^{-1}\mathbf{E}'\mathbf{a}' = -\mathbf{e}'^T_i (\mathbf{E}'\mathbf{E}'^T)^{-1}\mathbf{E}'\mathbf{F}'\mathbf{R}'\mathbf{w}' + \mathbf{e}'^T_i \mathbf{R}'_i \mathbf{w}', \quad i = 1, \ldots, n. \tag{6.19}$$

Assuming that the accelerometer readouts $\mathbf{a}'$ are known and that one seeks to identify their corresponding rigid-body acceleration field, eq. (6.18) may be regarded as a system of n linear equations in two unknowns. Accordingly, we rewrite eq. (6.19) in compact form:

$$\mathbf{N}'\mathbf{w}' = \mathbf{P}'\mathbf{a}', \tag{6.20}$$

where $\mathbf{P}' \equiv \mathbf{1}_{n\times n} - \mathbf{E}'^T(\mathbf{E}'\mathbf{E}'^T)^{-1}\mathbf{E}'$ is the orthogonal projector onto the nullspace of $\mathbf{E}'$, and $\mathbf{N}' \equiv \mathbf{P}'\mathbf{F}'\mathbf{R}'$. Assuming that $\mathbf{N}'$ is of full rank, 2, we may compute

its left Moore-Penrose generalized inverse as

$$\mathbf{N}'^{\dagger} = (\mathbf{N}'^{T}\mathbf{N}')^{-1}\mathbf{N}^{T} = (\mathbf{R}'^{T}\mathbf{F}'^{T}\mathbf{P}'\mathbf{F}'\mathbf{R}')^{-1}\mathbf{R}'^{T}\mathbf{F}'^{T}\mathbf{P}', \tag{6.21}$$

the last equality following because $\mathbf{P}'$ is symmetric and idempotent, as any projection matrix. This allows for the computation of the least-square approximation of eq. (6.20) as

$$\mathbf{w}' = \mathbf{N}'^{\dagger}\mathbf{a}' = (\mathbf{R}'^{T}\mathbf{F}'^{T}\mathbf{P}'\mathbf{F}'\mathbf{R}')^{-1}\mathbf{R}'^{T}\mathbf{F}'^{T}\mathbf{P}'\mathbf{a}'. \tag{6.22}$$

Furthermore, substitution of eq. (6.22) into eq. (6.17) yields

$$\ddot{\mathbf{b}}' = (\mathbf{E}'\mathbf{E}'^{T})^{-1}\mathbf{E}'\left(\mathbf{1}_{n\times n} - \mathbf{F}'\mathbf{R}'(\mathbf{R}'^{T}\mathbf{F}'^{T}\mathbf{P}'\mathbf{F}'\mathbf{R}')^{-1}\mathbf{R}'^{T}\mathbf{F}'^{T}\mathbf{P}'\right)\mathbf{a}'. \tag{6.23}$$

In summary, let us rewrite eqs. (6.22) and (6.23) in compact form as

$$\mathbf{z}' \equiv \begin{bmatrix} \mathbf{w}' \\ \ddot{\mathbf{b}}' \end{bmatrix} = \mathbf{A}'\mathbf{a}', \tag{6.24}$$

where

$$\mathbf{A}' \equiv \begin{bmatrix} (\mathbf{R}'^{T}\mathbf{F}'^{T}\mathbf{P}'\mathbf{F}'\mathbf{R}')^{-1}\mathbf{R}'^{T}\mathbf{F}'^{T}\mathbf{P}' \\ (\mathbf{E}'\mathbf{E}'^{T})^{-1}\mathbf{E}'\left(\mathbf{1}_{n\times n} - \mathbf{F}'\mathbf{R}'(\mathbf{R}'^{T}\mathbf{F}'^{T}\mathbf{P}'\mathbf{F}'\mathbf{R}')^{-1}\mathbf{R}'^{T}\mathbf{F}'^{T}\mathbf{P}'\right) \end{bmatrix}.$$

Interestingly, the upper block-matrix of $\mathbf{A}'$ is independent of the choice of the reference point B. Indeed, upon translating all points P_i' by an arbitrary value of $\mathbf{r}_*'$, one obtains a new matrix $\mathbf{R}_*' \equiv [-\mathbf{r}_*' \quad \mathbf{S}\mathbf{r}_*']$, which can be added to the former matrices $\mathbf{R}_i'$, $i = 1, \ldots, n$. From the equality

$$\mathbf{P}'\mathbf{F}'\begin{bmatrix} \mathbf{R}_*'^{T} & \mathbf{R}_*'^{T} & \cdots & \mathbf{R}_*'^{T} \end{bmatrix}^{T} = \mathbf{P}'\mathbf{E}'^{T}\mathbf{R}_*' = \mathbf{O}_{n\times 2}, \tag{6.25}$$

one realizes that matrix $\mathbf{N}'$ is immutable to the addition of an arbitrary vector $\mathbf{r}_*'$ to all position vectors $\mathbf{r}_i'$, $i = 1, \ldots, n$, and so is the upper block-matrix of $\mathbf{A}'$. One may also verify that matrices $\mathbf{F}'\mathbf{R}'$ and $\mathbf{P}'$ are independent of any

choice of basis, which leads to the conclusion that $\mathbf{N}'$ and the upper block-matrix of $\mathbf{A}'$ are immutable. On the other hand, the lower block-matrix of $\mathbf{A}'$ can be expressed in a different frame through a pre-multiplication by the corresponding 2×2 rotation matrix.

Hence, it is seen that $\mathbf{A}'$ is *as invariant as can be*, in that its expression depends solely on the frame and reference point B with respect to which $\ddot{\mathbf{b}}'$ needs to be written, and because only its lower $2 \times n$ block is not immutable. Moreover, $\mathbf{A}'$ has minimum dimensions, i.e., minimum numbers of rows and columns, since it relates linearly the array of n accelerometer measurements to the four parameters of the rigid body acceleration field. Notice that one or either of these features were not present in previous formulations (Grammatikos, 1965; Schuler, 1965; Mostov, 2000; Parsa, 2003; Chevalier, 2002). Because of the unicity of $\mathbf{A}'$ up to the choice of a frame and a reference point of expression for $\ddot{\mathbf{b}}'$, we refer to matrix $\mathbf{A}'$ as the accelerometer array matrix. Notice also that the rotational and translational components of the acceleration field are completely decoupled in eq. (6.24), which eases computations in further analysis and synthesis of accelerometer arrays.

6.5 An Accelerometer Array Moving in Space

We start from the general case where n accelerometers are attached at n points $\{P_i\}_{i=1}^n$ of a rigid body moving in space, as shown in Fig. 6.5.

The position of each point P_i in a frame with origin at the fixed point O is given by vector $\mathbf{p}_i \in \mathbb{R}^3$. Let us also define point B, a landmark point on the rigid body that may or may not be located at its centre of mass, and its position $\mathbf{b} \in \mathbb{R}^3$ in the same frame. This allows the definition of body-fixed

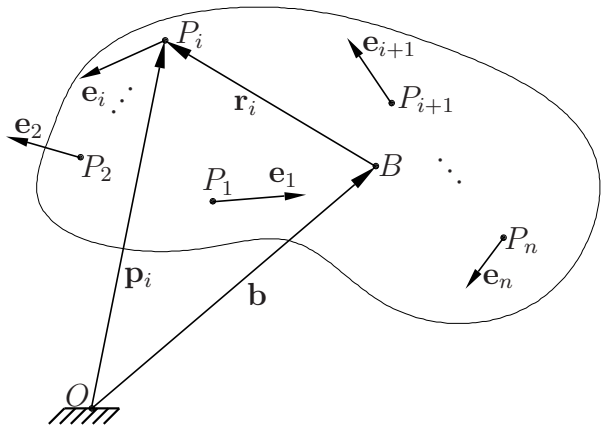

Figure 6.3: A rigid body equipped with n accelerometers moving in space

vectors $\mathbf{r}_i \equiv \mathbf{p}_i - \mathbf{b}$, $i = 1, \ldots, n$. Moreover, let the positive direction of the i^{th} accelerometer sensitive axis be given by the three-dimensional unit vector $\mathbf{e}_i$. Hence, the geometry of the accelerometer array is fully determined by the set $\{(\mathbf{r}_i, \mathbf{e}_i)\}_{i=1}^n$ of couples of position and direction vectors, each couple being associated to one of the sensors[2] .

As it is similar to the analysis of Section 6.4, the ensuing development is streamlined. From eq. (6.8), we write

$$\ddot{\mathbf{b}} = \ddot{\mathbf{p}}_j - \mathbf{W}\mathbf{r}_j = \ddot{\mathbf{p}}_j - \mathbf{R}_j^T \dot{\boldsymbol{\omega}} - \boldsymbol{\Sigma}_j^T \boldsymbol{\xi}, \tag{6.26}$$

[2] Notice that $\{(\mathbf{r}_i, \mathbf{e}_i)\}_{i=1}^n$ does not generally represent a vector field, since the association between the position and the direction vectors is not necessarily a map. Indeed, the presence of a multiaxial accelerometer in the IMU implies that two or three direction vectors are associated to the same position vector.

where $\boldsymbol{\xi} \equiv [\omega_1^2 \quad \omega_2^2 \quad \omega_3^2 \quad \omega_2\omega_3 \quad \omega_3\omega_1 \quad \omega_1\omega_2]^T$ is formed by the quadratic products of the entries of $\boldsymbol{\omega}$, and

$$\mathbf{R}_j \equiv \mathrm{CPM}(\mathbf{r}_j), \quad \boldsymbol{\Sigma}_j \equiv \begin{bmatrix} 0 & -r_{j1} & -r_{j1} & 0 & r_{j3} & r_{j2} \\ -r_{j2} & 0 & -r_{j2} & r_{j3} & 0 & r_{j1} \\ -r_{j3} & -r_{j3} & 0 & r_{j2} & r_{j1} & 0 \end{bmatrix}^T,$$

in which r_{j1}, r_{j2}, and r_{j3} are the first, second, and third component of $\mathbf{r}_j$, respectively. Upon pre-multiplying both sides of eq. (6.26) with matrix $\mathbf{e}_j\mathbf{e}_j^T$, we obtain

$$\mathbf{e}_j\mathbf{e}_j^T\ddot{\mathbf{b}} = a_j\mathbf{e}_j - \mathbf{e}_j\mathbf{e}_j^T\mathbf{R}_j^T\dot{\boldsymbol{\omega}} - \mathbf{e}_j\mathbf{e}_j^T\boldsymbol{\Sigma}_j^T\boldsymbol{\xi}. \tag{6.27}$$

Further, add both sides of eq. (6.27), for $j = 1, \ldots, n$, which yields

$$\mathbf{E}\mathbf{E}^T\ddot{\mathbf{b}} = \mathbf{E}\mathbf{a} - \sum_{j=1}^{n}\mathbf{e}_j\mathbf{e}_j^T\mathbf{R}_j^T\dot{\boldsymbol{\omega}} - \sum_{j=1}^{n}\mathbf{e}_j\mathbf{e}_j^T\boldsymbol{\Sigma}_j^T\boldsymbol{\xi}, \tag{6.28}$$

where $\mathbf{E} \equiv [\mathbf{e}_1 \quad \mathbf{e}_2 \quad \cdots \quad \mathbf{e}_n]$ and $\mathbf{a} \equiv [a_1 \quad a_2 \quad \cdots \quad a_n]^T$. At this point, let us remark that eq. (6.16) is still valid in 3D space, that is, $\mathrm{span}\{\mathbf{E}\mathbf{E}^T\} = \mathrm{span}\{\mathbf{e}_1\mathbf{e}_1^T\} + \mathrm{span}\{\mathbf{e}_2\mathbf{e}_2^T\} + \cdots + \mathrm{span}\{\mathbf{e}_n\mathbf{e}_n^T\} = \mathrm{span}\{\mathbf{e}_1, \mathbf{e}_2, \ldots, \mathbf{e}_n\}$. Now, assuming that the sensitive directions of the accelerometer array span the whole Cartesian space $\mathbb{R}^3$, we may write

$$\ddot{\mathbf{b}} = (\mathbf{E}\mathbf{E}^T)^{-1}\mathbf{E}\mathbf{a} - (\mathbf{E}\mathbf{E}^T)^{-1}\mathbf{E}\mathbf{F}\mathbf{R}\mathbf{w}, \tag{6.29}$$

where

$$\mathbf{F} \equiv \begin{bmatrix} \mathbf{e}_1^T & \mathbf{0}_3^T & \cdots & \mathbf{0}_3^T \\ \mathbf{0}_3^T & \mathbf{e}_2^T & \cdots & \mathbf{0}_3^T \\ \vdots & \vdots & \ddots & \vdots \\ \mathbf{0}_3^T & \mathbf{0}_3^T & \cdots & \mathbf{e}_n^T \end{bmatrix}, \quad \mathbf{R} \equiv \begin{bmatrix} \mathbf{R}_1 & \boldsymbol{\Sigma}_1 \\ \mathbf{R}_2 & \boldsymbol{\Sigma}_2 \\ \vdots & \vdots \\ \mathbf{R}_n & \boldsymbol{\Sigma}_n \end{bmatrix}, \quad \text{and} \quad \mathbf{w} \equiv \begin{bmatrix} \dot{\boldsymbol{\omega}} \\ \boldsymbol{\xi} \end{bmatrix}.$$

Equation (6.29) allows for the elimination of $\ddot{\mathbf{b}}$ from eq. (6.8). This yields, after projection of both sides of eq. (6.8) onto the sensitive direction of the

corresponding accelerometer,

$$a_i - \mathbf{e}_i^T(\mathbf{E}\mathbf{E}^T)^{-1}\mathbf{E}\mathbf{a} = \mathbf{e}_i^T(\mathbf{E}\mathbf{E}^T)^{-1}\mathbf{F}\mathbf{R}\mathbf{w}, \quad i = 1, \ldots, n. \tag{6.30}$$

These equations may be cast into a compact form analogous to that of eq. (6.20), which gives

$$\mathbf{N}\mathbf{w} = \mathbf{P}\mathbf{a}, \tag{6.31}$$

where $\mathbf{P} \equiv \mathbf{1}_{n\times n} - \mathbf{E}^T(\mathbf{E}\mathbf{E}^T)^{-1}\mathbf{E}$ is the orthogonal projector onto the null space of $\mathbf{E}$, and $\mathbf{N} \equiv \mathbf{P}\mathbf{F}\mathbf{R}$. Hence, the array $\mathbf{a}$ may be decomposed into two orthogonal components $\mathbf{a}_\perp$—read *a-perp*—and $\mathbf{a}_\parallel$—read *a-par*—which lie in the nullspace and the row space (or support space) of $\mathbf{E}$, respectively. Apparently, from eq. (6.31), the angular acceleration matrix $\mathbf{W}$ depends on $\mathbf{a}_\perp$, and not on $\mathbf{a}_\parallel$.

Assuming that $\mathbf{N}$ has full rank 3, the least-square approximation of eq. (6.31) may be written as

$$\mathbf{w} = \mathbf{N}^\dagger\mathbf{P}\mathbf{a} = (\mathbf{R}^T\mathbf{F}^T\mathbf{P}\mathbf{F}\mathbf{R})^{-1}\mathbf{R}^T\mathbf{F}^T\mathbf{P}\mathbf{a}, \tag{6.32}$$

where $\mathbf{N}^\dagger$ is seen to be the left Moore-Penrose generalized inverse of $\mathbf{N}$. Again, we substitute $\mathbf{w}$ of eq. (6.32) into eq. (6.29), which yields

$$\ddot{\mathbf{b}} = (\mathbf{E}\mathbf{E}^T)^{-1}\mathbf{E}(\mathbf{1}_{n\times n} - \mathbf{F}\mathbf{R}(\mathbf{R}^T\mathbf{F}^T\mathbf{P}\mathbf{F}\mathbf{R})^{-1}\mathbf{R}^T\mathbf{F}^T\mathbf{P})\mathbf{a}. \tag{6.33}$$

We then reassemble eqs. (6.32) and (6.33) into the unique expression

$$\mathbf{z} \equiv \begin{bmatrix} \mathbf{w} \\ \ddot{\mathbf{b}} \end{bmatrix} = \mathbf{A}\mathbf{a}, \tag{6.34}$$

where

$$\mathbf{A} \equiv \begin{bmatrix} (\mathbf{R}^T\mathbf{F}^T\mathbf{P}\mathbf{F}\mathbf{R})^{-1}\mathbf{R}^T\mathbf{F}^T\mathbf{P} \\ (\mathbf{E}\mathbf{E}^T)^{-1}\mathbf{E}(\mathbf{1}_{n\times n} - \mathbf{F}\mathbf{R}(\mathbf{R}^T\mathbf{F}^T\mathbf{P}\mathbf{F}\mathbf{R})^{-1}\mathbf{R}^T\mathbf{F}^T\mathbf{P}) \end{bmatrix}$$

will be referred to as the accelerometer array matrix. Again, upon defining an arbitrary displacement $\mathbf{r}_*$, one obtains the two corresponding matrices $\mathbf{R}_*$ and $\mathbf{\Sigma}_*$, and, since

$$\mathbf{P}\mathbf{F}\mathbf{R} = \mathbf{P}\mathbf{F}\begin{bmatrix} \mathbf{R}_*^T & \mathbf{R}_*^T & \cdots & \mathbf{R}_*^T \\ \mathbf{\Sigma}_*^T & \mathbf{\Sigma}_*^T & \cdots & \mathbf{\Sigma}_*^T \end{bmatrix}^T = \mathbf{P}\mathbf{E}^T\begin{bmatrix} \mathbf{R}_* & \mathbf{\Sigma}_* \end{bmatrix} = \mathbf{O}_{n\times 9}, \qquad (6.35)$$

it is apparent that the upper-block of $\mathbf{A}$ does not depend on the choice of the reference point B. On the other hand, if the orthogonal projector $\mathbf{P}$ turns out to be independent of the vector basis chosen, this is not the case of matrix $\mathbf{F}\mathbf{R}$. As a result, $\mathbf{A}$ is apparently unique, up to a choice of frame and reference point, and decouples the rotational and translational components of the acceleration field.

6.6 Summary

As a summary, let us recall that this Chapter is twofold. Firstly, Sections 6.1 and 6.2 describe the acceleration fields of a rigid body moving in the plane and in space, respectively. Secondly, the accelerometer model presented in Section 6.3 allows for the derivation of sets of linear equations that relate the accelerometer measurements to the rigid-body acceleration-field parameters. This is done for both planar and spatial cases in Sections 6.4 and 6.5, respectively. In these Sections, the symbolic least-square solutions to the corresponding sets of linear equations are also derived. The following Chapter examines under which conditions an accelerometer array allows for an approximate—or exact—solution.

Chapter 7

Feasibility of Accelerometer Arrays

This chapter is devoted to the categorization of accelerometer arrays according to their ability to identify the rigid-body acceleration field. In other words, from the terminology introduced by Williams and Fyfe (2004), we are seeking to determine which accelerometer arrays are *feasible* and which ones are not.

Definition 1 *An accelerometer array is* feasible *if it allows for the complete identification of any rigid-body acceleration field. Otherwise, the accelerometer array is called* unfeasible. □

7.1 First Necessary Condition

From Definition 1, we can readily see that a necessary condition for an accelerometer array to be feasible is that the sensitive directions of its accelerometers span its whole space of motion. Symbolically, this condition may be stated as $\mathcal{R}\{\mathbf{E}'\} = \mathbb{R}^2$ in the planar case, and $\mathcal{R}\{\mathbf{E}\} = \mathbb{R}^3$ in the spatial case. Necessity may be verified by simply observing that a set of sensitive accelerometer directions that do not span the whole space leaves a subspace in which translational accelerations of the rigid body cannot be measured.

Hence, whenever this first condition is not satisfied, it is impossible to solve eqs. (6.15) and (6.28) for unique $\ddot{\mathbf{b}}'$ and $\ddot{\mathbf{b}}$, respectively, and it is impossible to associate eqs. (6.20) and (6.31) to these unfeasible accelerometer arrays.

7.2 Second Necessary Condition

Notice, however, that the foregoing condition is necessary, but not sufficient. Indeed, having written eqs. (6.20) and (6.31) for given planar and spatial arrays of accelerometers does not imply that they admit unique solutions. In fact, we see that the arrays $\mathbf{w}'$ and $\mathbf{w}$ cannot be uniquely identified unless $\text{rank}(\mathbf{N}') = 2$ and $\text{rank}(\mathbf{N}) = 9$, respectively. This will be referred to as the second necessary condition.

In the planar case, we push the analysis further, as it is of practical interest to establish a link between the geometry of a planar accelerometer array and its feasibility.

7.3 Geometry of Feasible Planar Accelerometer Arrays

In this section, we revisit the problem of the feasibility of accelerometer arrays that was already addressed by Williams and Fyfe (2004). Three novelties are added:

1. The acceleration centre is introduced, which turns the design challenge into a purely geometric problem.
2. The solution of Williams and Fyfe (2004) is extended to strapdown accelerometer-only IMUs of $n > 4$ accelerometers.
3. The conditions for an accelerometer array to be nonsingular or *feasible* are reformulated in a more concise manner.

Two examples from the literature are also included in order to illustrate the underlying concepts.

We start from the general case where n accelerometers are attached at n points $\{P_i\}_{i=1}^n$ of a rigid body moving in the plane, as shown in Fig. 6.2. In the case where the rigid body is under pure translation, i.e. $\dot{\theta} = 0$ rad/s and $\ddot{\theta} = 0$ rad/s^2, the acceleration centre A lies at infinity, and the acceleration of a rigid-body point cannot be expressed in terms of the position of A. In that case, we may readily see from eq. (6.15) that the acceleration field can be computed if and only if the accelerometer sensitive directions $\mathbf{e}'_i$, $i = 1, \ldots, n$, are not mutually parallel, which corresponds to the first necessity condition stated in Section 7.1.

In any other case—i.e. when $\dot{\theta} \neq 0$ rad/s or $\ddot{\theta} \neq 0$ rad/s^2—the acceleration centre A has a finite-norm position vector $\mathbf{r}'_A$. In these cases, it is of practical interest to write eq. (6.2) for point P_i, $i = 1, \ldots, n$, as a function of the acceleration centre, which gives

$$\ddot{\mathbf{p}}'_i = \mathbf{W}'(\mathbf{r}'_i - \mathbf{r}'_A), \quad i = 1, \ldots, n. \tag{7.1}$$

Upon projecting these equations onto their respective sensitive directions, we obtain

$$a_i = \mathbf{e}_i'^T \ddot{\mathbf{p}}'_i = -\mathbf{e}_i'^T(\mathbf{1}_{2\times 2}\dot{\theta}^2 - \mathbf{S}\ddot{\theta})(\mathbf{r}'_i - \mathbf{r}'_A), \tag{7.2}$$

for $i = 1, \ldots, n$. These equations may be rewritten as

$$\begin{bmatrix} a'_1 \\ \vdots \\ a'_n \end{bmatrix} = \begin{bmatrix} -\mathbf{e}_1'^T(\mathbf{r}'_1 - \mathbf{r}'_A) & \mathbf{e}_1'^T\mathbf{S}(\mathbf{r}'_1 - \mathbf{r}'_A) \\ \vdots & \vdots \\ -\mathbf{e}_n'^T(\mathbf{r}'_n - \mathbf{r}'_A) & \mathbf{e}_n'^T\mathbf{S}(\mathbf{r}'_n - \mathbf{r}'_A) \end{bmatrix} \begin{bmatrix} \dot{\theta}^2 \\ \ddot{\theta} \end{bmatrix}, \tag{7.3}$$

from which it is apparent that $\dot{\theta}^2$ and $\ddot{\theta}$ are uniquely determined if and only if the linear system has full rank. In this case, unlike the linear system of eq. (6.20), the rank is not independent of the acceleration field; rank depends on the position of the acceleration centre. Let us now express the necessary and sufficient condition for the linear system of eq. (7.3) to be rank-deficient as

$$\det\left(\begin{bmatrix} \mathbf{e}_i'^T(\mathbf{r}'_A - \mathbf{r}'_i) & -\mathbf{e}_i'^T\mathbf{S}(\mathbf{r}'_A - \mathbf{r}'_i) \\ \mathbf{e}_j'^T(\mathbf{r}'_A - \mathbf{r}'_j) & -\mathbf{e}_j'^T\mathbf{S}(\mathbf{r}'_A - \mathbf{r}'_j) \end{bmatrix}\right) = 0 \tag{7.4}$$

$\forall\, i, j = 1, \ldots, n,\ i \neq j$. Each of the foregoing $n(n-1)/2$ equations defines a contour $\mathcal{A}_{ij}$ in the plane of motion, as it involves only the unknown parameter $\mathbf{r}'_A$, namely,

$$\mathcal{A}_{ij}: \quad (\mathbf{r}'_A - \mathbf{r}'_i)^T\mathbf{E}'_{ij}(\mathbf{r}'_A - \mathbf{r}'_j) = 0, \tag{7.5}$$

where $\mathbf{E}'_{ij} \equiv \mathbf{e}'_i\mathbf{e}_j'^T\mathbf{S}^T - \mathbf{S}\mathbf{e}'_i\mathbf{e}_j'^T$, and the invariant form of the 2×2 determinant was taken from (Angeles, 2007). Contours $\{\mathcal{A}_{ij}\}_{i,j=1}^n$ represent the loci of the acceleration centre for which a given pair of accelerometer outputs (a_i, a_j) cannot uniquely determine $\dot{\theta}^2$ and $\ddot{\theta}$. Hence, having all contours $\{\mathcal{A}_{ij}\}_{i,j=1}^n$ intersecting at the same point implies that there exists an acceleration centre for which the accelerometer array is unable to identify the rotational parameters of the acceleration field. As a result, the contours $\{\mathcal{A}_{ij}\}_{i,j=1}^n$ having no common intersection is a necessary condition for a planar accelerometer array to be feasible. This condition, which is equivalent to the second necessary condition of Section 7.2, may be expressed symbolically as

$$\bigcap_{i,j=1}^{n} \mathcal{A}_{ij} = \emptyset. \tag{7.6}$$

7.3.1 Properties of Matrix $\mathbf{E}'_{ij}$

It is now apparent that understanding which arrays of accelerometers generate sets of contours having one or more common intersection points is

of primary importance for accelerometer-array design. As it determines the properties of contour $\mathcal{A}_{ij}$, let us analyze $\mathbf{E}'_{ij}$. Interestingly, this matrix turns out to be orthogonal, as we show below. Consider the two products:

$$\begin{aligned}\mathbf{E}'_{ij}[\mathbf{e}'_j \quad \mathbf{S}\mathbf{e}'_j] &= (\mathbf{e}'_i\mathbf{e}'^T_j\mathbf{S}^T - \mathbf{S}\mathbf{e}'_i\mathbf{e}'^T_j)[\mathbf{e}'_j \quad \mathbf{S}\mathbf{e}'_j] \\ &= [-\mathbf{S}\mathbf{e}'_i \quad \mathbf{e}'_i] \qquad (7.7)\\ \mathbf{E}'^T_{ij}[-\mathbf{S}\mathbf{e}'_i \quad \mathbf{e}'_i] &= (\mathbf{S}\mathbf{e}'_j\mathbf{e}'^T_i - \mathbf{e}'_j\mathbf{e}'^T_i\mathbf{S}^T)[-\mathbf{S}\mathbf{e}'_i \quad \mathbf{e}'_i] \\ &= [\mathbf{e}'_j \quad \mathbf{S}\mathbf{e}'_j]. \qquad (7.8)\end{aligned}$$

Upon substituting eq. (7.7) into eq. (7.8), we obtain

$$\mathbf{E}'^T_{ij}\mathbf{E}'_{ij}[\mathbf{e}'_j \quad \mathbf{S}\mathbf{e}'_j] = [\mathbf{e}'_j \quad \mathbf{S}\mathbf{e}'_j]$$

and, since $[\mathbf{e}'_j \quad \mathbf{S}\mathbf{e}'_j]$ is nonsingular,

$$\mathbf{E}'^T_{ij}\mathbf{E}'_{ij} = [\mathbf{e}'_j \quad \mathbf{S}\mathbf{e}'_j][\mathbf{e}'_j \quad \mathbf{S}\mathbf{e}'_j]^{-1} = \mathbf{1}_{2\times 2}, \qquad (7.9)$$

thereby showing that $\mathbf{E}'_{ij}$ is orthogonal. Now, coming back to eq. (7.7), we write[1]

$$\begin{aligned}\det(\mathbf{E}'_{ij}[\mathbf{e}'_j \quad \mathbf{S}\mathbf{e}'_j]) &= \det(\mathbf{E}'_{ij})\det([\mathbf{e}'_j \quad \mathbf{S}\mathbf{e}'_j]) \\ &= \det(\mathbf{E}'_{ij})\mathbf{e}'^T_j\mathbf{S}^T\mathbf{S}\mathbf{e}'_j = \det(\mathbf{E}'_{ij}) \\ &= \det([-\mathbf{S}\mathbf{e}'_i \quad \mathbf{e}'_i]) \\ &= \mathbf{e}'^T_i\mathbf{S}\mathbf{S}^T\mathbf{e}'_i = 1, \qquad (7.10)\end{aligned}$$

which implies that $\mathbf{E}'_{ij}$ is proper, or, equivalently, represents a rotation in the plane. Its associated angle of rotation θ_{ij} is found from

[1] Notice that $\det([\mathbf{e}'_j \quad \mathbf{S}\mathbf{e}'_j])$ is computed using a formula given in (Angeles, 2007).

$$\begin{aligned}\cos(\theta_{ij}) &= \mathbf{e}_j'^T\mathbf{E}'_{ij}\mathbf{e}'_j = \mathbf{e}_i'^T\mathbf{S}\mathbf{e}'_j \\ &= -\sin(\phi_{ij}) = \cos(-\phi_{ij} - \pi/2), \\ \sin(\theta_{ij}) &= \mathbf{e}_j'^T\mathbf{S}^T\mathbf{E}'_{ij}\mathbf{e}'_j = -\mathbf{e}_i'^T\mathbf{e}'_j \\ &= -\cos(\phi_{ij}) = \sin(-\phi_{ij} - \pi/2),\end{aligned} \tag{7.11}$$

where ϕ_{ij} is the angle between $\mathbf{e}'_i$ and $\mathbf{e}'_j$ measured from $\mathbf{e}'_i$. Notice that ϕ_{ij} is defined positive for rotations in the counter-clockwise direction, in order to remain consistent with eqs. (6.1) and (6.2). Apparently, from eq. (7.11), we have

$$\theta_{ij} = -\phi_{ij} - \pi/2. \tag{7.12}$$

7.3.2 $\mathcal{A}_{ij}$ Contours

We rewrite eq. (7.5) as

$$0 = (\mathbf{r}'_A - \mathbf{r}'_i)^T\mathbf{E}'_{ij}(\mathbf{r}'_A - \mathbf{r}'_j) + (\mathbf{r}'_A - \mathbf{r}'_j)^T\mathbf{E}_{ij}'^T(\mathbf{r}'_A - \mathbf{r}'_i),$$

or, equivalently,

$$0 = \mathbf{s}_A'^T\mathbf{F}'_{ij}\mathbf{s}'_A, \tag{7.13}$$

where

$$\mathbf{F}'_{ij} \equiv \begin{bmatrix} \mathbf{E}'_{ij} + \mathbf{E}_{ij}'^T & -\mathbf{E}_{ij}'^T\mathbf{r}'_i - \mathbf{E}'_{ij}\mathbf{r}'_j \\ -\mathbf{r}_i'^T\mathbf{E}'_{ij} - \mathbf{r}_j'^T\mathbf{E}_{ij}'^T & 2\mathbf{r}_i'^T\mathbf{E}'_{ij}\mathbf{r}'_j \end{bmatrix},$$

and $\mathbf{s}'_A \equiv [\mathbf{r}_A'^T \quad 1]^T$. Using the formula for the determinant of a matrix partitioned in blocks (Kailath et al., 2000), it can be shown that

$$\det(\mathbf{F}'_{ij}) = 2(\mathbf{e}_i'^T\mathbf{S}\mathbf{e}'_j)\|\mathbf{r}'_i - \mathbf{r}'_j\|_2^2, \tag{7.14}$$

which brings us to the conclusion that the conic $\mathcal{A}_{ij}$ is degenerate if at least one of two conditions holds, which are: (i) $\mathbf{e}'_i = \pm\mathbf{e}'_j$; (ii) $\mathbf{r}'_i = \mathbf{r}'_j$. If the two conditions hold, the two accelerometers are virtually the same, and the associated locus of singularities is the whole plane, i.e., $\mathcal{A}_{ij} = \mathbb{R}^2$. In case (i),

$\mathcal{A}_{ij} = \mathcal{L}_{ij}$, where $\mathcal{L}_{ij}$ is the line passing through points P_i and P_j. In case (ii), $\mathcal{A}_{ij} = P_i = P_j$, i.e., the conic degenerates into a point, which is the point where the accelerometers are located.

Let us focus on the case where $\mathbf{F}'_{ij}$ is nonsingular, that is, where $\mathcal{A}_{ij}$ is a conic. Upon noticing that the first 2×2 diagonal block of $\mathbf{F}'_{ij}$ is proportional to the 2×2 identity matrix, namely,

$$\mathbf{E}'_{ij} + \mathbf{E}'^{T}_{ij} = 2\cos\theta_{ij}\mathbf{1}_{2\times 2} = -2\sin\phi_{ij}\mathbf{1}_{2\times 2}, \tag{7.15}$$

we can readily conclude that the conic in question is, in fact, a circle.

From eq. (7.5), we can readily find that circle $\mathcal{A}_{ij}$ passes through points P_i and P_j. A third point is necessary to fully define the circle. In many applications, the centre is the most useful point to know when constructing a circle. In order to find the centre, let us rewrite eq. (7.13) as

$$\mathbf{r}'^{T}_{A}(\mathbf{E}'_{ij} + \mathbf{E}'^{T}_{ij})\mathbf{r}'_{A} - 2\mathbf{r}'^{T}_{A}(\mathbf{E}'^{T}_{ij}\mathbf{r}'_{i} + \mathbf{E}'_{ij}\mathbf{r}'_{j}) + 2\mathbf{r}'^{T}_{i}\mathbf{E}'_{ij}\mathbf{r}'_{j} = 0 \tag{7.16}$$

The position vector $\mathbf{c}'_{ij}$ of the centre of the circle $\mathcal{A}_{ij}$ is obtained from the derivative of the left-hand side of eq. (7.16) with respect to $\mathbf{r}'_{A}$, and evaluated at $\mathbf{r}'_{A} = \mathbf{0}_2$, which yields[2],

$$\mathbf{c}'_{ij} = (\mathbf{E}'_{ij} + \mathbf{E}'^{T}_{ij})^{-1}(\mathbf{E}'^{T}_{ij}\mathbf{r}'_{i} + \mathbf{E}'_{ij}\mathbf{r}'_{j}), \tag{7.17}$$

[2] If the circle equation is written in the form $f(\mathbf{r}) \equiv k\|\mathbf{r} - \mathbf{c}\|_2^2 - kr^2 = 0$, in which $\mathbf{r}$ is the position vector of a point on the circle, $\mathbf{c}$ is the position vector of its centre, r is its radius, and k is a scalar different from zero, then $\mathbf{c} = -[1/(2k)](\partial f/\partial \mathbf{r})|_{\mathbf{r}=\mathbf{0}_2}$.

where we recall that $\mathbf{E}'_{ij} + \mathbf{E}'^{T}_{ij}$ is singular if and only if $\mathcal{A}_{ij}$ is a degenerate conic. Since this case was ruled out at the outset, eq. (7.17) always holds, and can be further simplified to

$$\begin{aligned}\mathbf{c}'_{ij} &= \frac{1}{2\cos\theta_{ij}}\left[(\mathbf{1}_{2\times 2}\cos\theta_{ij} - \mathbf{S}\sin\theta_{ij})\mathbf{r}'_i + (\mathbf{1}_{2\times 2}\cos\theta_{ij} + \mathbf{S}\sin\theta_{ij})\mathbf{r}'_j\right], \\ &= (1/2)\left(\mathbf{r}'_i + \mathbf{r}'_j\right) - (1/2)\tan\theta_{ij}\mathbf{S}\left(\mathbf{r}'_i - \mathbf{r}'_j\right) \end{aligned} \tag{7.18}$$

A geometric interpretation of the foregoing relation is depicted in Fig. 7.1. From eq. (7.18), it is apparent that $\triangle P_i P_j C_{ij}$ is isosceles, since segments $\overline{C_{ij}P_i}$

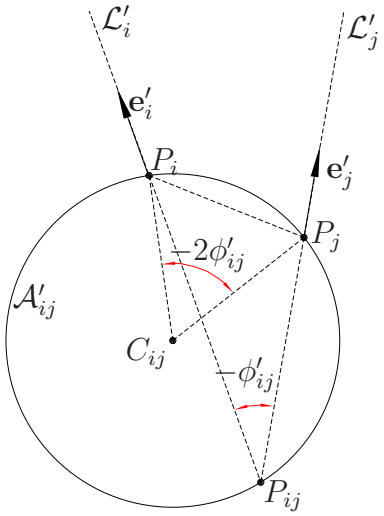

Figure 7.1: Contour $\mathcal{A}_{ij}$ for $P_i \neq P_j$ and $\mathbf{e}'_i \nparallel \mathbf{e}'_j$

and $\overline{C_{ij}P_j}$ have both the same length, the radius of the circle. The distance from C_{ij} to $\overline{P_iP_j}$ is given by $\|\mathbf{r}'_i - \mathbf{r}'_j\|_2/(2\tan\phi_{ij})$, which implies that the apex angle is $2\phi_{ij}$, and the circle radius is

$$r_{ij} = \|\mathbf{r}'_i - \mathbf{r}'_j\|_2/|2\sin\phi_{ij}|. \tag{7.19}$$

Consider now lines $\mathcal{L}_i$ and $\mathcal{L}_j$ passing through points P_i and P_j and parallel to vectors $\mathbf{e}'_i$ and $\mathbf{e}'_j$, respectively. It is noteworthy that the intersection P_{ij} of $\mathcal{L}_i$ and $\mathcal{L}_j$ also lies on $\mathcal{A}_{ij}$, which facilitates the circle construction. To show this, let us introduce parameters ρ_i and ρ_j such that the position vector $\mathbf{r}'_{ij}$ of

P_{ij} may be written as

$$\mathbf{r}'_{ij} = \mathbf{r}'_i + \rho_i \mathbf{e}'_i = \mathbf{r}'_j + \rho_j \mathbf{e}'_j. \tag{7.20}$$

Upon comparing the latter equations and defining the array $\boldsymbol{\rho}_{ij} \equiv [\rho_i \quad \rho_j]^T$, we obtain

$$\begin{bmatrix} \mathbf{e}'_i & -\mathbf{e}'_j \end{bmatrix} \boldsymbol{\rho}_{ij} = -(\mathbf{r}'_i - \mathbf{r}'_j), \tag{7.21}$$

whence,

$$\boldsymbol{\rho}_{ij} = \frac{1}{\mathbf{e}'^T_i \mathbf{S} \mathbf{e}'_j} \begin{bmatrix} \mathbf{e}'^T_j \\ \mathbf{e}'^T_i \end{bmatrix} \mathbf{S}(\mathbf{r}'_i - \mathbf{r}'_j), \tag{7.22}$$

where the last equality is valid since, by assumption, $\mathbf{e}'_i$ and $\mathbf{e}'_j$ are not parallel. We then solve for $\mathbf{r}'_{ij}$ by summing the two eqs. (7.20), in order to preserve symmetry in the equations; substituting the result of eq. (7.22) yields

$$\begin{aligned} \mathbf{r}'_{ij} &= \frac{1}{2}(\mathbf{r}'_i + \mathbf{r}'_j) + \frac{1}{2} \begin{bmatrix} \mathbf{e}'_i & \mathbf{e}'_j \end{bmatrix} \boldsymbol{\rho}_{ij}, \\ \mathbf{r}'_{ij} &= \frac{1}{2}(\mathbf{r}'_i + \mathbf{r}'_j) - \frac{1}{2 \sin \phi_{ij}} (\mathbf{e}'_i \mathbf{e}'^T_j + \mathbf{e}'_j \mathbf{e}'^T_i) \mathbf{S}(\mathbf{r}'_i - \mathbf{r}'_j). \end{aligned} \tag{7.23}$$

From eqs. (7.18) and (7.23), we compute the difference

$$\mathbf{r}'_{ij} - \mathbf{c}'_{ij} = \frac{1}{2 \sin \phi_{ij}} \mathbf{G}'_{ij} \mathbf{S}(\mathbf{r}'_i - \mathbf{r}'_j), \tag{7.24}$$

where $\mathbf{G}'_{ij} \equiv (\mathbf{e}'^T_i \mathbf{e}'_j) \mathbf{1}_{2\times 2} - \mathbf{e}'_i \mathbf{e}'^T_j - \mathbf{e}'_j \mathbf{e}'^T_i$. On the other hand, since ϕ_{ij} is the angle between $\mathbf{e}'_i$ and $\mathbf{e}'_j$, we have the relation

$$\mathbf{e}'_j = (\mathbf{1}_{2\times 2} \cos \phi_{ij} + \mathbf{S} \sin \phi_{ij}) \mathbf{e}'_i., \tag{7.25}$$

which allows us to express $\mathbf{G}'_{ij}$ as a function of $\mathbf{e}'_i$ and ϕ_{ij} only, thus yielding

$$\mathbf{G}'_{ij} = \cos \phi_{ij} \mathbf{1}_{2\times 2} - 2 \cos \phi_{ij} \mathbf{e}'_i \mathbf{e}'^T_i - \sin \phi_{ij} (\mathbf{e}'_i \mathbf{e}'^T_i \mathbf{S}^T + \mathbf{S} \mathbf{e}'_i \mathbf{e}'^T_i). \tag{7.26}$$

Let us now compute the product

$$\begin{aligned}\mathbf{G}'_{ij}\mathbf{G}'^{T}_{ij} &= \cos^2\phi_{ij}\mathbf{1}_{2\times 2} + \sin^2\phi_{ij}(\mathbf{S}\mathbf{e}'_i\mathbf{e}'^{T}_i\mathbf{S}^T + \mathbf{e}'_i\mathbf{e}'^{T}_i) \\ &= \cos^2\phi_{ij}\mathbf{1}_{2\times 2} + \sin^2\phi_{ij}\mathbf{1}_{2\times 2} = \mathbf{1}_{2\times 2}, \end{aligned} \tag{7.27}$$

which demonstrates that $\mathbf{G}'_{ij}$ is orthogonal. As a result, the square of the distance from P_{ij} to C_{ij} is computed as

$$\begin{aligned}\|\mathbf{r}'_{ij} - \mathbf{c}'_{ij}\|_2^2 &= \frac{(\mathbf{r}'_i - \mathbf{r}'_j)^T\mathbf{S}^T\mathbf{G}'^{T}_{ij}\mathbf{G}'_{ij}\mathbf{S}(\mathbf{r}'_i - \mathbf{r}'_j)}{4\sin^2\phi_{ij}} \\ &= \|\mathbf{r}'_i - \mathbf{r}'_j\|_2^2/(4\sin^2\phi_{ij}) = r_{ij}^2, \end{aligned} \tag{7.28}$$

thereby showing that P_{ij} lies on circle $\mathcal{A}_{ij}$.

7.3.3 Examples

Let us analyze two strapdown IMUs taken from the literature according to the method proposed by Williams and Fyfe (2004) for four accelerometers, which we generalize here for n accelerometers.

A Six-Accelerometer IMU

Consider the accelerometer array proposed by Chen et al. (1994), which is depicted in Fig. 7.2. Each of the six accelerometers of the arrangement is located at the centre of the face of a cube, with its sensitive axis parallel to one of the diagonals of the corresponding face. Under the assumption that the IMU is subjected only to planar motion in the plane $\mathcal{P}$, we can "project" the IMU onto $\mathcal{P}$, thus obtaining its equivalent planar array, as illustrated in Fig. 7.2.

From the planar accelerometer array geometry, reproduced in Fig. 7.3, we see that vectors $\{\mathbf{e}'_i\}_{i=1}^n$ span plane $\mathcal{P}$, which eliminates the first type of singularity described in Section 7.1. Hence, we need to draw contours $\{\mathcal{A}_{ij}\}_{i,j=1}^n$,

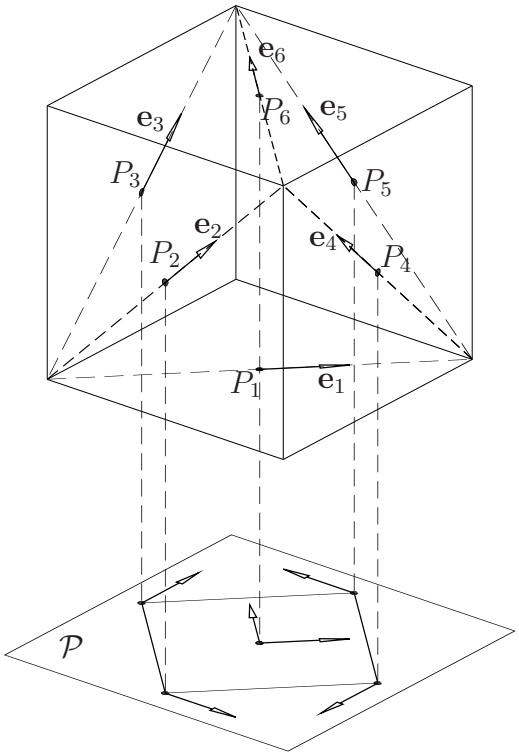

Figure 7.2: The accelerometer array proposed in Chen et al. (1994) along with its "projection" onto plane $\mathcal{P}$

where $n = 6(6-1)/2 = 15$, as defined in Section 7.3.2. Since the projection of points P_1 and P_6 onto $\mathcal{P}$ yields the same point, the singularity locus associated with this pair of projected points is the common projected point itself, i.e., $\mathcal{A}_{16} = P_1 = P_6$. Also, we have $\mathbf{e}'_2 = -\mathbf{e}'_5$ and $\mathbf{e}'_3 = -\mathbf{e}'_4$, which implies that contours $\mathcal{A}_{25}$ and $\mathcal{A}_{34}$ are lines passing through their corresponding pairs of points. The twelve remaining contours are all circles. Because of the square geometry, and because accelerometers 1 and 6 are placed along the diagonal of the square, some of the circles coincide. Indeed, from Fig. 7.3, we see that $\mathcal{A}_{12} = \mathcal{A}_{23} = \mathcal{A}_{13}$, $\mathcal{A}_{14} = \mathcal{A}_{45} = \mathcal{A}_{15}$, $\mathcal{A}_{24} = \mathcal{A}_{46} = \mathcal{A}_{26}$, and $\mathcal{A}_{35} = \mathcal{A}_{56} = \mathcal{A}_{36}$, which leaves us with four distinct circles.

Once all the singularity loci are defined, their common intersection is found by simple inspection. This intersection is

$$\bigcap_{i,j=1}^{n} \mathcal{A}_{ij} = P_1 = P_6 \neq \emptyset. \tag{7.29}$$

Hence, the planar IMU is unable to detect all parameters of the acceleration field whenever the acceleration centre A coincides with P_1. Indeed, for such an acceleration field, the centripetal acceleration component is orthogonal to all sensors, and is, therefore, undetermined. In fact, this is no surprise, since the accelerometer array proposed by Chen et al. (1994) was designed to measure only the angular acceleration of the rigid body on which it is mounted. Nevertheless, according to the definition, this strapdown IMU is *unfeasible*.

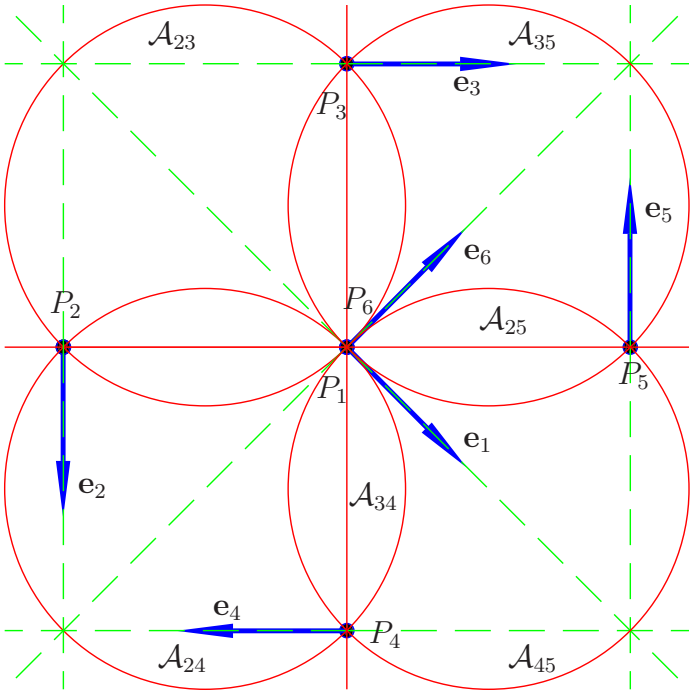

Figure 7.3: The equivalent planar accelerometer array and the singularity loci $\{\mathcal{A}_{ij}\}_{i,j=1}^{n}$ associated with each pair of accelerometers

7.3.4 A Seven-Accelerometer IMU

Figure 7.4 shows the accelerometer array used by Shea and Viano (1994) to estimate the planar trajectory of the head of a Hybrid III dummy during and after impact. It is composed of seven accelerometers, which requires that $7(7-1)/2 = 21$ contours be traced. Notice, however, that six of the seven accelerometer sensitive directions are parallel, and, therefore, their associated contours are straight lines. Moreover, since points $\{P_i\}_{i=3}^{7}$ are collinear, lines $\{\mathcal{A}_{ij}\}_{i,j=3,i\neq j}^{7}$ are the same, which reduces the number of contours to be traced by $5(5-1)/2 - 1 = 9$.

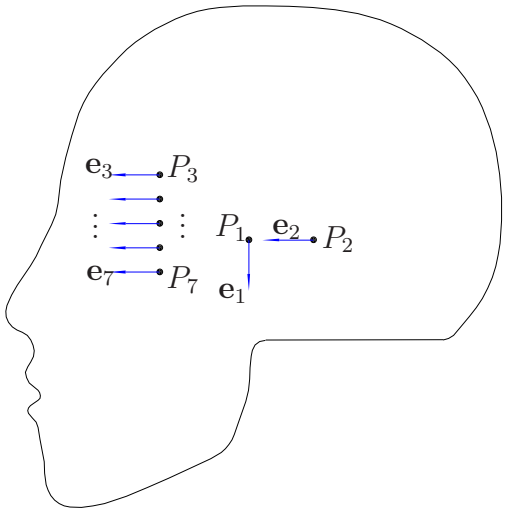

Figure 7.4: The accelerometer array used to estimate the trajectory of the head of a Hybrid III dummy

All contours are drawn in Fig. 7.5, from which one can conclude that

$$\bigcap_{i,j=1}^{7} \mathcal{A}_{ij} = \emptyset, \tag{7.30}$$

and, therefore, this accelerometer array is *feasible*. Notice, however, that removing the accelerometer located at P_2 renders the array unfeasible, since

there is a point in segment $\overline{P_5P_6}$ which is common to all contours $\mathcal{A}_{ij}$ for which $i \neq 2$ and $j \neq 2$.

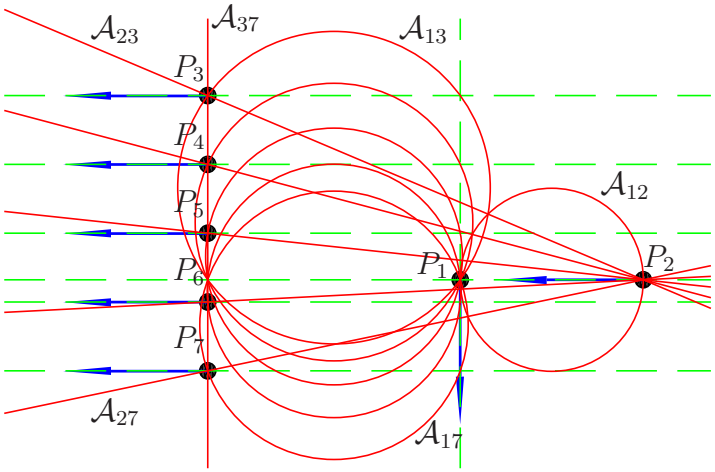

Figure 7.5: The associated singularity loci $\{\mathcal{A}_{ij}\}_{i,j=1}^{7}$

7.4 Summary

In this chapter, we first recall the *feasibility* of an accelerometer array according to the definition of Williams and Fyfe (2004). Thence, two conditions necessary to the feasibility of an accelerometer array are drawn. Finally, the feasibility of a planar accelerometer array is related to its geometry in Section 7.3. As it turns out, one may associate a singularity locus to each pair of accelerometers in the array. Each locus represents the set of acceleration centres for which the pair of accelerometers cannot unambiguously determine the angular acceleration and angular-velocity squared. As a result, any intersection common to all singularity loci of an accelerometer array corresponds to the acceleration centre of an acceleration field that cannot be identified, implying thereby that the accelerometer array is unfeasible.

Chapter 8

Angular-Velocity Estimation from Centripetal-Acceleration Measurements

8.1 Introduction: The Pose and Twist Estimation Algorithm

Having proposed a method to assess the feasibility of an accelerometer array in Chapter 7, we may now turn our attention towards those arrays that are feasible, i.e., the ones that allow the full estimation of the acceleration field. From the acceleration field, one may obtain estimates of the time-derivative of the twist, of the twist itself, and of the pose of a rigid body moving in space or in the plane.

The associated computation scheme is shown in Fig. 8.1, where CA and TA stand for the centripetal and tangential components of the acceleration field, respectively, whereas T and R stand for translation and rotation in space, respectively. Moreover, let us recall that all kinematic variables displayed in Fig. 8.1 have been defined in Chapter 6.

The problem of estimating the kinematic variables that pertain to the translation subgroup is purely linear, as it involves only time-integrations. Therefore, it is a fairly simple problem and, in the opinion of the author, the

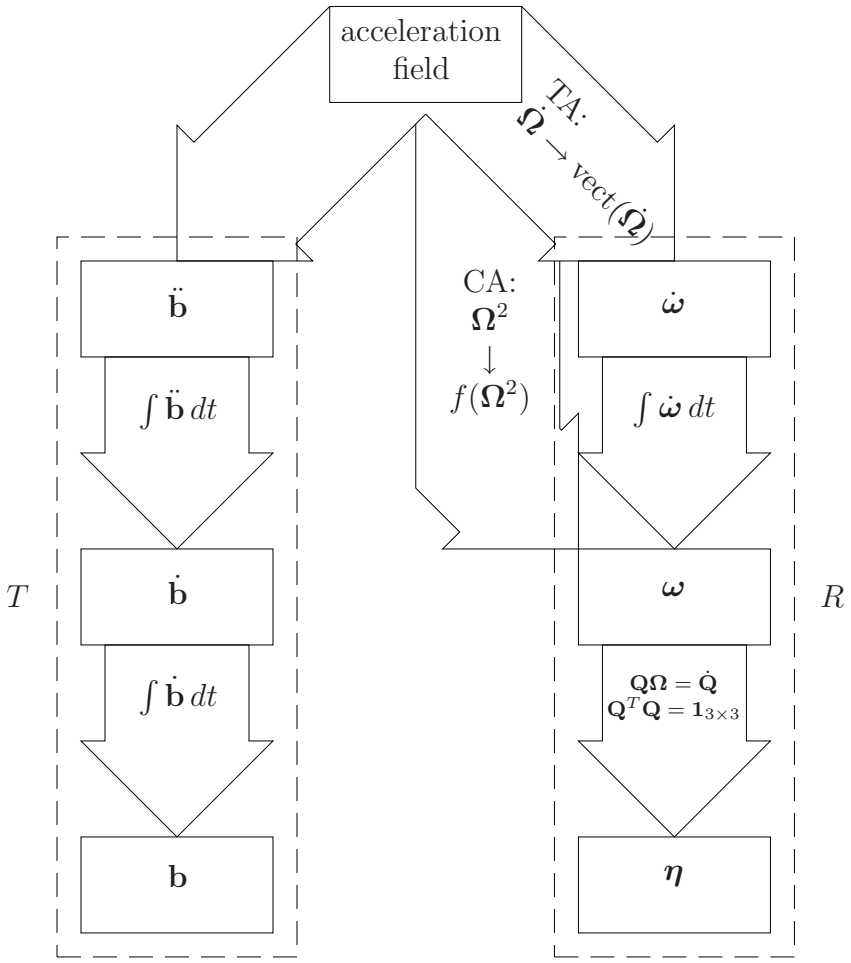

Figure 8.1: A generic pose-and-twist estimation algorithm from point-acceleration measurements

only potential improvements to its solution are to come from the choice of the integration method. For this reason, it was decided to focus rather on the part of the algorithm that involves rotational displacements only, that is the right-hand side of Fig. 8.1.

Within this sequence, the estimation of the attitude of a rigid body from angular-velocity estimates has already received extensive attention—see for example, (Stuelpnagel, 1964; Bortz, 1971; Wertz, 1984; Choukroun et al., 2004)—as these estimates are key in the gyroscope-based navigation of aircraft and spacecraft. Moreover, the estimation of the angular velocity from the TA boils down to a simple time-integration, which leaves room for little improvement.

The remaining problem is that of estimating the angular velocity from the CA, which turns out to be nonlinear. This problem has received little attention, as can be seen from the small but nonetheless comprehensive list of works cited in Section 1.4.2. The goal of this section is thus to reduce this gap by proposing robust algorithms that allow for the estimation of the angular velocity from the centripetal component of the acceleration field of a rigid body.

Let us recall, from Section 6.2, that the centripetal acceleration is represented by the symmetric component of the angular acceleration matrix, and, therefore, it may be written explicitly as

$$\mathbf{W}_S = \frac{1}{2}\left(\mathbf{W} + \mathbf{W}^T\right) = \boldsymbol{\Omega}^2. \tag{8.1}$$

Here, the problem consists in extracting the angular velocity $\boldsymbol{\omega}$ from $\mathbf{W}_S$, up to a sign ambiguity, since $\boldsymbol{\omega}$ and $-\boldsymbol{\omega}$ yield the same centripetal acceleration field. One needs to resort to an external aid in order to find the sign of $\boldsymbol{\omega}$. As suggested in Section 1.4.2, it is chosen to use the TA estimates in order to resolve the ambiguity. Indeed, in most instances, recorded from the literature, the accelerometer arrays are feasible and, therefore, allow for both TA and CA estimates of the angular velocity. The first two methods presented in this Chapter are discussed with more detail in Cardou and Angeles (2008a), while

the other two are described in Cardou and Angeles (2008b).

8.2 First Method: Expressing W in a Preferred Frame

One of the major drawbacks of the CA method is that, due to the square-root operation, the error amplification is unbounded when any component of the angular velocity approaches zero. This can be seen by computing the partial derivative of the three-dimensional array $\boldsymbol{\zeta}$ containing the squares of the components of $\boldsymbol{\omega}$ with respect to $\mathbf{w}' \equiv \mathrm{diag}(\mathbf{W})$, where $\mathrm{diag}(\cdot)$ returns the vector formed with the diagonal entries of $(\cdot)$. This gives

$$\frac{\partial \boldsymbol{\zeta}}{\partial \mathbf{w}'} = 2\Delta \frac{\partial \boldsymbol{\omega}}{\partial \mathbf{w}'} = (1/2)\mathbf{B}, \text{ where } \boldsymbol{\Delta} \equiv \begin{bmatrix} \omega_1 & 0 & 0 \\ 0 & \omega_2 & 0 \\ 0 & 0 & \omega_3 \end{bmatrix} \text{ and } \mathbf{B} \equiv \begin{bmatrix} 1 & -1 & -1 \\ -1 & 1 & -1 \\ -1 & -1 & 1 \end{bmatrix}. \tag{8.2}$$

Matrix $\partial\boldsymbol{\omega}/\partial\mathbf{w}'$ gives the sensitivity of the angular-velocity estimate to the diagonal entries of the angular acceleration matrix for a given estimation method. From eq. (8.2), we also see that $\partial\boldsymbol{\omega}/\partial\mathbf{w}'$ is undetermined whenever $\boldsymbol{\Delta}$ becomes singular. This situation is to be avoided at all costs, as it means that a small error in $\mathbf{w}'$ leads to unpredictably large errors in $\boldsymbol{\omega}$. On the other hand, from mere intuition, the best situation may be when $\boldsymbol{\Delta}$ is "farthest" from being singular, that is, when it is isotropic. This happens when all the absolute values of the components of $\boldsymbol{\omega}$ are identical. In such a case, upon noticing that $\mathbf{W}$ is a tensor, i.e., a frame-invariant matrix, we can express it in a frame $\mathcal{C}$ different from the body frame $\mathcal{B}$, that minimizes the error amplification. This approach will be referred to as the *preferred-frame method*, which we will label CAPF, since it resorts mainly to measurements of the centripetal component of the acceleration field.

8.2.1 Optimization Problem

To substantiate the above claim, we first need to formulate the problem. Equation (8.2) is still valid in frame $\mathcal{C}$. We rewrite this equation as

$$[\boldsymbol{\Delta}]_{\mathcal{C}} \left[\frac{\partial \boldsymbol{\omega}}{\partial \mathbf{w}'}\right]_{\mathcal{C}} = \frac{1}{4}\mathbf{B}, \tag{8.3}$$

where $[\,\cdot\,]_{\mathcal{C}}$ means that $(\cdot)$ is expressed in frame $\mathcal{C}$. Hence, we aim at minimizing the p-norm of the Jacobian matrix of the CA method, that is,

$$f_p \equiv \left\| \left[\frac{\partial \boldsymbol{\omega}}{\partial \mathbf{w}'}\right]_{\mathcal{C}} \right\|_p \rightarrow \min_{\mathcal{C}}, \tag{8.4}$$

frame $\mathcal{C}$ being free of any constraint. The Euclidean norm, which corresponds to $p = 2$, is chosen here because, due to its invariance, it is a common metric in vector spaces. Notice that the Frobenius norm is also frame-invariant. However, unlike the p-norms, it does not bound any ratio of norms of the input and output vectors[1] and, therefore, it is meaningless in our application.

The optimum frame $\mathcal{C}$ under which f is a minimum is found to be any frame for which we have

$$[\boldsymbol{\omega}]_{\mathcal{C}} = \|\boldsymbol{\omega}\|_2 \mathbf{u}_{\boldsymbol{\omega}}, \tag{8.5}$$

where $\mathbf{u}_{\boldsymbol{\omega}} = (1/\sqrt{3})[\pm 1 \quad \pm 1 \quad \pm 1]^T$. Because the proof of this statement is lengthy, it is relegated to Appendix C. Also found in Appendix C are proofs that choosing either the 1- or the ∞-norms, which correspond to $p = 1$ and $p = \infty$, respectively, leads to the same optimum frame $\mathcal{C}$.

[1] The p-norm of a matrix $\mathbf{A} \in \mathbb{R}^{m\times n}$ is defined as $\|\mathbf{A}\|_p \equiv \max_{\mathbf{x}\in\mathbb{R}^n,\, \mathbf{x}\neq\mathbf{0}_n} \|\mathbf{A}\mathbf{x}\|_p / \|\mathbf{x}\|_p$, where $\|\cdot\|_p$ is the p-norm of the vector argument $(\,\cdot\,)$.

8.2.2 Implementation

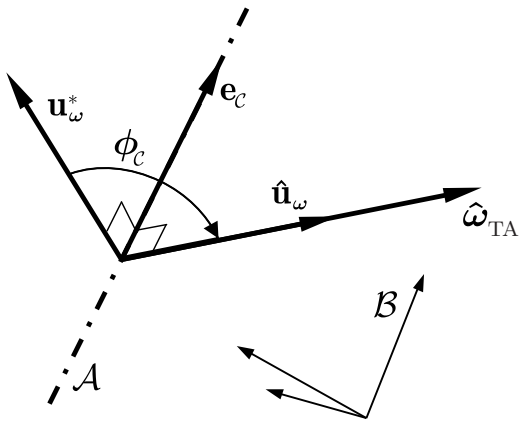

Figure 8.2: Rotating $\mathbf{u}^*_{\boldsymbol{\omega}}$ onto $\hat{\mathbf{u}}_{\boldsymbol{\omega}}$

Let us first use $\hat{\boldsymbol{\omega}}_{TA}$, obtained through the TA method, to compute an estimate $\hat{\mathbf{u}}_{\boldsymbol{\omega}} \equiv \hat{\boldsymbol{\omega}}_{TA}/\|\hat{\boldsymbol{\omega}}_{TA}\|_2$ of the direction of the angular velocity. Thus, we need to find a frame $\mathcal{C}$ such that $[\hat{\mathbf{u}}_{\boldsymbol{\omega}}]_{\mathcal{C}} = \mathbf{u}^*_{\boldsymbol{\omega}} = [\mathbf{u}^*_{\boldsymbol{\omega}}]_{\mathcal{B}}$, where $\mathbf{u}^*_{\boldsymbol{\omega}} \equiv (1/\sqrt{3})[1 \quad 1 \quad 1]^T$. One solution to this problem can be found by performing a rotation around axis $\mathcal{A}$ orthogonal to $\hat{\mathbf{u}}_{\boldsymbol{\omega}}$ and $\mathbf{u}^*_{\boldsymbol{\omega}}$ by an angle $\phi_{\mathcal{C}}$, as shown in Fig. 8.2. Thus, we obtain $[\hat{\mathbf{u}}_{\boldsymbol{\omega}}]_{\mathcal{B}} = \mathbf{Q}_{\mathcal{C}}[\mathbf{u}^*_{\boldsymbol{\omega}}]_{\mathcal{B}} = \mathbf{Q}_{\mathcal{C}}[\hat{\mathbf{u}}_{\boldsymbol{\omega}}]_{\mathcal{C}}$. Apparently, $\mathbf{Q}_{\mathcal{C}}$ is a matrix rotating frame $\mathcal{B}$ into frame $\mathcal{C}$, which takes the form (Angeles, 2007)

$$\mathbf{Q}_{\mathcal{C}} = \mathbf{e}_{\mathcal{C}}\mathbf{e}_{\mathcal{C}}^T + \cos\phi_{\mathcal{C}}(\mathbf{1}_{3\times 3} - \mathbf{e}_{\mathcal{C}}\mathbf{e}_{\mathcal{C}}^T) + \sin\phi_{\mathcal{C}}\mathbf{E}_{\mathcal{C}}, \tag{8.6}$$

where $\mathbf{e}_{\mathcal{C}}$ is the unit vector giving the direction of $\mathcal{A}$, and $\mathbf{E}_{\mathcal{C}} \equiv \mathrm{CPM}(\mathbf{e}_{\mathcal{C}})$. Upon noticing that $\mathbf{e}_{\mathcal{C}}\sin\phi_{\mathcal{C}} = \mathbf{u}^*_{\boldsymbol{\omega}} \times \hat{\mathbf{u}}_{\boldsymbol{\omega}}$ and $\cos\phi_{\mathcal{C}} = \hat{\mathbf{u}}^T_{\boldsymbol{\omega}}\mathbf{u}^*_{\boldsymbol{\omega}}$, eq. (8.6) is rewritten as

$$\mathbf{Q}_{\mathcal{C}} = \frac{(\mathbf{u}^*_{\boldsymbol{\omega}} \times \hat{\mathbf{u}}_{\boldsymbol{\omega}})(\mathbf{u}^*_{\boldsymbol{\omega}} \times \hat{\mathbf{u}}_{\boldsymbol{\omega}})^T}{1 + \hat{\mathbf{u}}^T_{\boldsymbol{\omega}}\mathbf{u}^*_{\boldsymbol{\omega}}} + \hat{\mathbf{u}}^T_{\boldsymbol{\omega}}\mathbf{u}^*_{\boldsymbol{\omega}}\mathbf{1}_{3\times 3} + \mathrm{CPM}(\mathbf{u}^*_{\boldsymbol{\omega}} \times \hat{\mathbf{u}}_{\boldsymbol{\omega}}), \tag{8.7}$$

where it is assumed that $\hat{\mathbf{u}}^T_{\boldsymbol{\omega}}\mathbf{u}^*_{\boldsymbol{\omega}} \neq -1$. In fact, $\hat{\mathbf{u}}^T_{\boldsymbol{\omega}}\mathbf{u}^*_{\boldsymbol{\omega}} = -1$ implies that $\hat{\mathbf{u}}_{\boldsymbol{\omega}} = -\mathbf{u}^*_{\boldsymbol{\omega}}$, which is also an optimum orientation. In this case, it is not necessary to change the coordinate frame, and hence, we choose $\mathbf{Q}_{\mathcal{C}} = \mathbf{1}_{3\times 3}$.

Hence the algorithm below:

```
if tr(Ŵ) ≠ 0 and ‖ω̂_TA‖_2 ≠ 0
  û_ω = ω̂_TA / ‖ω̂_TA‖_2
  if û*_ω^T u*_ω ≠ −1
    Q_C = (u*_ω × û_ω)(u*_ω × û_ω)^T / (1 + û*_ω^T u*_ω) + û*_ω^T u*_ω 1_{3×3} + CPM(u*_ω × û_ω)
  else
    Q_C = 1_{3×3}
  end
  [Ŵ]_C = Q_C^T Ŵ Q_C
  [ŵ′]_C = diag([Ŵ]_C)
  [ζ̂]_C = (1/2) B [ŵ′]_C
  for i = 1, 2, 3
    [ω̂_CAPF,i]_C = sqrt(h([ζ̂_i]_C)[ζ̂_i]_C)
  end
  ω̂_CAPF = Q_C [ω̂_CAPF]_C
else
  ω̂_CAPF = 0_3
end
```

8.3 Second Method: Estimating the Nullspace of $\mathbf{W}_S$

The idea behind this method is to use the invariants of $\mathbf{W}_S$ instead of expressing it in an optimum frame. When neglecting the measurement errors, we have $\mathbf{W}_S = \boldsymbol{\Omega}^2$, a symmetric negative-semidefinite matrix. One may verify that its eigenvalues are $\lambda_1 = 0$, $\lambda_2 = -\|\boldsymbol{\omega}\|_2^2$, $\lambda_3 = -\|\boldsymbol{\omega}\|_2^2$, whereas its

corresponding eigenvectors $\{\boldsymbol{\mu}_i\}_1^3$ are

$$\boldsymbol{\mu}_1 = \mathbf{u}_{\boldsymbol{\omega}}, \quad \boldsymbol{\mu}_2 = \frac{1}{\sqrt{\omega_1^2 + \omega_2^2}} \begin{bmatrix} -\omega_2 \\ \omega_1 \\ 0 \end{bmatrix}, \quad \text{and} \quad \boldsymbol{\mu}_3 = \frac{1}{\sqrt{\omega_1^2 + \omega_3^2}} \begin{bmatrix} -\omega_3 \\ 0 \\ \omega_1 \end{bmatrix}.$$

No information regarding the orientation of $\boldsymbol{\omega}$ can be extracted from the eigenvalues: only $\|\boldsymbol{\omega}\|_2$ is available. In fact, although it never was explicitly stated, this information was already present in the CA method, through the relation

$$-(1/2)\text{tr}(\mathbf{W}) = -(1/2)\text{tr}(\mathbf{W}_S) = -(1/2)(\lambda_1 + \lambda_2 + \lambda_3) = \|\boldsymbol{\omega}\|_2^2. \tag{8.8}$$

The novelty of this approach lies in the information extracted from the eigenvectors of $\boldsymbol{\Omega}^2$. As $\boldsymbol{\Omega}^2$ is symmetric, and provided that $\|\boldsymbol{\omega}\|_2 \neq 0$, its eigenvectors are bound to be mutually orthogonal; moreover, since its rank is 2, two of these eigenvectors span its range, while the remaining one, linearly dependent with $\boldsymbol{\omega}$, spans the nullspace of $\boldsymbol{\Omega}$, and hence, of $\boldsymbol{\Omega}^2$. As a result, the problem amounts to the estimation of the nullspace of $\mathbf{W}_S$; therefore, its solution method will be referred to as the CANS method.

8.3.1 Implementation

We will rely on the QR factorization to compute the nullspace of interest in a predetermined number of steps[2]. Let us use Householder reflections with pivoting (Golub and Van Loan, 1996) to decompose $\mathbf{W}_S$ into $\mathbf{QR}$, where $\mathbf{R}$ is an upper-triangular matrix and $\mathbf{Q}$ is an orthogonal matrix. Moreover, since $\mathbf{W}_S$ has one null eigenvalue, it has a rank of two, which implies that the third

[2] It is common practice to find the nullspace of a matrix using the singular-value decomposition (SVD). However, algorithms which perform SVD are iterative, which is undesirable for angular velocity estimation in real time, even for a relatively small matrix.

diagonal entry of $\mathbf{R}$ will be null. This indicates also that the Householder method requires only two reflections. We obtain

$$\mathbf{0}_3 = \mathbf{W}_S\boldsymbol{\mu}_1 = (\mathbf{W}_S)^T\boldsymbol{\mu}_1 = \mathbf{R}^T\mathbf{Q}^T\boldsymbol{\mu}_1 = \mathbf{R}^T\boldsymbol{\nu}, \tag{8.9}$$

where $\boldsymbol{\nu} \equiv \mathbf{Q}^T\boldsymbol{\mu}_1$. From eq. (8.9), we see that $\boldsymbol{\nu}$ must lie in the nullspace of $\mathbf{R}^T$. Because the third column of $\mathbf{R}^T$ is null, we conclude directly that $\boldsymbol{\nu} = \mathbf{e}_3$ is a suitable solution. The eigenvector is obtained from the definition of $\boldsymbol{\mu}$, that is, $\boldsymbol{\mu}_1 = \mathbf{Q}\boldsymbol{\nu} = \mathbf{q}_3$, where $\mathbf{q}_3$ is the vector formed from the third column of $\mathbf{Q}$.

There is still one issue that needs to be resolved: we have obtained a vector that is parallel to $\boldsymbol{\omega}$, but we do not know whether it points in the correct direction. To resolve this ambiguity, we use the estimate $\hat{\boldsymbol{\omega}}_{TA}$ obtained from the TA method, and take the direction that minimizes the magnitude of the error $\|\boldsymbol{\omega} - \hat{\boldsymbol{\omega}}_{\text{TA}}\|_2$. As a result, $\boldsymbol{\omega}$ is computed as $\boldsymbol{\omega} = \text{sgn}(\boldsymbol{\mu}_1^T\hat{\boldsymbol{\omega}})\|\boldsymbol{\omega}\|_2\boldsymbol{\mu}_1$. Thus, the algorithm takes the form

```
if tr(Ŵ) < 0
   ‖ω̂_CANS‖_2 = √(−(1/2)tr(Ŵ))
   Ŵ_S = (1/2)(Ŵ + Ŵ^T)
   {Q, R} ← Householder(Ŵ_S)
   ω̂_CANS = sgn(q_3^T ω̂_TA)‖ω̂_CANS‖_2 q_3
else
   ω̂_CANS = 0_3
end
```

8.4 Third Method: Computing the Matrix-Adjoint of $\mathbf{W}_S$

Apparently, the former method is relatively robust. Nevertheless, let us introduce an alternative method that presents the advantage of being less costly in computation time and symbolically simpler. As it is bound to be singular, the inverse of $\mathbf{W}_S$ does not exist. Nevertheless, its adjoint does exist, as one may verify that

$$\text{adj}(\mathbf{W}_S) = \text{adj}(\boldsymbol{\Omega}^2) = \|\boldsymbol{\omega}\|_2^2 \boldsymbol{\omega}\boldsymbol{\omega}^T, \tag{8.10}$$

where $\text{adj}(\mathbf{A})$ is the adjoint[3] of $\mathbf{A} \in \mathbb{R}^{n\times n}$ such that

$$\text{adj}(\mathbf{A})\mathbf{A} = \mathbf{A}\text{adj}(\mathbf{A}) = \det(\mathbf{A})\mathbf{1}_{n\times n}. \tag{8.11}$$

The eigenvector corresponding to the non-null eigenvalue of $\text{adj}(\boldsymbol{\Omega}^2)$ is parallel to the eigenvector corresponding to the null eigenvalue of $\boldsymbol{\Omega}^2$. The difference is that the eigenvector of $\text{adj}(\boldsymbol{\Omega}^2)$ can be readily obtained by multiplying any vector that is not orthogonal to $\boldsymbol{\omega}$ by the matrix itself. To mark the difference between this method and the other CA methods, we will refer to it as the CAMA method, MA standing for "Matrix-Adjoint".

8.4.1 Implementation

Since any vector that is not orthogonal to $\boldsymbol{\omega}$ may be premultiplied by $\text{adj}(\boldsymbol{\Omega}^2)$ to yield an estimate of the direction of the angular velocity vector, we choose, for robustness, a vector that is as parallel to $\boldsymbol{\omega}$ as possible. An estimate

[3] Not to be confused with the adjoint or Hermitian transpose of a linear operator.

of this vector is given by the TA method, thus leading to the algorithm

$$
\begin{aligned}
&\texttt{if } \operatorname{tr}(\hat{\mathbf{W}}) < 0 \\
&\quad \|\hat{\boldsymbol{\omega}}_{\mathrm{CAMA}}\|_2 = \sqrt{-(1/2)\operatorname{tr}(\hat{\mathbf{W}})} \\
&\quad \hat{\mathbf{W}}_S = (1/2)(\hat{\mathbf{W}} + \hat{\mathbf{W}}^T) \\
&\quad \mathbf{v} = \operatorname{adj}(\hat{\mathbf{W}}_S)\hat{\boldsymbol{\omega}}_{\mathrm{TA}} \\
&\quad \hat{\boldsymbol{\omega}}_{\mathrm{CAMA}} = (\|\hat{\boldsymbol{\omega}}_{\mathrm{CAMA}}\|_2/\|\mathbf{v}\|_2)\mathbf{v} \\
&\texttt{else} \\
&\quad \hat{\boldsymbol{\omega}}_{\mathrm{CAMA}} = \mathbf{0}_3 \\
&\texttt{end}
\end{aligned}
$$

8.4.2 A Special Case: Using the CANS Method with Gram-Schmidt Orthogonalization

The CANS method may be modified by replacing the Householder algorithm with an alternative QR factorization method. As it turns out, when choosing the Gram-Schmidt orthogonalization without pivoting—which we may label CAGS for short—the resulting algorithm yields exactly the same estimates as a special case of the CAMA method. Indeed, when using the CANS method with Gram-Schmidt orthogonalization to compute the QR factorization of $\hat{\mathbf{W}}_S$, the estimate of $\mathbf{W}_S$, one may verify that the resulting estimate $\mathbf{q}_3$ of the direction of $\boldsymbol{\omega}$ is

$$\mathbf{q}_3 = \frac{1}{\sqrt{\alpha_{1,3}^2 + \alpha_{2,3}^2 + \alpha_{3,3}^2}} \begin{bmatrix} \alpha_{3,1} \\ \alpha_{2,3} \\ \alpha_{3,3} \end{bmatrix}, \tag{8.12}$$

where $\alpha_{i,j}$ is the (i,j) cofactor of $\hat{\mathbf{W}}_S$. As the adjoint matrix of $\hat{\mathbf{W}}_S$ is nothing but the transpose of its matrix of cofactors, we can write

$$[\alpha_{1,3} \quad \alpha_{2,3} \quad \alpha_{3,3}]^T = \operatorname{adj}(\hat{\mathbf{W}}_S)^T\mathbf{e}_3 = \operatorname{adj}(\hat{\mathbf{W}}_S)\mathbf{e}_3. \tag{8.13}$$

Hence, Gram-Schmidt orthogonalization yields the same direction vector as if the adjoint were multiplied by vector $\mathbf{e}_3$.

In the case where the measurements are exact, we obtain, from eq. (8.10),

$$\mathbf{v} = \text{adj}(\mathbf{W}_S)\mathbf{e}_3 = \text{adj}(\boldsymbol{\Omega}^2)\mathbf{e}_3 = \|\boldsymbol{\omega}\|_2^2 \boldsymbol{\omega}\boldsymbol{\omega}^T \mathbf{e}_3, \tag{8.14}$$

whence it is now apparent that the direction of an angular-velocity vector orthogonal to $\mathbf{e}_3$ is left undetermined by this method. Because of this singularity, this method is not reliable, and we will leave it aside in further comparisons.

8.4.3 Another Special Case: Taking the Cross-Products of the Columns of $\mathbf{W}_S$

Another interesting method is obtained by defining the estimate of the angular velocity direction $\mathbf{v}$ to be

$$\mathbf{v} = \text{adj}(\mathbf{W}_S)\mathbf{e}^* = \|\boldsymbol{\omega}\|_2^2 \boldsymbol{\omega}\boldsymbol{\omega}^T \mathbf{e}^*, \tag{8.15}$$

where $\mathbf{e}^* \equiv [1 \quad 1 \quad 1]^T$. This method can be referred to as the cross-product method (CACP), because of its underlying geometric interpretation. Indeed, one can verify that

$$\mathbf{v} = \text{adj}(\mathbf{W}_S)\mathbf{e}^* = \mathbf{w}_1^S \times \mathbf{w}_2^S + \mathbf{w}_2^S \times \mathbf{w}_3^S + \mathbf{w}_3^S \times \mathbf{w}_1^S, \tag{8.16}$$

where $\mathbf{w}_i^S$ is the i^{th} column—and row—vector of $\mathbf{W}_S$. Upon multiplying the latter by $\mathbf{v}$, we obtain

$$\mathbf{W}_S\mathbf{v} = \begin{bmatrix} (\mathbf{w}_1^S)^T(\mathbf{w}_2^S \times \mathbf{w}_3^S) \\ (\mathbf{w}_2^S)^T(\mathbf{w}_3^S \times \mathbf{w}_1^S) \\ (\mathbf{w}_3^S)^T(\mathbf{w}_1^S \times \mathbf{w}_2^S) \end{bmatrix}, \tag{8.17}$$

from which it is apparent that $\mathbf{v}$ lies in the nullspace of $\mathbf{W}_S$, since, in the absence of noise, $\mathbf{w}_1^S$, $\mathbf{w}_2^S$ and $\mathbf{w}_3^S$ are linearly dependent. However, the estimated matrix $\hat{\mathbf{W}}_S$ is likely to have an empty nullspace. In the deterministic case,

$$\hat{\mathbf{v}} \equiv \hat{\mathbf{w}}_1^S \times \hat{\mathbf{w}}_2^S + \hat{\mathbf{w}}_2^S \times \hat{\mathbf{w}}_3^S + \hat{\mathbf{w}}_3^S \times \hat{\mathbf{w}}_1^S, \tag{8.18}$$

where $\hat{\mathbf{w}}_i^S$ is the i^{th} column—or the i^{th} row—vector of $\hat{\mathbf{W}}_S$, gives a *reasonable estimate* of the nullspace of $\mathbf{W}_S$. Indeed, consider Fig. 8.3, in which the column-vectors of $\mathbf{W}_S$ and $\hat{\mathbf{W}}_S$ are represented in the three-dimensional Euclidean space. $\mathcal{V}$ being the plane spanned by the column-vectors of $\mathbf{W}_S$, one

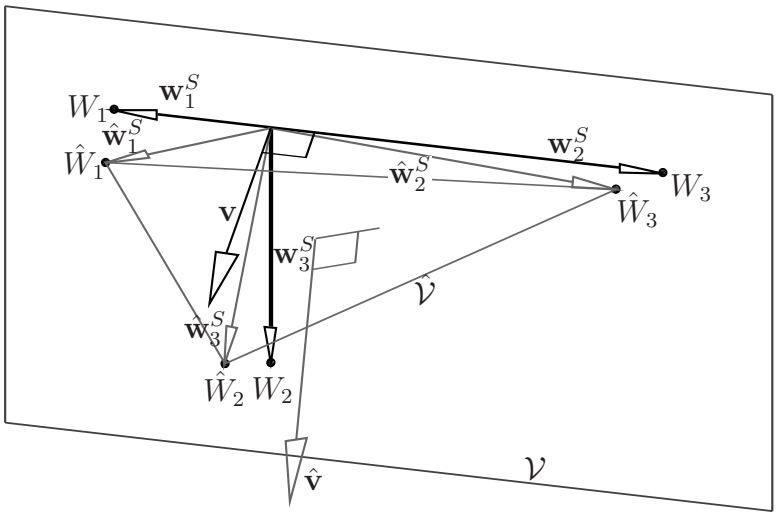

Figure 8.3: Estimating the nullspace of $\mathbf{W}_S$ using the CACP method

may verify that $\mathbf{v}$ is indeed a vector normal to $\mathcal{V}$. Taking $\mathbf{w}_i^S$ as the position vector of a point W_i in space, the magnitude of $\mathbf{v}$ is twice the area of the triangle with vertices W_1, W_2 and W_3. Similarly, plane $\hat{\mathcal{V}}$ is the plane passing through points $\hat{W}_1$, $\hat{W}_2$ and $\hat{W}_3$, with position vectors $\hat{\mathbf{w}}_1^S$, $\hat{\mathbf{w}}_2^S$ and $\hat{\mathbf{w}}_3^S$, respectively. Also notice that $\hat{\mathbf{v}}$ is then normal to $\hat{\mathcal{V}}$, with its magnitude twice the area of the triangle with vertices $\hat{W}_1$, $\hat{W}_2$ and $\hat{W}_3$.

However, as for the CAGS method, the CACP method becomes useless whenever $\boldsymbol{\omega}$ is orthogonal to $\mathbf{e}^*$. In this situation, we can readily see from eq. (8.15) that $\mathbf{v} = \mathbf{0}_3$. Geometrically, this corresponds to having points W_1, W_2 and W_3 collinear, or, equivalently, the corresponding triangle being stretched to the point that it becomes a segment of a line. Plane $\mathcal{V}$ thus becomes undetermined and the method fails to provide a vector $\mathbf{v}$ parallel to $\boldsymbol{\omega}$. As in the CAPF method, this problem could be fixed by using the TA estimate of the angular velocity in order to find a new frame $\mathcal{C}$ such that $\hat{\boldsymbol{\omega}}_{\text{TA}}$ is parallel to $\mathbf{e}^*$. This would allow one to compute the estimate $\hat{\mathbf{v}}$ of the direction of $\boldsymbol{\omega}$ univocally from $[\hat{\mathbf{W}}_S]_{\mathcal{C}}$. However, this approach is thought to be cumbersome and computationally costly. For that reason, it is left out of the rest of the analysis.

8.4.4 Estimating the Magnitude of the Angular Velocity from the Matrix-Adjoint of $\mathbf{W}_S$

The only method available in the literature to estimate the Euclidean norm of the angular velocity vector from centripetal acceleration measurements is through the trace of the angular acceleration matrix (Parsa, 2003). The expression of this magnitude is

$$\|\boldsymbol{\omega}\|_2 = \sqrt{(-1/2)\text{tr}(\mathbf{W}_S)}, \tag{8.19}$$

which can be regarded as the average of $\sigma_1 = \|\boldsymbol{\omega}\|_2^2$ and $\sigma_2 = \|\boldsymbol{\omega}\|_2^2$, the two non-null singular values of $\mathbf{W}_S$. Indeed, since $\mathbf{W}_S$ is symmetric, negative semi-definite, we have the relations $\sigma_i = -\lambda_i$, $i = 1, 2, 3$, where σ_i and λ_i represent the i^{th} singular value and the i^{th} eigenvalue of $\mathbf{W}_S$, respectively. Hence, since $\lambda_3 = \sigma_3 = 0$, we can write

$$\|\boldsymbol{\omega}\|_2^2 = (-1/2)\text{tr}(\mathbf{W}_S) = -(1/2)(\lambda_1 + \lambda_2 + \lambda_3) = (1/2)(\sigma_1 + \sigma_2). \tag{8.20}$$

Consequently, let us label this method CAMAM, "CA" standing for centripetal acceleration, "M" for magnitude, and "AM" for arithmetic mean of the non-null eigenvalues.

Turning now our attention to eq. (8.10), we realize that another interesting implication of this relation is that the adjoint of $\mathbf{W}_S$ can be used to compute the Euclidean norm of $\boldsymbol{\omega}$ as

$$\|\boldsymbol{\omega}\|_2 = \sqrt[4]{\|\boldsymbol{\omega}\|_2^2 \mathrm{tr}(\boldsymbol{\omega}\boldsymbol{\omega}^T)} = \sqrt[4]{\mathrm{tr}(\mathrm{adj}(\mathbf{W}_S))}. \tag{8.21}$$

In general, the eigenvalues ν_i, $i = 1, 2, 3$, of the adjoint of the matrix are connected to the eigenvalues of the matrix through the relation

$$\nu_i = \lambda_j \lambda_k, \quad i \neq j, k. \tag{8.22}$$

Hence, in our case, we obtain

$$\|\boldsymbol{\omega}\|_2^2 = \sqrt{\lambda_1 \lambda_2} = \sqrt{\sigma_1 \sigma_2}, \tag{8.23}$$

where it is now apparent that the estimate of the norm squared is nothing but the geometric mean of the nonzero singular values of $\hat{\mathbf{W}}_S$. For that reason, we will call this approach the CAMGM method, "GM" standing for geometric mean.

In the case of noisy measurements, let us label the singular values of $\hat{\mathbf{W}}_S$ as $\hat{\sigma}_i$, $i = 1, 2, 3$. Then, in general, we have $\hat{\sigma}_3 \neq 0$ and $\hat{\sigma}_1 \neq \hat{\sigma}_2$. For the sake of analysis, assume that the condition $\hat{\sigma}_3 = 0$ still holds. Then, the mapping of vectors $\mathbf{x}$ regarded as the position vectors of points on the surface of the unit sphere centered at the origin—i.e. $\|\mathbf{x}\|_2 = 1$—by matrix $\hat{\mathbf{W}}_S$ is an elliptic disc in space with major axis $\hat{\sigma}_1$ and minor axis $\hat{\sigma}_2$, as depicted in Fig. 8.4.

Since we have $\sigma_1 = \sigma_2$ for the case of perfect measurements, we are to approximate this ellipse with a circle of radius $\|\hat{\boldsymbol{\omega}}_{\mathrm{C}}\|_2^2$. It turns out that taking the

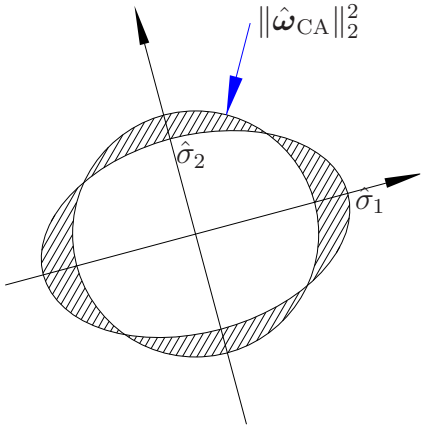

Figure 8.4: Approximating an ellipse with a circle

geometric mean of $\hat{\sigma}_1$ and $\hat{\sigma}_2$, as per eq. (8.23), minimizes the total area of the surface comprised in one or the other closed curves, but not in both, i.e., the area of the hatched region in Fig. 8.4. This also corresponds to choosing a circle having the same area as the ellipse. Hence, apparently, this method is justified when $\hat{\sigma}_3 = 0$.

8.5 Fourth Method: Augmenting Matrix $\mathbf{W}_S$ With the Range of its Adjoint

The method introduced in this section is best understood from the diagram of the linear mapping associated with tensor $\mathbf{W}_S$, as shown in Fig. 8.5. In this diagram, the larger rectangle on the left-hand side represents the domain of the linear operator—$\mathbb{R}^3$, in our case—while the larger rectangle on the right hand side represents its image—$\mathbb{R}^3$ as well, in our case. The nullspace of $\mathbf{W}_S$ is $\mathcal{N}\{\mathbf{W}_S\} = \mathrm{span}\{\boldsymbol{\omega}\}$, while the support space[4] is $\mathcal{S}\{\mathbf{W}_S\}$, the set of

[4] This is the orthogonal complement of the nullspace, often also called the row space.

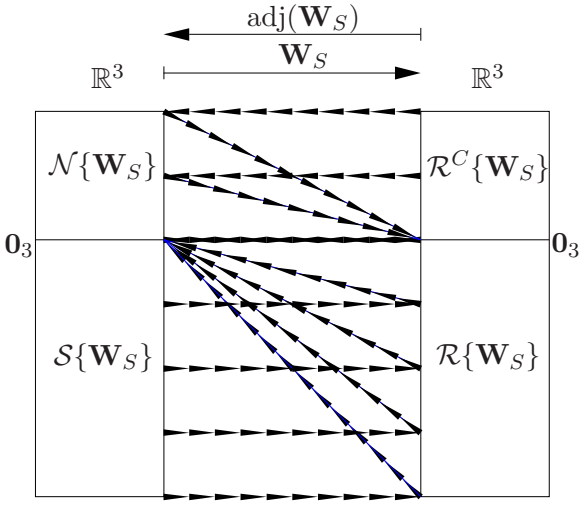

Figure 8.5: The subspaces of $\mathbb{R}^3$ associated to $\mathbf{W}_S$

all three-dimensional vectors orthogonal to $\boldsymbol{\omega}$. Since the matrix is symmetric, its range is the same as its support space, that is, $\mathcal{R}\{\mathbf{W}_S\} = \mathcal{S}\{\mathbf{W}_S\}$. As a result, the orthogonal complement of the range $\mathcal{R}^C\{\mathbf{W}_S\}$ is the same as the nullspace of $\mathbf{W}_S$.

The linear mapping associated with the adjoint of $\mathbf{W}_S$ is also represented in Fig. 8.5 with, this time, its domain on the right-hand side and its image on the left-hand side. Hence, on the diagram, all the arrows pointing towards the right correspond to $\mathbf{W}_S$, while the arrows pointing towards the left are associated with its adjoint. From eq. (8.11), we have

$$\text{adj}(\mathbf{W}_S)\mathbf{W}_S = \mathbf{W}_S\text{adj}(\mathbf{W}_S) = \mathbf{O}_{3\times 3}, \tag{8.24}$$

since $\mathbf{W}_S$ is singular. Hence, the range of $\mathbf{W}_S$ lies in the nullspace of adj($\mathbf{W}_S$) and, conversely, the range of adj($\mathbf{W}_S$) lies in the nullspace of $\mathbf{W}_S$, which leads to $\mathcal{N}\{\text{adj}(\mathbf{W}_S)\} = \mathcal{R}\{\mathbf{W}_S\}$, $\mathcal{S}\{\text{adj}(\mathbf{W}_S)\} = \mathcal{R}^C\{\mathbf{W}_S\}$, $\mathcal{R}\{\text{adj}(\mathbf{W}_S)\} = \mathcal{N}\{\mathbf{W}_S\}$, and $\mathcal{R}^C\{\text{adj}(\mathbf{W}_S)\} = \mathcal{S}\{\mathbf{W}_S\}$.

From the foregoing facts, the idea is to construct a full-rank matrix $\mathbf{X}$, so that we are bound to have $\boldsymbol{\omega} \in \mathcal{S}\{\mathbf{X}\}$, and for which we have an estimate of the mapping of $\boldsymbol{\omega}$ in the image space. Such a matrix can be obtained by stacking the additional row $\mathbf{x}^T \text{adj}(\mathbf{W}_S)$ at the bottom of $\mathbf{W}_S$, where $\mathbf{x} \in \mathbb{R}^3$ is not orthogonal to $\boldsymbol{\omega}$. Since $\text{adj}(\mathbf{W}_S)^T\mathbf{x} = \text{adj}(\mathbf{W}_S)\mathbf{x} \in \mathcal{R}\{\text{adj}(\mathbf{W}_S)\} = \mathcal{N}\{\mathbf{W}_S\}$, we have

$$\mathcal{S}\{\begin{bmatrix} \mathbf{W}_S \\ \mathbf{x}^T \text{adj}(\mathbf{W}_S) \end{bmatrix}\} = \mathcal{S}\{\mathbf{W}_S\} \oplus \mathcal{N}\{\mathbf{W}_S\} = \mathbb{R}^3, \tag{8.25}$$

with $\oplus$ indicating, as usual, the *direct sum* of the two vector-space operands. As in the adjoint method, let us choose $\mathbf{x} = \hat{\boldsymbol{\omega}}_{\text{TA}}$ to be our best estimate of a vector that is not orthogonal to $\boldsymbol{\omega}$. The resulting matrix is

$$\begin{bmatrix} \mathbf{W}_S \\ \hat{\boldsymbol{\omega}}_{\text{TA}}^T \text{adj}(\mathbf{W}_S) \end{bmatrix}, \tag{8.26}$$

and, because it combines $\mathbf{W}_S$ and its adjoint matrix, we will call this approach the augmented matrix method, or, for short, CAAM. However, the current form of the augmented matrix is not yet satisfactory because it is not dimensionally homogeneous. Indeed, in such a case, choosing inappropriate units renders the matrix ill-conditioned and prone to round-off errors due to the finiteness of the machine precision. To avoid such problems, we normalize all quantities using the estimate of the norm from the CAMAM method, $\|\hat{\boldsymbol{\omega}}_{\text{CA}}\|_2^2 = -(1/2)\text{tr}(\mathbf{W}_S)$, which yields

$$\mathbf{X} \equiv \begin{bmatrix} -2\mathbf{W}_S/\text{tr}(\mathbf{W}_S) \\ 4\hat{\boldsymbol{\omega}}_{\text{TA}}^T \text{adj}(\mathbf{W}_S)/(\text{tr}(\mathbf{W}_S)^2 \|\hat{\boldsymbol{\omega}}_{\text{TA}}\|_2) \end{bmatrix} = \begin{bmatrix} \boldsymbol{\Omega}^2/\|\boldsymbol{\omega}\|_2^2 \\ \hat{\boldsymbol{\omega}}_{\text{TA}}^T \boldsymbol{\omega}\boldsymbol{\omega}^T/(\|\boldsymbol{\omega}\|_2^2 \|\hat{\boldsymbol{\omega}}_{\text{TA}}\|_2) \end{bmatrix}. \tag{8.27}$$

It can be seen that $\mathbf{X}$, in addition to satisfying the required properties, has other interesting features. Indeed, if the TA estimate were to be perfect, that

is, if $\hat{\boldsymbol{\omega}}_{\mathrm{TA}} = \boldsymbol{\omega}$, we would have

$$\begin{aligned}
\mathbf{X}^T\mathbf{X} &= (1/\|\boldsymbol{\omega}\|_2^4)\begin{bmatrix}\boldsymbol{\Omega}^2 & \boldsymbol{\omega}\boldsymbol{\omega}^T\boldsymbol{\omega}/\|\boldsymbol{\omega}\|_2\end{bmatrix}\begin{bmatrix}\boldsymbol{\Omega}^2 \\ \boldsymbol{\omega}^T\boldsymbol{\omega}\boldsymbol{\omega}^T/\|\boldsymbol{\omega}\|_2\end{bmatrix} \\
&= (1/\|\boldsymbol{\omega}\|_2^4)(\boldsymbol{\Omega}^4 + \|\boldsymbol{\omega}\|_2^2\boldsymbol{\omega}\boldsymbol{\omega}^T) \\
&= (1/\|\boldsymbol{\omega}\|_2^4)((\boldsymbol{\omega}\boldsymbol{\omega}^T - \|\boldsymbol{\omega}\|_2^2\mathbf{1}_{3\times3})^2 + \|\boldsymbol{\omega}\|_2^2\boldsymbol{\omega}\boldsymbol{\omega}^T) \\
&= (1/\|\boldsymbol{\omega}\|_2^4)(\boldsymbol{\omega}\boldsymbol{\omega}^T\boldsymbol{\omega}\boldsymbol{\omega}^T - 2\|\boldsymbol{\omega}\|_2^2\boldsymbol{\omega}\boldsymbol{\omega}^T + \|\boldsymbol{\omega}\|_2^4\mathbf{1}_{3\times3} + \|\boldsymbol{\omega}\|_2^2\boldsymbol{\omega}\boldsymbol{\omega}^T) \\
&= \mathbf{1}_{3\times3}.
\end{aligned} \tag{8.28}$$

From eq. (8.28), it is apparent that the columns of $\mathbf{X}$ form an orthonormal set and, hence, for perfect measurements, $\mathbf{X}$ is isotropic. Having $\mathbf{X}$ close to isotropy guarantees a well conditioned linear system, and hence, a low roundoff-error amplification.

8.5.1 Implementation

For ideal measurements, the mapping of $\mathbf{u}_{\boldsymbol{\omega}} \equiv \boldsymbol{\omega}/\|\boldsymbol{\omega}\|_2$ onto the range of $\mathbf{X}$ is

$$\mathbf{X}\mathbf{u}_{\boldsymbol{\omega}} = [0 \quad 0 \quad 0 \quad 1]^T \equiv \boldsymbol{\xi}. \tag{8.29}$$

The least-square solution of eq. (8.29) is found using Householder reflections, which yields the algorithm

$$
\begin{aligned}
&\texttt{if } \operatorname{tr}(\hat{\mathbf{W}}) < 0 \\
&\quad \|\hat{\boldsymbol{\omega}}_{\mathrm{CAAM}}\|_2 = \sqrt{-(1/2)\operatorname{tr}(\hat{\mathbf{W}})} \\
&\quad \hat{\mathbf{W}}_S = (1/2)(\hat{\mathbf{W}} + \hat{\mathbf{W}}^T) \\
&\quad \hat{\mathbf{X}} = \begin{bmatrix} -2\hat{\mathbf{W}}_S/\operatorname{tr}(\hat{\mathbf{W}}_S) \\ 4\hat{\boldsymbol{\omega}}_{\mathrm{TA}}^T \operatorname{adj}(\hat{\mathbf{W}}_S)/(\operatorname{tr}(\hat{\mathbf{W}}_S)^2 \|\hat{\boldsymbol{\omega}}_{\mathrm{TA}}\|_2) \end{bmatrix}, \quad \boldsymbol{\xi} = \begin{bmatrix} \mathbf{0}_3 \\ 1 \end{bmatrix} \\
&\quad \{\mathbf{Q}, \mathbf{R}\} \leftarrow \texttt{Householder}(\hat{\mathbf{X}}) \\
&\quad \mathbf{u}_{\boldsymbol{\omega}} \leftarrow \texttt{Backsubstitution}(\mathbf{R}, \mathbf{Q}^T\boldsymbol{\xi}) \\
&\quad \boldsymbol{\omega} = (\|\hat{\boldsymbol{\omega}}_{\mathrm{CAAM}}\|_2/\|\mathbf{u}_{\boldsymbol{\omega}}\|_2)\mathbf{u}_{\boldsymbol{\omega}} \\
&\texttt{else} \\
&\quad \hat{\boldsymbol{\omega}}_{\mathrm{CAAM}} = \mathbf{0}_3 \\
&\texttt{end}.
\end{aligned}
$$

Notice that all quantities in this algorithm may be stained with noise, and, therefore, vector $\mathbf{u}_{\boldsymbol{\omega}}$ may not have a unit norm. This explains its normalization prior to its multiplication by the angular-velocity-norm estimate. Notice also that we are resorting to the Householder algorithm without pivoting. Indeed, $\mathbf{X}$ was shown to be isotropic when calculated from ideal accelerometer measurements, which eliminates the need for pivoting. On the other hand, there is no reason why $\hat{\mathbf{X}}$ should be isotropic, even though its condition number should be close to unity, provided that the errors are sufficiently small. In that case, it is still not clear whether pivoting would add robustness to the method, since the columns of $\hat{\mathbf{X}}$ that exhibit a larger magnitude might as well be the ones

that contain the largest error component. For that reason, and because pivoting adds to the computational burden of the algorithm, we decide to use Householder reflections without pivoting.

8.6 Simulation #1

In order to compare the robustness of the four foregoing methods with that of the previously proposed ones, the motion of a brick freely rotating in space was simulated. As the current objective is to compare different algorithms for the estimation of $\boldsymbol{\omega}$, the simulations were simplified to the minimum.

8.6.1 Accelerometer Array

The IMU used to estimate the angular velocity of the brick is assumed to be an array of four triplets of mutually orthogonal accelerometers, attached to four of the vertices of the parallelepiped. The layout is depicted in Fig. 8.6, where unit vector $\mathbf{e}_i$ gives the sensitive direction of the i^{th} accelerometer, whereas point P_i gives its location on the brick. Apparently, all direction vectors are parallel to four of the parallelepiped edges; moreover, $P_1 = P_2 = P_3$, $P_4 = P_5 = P_6$, $P_7 = P_8 = P_9$ and $P_{10} = P_{11} = P_{12}$. The brick dimensions are chosen to be $a = 0.07$ m, $b = 0.14$ m and $c = 0.21$ m, in the X-, Y- and Z-axis direction, respectively. Let us also define frame $\mathcal{B}$, which is attached to the brick and has its origin B located at the brick centroid. All vector quantities in this simulation are to be expressed in frame $\mathcal{B}$.

8.6.2 Trajectory

We assume that neither force nor moment is applied to the brick throughout the simulation. Hence, the angular momentum is preserved, which gives

$$\mathbf{I}_B\dot{\boldsymbol{\omega}} + \boldsymbol{\omega} \times \mathbf{I}_B\boldsymbol{\omega} = \mathbf{0}_3, \tag{8.30}$$

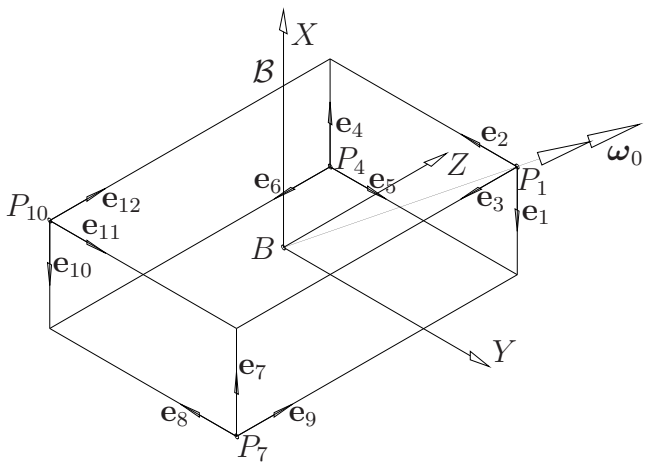

Figure 8.6: A brick rotating freely in space

where $\mathbf{I}_B$ is the brick inertia matrix calculated with respect to point B and expressed in frame $\mathcal{B}$. Upon assuming a constant density ρ of the brick material, we obtain

$$\mathbf{I}_B = \frac{\rho abc}{12}\begin{bmatrix} b^2+c^2 & 0 & 0 \\ 0 & a^2+c^2 & 0 \\ 0 & 0 & a^2+b^2 \end{bmatrix} = \rho \begin{bmatrix} 10.9 & 0 & 0 \\ 0 & 8.4 & 0 \\ 0 & 0 & 4.2 \end{bmatrix} \cdot 10^{-6} \text{ m}^5. \quad (8.31)$$

Notice that, under these assumptions, the brick trajectory is independent of ρ. We choose the initial condition to be $\boldsymbol{\omega}_0 = [13.33 \quad 17.77 \quad 22.21]^T$ rad/s, as represented in Fig. 8.6, where one can see that this vector is parallel to one of the great diagonals of the parallelepiped, its magnitude being 10π rad/s.

8.6.3 Accelerometer Readouts

The i^{th} accelerometer output is decomposed into one deterministic part $a_{i,r}$, which is the actual point-acceleration, and two stochastic parts $\delta a_{i,b}$ and $\delta a_{i,n}$, which are the bias error and the noise error, respectively. This gives, at an instant t,

$$a_i(t) = a_{i,r}(t) + \delta a_{i,b} + \delta a_{i,n}(t). \quad (8.32)$$

In the above equation, the bias error is assumed to be time-independent and normally distributed, while the noise is assumed to be white and normally distributed as well. The mean and variance of $\delta a_{i,b}$ are taken to be 0 and 300 mg, respectively, while the mean and variance of $\delta a_{i,n}$ are taken to be 0 and 75 mg, respectively. Notice that a bias error of 300 mg corresponds to approximately 2.6% of the required range of the device. All random variables are assumed to be independent. A sampling rate of 100 Hz is assumed. In order to keep the simulation simple, no sensor orientation or position errors are included. Hence, the results obtained here serve as comparison among the different estimation methods.

8.6.4 Results

The estimated angular acceleration is shown in Fig. 8.7. Upon integrating the angular acceleration according to eq. (1.2a), we obtain the TA estimates of Fig. 8.8. As expected, these estimates drift constantly over time due to bias errors, which renders them useless for applications involving an IMU autonomy of more than 1 s.

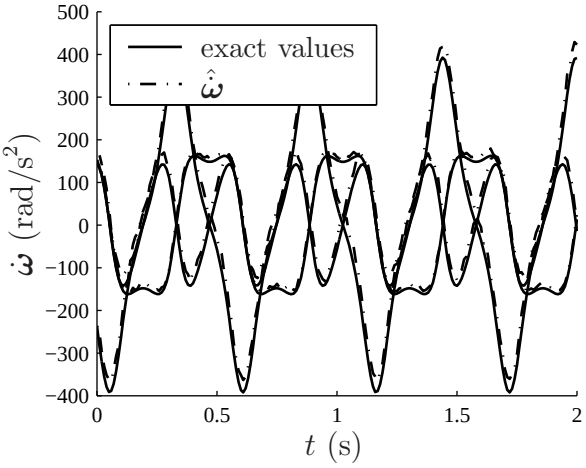

Figure 8.7: Angular acceleration estimates

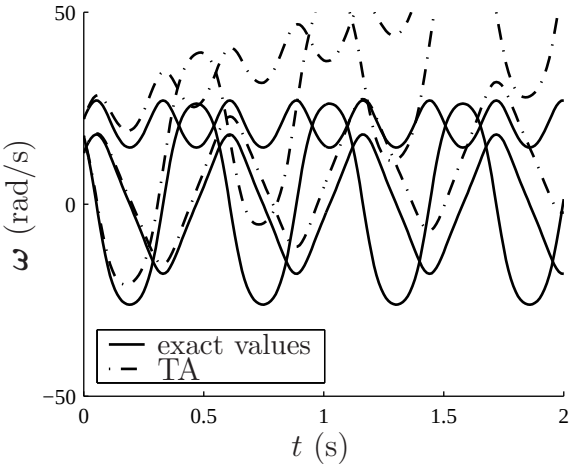

Figure 8.8: Angular velocity estimates from the existing TA method

The estimates obtained from the existing CA methods appear in Fig. 8.9. The CAD method exhibits discontinuities whenever one of the components approaches zero, and this, to the point that sign errors are introduced in the estimates. The same problem occurs with a higher amplitude in the CAOD method. Apparently, in this situation, the proposed CA methods are more robust than the existing ones, as can be seen from Figs. 8.10 and 8.15. Moreover, the CAPF, CANS, CAMA and CAAM methods behave well even when some of the components of the angular velocity vector are close to zero.

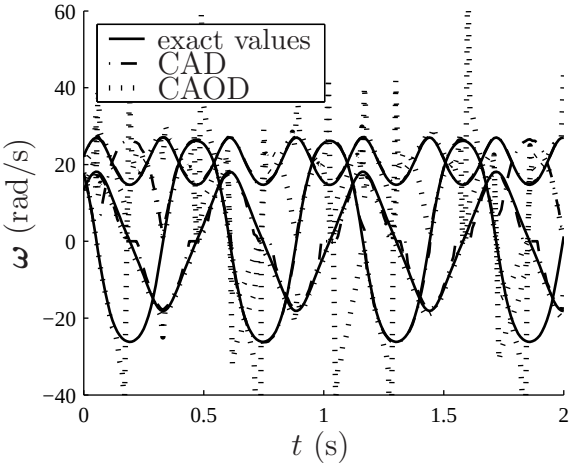

Figure 8.9: Angular velocity estimates from the existing CA methods

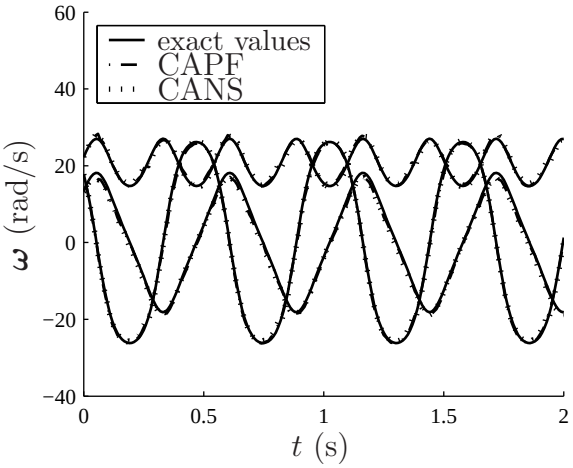

Figure 8.10: Angular velocity estimates from the proposed methods CAPF and CANS

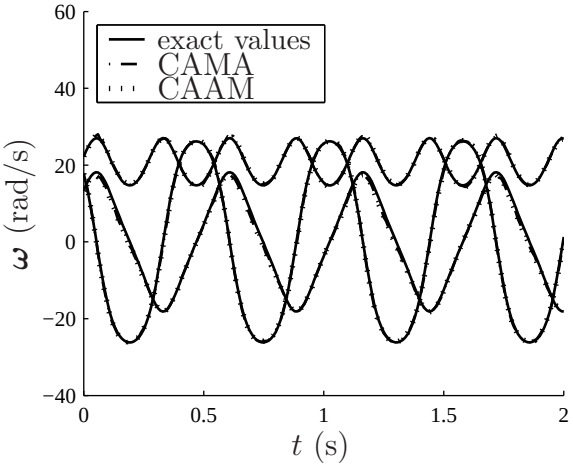

Figure 8.11: Angular velocity estimates from the proposed methods CAMA and CAAM

On the other hand, from Fig. 8.12, it is hard to discriminate the accuracy of the TCA methods from that of the proposed CA methods. One may notice, however, slight discontinuities in the TCAQ estimates. In order to better compare the proposed CA methods with the existing TCA methods, the errors on the angular velocity estimates are traced in Figs. 8.13, 8.14, 8.15, and 8.16. Due to the instability problems when a component approaches zero, the CAD and CAOD methods turn out to be much less accurate than the other ones.

Apparently, the CAPF, CANS, CAMA, CAAM, and TCAT methods are comparable, whereas the TCAQ method proves to be slightly less robust in this situation. In fact, from eq. (1.6), one may notice that this last method is close to being singular whenever one of the pairs of equations

$$2\omega_i = -\omega_j = -\omega_k, \quad i, j, k = 1, 2, 3, \quad i \neq j \neq k, \tag{8.33}$$

is approximately satisfied, as its associated discriminant approaches zero. Apparently, from Fig. 8.16, the recorded error peaks in the TCAQ estimates correspond to such situations.

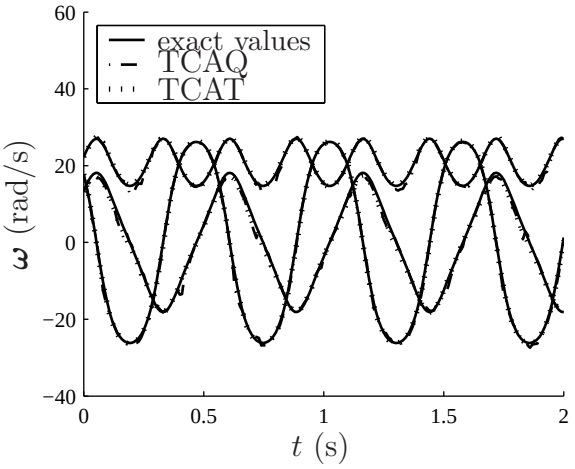

Figure 8.12: Angular velocity estimates from the existing TCA methods

In summary, we see that the errors on the centripetal acceleration estimates of the angular velocity are stable over time, unlike the errors on the tangential acceleration estimates. The Euclidean norms of the errors from the four most accurate methods in this simulation are displayed in Fig. 8.17. The performance of a method may be assessed by taking the rms-value of the magnitude of its associated error, i.e.,

$$\delta\omega_{rms} = \sqrt{\frac{1}{n}\sum_{i=1}^{n} \|\hat{\boldsymbol{\omega}}_i - \boldsymbol{\omega}_i\|_2^2}, \tag{8.34}$$

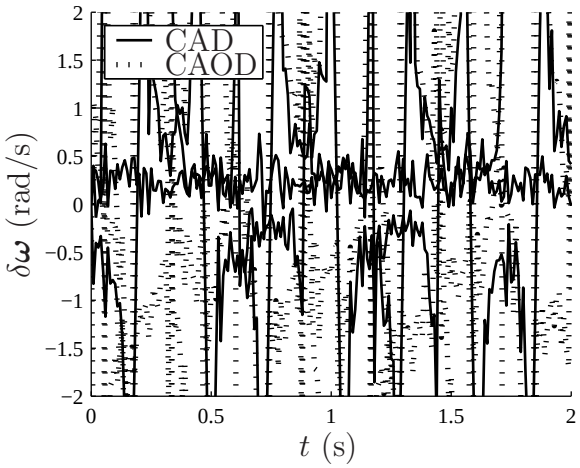

Figure 8.13: Errors on the angular velocity estimates

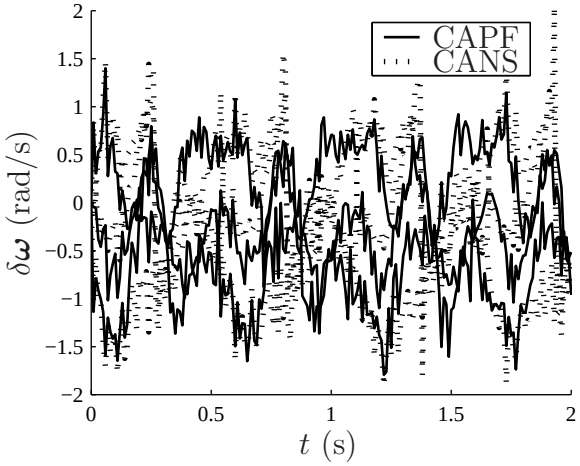

Figure 8.14: Errors on the angular velocity estimates

where $\boldsymbol{\omega}_i$ is the true angular velocity at the i^{th} measurement, $\hat{\boldsymbol{\omega}}_i$ is its estimate, and n is the number of samples considered. The rms-values resulting from the foregoing simulation are gathered in Table 8.1. Because of the unstable nature of the TA method, its drift rate is given instead of its error-norm rms-value.

Sign errors render the CAD and CAOD methods unreliable whenever one of the angular velocity components reaches zero, and, for that reason, their rms-values are significantly higher than those of the other methods. It may be possible to reduce these errors by resorting to TA or TCA methods in the time

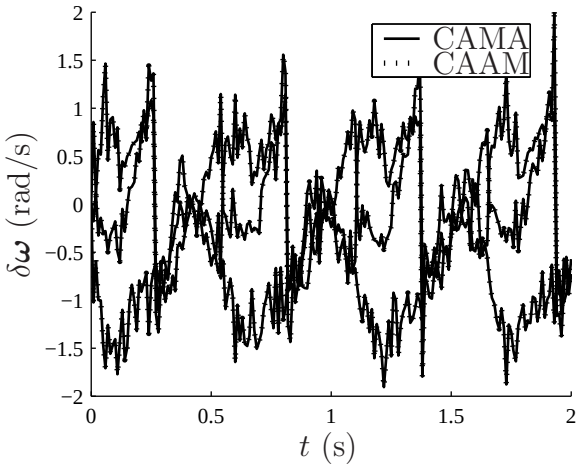

Figure 8.15: Errors on the angular velocity estimates

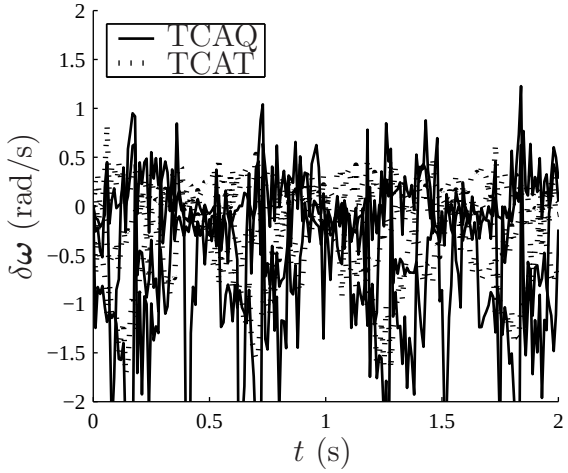

Figure 8.16: Errors on the angular velocity estimates

intervals over which the estimates are prone to instabilities. However, this option is hard to justify, since it requires the evaluation of such an interval, and even harder when seeing that other CA methods circumvent that problem—except, of course, when all the angular velocity components reach zero. We must state, however, that the CAD and CAOD methods are computationally less intensive than the proposed CA methods, as can be seen from Table 8.2.

On the other hand, it is hard to discriminate clearly the TCA methods and the proposed CA methods, as their performances are comparable in this

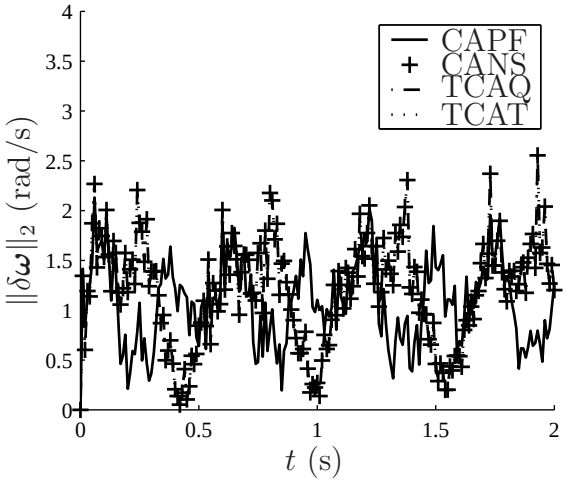

Figure 8.17: Norms of the errors on the angular velocity estimates

Table 8.1: Error comparison

method	$\delta\omega_{rms}$
TA	37.8 rad/s^2
CAD	27.2 rad/s
CAOD	37.4 rad/s
CAPF	1.16 rad/s
CANS	1.3 rad/s
CAMA	1.3 rad/s
CAAM	1.3 rad/s
TCAQ	1.44 rad/s
TCAT	0.844 rad/s

simulation. To the advantage of the proposed CA methods, we may recall that they do not make use of all the information available in the angular acceleration matrix in that they use only its skew-symmetric component to estimate the signs of the angular velocity estimates. Hence it is allowed to think that further recombination of the CAPF and the CANS estimates with the TA estimate may improve the robustness of these methods.

8.7 Simulation #2

In an attempt to assess which method is most accurate among the CA methods, the CAD, CAOD, CAPF, CANS, CAMA, and CAAM methods were used to compute angular-velocity estimates from fake angular acceleration

matrices $\hat{\mathbf{W}}_{i,j,k}$. As the subscript suggests, three parameters were varied in this simulation. Firstly, angular acceleration matrix estimates were generated according to the signal-to-noise ratios $\{\sigma_i\}_{i=1}^{m} = 10^{-1}, 10^{-0.9}, \ldots, 10^{2}$, where $m = 31$. The error component $\delta\mathbf{W}_{i,j,k}$ of $\hat{\mathbf{W}}_{i,j,k}$ was defined such that

$$\sigma_i = \|\mathbf{W}_j\|_2 / \|\delta\mathbf{W}_{i,j,k}\|_2, \tag{8.35}$$

where $\mathbf{W}_j$ is the true angular acceleration matrix, thus satisfying the relation $\hat{\mathbf{W}}_{i,j,k} = \delta\mathbf{W}_{i,j,k} + \mathbf{W}_j$. Notice that only the j index was kept for the true angular acceleration matrix, since this does not vary with the i and k indices. The entries of $\delta\mathbf{W}_{i,j,k}$ were generated orthogonally according to a zero-mean normal distribution. Secondly, the true angular velocities were chosen to have a constant Euclidean norm of 1 rad/s. In order to spread evenly their orientations on the unit sphere, the angular velocity vectors $\{\boldsymbol{\omega}_j\}_{j=1}^{n}$ were chosen to represent the coordinates of the vertices of two Platonic solids, the dodecahedron and the icosahedron. Moreover, these regular polyhedra were oriented and scaled so that one be the dual of the other, thus yielding a uniform distribution of their $n = 32$ vertices over the unit-sphere that circumscribes them. This is illustrated in Fig. 8.18, where each dot represents a vertex of one of the polyhedra, and the coordinate axes are those of frame $\mathcal{B}$ attached to the rigid body. In all CA methods, the estimates depend *weakly* on the angular acceleration through the TA estimate of the angular velocity. Therefore, to avoid overcomplicating the problem, we will assume the angular acceleration to be null and artificially add a random error $\delta\boldsymbol{\omega}_{TA,i,j,k}$ to the true angular velocity in order to obtain the TA estimates $\hat{\boldsymbol{\omega}}_{TA,i,j,k}$. This random error is chosen according to the same i^{th} signal-to-noise ratio, that is,

$$\sigma_i = \|\boldsymbol{\omega}_j\|_2 / \|\delta\boldsymbol{\omega}_{TA,i,j,k}\|_2 = 1/\|\delta\boldsymbol{\omega}_{A,i,j,k}\|_2. \tag{8.36}$$

As for $\delta\mathbf{W}_{i,j,k}$, the entries of $\delta\boldsymbol{\omega}_{TA,i,j,k}$ were generated according to identical independent normal distributions, and then normalized individually, so that each error had the right signal-to-noise ratio. Notice also that, since $\dot{\boldsymbol{\omega}}_{i,j,k} = \mathbf{0}_3$, $\forall\, i, j, k$, we have $\mathbf{W}_j = \mathrm{CPM}^2(\boldsymbol{\omega}_j)$ and, consequently, $\|\mathbf{W}_j\|_2 = \|\boldsymbol{\omega}_j\|_2^2 = 1$. Thirdly, subscript k is included because $p = 50$ pairs of angular-acceleration-matrix estimates and TA estimates were generated for each combination of the signal-to-noise ratio and the orientation of the angular velocity, for a total of $mnp = 49\,600$ angular-velocity estimates per method.

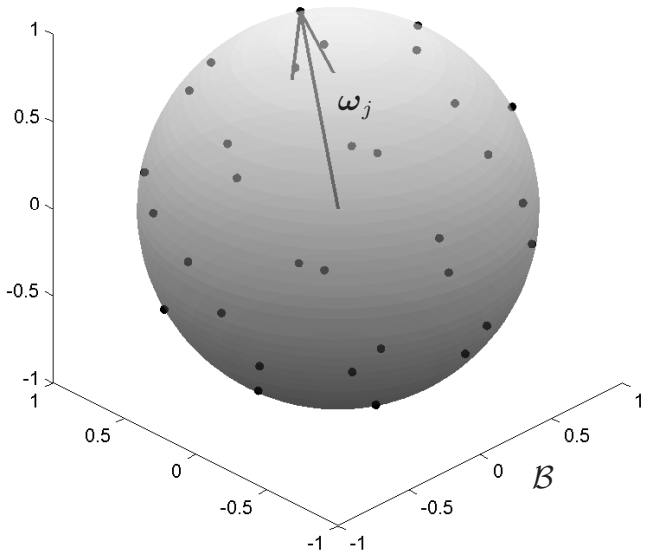

Figure 8.18: Simulated angular velocity vectors

The main results are displayed in Fig. 8.19, where the ordinate axis represents the rms values of the error amplification EA_{rms} obtained with the various estimation methods, while the abscissa axis is the signal-to-noise ratio of the inputs $\hat{\mathbf{W}}$ and $\hat{\boldsymbol{\omega}}_{TA}$. The error amplification is defined as the ratio of

the output signal-to-noise ratio to the input signal-to-noise ratio, that is,

$$EA_{i,j,k} \equiv \frac{\|\delta\boldsymbol{\omega}_{CA,i,j,k}\|_2\|\mathbf{W}_j\|_2}{\|\boldsymbol{\omega}_j\|_2\|\delta\mathbf{W}_{i,j,k}\|_2} = \frac{\|\delta\boldsymbol{\omega}_{CA,i,j,k}\|_2}{\|\delta\mathbf{W}_{i,j,k}\|_2} = \sigma_i\|\delta\boldsymbol{\omega}_{CA,i,j,k}\|_2. \tag{8.37}$$

The rms-value of the error amplification for a given method is thus obtained as

$$EA_{i,rms} = \sigma_i\sqrt{\frac{1}{np}\sum_{j=1}^{n}\sum_{k=1}^{p}\|\delta\boldsymbol{\omega}_{CA,i,j,k}\|_2^2}. \tag{8.38}$$

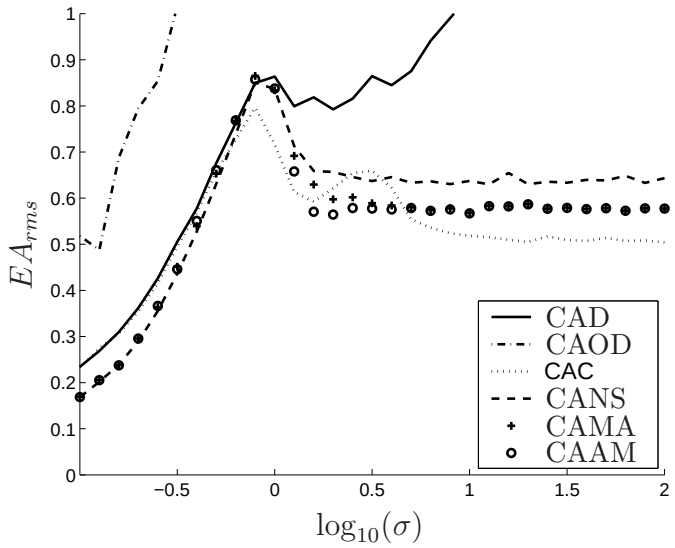

Figure 8.19: The error amplification vs. the input signal-to-noise ratios

Apparently, from Fig. 8.19, the CAOD and CAD methods are the least accurate: their error-amplification factors grow as the signal-to-noise ratio increases. This can be explained by the increased sensitivity to noise of these methods whenever any of the entries of $\hat{\mathbf{W}}$ approaches zero. On the other hand, the proposed CA methods exhibit behaviours that are fairly similar. Surprisingly, the CAPF method appears to be slightly more accurate than the other three for large signal-to-noise ratios. The CAMA and CAAM methods are very close to one another, whereas the CANS method seems somewhat less accurate. Notice that the range of smaller signal-to-noise ratios is attained whenever the magnitude of the angular velocity—the signal—approaches zero.

Therefore, it is noteworthy that the CAAM method is more robust than the others in the range $10^0 < \sigma < 10^{0.5}$.

The computational costs of the foregoing methods are unimportant when the objective is to reconstruct the trajectory of the head of a dummy off-line. However, when it comes to the control of a projectile or of a vibrating apparatus, this characteristic may determine the acquisition rate, and, hence, the performance of the controller. The computational costs associated with each method are displayed in Table 8.2.

Table 8.2: Computational cost of each method

method	flops	square-roots
TA	9	0
CAD	18	3
CAOD	21	3
CAPF	141	5
CANS	107	6
CAMA	60	2
CAAM	202	6

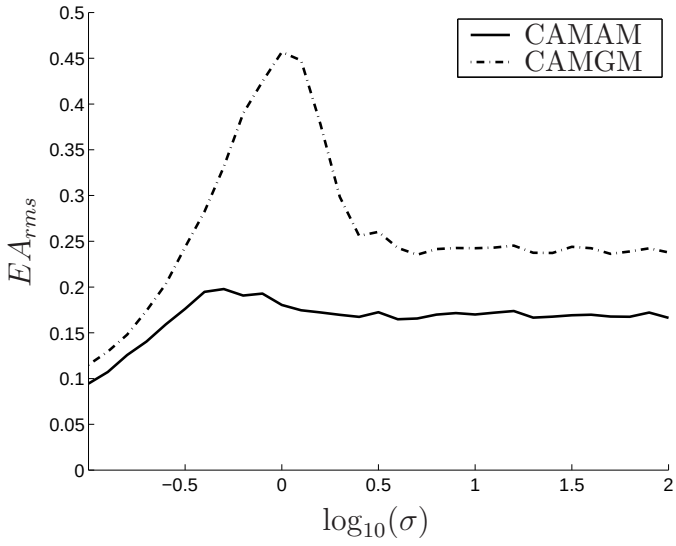

Figure 8.20: The error amplification of the magnitude estimates vs. the input signal-to-noise ratios

In Fig. 8.20 we compare the estimates of the magnitude of $\boldsymbol{\omega}$ obtained from the CAMAM and the CAMGM methods. In this case, the error amplifications of the magnitude were computed as

$$EA_{i,rms} = \sigma_i \sqrt{\frac{1}{np} \sum_{j=1}^{n} \sum_{k=1}^{p} (\|\boldsymbol{\omega}_{CA,i,j,k}\|_2 - \|\boldsymbol{\omega}_j\|_2)^2}, \tag{8.39}$$

$$= \sigma_i \sqrt{\frac{1}{np} \sum_{j=1}^{n} \sum_{k=1}^{p} (\|\boldsymbol{\omega}_{CA,i,j,k}\|_2 - 1)^2}. \tag{8.40}$$

Clearly, the CAMGM method is less accurate than the CAMAM method. Since the former is also computationally costlier, it should never be preferred to the latter. However, as CAMGM uses only the three diagonal entries of $\mathbf{W}$, there should be a way of combining the two methods so that noise and errors are better filtered.

Chapter 9

Angular-Velocity Estimation From Tangential- and Centripetal-Acceleration Measurements: The Planar Case

From the drawbacks of the TA and the CA methods, one may naturally intuite that an *informed* combination of the estimates of these two methods is more accurate than the estimate of any of the two alone. Such mergings have already been proposed in Subsection 1.4.3. Prospecting for a clearer understanding of the problem, let us shift the focus of this chapter on the simpler case of a rigid body moving in the plane. This calls for some adaptation of the TCAQ and TCAT methods, which were outlined in Subsection 1.4.3 for the spatial case. However, since the TCAQ method does not lend itself to a transposition in the plane, we will have to leave it aside in further comparisons. On the other hand, the TCAT method proposed by Parsa et al. (2005) accepts a planar-motion counterpart, as shown below.

We define function $\zeta(\omega) \equiv \omega^2$ and compute its series expansion around $\hat{\omega}_{\mathrm{TA}}$, which gives

$$\zeta(\omega) = \zeta(\hat{\omega}_{\mathrm{TA}}) + (\partial\zeta(\omega)/\partial\omega)\Delta\omega + O(2), \tag{9.1}$$

where $\Delta\omega$ is the difference between the TA estimate and the exact angular velocity ω, up to a second order approximation. We can readily compute $\partial\zeta(\omega)/\partial\omega = 2\omega$, which is to be approximated, according to Parsa et al. (2005), by its value at $\omega = \hat{\omega}_{\mathrm{TA}}$. Hence, we write

$$\Delta\omega = \frac{\zeta_{\mathrm{CA}} - \zeta(\hat{\omega}_{\mathrm{TA}})}{[\partial\zeta(\omega)/\partial\omega]_{\omega=\hat{\omega}_{\mathrm{TA}}}}, \tag{9.2}$$

where $\zeta_{\mathrm{CA}} \equiv \hat{\omega}^2_{\mathrm{CA}}$. Consequently, we obtain

$$\begin{aligned} \hat{\omega}_{\mathrm{TCAT}} &= \hat{\omega}_{\mathrm{TA}} + \Delta\omega, \\ &= \hat{\omega}_{\mathrm{TA}} + \frac{\zeta_{\mathrm{CA}} - \hat{\omega}^2_{\mathrm{TA}}}{2\hat{\omega}_{\mathrm{TA}}}, \\ &= \frac{1}{2}\hat{\omega}_{\mathrm{TA}} + \frac{1}{2}\frac{\zeta_{\mathrm{CA}}}{\hat{\omega}_{\mathrm{TA}}}. \end{aligned} \tag{9.3}$$

Apparently, this method is singular whenever $\hat{\omega}_{\mathrm{TA}} = 0$, which presages large errors whenever $\omega \to 0$. Notice also that the TCAT provides a weighted sum of the angular-acceleration measurement and the ratio of the centripetal-acceleration to the tangential-acceleration measurements, where the weights are constant at 1/2. Hence, there may still be room for improvement, since the TCAT method does not take into account the error propagation in its weighted sum.

For the sake of comparison, let us also introduce the planar-motion equivalents to the TA and CAD methods defined in eqs. (1.2a) and (1.3), respectively. We obtain simply

$$\hat{\omega}_{\mathrm{TA}}(t) = \int_0^t \hat{\dot{\omega}}(\tau)d\tau, \tag{9.4}$$

in the case of the TA method, whereas the CA method is not more elaborate:

$$\begin{aligned}
&\texttt{if } \hat{\zeta} > 0 \texttt{ and } \hat{\omega}_{\mathrm{TA}} \neq 0 \\
&\quad \hat{\omega}_{\mathrm{CA}} = \mathrm{sgn}(\hat{\omega}_{\mathrm{TA}})\mathrm{u}(\hat{\zeta})\sqrt{\hat{\zeta}}, \\
&\texttt{else} \\
&\quad \hat{\omega}_{\mathrm{CA}} = 0 \\
&\texttt{end}.
\end{aligned} \tag{9.5}$$

The aim of this chapter is to provide an estimation method that combines the TA and CA estimates while taking into account their associated error levels. The accuracy of the proposed method is then compared with that of the existing TA, CA, and TCAT methods and of typical MEMS gyroscope measurements. As we are to use Kalman filtering in order to combine the estimates, we need: to model the error as white noise; write the estimation problem in the form of a state-space system; and then write explicitly the equations of its associated Kalman filter. Finally, a simulation example is proposed in which all existing estimation methods are compared.

9.1 The Modelling of Acceleration Measurements

The output $\hat{a}_i(t)$ of the i^{th} accelerometer at time t is modelled as the sum of three mutually independent components, namely,

$$\hat{a}_i(t) = a_i(t) + \delta a_{b,i} + \delta a_{n,i}(t), \tag{9.6}$$

where a_i is the actual value, as defined in eq. (6.13), that is, the projection of the acceleration of P_i over the sensitive axis of the corresponding accelerometer, $\delta a_{b,i}$ is a bias error—hence, constant through time—and $\delta a_{n,i}$ is white noise. Moreover, the bias and noise errors are modelled as orthogonal random variables following Gaussian distributions with zero mean and variances σ_b^2

and σ_n^2, respectively, which may be expressed as

$$\begin{bmatrix} \delta a_{b,i} \\ \delta a_{n,i} \end{bmatrix} \sim \mathcal{N}\{ \begin{bmatrix} 0 \\ 0 \end{bmatrix}, \begin{bmatrix} \sigma_b^2 & 0 \\ 0 & \sigma_n^2 \end{bmatrix} \}. \tag{9.7}$$

Let us also assume that the errors from distinct accelerometers are independent, which implies

$$\mathrm{E}(\delta a_{b,i} \delta a_{b,j}) = \mathrm{E}(\delta a_{n,i} \delta a_{n,j}) = 0, \quad i \neq j, \tag{9.8}$$

where $\mathrm{E}(\,\cdot\,)$ denotes the expectation of $(\,\cdot\,)$.

We gather all accelerometer outputs and their components into the arrays

$$\begin{aligned} \hat{\mathbf{a}}' &\equiv [\hat{a}_1 \quad \hat{a}_2 \quad \cdots \quad \hat{a}_n]^T, \\ \mathbf{a}' &\equiv [a_1 \quad a_2 \quad \cdots \quad a_n]^T, \\ \delta \mathbf{a}'_{b,i} &\equiv [a_{b,1} \quad a_{b,2} \quad \cdots \quad a_{b,n}]^T \quad \text{and} \\ \delta \mathbf{a}'_{n,i} &\equiv [a_{n,1} \quad a_{n,2} \quad \cdots \quad a_{n,n}]^T, \end{aligned} \tag{9.9}$$

which allows us to rewrite eq. (9.6) as

$$\hat{\mathbf{a}}' = \mathbf{a}' + \delta \mathbf{a}'_b + \delta \mathbf{a}'_n. \tag{9.10}$$

9.2 Error Propagation to ζ and α

Upon assuming that the accelerometer-only IMU is *feasible*, i.e., that the accelerometer array matrix $\mathbf{A}'$ exists, we have, from eq. (6.24),

$$\mathbf{z}' = \mathbf{A}' \mathbf{a}'. \tag{9.11}$$

Let us define the estimator $\hat{\mathbf{z}}'$ of $\mathbf{z}'$ as

$$\hat{\mathbf{z}}' \equiv \mathbf{A}' \hat{\mathbf{a}}', \tag{9.12}$$

which is apparently not biased, that is,

$$\mathrm{E}(\hat{\mathbf{z}}') = \mathbf{A}'\mathrm{E}(\mathbf{a}' + \delta\mathbf{a}'_b + \delta\mathbf{a}'_n) = \mathbf{z}'. \tag{9.13}$$

Moreover, we can decompose $\hat{\mathbf{z}}'$ in the same way as $\mathbf{a}'$, namely,

$$\hat{\mathbf{z}}' \equiv \mathbf{z}' + \delta\mathbf{z}'_b + \delta\mathbf{z}'_n, \tag{9.14}$$

where $\mathbf{z}' \equiv \mathbf{A}'\mathbf{a}'$, $\delta\mathbf{z}'_b \equiv \mathbf{A}'\delta\mathbf{a}'_b$, and $\delta\mathbf{z}'_n \equiv \mathbf{A}'\delta\mathbf{a}'_n$. Consequently, the arrays of random variables are orthogonal, that is,

$$\begin{aligned}
\mathrm{E}\left(\begin{bmatrix}\delta\mathbf{z}'_b \\ \delta\mathbf{z}'_n\end{bmatrix}\begin{bmatrix}\delta\mathbf{z}'_b & \delta\mathbf{z}'_n\end{bmatrix}^T\right) &= \begin{bmatrix}\mathbf{A}'\mathrm{E}(\delta\mathbf{a}'_b\delta\mathbf{a}'^T_b)\mathbf{A}'^T & \mathbf{A}'\mathrm{E}(\delta\mathbf{a}'_b\delta\mathbf{a}'^T_n)\mathbf{A}'^T \\ \mathbf{A}'\mathrm{E}(\delta\mathbf{a}'_n\delta\mathbf{a}'^T_b)\mathbf{A}'^T & \mathbf{A}'\mathrm{E}(\delta\mathbf{a}'_n\delta\mathbf{a}'^T_n)\mathbf{A}'^T\end{bmatrix}, \\
&= \begin{bmatrix}\sigma_b^2\mathbf{A}'\mathbf{A}'^T & \mathbf{O}_{n\times n} \\ \mathbf{O}_{n\times n} & \sigma_n^2\mathbf{A}'\mathbf{A}'^T\end{bmatrix}, \\
&\equiv \begin{bmatrix}\boldsymbol{\Sigma}'^2_{z,b} & \mathbf{O}_{n\times n} \\ \mathbf{O}_{n\times n} & \boldsymbol{\Sigma}'^2_{z,n}\end{bmatrix},
\end{aligned} \tag{9.15}$$

where the second equality follows from the assumption that the sets of random variables $\{a_{b,i}\}_{i=1}^n$ and $\{a_{n,i}\}_{i=1}^n$ are both identically and independently distributed. Hence, $\delta\mathbf{z}'_b$ and $\delta\mathbf{z}'_n$ represent, respectively, the bias and noise errors on the estimate $\hat{\mathbf{z}}'$ of $\mathbf{z}'$. Moreover, the two arrays of errors follow Gaussian distributions with zero-mean and covariance matrices $\boldsymbol{\Sigma}'^2_{z,b}$ for the bias error, and $\boldsymbol{\Sigma}'^2_{z,n}$ for the noise error.

Since the focus of this chapter is the estimation of the angular velocity, we are only interested in the first two components of $\mathbf{z}'$, namely, $\mathbf{w}' \equiv [\zeta \quad \alpha]^T$. Hence, we define matrix $\mathbf{T}' \equiv [\mathbf{1}_{2\times 2} \quad \mathbf{O}_{2\times 2}]$. As a result, the estimate $\hat{\mathbf{w}}'$ of $\mathbf{w}'$ and its associated bias and noise errors are defined as $\hat{\mathbf{w}}' \equiv \mathbf{T}'\mathbf{A}'\hat{\mathbf{a}}'$, $\delta\mathbf{w}'_b \equiv \mathbf{T}'\mathbf{A}'\delta\mathbf{a}'_b$ and $\delta\mathbf{w}'_n \equiv \mathbf{T}'\mathbf{A}'\delta\mathbf{a}'_n$, respectively. Again, we see that the

errors on $\hat{\mathbf{w}}'$ follow a Gaussian distribution such that

$$\begin{bmatrix} \delta\mathbf{w}'_b \\ \delta\mathbf{w}'_n \end{bmatrix} = \mathcal{N}\{\mathbf{0}_4, \begin{bmatrix} \boldsymbol{\Sigma}'^2_{w,b} & \mathbf{O}_{2\times2} \\ \mathbf{O}_{2\times2} & \boldsymbol{\Sigma}'^2_{w,n} \end{bmatrix}\}, \tag{9.16}$$

where $\boldsymbol{\Sigma}'^2_{w,b} \equiv \sigma_b^2 \mathbf{T}'\mathbf{A}'\mathbf{A}'^T\mathbf{T}'^T$, and $\boldsymbol{\Sigma}'^2_{w,n} \equiv \sigma_n^2 \mathbf{T}'\mathbf{A}'\mathbf{A}'^T\mathbf{T}'^T$.

9.3 State-Space System

We use a method analogous to the ones used by Bélanger (1992) and Zarchan and Musoff (2000), who estimated the time rates of displacements (velocity and acceleration) from position measurements. In the present case, the accelerometer-only IMU provides us with estimates of the angular velocity squared ζ, and the angular acceleration α. We are to combine these estimates so as to minimize the variance of the error on the angular velocity estimate. Furthermore, according to the proposed model, the available estimates $\hat{\mathbf{w}}'$ are stained with bias errors that must be accounted for in the definition of the state variables. Hence, the state-space system

$$\dot{\mathbf{x}} = \mathbf{F}\mathbf{x} + \mathbf{G}\mathbf{u} \tag{9.17}$$

$$\mathbf{y} = \mathbf{h}(\mathbf{x}) + \mathbf{v}_n, \tag{9.18}$$

where $\mathbf{x} \equiv [\omega\alpha \quad \delta\mathbf{w}'^T_b]^T$, $\mathbf{u} \equiv [\gamma \quad \beta_\zeta \quad \beta_\alpha]^T$, $\mathbf{y} \equiv \hat{\mathbf{w}}'$, $\mathbf{v} \equiv \delta\mathbf{w}'_n$,

$$\mathbf{F} \equiv \begin{bmatrix} 0 & 1 & 0 & 0 \\ 0 & 0 & 0 & 0 \\ 0 & 0 & 0 & 0 \\ 0 & 0 & 0 & 0 \end{bmatrix}, \quad \mathbf{G} \equiv \begin{bmatrix} \mathbf{0}_3^T \\ \mathbf{1}_{3\times3} \end{bmatrix},$$

$\mathbf{h}(\mathbf{x}) \equiv [h_1(\mathbf{x}) \quad h_2(\mathbf{x})]^T$, $h_1(\mathbf{x}) \equiv \omega^2 + \delta\zeta_b$, and $h_2(\mathbf{x}) \equiv \alpha + \delta\alpha_b$. In words, the state-space equations (9.17) represent the relations below:

1. The time-rate of the angular velocity is the angular acceleration;

2. The time-rate of the angular acceleration, or angular jerk, is the system input γ;
3. The time-rate of the bias error $\delta\zeta_b$ is the system input β_ζ;
4. The time-rate of the bias error $\delta\alpha_b$ is the system input β_α.

Notice that, by definition, the time-rate of a bias error has to be null. However, in practice, sensor bias errors tend to drift with time, and, therefore, we add inputs β_ζ and β_α in order to take this problem into account. Furthermore, from eq. (9.18), we see that, unlike the state-space equations, the output equations are nonlinear. This is only natural, since the centripetal acceleration is proportional to the square of the rigid-body angular velocity. This peculiarity further complicates the problem, and commands the use of a nonlinear filtering method.

Notice also that an accelerometer-only IMU alone does not provide any direct measurement of the angular jerk and the bias error time-rates. Nevertheless, the designer of an IMU generally has an idea of the magnitudes of these quantities, and, for that reason, we model them as step functions with their k^{th} step covering the time interval bounded by t_k and t_{k+1}, $k = 0, 1, 2, \ldots$. The values of γ_k, $\beta_{\zeta,k}$, and $\beta_{\alpha,k}$ on the time interval $[t_k, t_{k+1}[$ are taken to be random constant values which follow a joint Gaussian distribution with zero-mean and covariance $\mathbf{\Sigma}_{\mathbf{u}}^2$, and which are independent from the other random

variables γ_j, $\beta_{\zeta,j}$, and $\beta_{\alpha,j}$, $j \neq k$. This is expressed symbolically as

$$\mathbf{u}(t) = \begin{cases} \mathbf{u}_0, & \text{for} \quad t_0 \leq t < t_1; \\ \mathbf{u}_1, & \text{for} \quad t_1 \leq t < t_2; \\ \vdots & \vdots \\ \mathbf{u}_k, & \text{for} \quad t_k \leq t < t_{k+1}; \\ \vdots & \vdots \end{cases}, \tag{9.19}$$

where $\mathbf{u}_k \sim \mathcal{N}\{\mathbf{0}_3, \mathbf{\Sigma}^2_{\mathbf{u}}\}$ are constant three-dimensional vectors that follow Gaussian distributions with zero mean and covariance matrix $\mathbf{\Sigma}^2_{\mathbf{u}}$. Now, the angular jerk and the time-rates of the bias errors will be taken to be independent, thereby implying a covariance matrix of the form

$$\mathbf{\Sigma}^2_{\mathbf{u}} = \begin{bmatrix} \sigma^2_\gamma & \mathbf{0}^T_2 \\ \mathbf{0}_2 & \mathbf{\Sigma}^2_\beta \end{bmatrix}, \tag{9.20}$$

where σ^2_γ is the variance of γ_k, and $\mathbf{\Sigma}^2_\beta$ is the covariance matrix of the array $[\beta_\zeta \quad \beta_\alpha]^T$. Under the assumption that, as $\mathbf{u}(t)$, the time-rates of the bias errors $\delta a_{b,i}$ on the accelerometer measurements follow step functions of the form of eq. (9.19), and that their step values follow mutually independent identical Gaussian distributions of zero-mean and variance σ^2_β, we obtain

$$\mathbf{\Sigma}^2_\beta = \sigma^2_\beta \mathbf{T}' \mathbf{A}' \mathbf{A}'^T \mathbf{T}'^T. \tag{9.21}$$

The proposed model is certainly quite far from the angular jerks and the bias error drifts seen in most applications. Nevertheless, this rough-looking approximation shall be justified by the accuracy of the resulting angular velocity estimates.

Turning now our attention towards the initial conditions $\mathbf{x}_0$, we first recall that, in accordance with the state-space system of eq. (9.17), $\delta\mathbf{w}_b'$ is to remain constant, and, therefore, is equal to its initial value. On the other hand, we assume that we have independent estimates of the initial angular velocity $\hat{\omega}_0$ and the initial angular acceleration $\hat{\alpha}_0$ that follow Gaussian distributions of means ω_0 and α_0, respectively, and variances $\sigma_{\omega,0}$ and $\sigma_{\alpha,0}$, respectively. Hence, from all the foregoing relations and assumptions, we may write the estimate $\hat{\mathbf{x}}_0$ of the initial state as

$$\hat{\mathbf{x}}_0 \equiv \begin{bmatrix} \hat{\omega}_0 \\ \hat{\alpha}_0 \\ \delta\hat{\zeta}_b \\ \delta\hat{\alpha}_b \end{bmatrix} \sim \mathcal{N}\{ \begin{bmatrix} \omega_0 \\ \alpha_0 \\ 0 \\ 0 \end{bmatrix}, \begin{bmatrix} \sigma_{\omega,0}^2 & 0 & \mathbf{0}_2^T \\ 0 & \sigma_{\alpha,0}^2 & \mathbf{0}_2^T \\ \mathbf{0}_2 & \mathbf{0}_2 & \mathbf{\Sigma}_{w,b}'^2 \end{bmatrix} \}. \tag{9.22}$$

9.4 Observability

At the outset, we discard the noise from this observability analysis, which leaves us with the simpler homogeneous state-space system

$$\begin{aligned} \dot{\mathbf{x}} &= \mathbf{F}\mathbf{x} \\ \mathbf{y} &= \mathbf{h}(\mathbf{x}). \end{aligned} \tag{9.23}$$

The *observation space* $\mathcal{O}$ of the state-space system described in eq. (9.23) is defined, according to Isidori (1989), as the smallest subspace of $C^\infty(\mathbb{R})$ containing functions $h_1(\mathbf{x})$ and $h_2(\mathbf{x})$, and which is closed under differentiation along $\mathbf{F}\mathbf{x}$. Let $\Omega_\mathcal{O}$ be the codistribution associated with the observation space, and $\Omega_\mathcal{O}(\mathbf{x})$ be the space spanned by this codistribution at state $\mathbf{x}$. Then, as shown by Isidori (1989), the state-space system is locally observable on the the set $\mathcal{X}$ if

$$\dim\{\Omega_\mathcal{O}(\mathbf{x})\} = 4, \quad \forall \mathbf{x} \in \mathcal{X}, \tag{9.24}$$

where $\dim\{\cdot\}$ denotes the dimension of the space $\cdot$.

In order to evaluate the observation space, we resort to the recursive algorithm proposed by Isidori (1989). Accordingly, we first define the codistribution Ω_0 spanned by the covector fields $\boldsymbol{\omega}_1 \equiv \partial h_1/\partial \mathbf{x}$ and $\boldsymbol{\omega}_2 \equiv \partial h_2/\partial \mathbf{x}$, which gives

$$\begin{aligned} \Omega_0 &\equiv \operatorname{span}\{\boldsymbol{\omega}_1, \boldsymbol{\omega}_2\} \\ &= \operatorname{span}\{\begin{bmatrix} 2\omega & 0 & 1 & 0 \end{bmatrix}^T, \begin{bmatrix} 0 & 1 & 0 & 1 \end{bmatrix}^T\}. \end{aligned} \tag{9.25}$$

Starting from this codistribution, we compute the sequence of codistributions

$$\Omega_k = \Omega_{k-1} + \sum_{\boldsymbol{\omega}_i \in \Omega_{k-1}} \operatorname{span}\{L_{\mathbf{Fx}} \boldsymbol{\omega}_i\}, \tag{9.26}$$

which is bound to converge to the smallest codistribution containing $\Omega_{\mathcal{O}}$ and which is invariant under the vector field $\mathbf{Fx}$. The linear operator $L_{\mathbf{f}}(\,\cdot\,)$ is the Lie derivative of the covector field $(\,\cdot\,) \in \mathbb{R}^n$ along the vector field $\mathbf{f}(\mathbf{x}) \in \mathbb{R}^n$, that is,

$$L_{\mathbf{f}} \boldsymbol{\omega} \equiv \frac{\partial \boldsymbol{\omega}}{\partial \mathbf{x}} \mathbf{f} + \left(\frac{\partial \mathbf{f}}{\partial \mathbf{x}} \right)^T \boldsymbol{\omega}. \tag{9.27}$$

Hence,

$$\begin{aligned} L_{\mathbf{Fx}} \boldsymbol{\omega}_1 &= \begin{bmatrix} 2 & 0 & 0 & 0 \\ 0 & 0 & 0 & 0 \\ 0 & 0 & 0 & 0 \\ 0 & 0 & 0 & 0 \end{bmatrix} \begin{bmatrix} \alpha \\ 0 \\ 0 \\ 0 \end{bmatrix} + \begin{bmatrix} 0 & 0 & 0 & 0 \\ 1 & 0 & 0 & 0 \\ 0 & 0 & 0 & 0 \\ 0 & 0 & 0 & 0 \end{bmatrix} \begin{bmatrix} 2\omega \\ 0 \\ 1 \\ 0 \end{bmatrix} \\ &= \begin{bmatrix} 2\alpha & 2\omega & 0 & 0 \end{bmatrix}^T \equiv \boldsymbol{\omega}_3, \quad \text{and} \quad L_{\mathbf{Fx}} \boldsymbol{\omega}_2 = \mathbf{0}_4, \end{aligned} \tag{9.28}$$

which leads to

$$\Omega_1 = \operatorname{span}\{\boldsymbol{\omega}_1, \boldsymbol{\omega}_2, \boldsymbol{\omega}_3\}. \tag{9.29}$$

The second step is

$$L_{\mathbf{Fx}}\boldsymbol{\omega}_3 = \begin{bmatrix} 0 & 4\alpha & 0 & 0 \end{bmatrix}^T \equiv \boldsymbol{\omega}_4, \tag{9.30}$$

thus yielding the codistribution

$$\Omega_2 = \text{span}\{\boldsymbol{\omega}_1, \boldsymbol{\omega}_2, \boldsymbol{\omega}_3, \boldsymbol{\omega}_4\}. \tag{9.31}$$

As it turns out, $L_{\mathbf{Fx}}\boldsymbol{\omega}_4 = \mathbf{0}_4$, and $\Omega_3 = \Omega_2$, which completes the calculation of the observation space

$$\Omega_{\mathcal{O}} = \text{span}\{\boldsymbol{\omega}_1, \boldsymbol{\omega}_2, \boldsymbol{\omega}_3, \boldsymbol{\omega}_4\}. \tag{9.32}$$

Moreover,

$$\det\left(\begin{bmatrix} \boldsymbol{\omega}_1 & \boldsymbol{\omega}_2 & \boldsymbol{\omega}_3 & \boldsymbol{\omega}_4 \end{bmatrix}\right) = 8\alpha^2, \tag{9.33}$$

which shows that the codistribution has a dimension of 4 whenever $\alpha \neq 0$. Hence, we can conclude that the system is locally observable for all states in $\mathbb{R}^4$, but those pertaining to the hyperplane $\alpha = 0$.

9.5 Extended Kalman Filter

In this Section, the estimates coming from the TA and the CA methods are combined through the application of an extended Kalman filter to the linear system of eq. (9.17). This estimation method will be referred to as the TCAEKF method. Notice that, in the developments below, it is assumed that the orders of magnitude of the rigid-body angular jerks, the bias errors, and the noise errors are known. For starters, let us compute the state-transition matrix between the times t_k and $t_{k+1} > t_k$, which yields

$$\boldsymbol{\Phi}(t_k, t_{k+1}) = e^{\mathbf{F}(t_{k+1}-t_k)} = \mathbf{1}_{4\times 4} + \mathbf{F}(t_{k+1} - t_k), \tag{9.34}$$

where the last equality is obtained upon noticing that $\mathbf{F}$ is nilpotent with index 2. Furthermore, if we assume that $t_{k+1} - t_k = \tau$, $\forall k = 0, 1, \ldots$, i.e., that two

consecutive samples are separated by a constant time period τ, we may write

$$\mathbf{\Phi}(t_k, t_k + \tau) = \mathbf{1}_{4\times 4} + \mathbf{F}\tau \equiv \mathbf{\Phi}. \tag{9.35}$$

Hence, the system state at time t_{k+1} is

$$\begin{aligned}
\mathbf{x}_{k+1} \equiv \mathbf{x}(t_{k+1}) &= \mathbf{\Phi}\mathbf{x}_k + \int_{t_k}^{t_{k+1}} \mathbf{\Phi}(v, t_{k+1})\mathbf{G}\mathbf{u}(v)dv \\
&= \mathbf{\Phi}\mathbf{x}_k + \left(\int_{t_k}^{t_{k+1}} (\mathbf{G} + \mathbf{F}\mathbf{G}(t_{k+1} - v))dv\right)\mathbf{u}_k \\
&= \mathbf{\Phi}\mathbf{x}_k - \left(\int_{\tau}^{0} (\mathbf{G} + \mathbf{F}\mathbf{G}w)dw\right)\mathbf{u}_k \\
&= \mathbf{\Phi}\mathbf{x}_k + \mathbf{\Upsilon}\mathbf{u}_k,
\end{aligned} \tag{9.36}$$

where $\mathbf{\Upsilon} \equiv \mathbf{G}\tau + (1/2)\mathbf{F}\mathbf{G}\tau^2$. On the other hand, the discrete-time output equation is identical to the continuous-time counterpart of eq. (9.17), that is,

$$\mathbf{y}_k \equiv \mathbf{y}(t_k) = \mathbf{h}(\mathbf{x}_k) + \mathbf{v}_k, \tag{9.37}$$

where $\mathbf{v}_k \equiv \delta\mathbf{w}'_n(t_k)$. Application of the extended Kalman filter also requires that the jacobian matrix $\mathbf{H}$ of $\mathbf{h}$ be computed, which gives

$$\mathbf{H}(\mathbf{x}) \equiv \frac{\partial \mathbf{h}(\mathbf{x})}{\partial \mathbf{x}} = \begin{bmatrix} 2\omega & 0 & 1 & 0 \\ 0 & 1 & 0 & 1 \end{bmatrix}. \tag{9.38}$$

These definitions allow the calculation of $\hat{\mathbf{x}}_k^-$, the *a priori* state estimate at time t_k, from $\hat{\mathbf{x}}_{k-1}^+$, the *a posteriori* state estimate at time t_{k-1}, which yields

$$\hat{\mathbf{x}}_k^- = \mathbf{\Phi}\hat{\mathbf{x}}_{k-1}^+. \tag{9.39}$$

The covariance $\mathbf{V}_k^-$ of the error on the a priori state estimate $\hat{\mathbf{x}}_k^-$ is computed from the covariance of the a posteriori state estimate error $\mathbf{V}_{k-1}^+$, i.e.,

$$\mathbf{V}_k^- = \mathbf{\Phi}\mathbf{V}_{k-1}^+\mathbf{\Phi}^T + \mathbf{\Upsilon}\mathbf{\Sigma}_{\mathbf{u}}^2\mathbf{\Upsilon}^T. \tag{9.40}$$

We obtain then an a posteriori estimate at time t_k by correcting the a priori estimate, which gives, symbolically,

$$\hat{\mathbf{x}}_k^+ = \hat{\mathbf{x}}_k^- + \mathbf{K}_k(\mathbf{y}_k - \mathbf{h}(\hat{\mathbf{x}}_k^-)), \tag{9.41}$$

where the Kalman gain is estimated from a first-order approximation of the effect of the angular jerk on the covariance of the measurements $\mathbf{y}_k$, i.e.,

$$\mathbf{K}_k \approx \mathbf{V}_k^- \mathbf{H}(\hat{\mathbf{x}}_k^-)^T \left(\mathbf{H}(\hat{\mathbf{x}}_k^-)\mathbf{V}_k^- \mathbf{H}(\hat{\mathbf{x}}_k^-)^T + \mathbf{\Sigma}_{w,n}'^2\right)^{-1}. \tag{9.42}$$

Similarly, the covariance of the error on the a posteriori estimate is estimated through the first-order approximation

$$\mathbf{V}_k^+ \approx \left[\mathbf{1}_{4\times 4} - \mathbf{K}_k \mathbf{H}(\hat{\mathbf{x}}_k^-)\right] \mathbf{V}_k^-. \tag{9.43}$$

Hence, at time t_k, the angular-velocity estimate produced by the TCAEKF method is

$$\hat{\omega}_{\text{TCAEKF}}(t_k) = \begin{bmatrix} 1 & 0 & 0 & 0 \end{bmatrix} \hat{\mathbf{x}}_k^+. \tag{9.44}$$

9.6 The Analogous Kalman Filter for Gyroscope Measurements

For comparison purposes, let us define the counterpart of the TCAEKF method, which uses only angular-velocity measurements in its output equations. In order to remain consistent with the acronyms proposed for the accelerometer-only methods, we label GKF this Kalman filtering method applied to gyroscope readouts. The gyroscope signals $\hat{\omega}^*$ are modelled in the same fashion as the accelerometer signals, that is,

$$\hat{\omega}^* = \omega + \delta\omega_b^* + \delta\omega_n^*, \tag{9.45}$$

where $\delta\omega_b^*$ and $\delta\omega_n^*$ are random bias and noise errors, respectively, with associated distributions

$$\begin{bmatrix} \delta\omega_b^* \\ \delta\omega_n^* \end{bmatrix} \sim \mathcal{N}\{ \begin{bmatrix} 0 \\ 0 \end{bmatrix}, \begin{bmatrix} {\sigma_b^*}^2 & 0 \\ 0 & {\sigma_n^*}^2 \end{bmatrix} \}. \tag{9.46}$$

9.6.1 State-Space System

The Kalman filter analogous to the one proposed in Section 9.5 is applied to the gyroscope signals, thereby ending up with the system:

$$\begin{aligned} \dot{\mathbf{x}}^* &= \mathbf{F}^*\mathbf{x}^* + \mathbf{G}^*\mathbf{u}^*, \\ y^* &= {\mathbf{h}^*}^T\mathbf{x}^* + \delta\omega_n^*, \end{aligned} \tag{9.47}$$

where $\mathbf{x}^* \equiv [\omega \quad \alpha \quad \delta\omega_b^*]^T$, $\mathbf{u}^* \equiv [\gamma \quad \beta_\omega]^T$, β_ω is the time-rate of the bias error $\delta\omega_b^*$,

$$\mathbf{F}^* \equiv \begin{bmatrix} 0 & 1 & 0 \\ 0 & 0 & 0 \\ 0 & 0 & 0 \end{bmatrix}, \quad \mathbf{G}^* \equiv \begin{bmatrix} \mathbf{0}_2^T \\ \mathbf{1}_{2\times 2} \end{bmatrix}, \text{ and } \mathbf{h}^* \equiv \begin{bmatrix} 1 \\ 0 \\ 1 \end{bmatrix}.$$

The input is modelled as a step function which may be represented symbolically by substituting $\mathbf{u}$ for $\mathbf{u}^*$ in eq. (9.19). This results in step values $\mathbf{u}_k^*$ following normal distributions

$$\mathbf{u}_k^* \sim \mathcal{N}\{\mathbf{0}_2, {\mathbf{\Sigma}_\mathbf{u}^*}^2\}, \text{ where } {\mathbf{\Sigma}_\mathbf{u}^*}^2 = \begin{bmatrix} \sigma_\gamma^2 & 0 \\ 0 & {\sigma_\beta^*}^2 \end{bmatrix}, \tag{9.48}$$

and ${\sigma_\beta^*}^2$ is the variance of the step values of β_ω.

9.6.2 Observability

The observation space $\Omega^*_{\mathcal{O}}$ of this linear state-space system is

$$\Omega^*_{\mathcal{O}} = \ker\{ \begin{bmatrix} \mathbf{h}^{*T} \\ \mathbf{h}^{*T}\mathbf{F}^* \\ \mathbf{h}^{*T}\mathbf{F}^{*2} \end{bmatrix} \}^{\perp} = \ker\{ \begin{bmatrix} 1 & 0 & 1 \\ 0 & 1 & 0 \\ 0 & 0 & 0 \end{bmatrix} \}^{\perp} = \text{span}\{ \begin{bmatrix} 1 \\ 0 \\ 1 \end{bmatrix}, \begin{bmatrix} 0 \\ 1 \\ 0 \end{bmatrix} \}, \tag{9.49}$$

where $(\,\cdot\,)^{\perp}$ denotes the orthogonal complement of subspace $(\,\cdot\,)$, and $\ker\{\,\cdot\,\}$ returns the nullspace of matrix $(\,\cdot\,)$. Equation (9.49) leads to the conclusion, that, unlike the TCAEKF method, the angular velocity alone is not observable; only its sum with the gyroscope bias error is.

9.6.3 Kalman Filter

The corresponding discrete-time system is

$$\begin{aligned} \mathbf{x}^*_{k+1} &= \mathbf{\Phi}^*\mathbf{x}^*_k + \mathbf{\Upsilon}^*\mathbf{u}^*_k, \\ y^*_k &= \mathbf{h}^{*T}\mathbf{x}^*_k + \delta\omega^*_{n,k}, \end{aligned} \tag{9.50}$$

where $\mathbf{x}^*_k \equiv \mathbf{x}^*(t_k)$, $y^*_k \equiv y^*(t_k)$, $\mathbf{\Phi}^* = \mathbf{1}_{3\times3} + \mathbf{F}^*\tau$ and $\mathbf{\Upsilon}^* \equiv \mathbf{G}^*\tau + (1/2)\mathbf{F}^*\mathbf{G}^*\tau^2$. The associated Kalman filter is described below:

$$\hat{\mathbf{x}}^{*-}_k = \mathbf{\Phi}^*\hat{\mathbf{x}}^{*+}_{k-1}, \tag{9.51}$$

$$\mathbf{V}^{*-}_k = \mathbf{\Phi}^*\mathbf{V}^{*+}_{k-1}\mathbf{\Phi}^{*T} + \mathbf{\Upsilon}^*\mathbf{\Sigma}^{*2}_{\mathbf{u}}\mathbf{\Upsilon}^{*T}, \tag{9.52}$$

$$\hat{\mathbf{x}}^{*+}_k = \hat{\mathbf{x}}^{*-}_k + \mathbf{k}^*_k(y^*_k - \mathbf{h}^{*T}\hat{\mathbf{x}}^{*-}_k), \tag{9.53}$$

$$\mathbf{k}^*_k = \mathbf{V}^{*-}_k\mathbf{h}^* \left(\mathbf{h}^{*T}\mathbf{V}^{*-}_k\mathbf{h}^* + \sigma^{*2}_n\right)^{-1}. \tag{9.54}$$

$$\mathbf{V}^{*+}_k = \left(\mathbf{1}_{3\times3} - \mathbf{k}^*_k\mathbf{h}^{*T}\right)\mathbf{V}^{*-}_k, \tag{9.55}$$

where $\hat{\mathbf{x}}^{*-}_k$ and $\mathbf{V}^{*-}_k$ are the a priori estimate of $\mathbf{x}^*_k$ and the covariance of its error, respectively; $\hat{\mathbf{x}}^{*+}_k$ and $\mathbf{V}^{*+}_k$ are the a-posteriori estimate of $\mathbf{x}^*_k$ and the variance of its error, respectively; and $\mathbf{k}^*_k$ is the Kalman gain at time t_k.

Therefore, the angular velocity estimate provided by the GKF method is given by

$$\hat{\omega}_{\mathrm{GKF}}(t_k) = \boldsymbol{\epsilon}_1^T \hat{\mathbf{x}}_k^{*+}, \quad \boldsymbol{\epsilon}_1 \equiv \begin{bmatrix} 1 & 0 & 0 \end{bmatrix}^T. \tag{9.56}$$

9.7 Example: Estimating the Angular Velocity of a Camera Mounted on a Vehicle

One of the contemplated applications for accelerometer-only IMUs is the stabilization of a camera submitted to parasitic vibrations. An instance of this problem occurs when the camera is mounted on a vehicle rolling on an uneven terrain. An example of such a system is depicted in Fig. 9.1, where it is seen that four accelerometers are rigidly attached to the camera. We assume that the vehicle heading velocity is constant, i.e., that all accelerations take place in the XY plane. For comparison purposes, we also add a gyroscope to the assembly, which provides a direct estimate of the angular velocity of the camera in the XY plane.

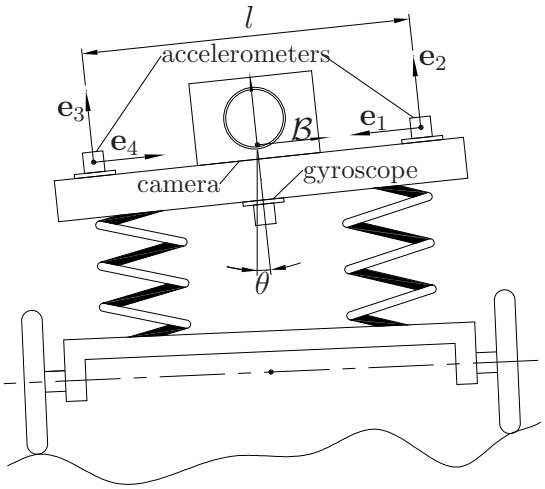

Figure 9.1: A camera equipped with an accelerometer-only IMU and a gyroscope mounted on a vehicle.

9.7.1 Trajectory

We assume that the camera–accelerometer–gyroscope assembly suspended by two vertical springs undergoes a harmonic angular oscillation, i.e.,

$$\theta(t) = \theta^\star \cos(2\pi f^\star t), \tag{9.57}$$

where $\theta^\star$ is the oscillation amplitude and $f^\star$ its frequency. In turn, the angular velocity, angular acceleration and angular jerk become, respectively,

$$\begin{aligned} \omega(t) &= -2\pi f^\star \theta^\star \sin(2\pi f^\star t), \\ \alpha(t) &= -4(\pi f^\star)^2 \theta^\star \cos(2\pi f^\star t) \quad \text{and} \\ \gamma(t) &= 8(\pi f^\star)^3 \theta^\star \sin(2\pi f^\star t). \end{aligned} \tag{9.58}$$

Yet, the proposed model requires that $\gamma(t)$ be a function of the random variables γ_k, $k = 1, 2, \ldots$, as defined in eq. (9.19). Hence, we approximate the imposed angular jerk by choosing its root-mean square value to be the variance of γ_k, i.e.,

$$\begin{aligned} \sigma_\gamma^2 &= \lim_{t\to\infty} \left(\frac{1}{t} \int_0^t \gamma(u)^2 du \right), \\ &= f^\star \int_0^{1/f^\star} \gamma(u)^2 du, \\ &= 64\pi^6 (f^\star)^7 (\theta^\star)^2 \int_0^{1/f^\star} \sin^2(2\pi f^\star u) du, \\ &= 32\pi^6 (f^\star)^6 (\theta^\star)^2. \end{aligned} \tag{9.59}$$

9.7.2 Accelerometer-Only IMU

All vector quantities are expressed in the frame $\mathcal{B}$ attached to the camera-accelerometers-gyroscope assembly, which gives

$$\mathbf{e}_1' = \begin{bmatrix} -1 \\ \\ 0 \end{bmatrix}, \quad \mathbf{e}_2' = \mathbf{e}_3' = \begin{bmatrix} 0 \\ \\ 1 \end{bmatrix}, \quad \mathbf{e}_4' = \begin{bmatrix} 1 \\ \\ 0 \end{bmatrix}, \tag{9.60}$$

as well as

$$\mathbf{r}'_1 = \mathbf{r}'_2 = \begin{bmatrix} l/2 \\ 0 \end{bmatrix} \text{ and } \mathbf{r}'_3 = \mathbf{r}'_4 = \begin{bmatrix} -l/2 \\ 0 \end{bmatrix}. \tag{9.61}$$

Accordingly, the accelerometer-array matrix becomes

$$\mathbf{A}' = \begin{bmatrix} 1/l & 0 & 0 & 1/l \\ 0 & 1/l & -1/l & 0 \\ -1/2 & 0 & 0 & 1/2 \\ 0 & 1/2 & 1/2 & 0 \end{bmatrix}. \tag{9.62}$$

This allows the calculation of the covariances of the bias and noise errors on the output $\mathbf{y}$, which yields

$$\mathbf{\Sigma}^2_{w,b} = (2\sigma_b^2/l^2)\mathbf{1}_{2\times 2} \text{ and } \mathbf{\Sigma}^2_{w,n} = (2\sigma_n^2/l^2)\mathbf{1}_{2\times 2}. \tag{9.63}$$

9.7.3 Comparison of the TCAEKF and the GKF Methods

The aim of this first example is to provide a clean comparison between the TCAEKF and the GKF estimates. Therefore, for both sensors, it is assumed that the distributions of the random errors are known accurately, which allows, in both cases, the design of the optimum filters.

Numerical Values

The numerical values of the simulation parameters are gathered in Table 9.1. The simulation is to last $t_f = 1$ s, which is enough to let the system stabilize. The harmonic motion generated by this choice of parameters produces a maximum angular velocity of 5.483 rad/s (314.2°/s) and maximum measured point accelerations of 44.11 m/s^2 (4.498 g). On the other hand, the standard deviations σ_b and σ_n were taken from the data sheets of the ADXL320 accelerometerAnalog Devices (2004a), whereas the standard deviations σ_b^* and σ_n^* come from the data sheets of the ADXRS300 gyroscopeAnalog Devices (2004b). These sensors are both manufactured by *Analog Devices*,

Table 9.1: Numerical values of the simulation parameters

parameter	value
l	0.4 m
τ	0.001 s
t_f	1 s
$\theta^\star$	10°
$f^\star$	5 Hz
σ_γ	3827 rad/s^3
σ_b	0.9807 m/s^2
σ_n	0.005482 m/s^2
σ_β	0 m/s^3
σ_b^*	0.01571 rad/s
σ_n^*	0.003903 rad/s
σ_β^*	0 rad/s^2
$\sigma_{\omega,0}$	0.1097 rad/s
$\sigma_{\alpha,0}$	3.445 rad/s^2

of Norwood, MA, USA, and their respective measurement ranges are $\pm 5g$ and $\pm 300^\circ/\text{s} = 5.24$ rad/s. Notice that, even though the measurement range of the gyroscope is somewhat too small for the simulated angular velocities, we still choose this model for comparison purposes, because it allows us to avoid comparing the accelerometers with a gyroscope possessing a much larger range than the one required. It is also worth noting that the bandwidths of the two chosen sensors are much larger than the minimum required to encompass the oscillation frequency $f^\star = 5$ Hz.

The standard deviation σ_γ was computed from eq. (9.59) and with the given values of $\theta^\star$ and $f^\star$. Since the simulation time is relatively short, we keep the bias errors constant throughout the simulation, and consequently, we set $\sigma_\beta = 0$ m/s^{3}and $\sigma_\beta^* = 0$ rad/s^2. The errors are generated with the *Matlab* pseudo-random number generator, which gives, for the accelerometer bias errors,

$$\delta \mathbf{a}_b' = [0.1746 \quad -1.106 \quad 1.435 \quad 0.031\ ]^T \text{ m/s}^2. \tag{9.64}$$

In the case of the gyroscope, since there is only one bias error, we choose the standard deviation to be its value, that is,

$$\delta\omega_b^* = \sigma_b. \tag{9.65}$$

We do the same for the estimates of the initial states $\hat{\omega}_0$ and $\hat{\alpha}_0$, i.e., we choose arbitrarily

$$\hat{\omega}_0 = \omega_0 + \sigma_{\omega,0}, \quad \text{and} \quad \hat{\alpha}_0 = \alpha_0 - \sigma_{\alpha,0}. \tag{9.66}$$

Notice that the numerical values of $\sigma_{\omega,0}$ and $\sigma_{\alpha,0}$ were selected to be both 2% of the maximum angular velocity and angular acceleration, respectively.

Results

The simulated accelerometer signals are plotted in Fig. 9.2 along with their exact values. Apparently, two of the four acceleremeters are submitted to smaller maximum accelerations. In fact, these two accelerometers are those that measure centripetal accelerations, whereas the two others measure the gravitational and the tangential accelerations. This observation suggests that we use accelerometers with smaller ranges to measure the accelerations in the directions $\mathbf{e}_1$ and $\mathbf{e}_3$, which would allow a better accuracy of the estimate of the centripetal acceleration. Nevertheless, for the sake of simplicity, we choose to use the same accelerometer specifications for all accelerometers, namely, those of the ADXL320.

The angular velocity estimates obtained using methods TA, CA, TCAT, TCAEKF, and GKF are plotted in Fig. 9.3 along with the exact values of the angular velocity. One can readily see that the TA-method estimates drift constantly through time, and this, at such a pace that they become completely useless after only a few cycles. Also, the CA and TCAT methods, as defined in

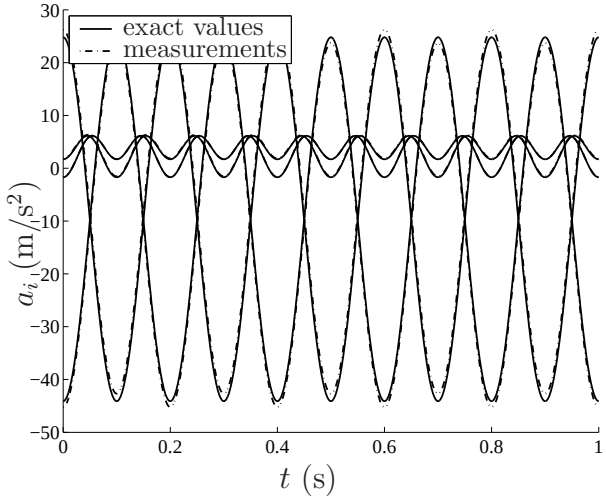

Figure 9.2: Accelerometer output signals

eqs. (9.5) and (9.3), are superimposed and, apparently, experience sign problems whenever the angular velocity goes to zero. The other estimates overlap one another, which renders their comparison difficult from Fig. 9.3 alone. We thus plot, in Fig. 9.4, the errors of the estimates obtained through the

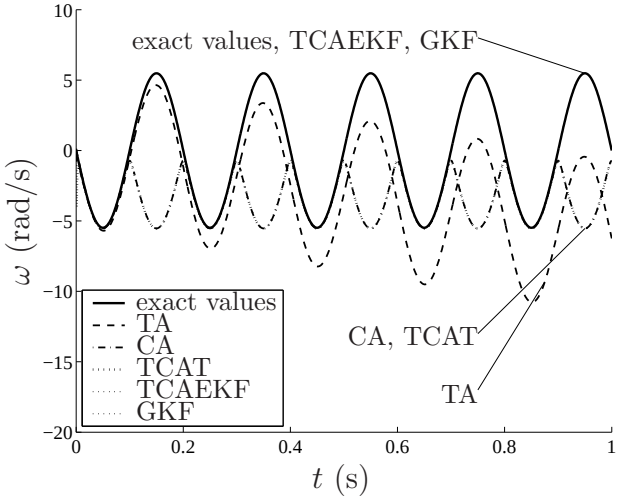

Figure 9.3: Angular velocity estimates

TCAEKF and GKF methods. Apparently, in this case, the TCAEKF method is more accurate than its gyroscope-based counterpart. The evaluation of the root-mean square values of the stabilized errors, that is, the rms-values over the time interval $[0.1\text{ s}, 1\text{ s}]$, yields 0.0005206 rad/s and 0.01814 rad/s for the

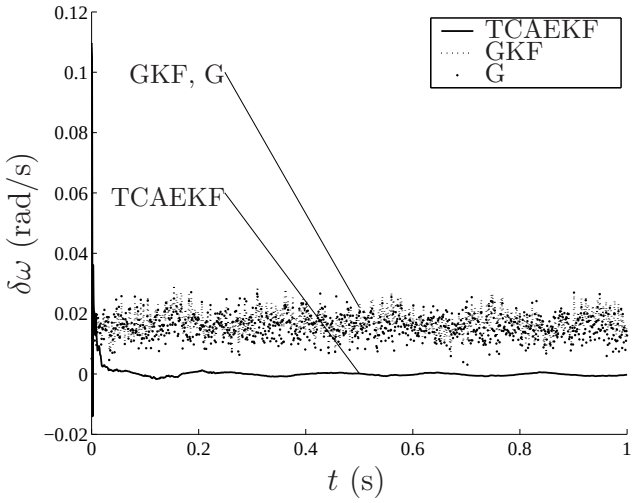

Figure 9.4: Errors on the angular velocity estimates obtained by Kalman filtering

TCAEKF and GKF methods, respectively. Hence, under these circumstances, the TCAEKF method is more than 10 times as accurate as the GKF method. The dots represent the raw measurements from the gyroscope, which is why they are given the label G. Interestingly, the error resulting from the TCAEKF method oscillates around zero, which implies that it is not dominated by bias errors. This may be surprising, since bias errors are more important than the noise errors in the accelerometer output signals, i.e.,

$$\sigma_b/\sigma_n = 178.9\,. \tag{9.67}$$

In fact, in the case of the TCAEKF method, the state-space system is observable, and, hence, permits the estimation of the bias errors on the angular velocity and the angular acceleration, thereby reducing drastically their effect on the estimates $\hat{\omega}_{\text{TCAEKF},k}$ and $\hat{\alpha}_{\text{TCAEKF},k}$. This can be verified from Fig. 9.5, where it is seen that the bias errors are estimated by the extended Kalman filter. On the other hand, as predicted from its observability analysis, the GKF method fails to estimate the bias error on the angular-velocity estimates. This

can be verified from Fig. 9.6.

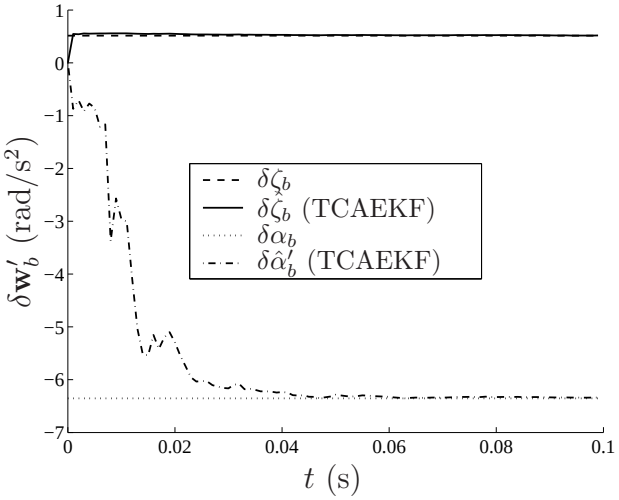

Figure 9.5: Estimates of the bias errors on the tangential and centripetal accelerations

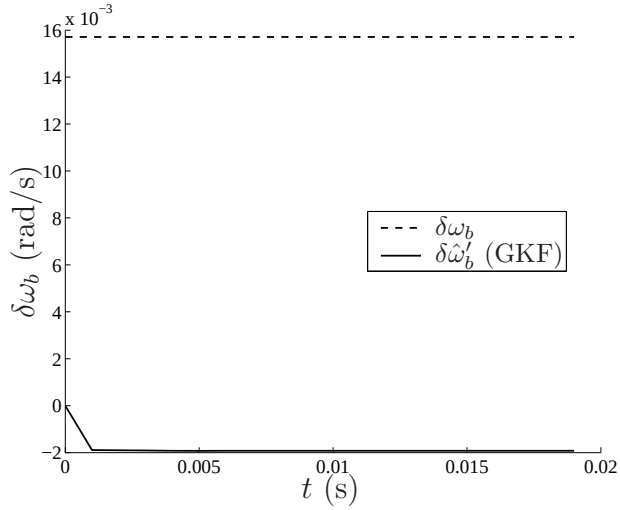

Figure 9.6: Estimates of the bias errors on the angular velocity

Figure 9.7 shows the exact angular acceleration of the camera–accelerometers–gyroscope assembly. Even though this kinematic variable is not the main focus of this chapter, the TCAEKF and GKF methods allow its estimation, and, since this may be a decisive factor when designing an inertial measurement unit, we plot the errors on their respective estimates in Fig. 9.8. We see that

the estimates obtained from the TCAEKF method are more accurate than those of the GKF method. In fact, the error rms-values for the time period $[0.1\text{ s}, 1\text{ s}]$—over which the influence of the initial conditions is negligible—are 0.01907 rad/s^2 and 4.453 rad/s^2 for the TCAEKF method and the GKF method, respectively.

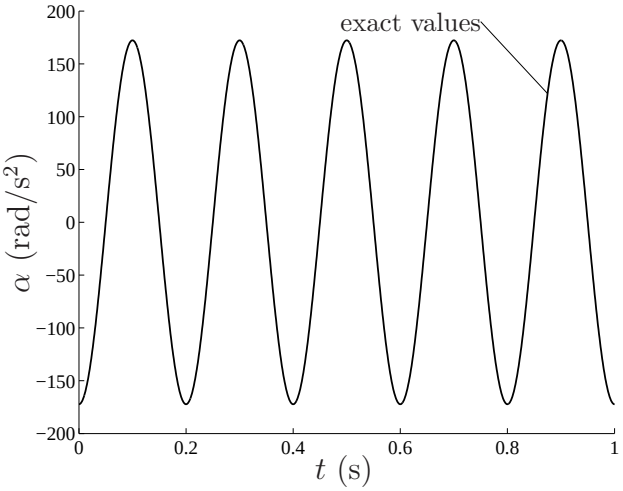

Figure 9.7: Angular acceleration estimates

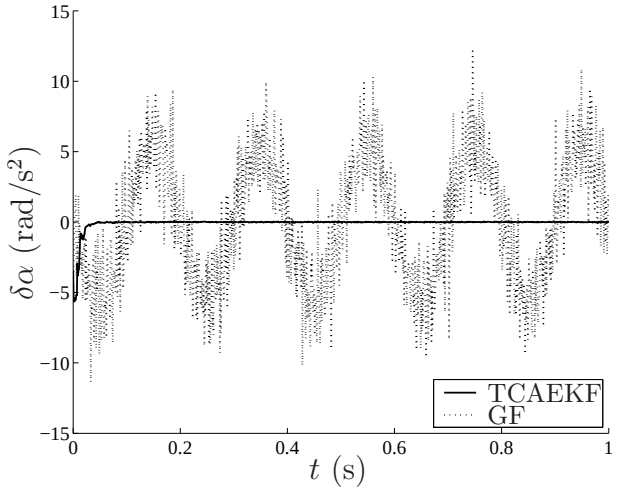

Figure 9.8: Errors on the angular acceleration estimates

Table 9.2: Accelerometer orientation errors

parameter	value
$\delta\psi_1$	-1.194°
$\delta\psi_2$	-1.465°
$\delta\psi_3$	-0.1755°
$\delta\psi_4$	-0.6308°
$\delta\psi_{rms}$	1°

9.7.4 Robustness of the TCAEKF and the GKF Methods

In this second example, we are to illustrate the robustness of the proposed method and compare it to that of the GKF method. To this end, let us introduce perturbations in the geometry of the camera-accelerometers-gyroscope assembly, the sensor signal errors, and the filter parameters.

Errors in the Geometry of the Camera-Accelerometers-Gyroscope Assembly

We start from the accelerometer array geometry described in eqs. (9.60) and (9.61). We assume all the accelerometer sensitive axes and the gyroscope sensitive axis are exactly parallel and orthogonal, respectively, to the plane of motion. However, we introduce orientation errors $\delta\psi_i$, $i = 1, 2, 3, 4$, on the in-plane orientation of the corresponding accelerometers. Hence, the direction vectors of eq. (9.60) are now the estimates $\{\hat{\mathbf{e}}_i\}_{i=1}^4$ of the accelerometers in-plane orientations, whereas their true values become

$$\mathbf{e}_i = (\mathbf{1}_{2\times 2} \cos\delta\psi_i + \mathbf{Q} \sin\delta\psi_i)\, \hat{\mathbf{e}}_i, \quad i = 1, 2, 3, 4. \tag{9.68}$$

The numerical values of the orientation errors are shown in Table 9.2, where it is seen that their root-mean square value is 1°. This last value was taken from the alignment error between the accelerometer chip and its package (ADXL320 Datasheet, Analog Devices).

Table 9.3: Accelerometer positioning errors

parameter	first entry	second entry
$\delta\mathbf{r}_1$	0.7488 mm	-0.1196 mm
$\delta\mathbf{r}_2$	1.55 mm	0.4873 mm
$\delta\mathbf{r}_3$	-0.2678 mm	-0.2397 mm
$\delta\mathbf{r}_4$	0.006712 mm	-0.8093 mm
δr_{rms}	1 mm	

Similarly, we introduce accelerometer in-plane positioning errors $\{\delta\mathbf{r}_i\}_{i=1}^4$. Notice that in the case of a pure planar motion, positioning errors occurring in a direction normal to the plane of motion have no effect on the accelerometer measurements. Of course, positioning errors have no effect on the gyroscope outputs. Hence, the accelerometer positions given in eq. (9.61) are now regarded as the estimates $\{\hat{\mathbf{r}}_i\}_{i=1}^4$ of the true accelerometer positions:

$$\mathbf{r}_i = \hat{\mathbf{r}}_i + \delta\mathbf{r}_i, \quad i = 1, 2, 3, 4. \tag{9.69}$$

The corresponding numerical values are displayed in Table 9.3, where it is seen that

$$\delta r_{rms} \equiv \sqrt{(1/4)\sum_{i=1}^{4} \|\delta\mathbf{r}_i\|_2^2} = 1 \text{ mm}. \tag{9.70}$$

Sensor Signal Errors

Let all noise errors follow uniform distributions instead of the Gaussian distributions of eqs. (9.7) and (9.46) for which the Kalman filters are designed. We choose the uniform distributions so that their means and variances are the same as those given in Table 9.1. As a result, we obtain

$$\begin{aligned} \delta a_n &\sim \mathcal{U}\{0, 2\sqrt{3}\sigma_n\}, \\ \delta\omega_n &\sim \mathcal{U}\{0, 2\sqrt{3}\sigma_n'\}, \end{aligned} \tag{9.71}$$

where $\mathcal{U}\{c, w\}$ symbolizes a uniform distribution with a power density function centered at c and with a width w.

Moreover, in order to evaluate the robustness of the filter, let the bias errors undergo a sign change at time $t^\star = 0.2$ s, which may be expressed as

$$\begin{aligned} \delta\mathbf{a}_b^* &\equiv [0.1746 \quad -1.106 \quad 1.435 \quad 0.031\ ]^T \text{ m/s}^2, \\ \delta\mathbf{a}_b' &= (1 - 2\mathrm{u}(t - t^\star))\delta\mathbf{a}_b^\star. \end{aligned} \tag{9.72}$$

Errors in the Filter Parameters

We model the estimates of the initial states of the systems of eqs. (9.17) and (9.47) as described in eq. (9.22), and with the same numerical values as those given in Table 9.1. On the other hand, let $\hat{\sigma}_\gamma$, $\hat{\sigma}_\beta$, $\hat{\sigma}_b$, $\hat{\sigma}_n$, $\hat{\sigma}_\gamma^*$, $\hat{\sigma}_\beta^*$, $\hat{\sigma}_b^*$, and $\hat{\sigma}_n^*$ be the estimates of the standard-deviation σ_γ, σ_β, σ_b, σ_n, σ_b^*, and σ_n^*. Here, we consider that the designer of the Kalman filters has very little knowledge of the errors that stain the signals to be processed. Let the only available information be the main frequency $\omega^\star = 2\pi f^\star$ of the trajectory, and an overall estimate $\phi = 0.1\%$ of the ratio between the sensor errors and the magnitudes of the signals to be measured. The standard-deviation estimates required for the Kalman filter are computed from the expressions listed in Table 9.4, for a length $l = 0.4$ m. Notice that the resulting estimates are far away from the exact values as given in Table 9.1. Despite this large initial error, the resulting filter is still reasonably accurate, since, in Kalman filtering, the magnitudes of the variances bear little importance. Indeed, provided that the digital representation of all numbers involved is sufficiently accurate, only the ratios of the standard deviations need to be respected. This is what is done in Table 9.4 by assuming a sinusoidal angular motion with an amplitude of 1 rad, and computing the amplitudes of its derivatives accordingly.

Table 9.4: Standard deviation estimates

parameter	expression	value
$\hat{\sigma}_\gamma$	$(\omega^\star)^3$	3.101e+004 rad/s^3
$\hat{\sigma}_\beta$	$\phi l(\omega^\star)^3$	12.4 m/s^3
$\hat{\sigma}_b$	$\phi l(\omega^\star)^2$	0.3948 m/s^2
$\hat{\sigma}_n$	$\phi l(\omega^\star)^2$	0.3948 m/s^2
$\hat{\sigma}_\beta$	$\phi(\omega^\star)^2$	0.987 rad/s^2
$\hat{\sigma}_b$	$\phi\omega^\star$	0.03142 rad/s
$\hat{\sigma}_n$	$\phi\omega^\star$	0.03142 rad/s

Results

For the sake of conciseness, we omit time evolutions of the resulting accelerometer signals, which are hardly distinguishable from those displayed in Fig. 9.2. However, the angular velocity estimates exhibit some variations, as may be seen from Fig. 9.9. The TA, CA, and TCAT methods bear the same flaws as before. Indeed, the first drifts constantly through time while the other two exhibit sign problems and discontinuities close to $\omega = 0$ rad/s.

Figure 9.10 eases the task of discriminating the other angular-velocity estimates. Apparently, the poor knowledge of the random-error distributions has affected both the TCAEKF and the GKF methods. As one can see, the TCAEKF estimate is not stabilized at $t = t^\star$, as opposed to the analogous estimate obtained for the unperturbed model and displayed in Fig. 9.4. Yet, the extended Kalman filter is able to identify and compensate roughly for the disturbance occasioned by the step in the bias errors, so as to obtain an estimate more accurate than that of the GKF method. However, as may be expected, the GKF estimates do not converge at all, so that they remain, in fact, less accurate than the raw measurements they stem from. Indeed, the direct gyroscope measurements seem to be more accurate, in this case, than the ones obtained from any of the proposed filtering methods with an rms-value

of 0.016 rad/s over the time interval [1 s, 2 s], as compared to rms-values of 0.1275 rad/s and 0.02327 rad/s for the TCAEKF and the GKF methods over the same periods of time, respectively.

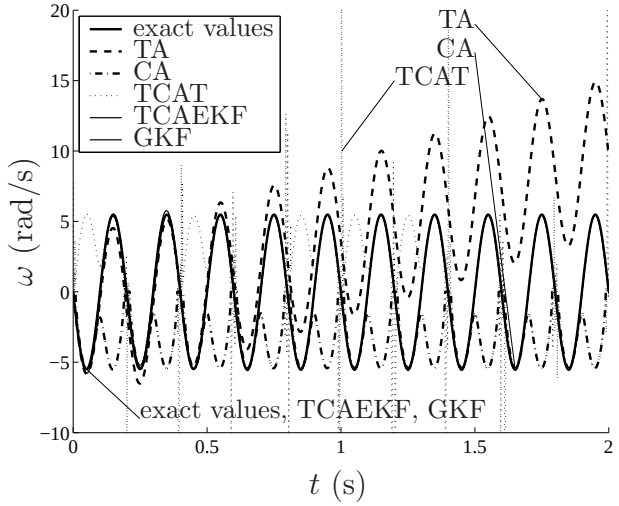

Figure 9.9: Angular velocity estimates

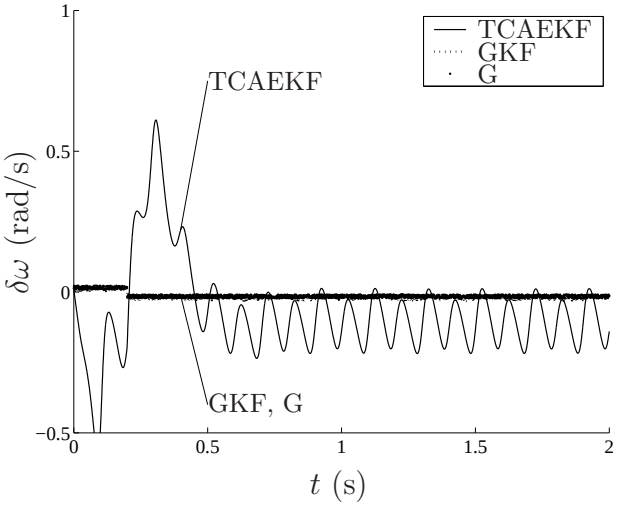

Figure 9.10: Errors on the angular velocity estimates

Even though the TCAEKF method is, in this case, less accurate than the gyroscope methods, its ability to identify the bias errors can be appreciated from Fig. 9.11. On the other hand, the GKF method remains completely indifferent to the sign change in the gyroscope bias error, as may be seen in

Fig. 9.12. Finally, the errors on the angular acceleration estimates provided by

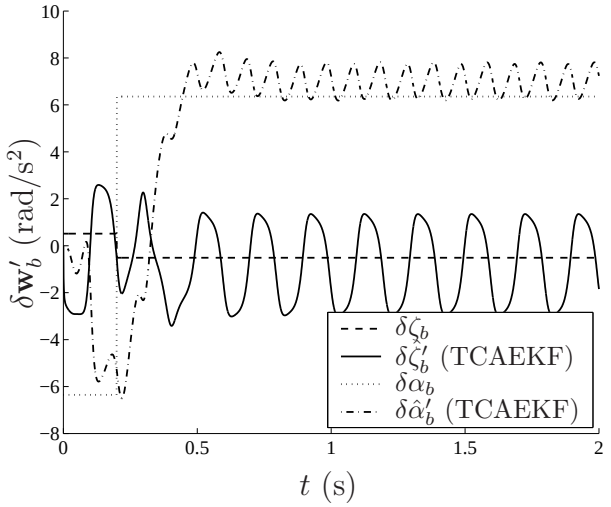

Figure 9.11: Estimates of the bias errors on the tangential and centripetal accelerations

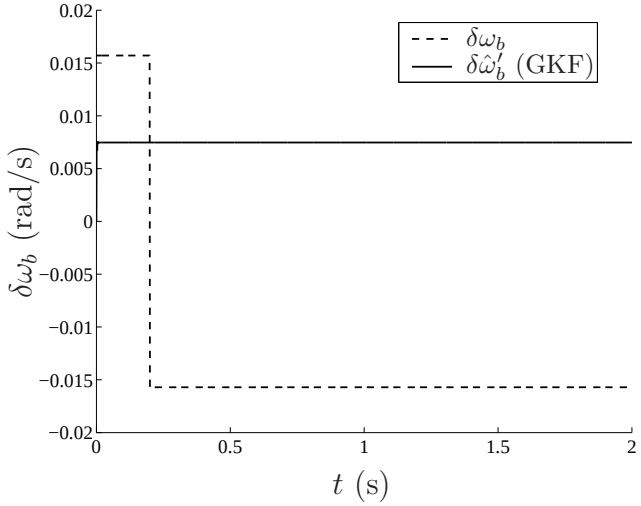

Figure 9.12: Estimates of the bias errors on the angular velocity

both the TCAEKF and the GKF methods are plotted in Fig. 9.13. Apparently, in this case, the TCAEKF method is more accurate than its gyroscope-based counterpart, with associated rms-values of 1.172 rad/s^2 for the former and 4.48 rad/s^2 for the latter, over the time interval [1 s, 2 s].

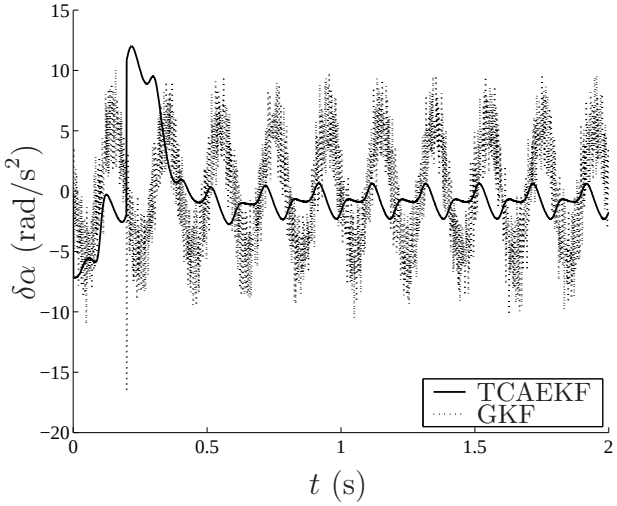

Figure 9.13: Errors on the angular acceleration estimates

Chapter 10

Conclusions and Recommendations

10.1 Summary

The contributions of this work all aim at improving the accuracy of the accelerometer arrays used for the estimation of the pose and the twist of rigid bodies. The estimation process may be divided into two: the point-acceleration measurement and the rigid-body pose-and-twist estimation, which correspond, respectively, to the subjects of Chapters 2–5 and 6–9.

Chapters 2–5 detail the synthesis, analysis, microfabrication, and testing of a novel mechanical architecture for biaxial accelerometers. This architecture, inspired from that of parallel-kinematics machines (PKM), which is introduced in Chapter 2. A common characteristic of the architectures of all three accelerometer types, monoaxial, biaxial, and triaxial, is their number of legs coupling the PKM base to the PKM platform, which is always greater than the PKM number of degrees of freedom by one. For this reason, the qualifier "simplicial" is attributed to these architectures. In Chapter 3, a micro-scale compliant realization of the proposed two-degree-of-freedom simplicial architecture is devised; the realization is referred to as the simplicial biaxial accelerometer (SBA). From the proposed dynamic model of the SBA and the vibration tests reported in Chapter 5, its lowest natural frequency

corresponds to its two sensitive directions, leaving its third natural frequency for the out-of-wafer-plane translations of the proof mass. Apparently, this result is somewhat different from that obtained for the mechanical architecture of the ADXL150, an accelerometer developed by Analog Devices. In the latter, the first natural frequency corresponds to out-of-wafer-plane proof-mass translations, which are directly linked to the sensor cross-axis sensitivity at low frequencies. The resulting frequency response is shown in Fig. 3.5, where it can be verified that the out-of-wafer-plane sensitivity is higher than the sensitivity along the ADXL150 sensitive direction for frequencies lower than 10000 rad/s. Hence, these relatively large out-of-plane proof-mass motions cause the larger share of the cross-axis sensitivity of the device, which accounts for 2% of its full-scale range. Hence, apparently, resorting to slightly more sophisticated mechanical architectures such as that of the SBA can decrease the cross-axis sensitivity of accelerometers.

Yet another way of improving the accuracy of accelerometer-based pose-and-twist estimation techniques is to propose algorithms that are more robust, i.e., less sensitive to accelerometer errors. This, along with the addition of some developments to the theory behind accelerometer arrays, is the objective pursued in the balance of the thesis. In Chapter 6, the linear relation between a generic feasible n-accelerometer array readouts and the parameters of the associated rigid-body acceleration field is given in closed form. This result is thought to be useful to the designers of accelerometer arrays, as it gives a systematic method for the solution of the associated kinematic problems, which are solved intuitively and individually in the literature. The concept of accelerometer-array feasibility, first defined by Williams and Fyfe (2004), is restated in Chapter 7. Also included in this Chapter is a geometric interpretation of the feasibility of planar accelerometer arrays of $n \geq 4$ accelerometers,

which is a generalization of the method initially proposed by Williams and Fyfe (2004) for $n = 4$ accelerometers. The introduction of the instant centre of acceleration turns this analysis into a purely geometric problem, thereby allowing for a deeper insight. Following these developments, four methods are devised in Chapter 8 for the estimation of the accelerometer-array angular velocity from the centripetal component of its acceleration field. Simulation results show that all these methods are more robust than the existing ones in the sense that their associated error amplifications are smaller, when integrated over all possible directions of the rigid-body angular velocity (see Fig. 8.19). Finally, in Chapter 9, the tangential and centripetal components of the planar rigid-body acceleration field are combined for the estimation of the angular velocity. The proposed algorithm, based on extended Kalman filtering, exhibits good robustness under independently identically distributed error contamination of the accelerometer measurements. Moreover, the proposed algorithm allows for the automatic identification and compensation of any bias (DC) error in the accelerometers. For the simulated example, the proposed method is more accurate than the one proposed by Parsa et al. (2005), and exhibits errors that are of the same orders of magnitude as those of a typical MEMS gyroscope.

10.2 Recommendations for Further Research

The further development of the SBA requires the addition of a sensing method in order to pickup the in-plane proof-mass translations. If capacitive sensing were to be employed, the author suggests a collaboration with researchers that have experience in the design and fabrication of on-chip circuits. Indeed, this method requires that parasitic capacitance be minimized,

and, therefore, the circuit should stand as close as possible to the sensing electrodes. Yet another important point to consider when implementing capacitive position sensing is the gap between the electrodes. The capacitance associated with the electrodes is roughly proportional to the inverse of the length of this gap, and, therefore, the smaller the gap, the higher the sensor resolution. In order to achieve resolutions that are comparable to those of the sensors currently used in industry, it may be necessary to reduce this gap, and, therefore, spend some effort on tuning the DRIE process so that it still allows for a deep etch, while bringing down the gap between the electrodes. The whole problem lies in this compromise between etch depth and width in order to improve the sensitivity, while maintaining a low cross-axis sensitivity of the accelerometer.

A natural sequel of the work on the theory of accelerometer arrays would be the generalization of the developments proposed for planar arrays to spatial arrays. Notice, however, that such a generalization may turn out to be quite challenging in the case of the assessment of the feasibility of planar accelerometer arrays, which is the topic of Chapter 7. As mentioned in this Chapter, the analogous spatial problem requires that the intersections of nonic surfaces be found, which is virtually impossible to do graphically. On the other hand, the combination of centripetal and tangential acceleration measurements reported in Chapter 9 for a planar rigid-body motion may readily be rewritten for the spatial case. This yields a state-space system similar to that of eqs. (9.17) and (9.18), with 15 state variables and 9 outputs, the nine entries of the estimated angular acceleration matrix. Another outcome of this thesis is the possibility of optimizing the geometry of an accelerometer array from the symbolic formulations of eqs. (6.24) and (6.34). Indeed, the generic nature of these expressions allows for the estimation and the eventual minimization of

the sensitivity of accelerometer arrays to perturbations in their accelerometer measurements and in their geometry. This is thought to be another possible direction for further investigations.

From a more practical point of view, the implementation of the proposed algorithms in some of the already-existing applications of accelerometer arrays is certainly of primary importance. Some other applications, where gyroscopes are the standard for angular velocity estimation, may also benefit from the relative robustness of accelerometers. Indeed, applications such as galloping robot control, spacecraft docking and shock simulation in haptic interfaces all involve high accelerations that can ruin the accuracy of angular rate sensors, thus giving an edge to accelerometers, which are known to be more rugged in that type of situation.

Bibliography

Algrain, M. C. and Quinn, J. (1993). Accelerometer based line-of-sight stabilization approach for pointing and tracking systems. In *Proceedings of 2nd IEEE Conference on Control Applications*, pages 159–163, Vancouver, Canada.

Analog Devices (2004a). *ADXL320 Datasheet*. One Technology Way, P.O. Box 9106, Norwood, MA, USA. www.analog.com.

Analog Devices (2004b). *ADXRS300 Datasheet*. One Technology Way, P.O. Box 9106, Norwood, MA, USA. www.analog.com.

Anderson, R. W. G., Brown, C. J., Blumbergs, P. C., McLean, A. J., and Jones, N. R. (2003). Impact mechanics and axonal injury in a sheep model. *Journal of Neurotrauma*, 20(10):961–974.

Ang, W. T., Khosla, P. K., and Riviere, C. N. (2003). Design of all-accelerometer inertial measurement unit for tremor sensing in hand-held microsurgical instrument. In *Proceedings of IEEE ICRA*, volume 3, pages 1781–1786, Taipei, Taiwan.

Ang, W. T., Khosla, P. K., and Riviere, C. N. (2004). Kalman filtering for real-time orientation tracking of handheld microsurgical instrument. In *Proceedings of IEEE International Conference on Intelligent Robots and Systems*, pages 2574–2580, Sendai, Taiwan.

Ang, W. T., Riviere, C. N., and Khosla, P. K. (2001). Design and implementation of active error canceling in hand-held microsurgical instrument. In *Proceedings of IEEE International Conference on Intelligent Robots and Systems*, pages 1106–1111, Maui, Hawaii.

Angeles, J. (1999). The angular-acceleration tensor of rigid-body kinematics and its properties. *Archive of Applied Mechanics*, 69(3):204–214.

Angeles, J. (2005). The degree of freedom of parallel robots: A group-theoretic approach. In *Proceedings of IEEE ICRA*, pages 1005–1012, Barcelona, Spain.

Angeles, J. (2007). *Fundamentals of Robotic Mechanical Systems*. Springer, New York, third edition.

Angeles, J., Zanganeh, K. E., and Ostrovskaya, S. (1999). The analysis of arbitrarily-damped linear mechanical systems. *Archive of Applied Mechanics*, 69:529–541.

Arai, T., Hervé, J. M., and Tanikawa, T. (1996). Development of 3 dof micro finger. In *Proceedings of IROS*, pages 981–987, Osaka, Japan.

Bélanger, P. R. (1992). Estimation of angular velocity and acceleration from shaft encoder measurements. In *IEEE International Conference on Robotics and Automation*, volume 1, pages 585–592.

Bernard, A., Foulon, B., and Clerc, G. M. L. (1985). Three-axis electrostatic accelerometer. In *DGON Symposium on Gyro Technology*, pages 12.0–12.23, Stuttgart, Germany.

Bokelberg, E. H., Hunt, K. H., and Ridley, P. R. (1992). Spatial motion-i : Points of inflection and the differential geometry of screws. *Mechanism and Machine Theory*, 27(1):1–15.

Bortz, J. E. (1971). A new mathematical formulation for strapdown inertial navigation. *IEEE Transactions on Aerospace and Electronic Systems*, AES–7(1):61–66.

Cardou, P. and Angeles, J. (2005). A comparative study of all-accelerometer strapdowns for uav ins. In *Symposium SET-092/RSY18/MSE on Advanced Sensor Payloads for UAV*, Lisbon, Portugal. NATO Research & Technology

Organization.

Cardou, P. and Angeles, J. (2006). Angular velocity estimation from the angular acceleration matrix. Technical Report 06.03, Mechanical Engineering Department & Centre for Intelligent Machines, McGill University, Montreal, Quebec, H3A 2K6, Canada.

Cardou, P. and Angeles, J. (2007a). Simplectic architectures for true multiaxial accelerometers: A novel application of parallel robots. In *IEEE International Conference on Robotics and Automation*, pages 181–186, Rome, Italy.

Cardou, P. and Angeles, J. (2007b). Singularity analysis of accelerometer strapdowns for the estimation of the acceleration field of a planar rigid-body motion. In *Proceedings of the 12th World Congress in Mechanism and Machine Science*, Besançon, France.

Cardou, P. and Angeles, J. (2008a). Angular velocity estimation from the angular acceleration matrix. *Journal of Applied Mechanics*, 75(2).

Cardou, P. and Angeles, J. (2008b). Angular-velocity estimation from the centripetal component of the rigid-body acceleration field. In *Advances in Robot Kinematics*, Batz-sur-Mer, France.

Cardou, P. and Angeles, J. (2008c). Estimating the angular velocity of a rigid body moving in the plane from tangential and centripetal acceleration measurements. *Multibody System Dynamics*. accepted for publication.

Chapsky, V., Portman, V., and Sandler, B.-Z. (2007). Single-mass 6-dof isotropic accelerometer with segmented psd sensors. *Sensors and Actuators A*, 135:558–569.

Chen, J. L., Lee, S. C., and DeBra, D. B. (1994). Gyroscope free strapdown inertial measurement unit by six linear accelerometers. *AIAA Journal of Guidance, Control and Dynamics*, 17(2):286–290.

Chevalier, R. (2002). Algorithms for rigid-body pose-and-twist estimation in the presence of noisy, redundant acceleration measurements. TR–CIM–02–03, Centre for Intelligent Machines, McGill University, Montreal, Canada.

Chou, C. C. and Sinha, S. C. (1976). On the kinematics of the head using linear acceleration measurements. *Journal of Biomechanics*, 9:607–613.

Choukroun, D., Bar-Itzhack, I. Y., and Oshman, Y. (2004). Optimal-request algorithm for attitude determination. *Journal of Guidance, Control, and Dynamics*, 27(3):418–425.

Clavel, R. (1988). Delta, a fast robot with parallel geometry. In *Proceedings of the 18th International Symposium on Industrial Robots*, pages 91–100, Lausanne, Switzerland.

Costello, M. (2000). Determining the angular velocity and angular acceleration of a projectile using triaxial acceleration measurements. In *Proceedings of AIAA Atmospheric Flight Mechanics Conference*, pages 564–574, Denver, CO, USA.

Deal, B. E. and Grove, A. S. (1965). General relationship for the thermal oxidation of silicon. *Journal of Applied Physics*, 36(12):3770–3778.

Derderian, J. M., Howell, L. L., Murphy, M. D., Lyon, S. M., and Pack, S. D. (1996). Compliant parallel-guiding mechanisms. In *Proceedings of the 1996 ASME Design Engineering Technical Conferences*, Irvine, CA, USA. 96-DETC/MECH-1208.

Dym, C. L. and Shames, I. H. (1973). *Solid Mechanics: A Variational Approach*. McGraw-Hill, New York, USA.

Freescale Semiconductor (2007). *MMA7260QT Datasheet*. Freescale Semiconductor Literature Distribution Center, P.O. Box 5405, Denver, Colorado 80217. www.freescale.com.

Gautschi, G. (2002). *Piezoelectric Sensorics: Force, Strain, Pressure, Acceleration and Acoustic Emission Sensors, Materials and Amplifiers*. Springer, Berlin, Germany.

Genin, J., Hong, J., and Xu, W. (1997). Accelerometer placement for angular velocity determination. *ASME Journal of Dynamic Systems, Measurements and Control*, 119:474–477.

Giansanti, D., Macellari, V., Maccioni, G., and Cappozzo, A. (2003). Is it feasible to reconstruct body segment 3-d position and orientation using accelerometric data? *IEEE Transactions on Biomedical Engineering*, 50(4):48–54.

Golub, G. and Van Loan, C. (1996). *Matrix Computations*. Johns Hopkins University Press, Baltimore.

Grammatikos, A. (1965). *Gimballess Inertial Systems for Space Navigation*. PhD thesis, University of Pennsylvania, PA, USA.

Hansen, K. S. (1997). A new design principle for triaxial piezoelectric accelerometers. Technical Report 1, Brüel & Kjær.

Hayes, W. C., Gran, J. D., Nagurka, M. L., Feldman, J. M., and Oatis, C. (1983). Leg motion analysis during gait by multiaxial accelerometry: Theoretical foundations and preliminary validations. *ASME Journal of Biomechanical Engineering*, 105:283–289.

Hervé, J. M. (1978). Analyse structurelle des mécanismes par groupes de déplacements. *Mechanism and Machine Theory*, 13:437–450.

Hervé, J. M. and Sparacino, F. (1992). Star, a new concept in robotics. In *Proceedings of the 3rd International Workshop on Advances in Robot Kinematics*, pages 176–183, Ferrara, Italy.

Hillier, F. S. and Lieberman, G. J. (1995). *Introduction to Mathematical Programming*. McGraw–Hill, New York, USA.

Huijser, R. H. (1992). Assembly of accelerometers for use in a system for measuring the three dimensional movements of a rigid body.

Ishikawa, A. (1999). Spherical integrated circuit for general application.

Isidori, A. (1989). *Nonlinear Control Systems*. Springer–Verlag, Berlin, Germany.

Kailath, T., Sayed, A. H., and Hassibi, B. (2000). *Linear Estimation*. Prentice Hall, Upper Saddle River, NJ, USA.

Kane, T. R., Hayes, W. C., and Priest, J. D. (1974). Experimental determination of forces exerted in tennis play. *Biomechanics IV*, pages 284–290.

Kim, H. C., Seok, S., Kim, I., Choi, S.-D., and Chun, K. (2005). Inertial-grade out-of-plane and in-plane differential resonant silicon accelerometers (drxls). In *IEEE 13th International Conference on Solid-State Sensors, Actuators and Microsystems*, pages 172–175, Seoul, Korea.

Kong, X. and Gosselin, C. (2007). *Type Synthesis of Parallel Mechanisms*. Springer Tracts in Advanced Robotics. Springer, Berlin, Germany.

Krishnan, V. (1965). Measurement of angular velocity and linear acceleration using linear accelerometers. *Journal of the Franklin Institute*, 280(4):307–315.

Le Traon, O., Janiaud, D., Muller, S., and Bouniol, P. (1998). The via vibrating beam accelerometer: concept and performance. In *IEEE 1998 Position Location and Navigation Symposium*, pages 25–29, Palm Springs, CA, USA.

Li, G., Li, Z., Wang, C., Hao, Y., Li, T., Zhang, D., and Wu, G. (2001). Design and fabrication of a highly symmetrical capacitive triaxial accelerometer. *Journal of Micromechanics and Microengineering*, 11:48–54.

Linder, A., Svensson, M., and Viano, D. (2002). Evaluation of the biorid p3 and the hybrid iii in pendulum impacts to the back: A comparison with human subject test data. *Traffic Injury Prevention*, 3:159–166.

Liu, C.-H., Barzilai, A. M., Reynolds, J. K., Partridge, A., Kenny, T. W., Grade, J. D., and Rockstad, H. K. (1998). Characterization of a high-sensitivity micromachined tunneling accelerometer with micro-g resolution. *IEEE Journal of Microelectromechanical Systems*, 7(2):235–244.

Liu, Y., Wen, Z., Wen, Z., Zhang, L., and Yang, H. (2007). Design and fabrication of a high-sensitive capacitive biaxial microaccelerometer. *Journal of Micromechanics and Microengineering*, 17:36–41.

Liu, Y. K. (1976). Discussion of measurement of angular accelerations of a rigid body using linear accelerometers. *ASME Journal of Applied Mechanics*, 43:377–378.

Mertz, H. J. (1967). *Kinematics and Kinetics of Whiplash*. PhD thesis, Wayne State University, Detroit, USA.

Miles, M. D. (1986). Measurement of six-degree of freedom model motions using strapdown accelerometers. In *21st American Towing Tank Conference*, pages 369–375, Washington DC, USA.

Mineta, T., Kobayashi, S., Watanabe, Y., Kanauchi, S., Nakagawa, I., Suganuma, E., and Esashi, M. (1996). Three-axis capacitive accelerometer with uniform axial sensitivities. *Journal of Micromechanics and Microengineering*, 6:431–435.

Mital, N. K. and King, A. I. (1979). Computation of rigid-body rotation in three-dimensional space from body-fixed linear acceleration measurements. *ASME Journal of Applied Mechanics*, 46:925–930.

Mohamed, M. G. (1997). Kinematics of rigid bodies in general spatial motion: Second-order motion properties. *Applied Mathematical Modelling*, 21(8):471–479.

Morris, J. R. W. (1973). Accelerometry—a technique for the measurement of human body movements. *Journal of Biomechanics*, 6:729–736.

Mostov, K. S. (2000). *Design of Accelerometer-Based Gyro-Free Navigation Systems*. PhD thesis, University of California, Berkeley.

Mostov, K. S., Soloviev, A. A., and Koo, T. K. (1997). Accelerometer based gyro-free multi-sensor generic inertial device for automotive applications. In *Proceedings of the IEEE Conference on Intelligent Transportation Systems*, pages 1047–1052, Boton, MA, USA.

Munson, B. R., Young, D. F., and Okiishi, T. H. (2006). *Fundamentals of Fluid Mechanics*. J. Wiley & Sons, Hoboken, NJ, USA, 5th edition.

Ohlmeyer, E. J. and Pepitone, T. R. (2002). Guidance, navigation and control without gyros: A gun-launched munition concept. In *Proceedings of AIAA Guidance, Navigation, and Control Conference and Exhibit*, pages 2336–2349, Monterey, CA.

Padgaonkar, A. J., Krieger, K. W., and King, A. I. (1975). Measurement of angular acceleration of a rigid body using linear accelerometers. *ASME Journal of Applied Mechanics*, pages 552–556.

Pamadi, K. B., Ohlmeyer, E. J., and Pepitone, T. R. (2004). Assessment of a gps guided spinning projectile using an accelerometer-only imu. In *Proceedings of AIAA Guidance, Navigation, and Control Conference and Exhibit*, pages 705–717, Providence, Rhode Island, USA.

Parsa, K. (2003). *Dynamics, State Estimation, and Control of Manipulators with Rigid and Flexible Subsystems*. PhD thesis, McGill University, Montreal, Canada.

Parsa, K., Lasky, T. A., and Ravani, B. (2005). Design and mechatronic implementation of an accelerometer-based, kinematically redundant inertial measurement unit. In *Proceedings of the 2005 IEEE/ASME International Conference on Advanced Intelligent Mechatronics*, pages 644–651, Monterey, CA, USA.

Peng, Y. K. and Golnaraghi, M. F. (2004). A vector-based gyro-free inertial navigation system by integrating existing accelerometer network in a passenger vehicle. In *IEEE Position Location and Navigation Symposium*, pages 234–242, Monterey, CA, USA.

Pham, H.-H., Chen, I.-M., and Yeh, H.-C. (2005). Micro-motion selective actuation xyz flexure parallel mechanism: Design and modeling. *Journal of Micromechatronics*, 3(1):51–73.

Pilkey, W. D. (2005). *Formulas for Stress, Strain, and Structural Matrices*. John Wiley & Sons, 2nd edition.

Puers, R. and Reyntjens, S. (1998). Design and processing experiments of a new miniaturized capacitive triaxial accelerometer. *Sensors and Actuators A*, 68:324–328.

Qu, H., Fang, D., and Xie, H. (2006). A monolithic cmos-mems 3-axis accelerometer with a low-noise, low-power dual chopper amplifier. In *Solid-state Sensors, Actuators and Microsystem Workshop*, pages 224–227, Hilton Head.

Ridley, P. R., Bokelberg, E. H., and Hunt, K. H. (1992). Spatial motion-ii : Acceleration and the differential geometry of screws. *Mechanism and Machine Theory*, 27(1):17–35.

Roark, R. J. and Young, W. C. (1975). *Formulas for Stress and Strain*. McGraw-Hill, fifth edition.

Roylance, L. M. (1978). *Miniature Integrated Circuit Accelerometer for Biomedical Applications*. PhD thesis, Stanford University, Stanford, CA, USA.

Schuler, A. R. (1965). *Design and Analysis of Analytic Platform Inertial Navigation Systems*. PhD thesis, University of Pennsylvania, PA, USA.

Senturia, S. (2001). *Microsystem Design*. Kluwer Academic Publishers, Boston, USA.

Shaad, T. P. and Paros, J. M. (2004). Triaxial acceleration sensor. Patent Number US6826960-B2.

Shea, R. T. and Viano, D. C. (1994). Computing body segment trajectories in the hybrid iii dummy using linear accelerometer data. *ASME Journal of Biomechanical Engineering*, 116:37–43.

Stuelpnagel, J. (1964). On the parametrization of the three-dimensional rotation group. *SIAM Review*, 6(4):422–430.

Subramanian, V. A. and Vendhan, C. P. (1993). An efficient algorithm for strapdown accelerometer-based motion measurement. *Ocean Engineering*, 20(4):421–432.

Takeda, N. (2000). Ball semiconductor technology and its application to mems. In *IEEE International Conference on Microelectromechanical Systems*, pages 11–16, Miyazaki, Japan.

Tan, C.-W., Park, S., Mostov, K., and Varaiya, P. (2001). Design of gyroscope-free navigation systems. In *IEEE Intelligent Transportation Systems Conf. Proc.*, pages 286–291, Oakland, CA, USA.

Toda, R., Takeda, N., Murakoshi, T., Nakamura, S., and Esashi, M. (2002). Electrostatically levitated spherical 3-axis accelerometer. In *Fifteenth IEEE International Conference on Micro Electro Mechanical Systems*, pages 710–713, Las Vegas, NV, USA.

Trease, B. P., Moon, Y.-M., and Kota, S. (2005). Design of large-displacement compliant joints. *Transactions of the ASME*, 127:788–798.

Veldkamp, G. R. (1969). Acceleration axes and acceleration distribution in spatial motion. *Journal of Engineering and Industry*, pages 147–151.

Walter, P. L. (1996). History of the accelerometer. *Sound and Vibration*, 31(3):16–22.

Wertz, J. R. (1984). *Spacecraft Attitude Determination and Control*. D. Reidel, Dordrecht, The Netherlands.

Williams, T. R. and Fyfe, K. R. (2004). Planar accelerometer configurations. *ASME Journal of Applied Mechanics*, 71:10–14.

Wilson, J. S., editor (2005). *Sensor Technology Handbook*. Elsevier, Amsterdam, Netherlands.

Wortman, J. J. and Evans, R. A. (1965). Young's modulus, shear modulus, and Poisson's ratio in silicon and germanium. *Journal of Applied Physics*, 36(1):153–156.

Xie, H., Fedder, G. K., Pan, Z., and Frey, W. (2004). Integrated monolithic tri-axial micro-machined accelerometer chip for medical application has single sensor microstructure made from single crystal silicon membrane layer that senses acceleration in all three orthogonal directions. Patent Numbers WO2004077073-A1 US2004231420-A1 and US2006260401-A1.

Yi, B.-J., Na, H.-Y., Chung, G. B., Kim, W. K., and Suh, I. H. (2002). Design and experiment of a 3dof parallel micro-mechanism utilizing flexure hinges. In *Proceedings of IEEE ICRA*, pages 1167–1172, Washington, DC, USA.

Yoganandan, N., Zhang, J., Pintar, F. A., and Liu, Y. K. (2006). Lightweight low-profile nine-accelerometer package to obtain head angular accelerations in short-duration impacts. *Journal of Biomechanics*, 39(7):1347–1354.

Zarchan, P. and Musoff, H. (2000). *Fundamentals of Kalman Filtering*, volume 190 of *Progress in Astronautics and Aeronautics*. American Institute of Aeronautics and Astronautics.

Zorn, A. H. (2002). A merging of system technologies: All-accelerometer inertial navigation and gravity gradiometry. In *IEEE Position, Location and*

Navigation Symposium, pages 66–73, Palm Springs, CA, USA.

Appendix A

Microfabrication Recipes

Table A.1: Growing a 5000 Å layer of silicon dioxide on silicon

parameter	value
tool	Tylan Oxidation & LPCVD Furnace Stack
gas	O_2+H_2 (wet environment)
temperature	1000°C
time	88 min

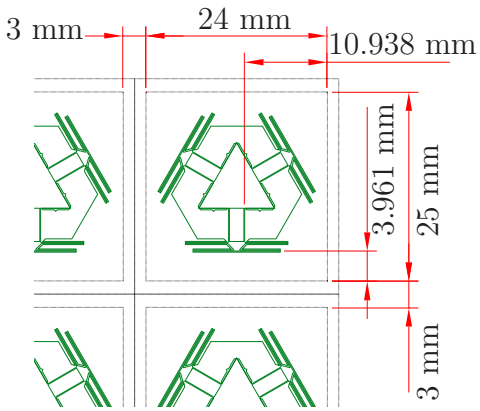

Figure A.1: Dicing dimensions of SBA samples

Table A.2: Spinning a 1.4 μm layer of Shipley-1813 photoresist on a six-inch silicon wafer

tool	Site Services Coater/Developer (SSCD)	
recipe	`6C14B115.ln`	
#	step	parameters
1	spin	200 rpm
2	dispense resist from edge to center	
3	accelerate	50000 rpm/s
4	spin	3950 rpm, during 30 s
5	spin	2000 rpm
6	perform an edge bead removal (EBR)	
7	decelerate	10000 rpm/s
8	softbake	115°C, during 1 min

Table A.3: Exposing a layer of photoresist on a six-inch silicon wafer using bottom-side alignment marks

tool	EVG 620 Aligner
recipe	`BottomSide-5inMask-6in-1.49m.rcp`
parameter	value
maskholder size	5 inches (125 mm)
substrate size	6 inches (150 mm)
separation	50 μm
mask thickness	2.28 mm
substrate thickness	1000 μm (handle wafer) 1300 μm (bonded pair)
resist thickness	2 μm (1.4 μm layer of Shipley-1813) 7 μm (6.5 μm layer of AZ9260)
process	bottom side
process mode	transparent
exposure mode	constant energy
contact mode	soft contact
energy	65 mJ (1.4 μm layer of Shipley-1813) 1100 mJ (6.5 μm layer of AZ9260)

Table A.4: Developing a 1.4 μm layer of Shipley-1813 photoresist on a six-inch silicon wafer

tool	Site Services Coater/Developer (SSCD)	
recipe	`D1813_45.L`	
#	step	parameters
1	accelerate	10000 rpm/s
2	spin	400 rpm, during 2.5 s
3	after 1 s, dispense developer from edge to center	
4	decelerate	10000 rpm/s
5	spin	50 rpm, during 2.5 s
6	decelerate	10000 rpm/s
7	stand still for 41 s	
8	dispense DI water in the center for 20 s	
9	spin	500 rpm, during 20 s
10	spin	3000 rpm, during 10 s
11	decelerate	10000 rpm/s
12	spin	100 rpm, during 5 s
13	decelerate	500 rpm/s
14	hardbake	90°C, during 90 s

Table A.5: Reactive ion etching of silicon dioxide

tool: Applied Materials P5000 RIE			
recipe: `NANOTOOL OX ETCH`			
depth: 0.55 μm			
step	STABILIZATION	MAIN ETCH	RAMPDOWN
Time (s)	15	120	30
Pressure (mTorr)	100	100	OPEN
Power (W)	0	720	100
B-Field (Gauss)	0	70	0
CHF_3 (sccm)	45	45	0
Ar (sccm)	70	70	100
CF_4-1 (sccm)	7	7	0

Table A.6: Reactive ion etching of silicon

tool: Applied Materials P5000 RIE				
recipe: `HBR-SI-ETCH-PHIL`				
depth: 2.5 μm				
step	STABILIZATION	MAIN ETCH	RAMPDOWN #1	RAMPDOWN #2
Time (s)	10	300	5	15
Pressure (mTorr)	50	50	OPEN	OPEN
Power (W)	0	500	200	75
B-Field (Gauss)	0	65	0	0
HBr (sccm)	70	70	0	0
Cl_2 (sccm)	40	40	0	0
He-O_2 (sccm)	7	7	50	50

Table A.7: Ashing of a photoresist layer

tool: `PVA TePla Microwave Plasma Asher`	
parameter	value
Time (min)	40
Power (W)	350
Pressure (mbar)	0.8-1.5
Faraday cage	NO

Table A.8: Standard RCA clean of silicon wafers

tool: `Bold non-HF Acids Wetbench`		
step	parameter	value
rinse	cycles	5
RCA-1	solution	H_2O:NH_4OH (27%):H_2O_2 (30%) 5:1:1
	temperature	80 °C
	time	10:00 min:sec
rinse	cycles	10
RCA-2	solution	H_2O:HCl:H_2O_2 (30%) 6:1:1
	temperature	80 °C
	time	10:00 min:sec
rinse	cycles	10

Table A.9: Cleaning of silicon wafers prior to bonding

#	step	parameter	value
perform the following steps on the handle wafer only			
1	piranha etch	H_2SO_4 (100%)	3 parts
		H_2O_2 (30%)	1 part
		time	10:00 min:sec
2	rinse	cycles	10
3	HF etch	HF	
		time	60:00 min:sec
		etch rate	
perform the following steps on handle and device wafers			
4	HF dip	HF	
		time	00:10 min:sec
5	rinse	cycles	10
6	RCA 1	H_2O	5 parts
		NH_4OH (27%)	1 part
		H_2O_2 (30%)	1 part
		temperature	80 °C
		time	10:00 min:sec
7	rinse	cycles	5
8	RCA 2	H_2O	6 parts
		HCl	1 part
		H_2O_2 (30%)	1 part
		temperature	80 °C
		time	10:00 min:sec
9	rinse	cycles	5

Table A.10: Direct bonding of two 150 mm silicon wafers

	tool	EVG 501 Universal Wafer Bonder		
	recipe	`PC-Si-Si.aba`		
#	time	command	parameter #1	parameter #2
1	00:00:00	pump on	high vacuum	
2		wait	pressure	10
3		waferbow		
4		pump off		
5		purge on		
6		wait	time	00:00:10
7	00:00:10	purge off		
8	pump on	high vacuum		
9		wait	pressure	1.00e-3
10		piston down	1000 N	
11		wait	time	00:30:00
12	00:30:10	piston up		
13		ramp heat. top	350°C	1°C
14		ramp heat. bot.	350°C	1°C
15		wait	temp. bottom	350°C
16		wait	time	4:00:00
17	4:30:10	ramp cool. top	40°C	1°C
18		ramp cool. bot.	40°C	1°C
19		wait	temp. bottom	40°C
20		pump off		
21		vent on		
22		wait	time	00:00:30
23	04:30:40	vent off		
24		end		

Table A.11: Annealing of bonded pairs of silicon wafers

	tool	Isotemp Programmable Oven	
#	type	parameter #1	parameter #2
1	set point	300°C	2.0°C/min
2	soak	8 h	
3	set point	25°C	2.0°C/min
4	end		

Table A.12: Sputter-deposition of a layer of aluminum

	tool	MRC DC-Sputter 603	
	recipe	`#16`	
	thickness	0.32 μm	
#	step	parameter	value
1	exchange	exchange type	0 (normal)
		cool time	00:00 min:sec
2	hivac	pressure	$1 \cdot 10^{-6}$
		hivac time	05:00 min:sec
`for` i `from` 1 `to` 8			
$2i+1$	sput3	B	0
		gas	1
		power	1.10 kW
		gas pressure	10 μm
		direction	>
		scan speed	40 cm/min
		presput	00:00 min:sec
		cycles	1
$2i+2$	pause	time	20:00 min
`end for`			
19	exchange	exchange type	0 (normal)
		time	00:00 min

Table A.13: Reactive ion etching of aluminum

tool: Applied Materials P5000 RIE			
recipe: `NANOTOOL AL ETCH`			
approximative etch depth: 0.4 μm			
step	STABILIZATION #1	OXIDE ETCH	STABILIZATION #2
Time (s)	30	45	30
Pressure (mTorr)	10	10	17
Power (W)	0	600	0
B-Field (Gauss)	0	0	0
N_2 (sccm)	50	50	25
Cl_2 (sccm)	0	0	35
step	PRIMARY ETCH	SECONDARY ETCH	RAMPDOWN
Time (s)	220	110	60
Pressure (mTorr)	17	17	OPEN
Power (W)	50	50	25
B-Field (Gauss)	0	70	0
N_2 (sccm)	25	25	50
Cl_2 (sccm)	35	35	0

Table A.14: Removing a photoresist mask without overheating the wafer

tools: a fumehood and a programmable oven			
#	step	parameter	value
1	acetone dip	time temperature	10 min room temperature
2	isopropyl alcohol dip	time temperature	10 min room temperature
3	evaporation	time temperature	15 min 50°C

Table A.15: Spinning, patterning and developing a 6.5 μm layer of AZ9260 Resist

#	step	actions
Perform these steps on the Bidtec R&D Spinner		
1	adherent product spinning	• Spin adhering product on the silicon wafer using the following recipe, which is normally preset as recipe #0 in the machine. • spin speed #1: 200 rpm • acceleration time #1: 0.1 s • spin time #1: 5 s • spin speed #2: 3950 rpm • acceleration/deceleration time #2: 0.1 s • spin time #2: 30 s • spin speed #3: 0 rpm • acceleration/deceleration time #3: 0 s • spin time #3: 0 s
2	photoresist dispensing	• Use a plastic syringe to dispense 5 ml of AZ9260 photoresist on the wafer. Take special care in spreading the photoresist as evenly as possible in a layer that covers the largest possible surface while remaining centered on the wafer. Execute this step as quickly as possible.
3	photoresist spinning	• Use the following recipe on the Bidtec R&D Spinner. • spin speed #1: 200 rpm • acceleration time #1: 0.1 s • spin time #1: 5 s • spin speed #2: 5000 rpm • acceleration/deceleration time #2: 0.2 s • spin time #2: 60 s • spin speed #3: 0 rpm • acceleration/deceleration time #3: 0 s • spin time #3: 0 s
4	softbake	• Softbake the photoresist by placing the wafer on a hotplate set at 110°C during 120 s.
Perform these steps on the EVG620 Aligner		
5	exposition	• Use the recipe `BottomSide-5inMask-6in-1.49m.rcp` of Table A.3 to expose the photoresist to a dose of 1100 mJ/cm^2.

Table A.16: Spinning, patterning and developing a 6.5 μm layer of AZ9260 Resist

#	step	actions
Perform these steps using pyrex dishes in the yellow room		
6	development preparation	• Place the wafer in a teflon basket and prepare two pyrex dishes; one containing deionized water, and the other containing a 4:1 solution of deionized water and AZ400K developer.
7	development	• Dip the teflon basket in the developer solution and stir gently by slowly moving the dish in circles on the table. In order to obtain a development rate as even as possible, one can turn the pyrex dish by an increment of 90° every 15 s, for example. • The development time may vary from 90 s to 150 s, and, for that reason, it is preferable to monitor the process by eye, and end it whenever all the patterns are all fully developed.
8	rinsing	• Quickly dip the teflon basket in the deionized water and stir gently by slowly moving the dish in circles during 120 s.
Perform this step on the Bidtec R&D Spinner		
9	dry	Dry the wafer by performing recipe #0 of the Bidtec R&D Spinner, as defined in Table A.15.
10	hardbake	• Hardbake the photoresist by placing the wafer on a hotplate set at 90°C during 120 s.

Table A.17: Deep Reactive Ion Etching (a.k.a. Bosch process) of the SBA structure

tool	ASE Plasma Etching System	
recipe	`DEEP 3`	
duration	135 min	
parameter	etch step	passivation step
process mode	discrete	
platen temperature	20°C	
step time	13 s	7 s
overrun	0 s	0 s
gas C_4F_8	0 sccm	85 sccm
gas SF_6	130 sccm	0 sccm
gas O_2	13 sccm	0 sccm
gas Ar	0 sccm	0 sccm
coil power	600 W	600 W
platen power	18	0
HBC pressure	9500 mTorr	
minimum flow	10 sccm	
minimum flow	40 sccm	

Appendix B

Microfabrication Photolithographic Masks

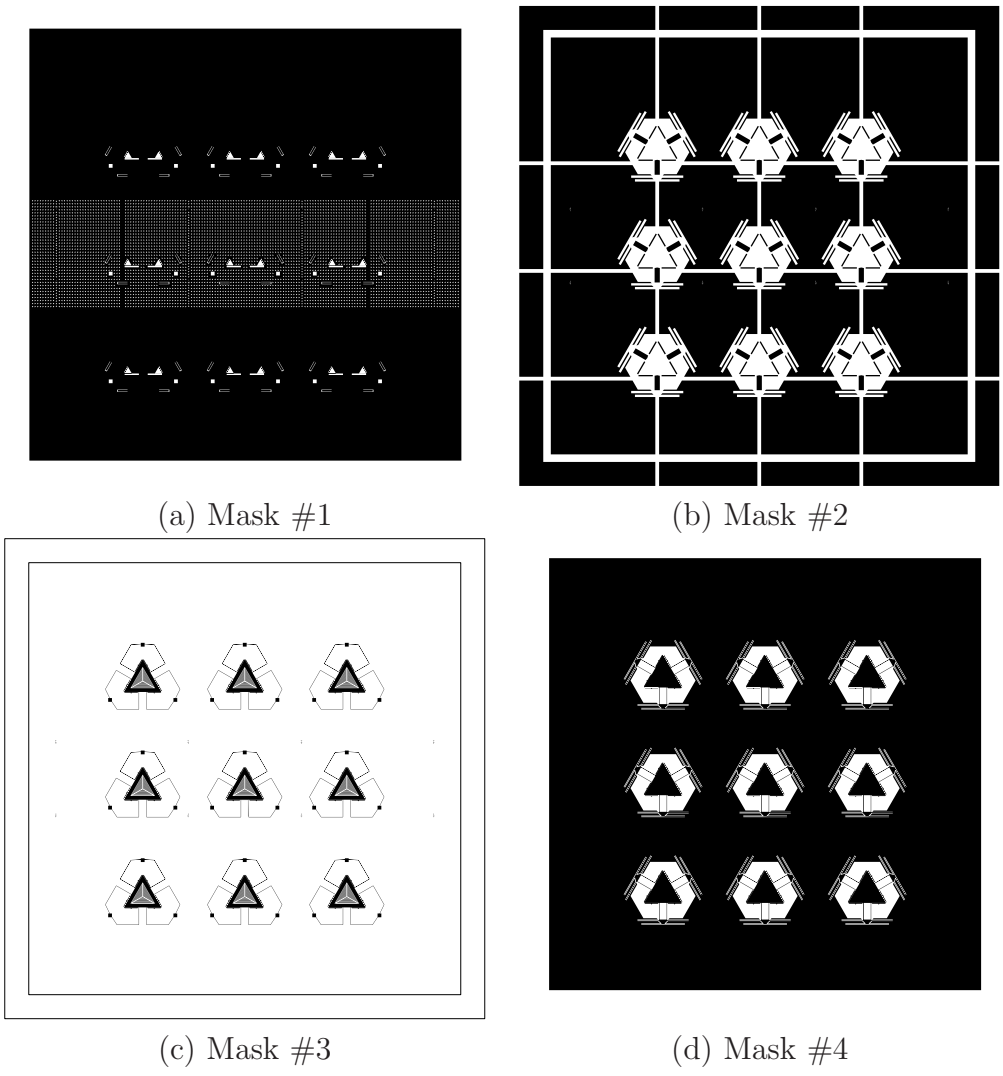

(a) Mask #1

(b) Mask #2

(c) Mask #3

(d) Mask #4

Figure B.2: Photolithographic masks (scale: 1:2, materials: chrome (dark areas) on soda lime glass (white areas))

Appendix C

Optimum Computational Frame of the CAC Method

In this Appendix we compute the global minimum of the objective function f as defined in Eq. (8.4). For starters, let us exclude the situation where $\boldsymbol{\omega} = \mathbf{0}_3$, in which case changing frame does not improve anything. Furthermore, as we are to find the frames that minimize the overall error sensitivity, we can readily discard the worst ones, that is, the frames for which the error sensitivity is unbounded. As stated previously, in these frames, at least one of the angular velocity components is null. From this last assumption, $\boldsymbol{\Delta}$ is nonsingular over the selected optimization domain, and we can write

$$[\partial\boldsymbol{\omega}/\partial\mathbf{w}']_{\mathcal{C}} = (1/4)[\boldsymbol{\Delta}^{-1}]_{\mathcal{C}}\mathbf{B}. \tag{C.1}$$

C.2.1 Minimizing f_2

As the Euclidean-norm of $\boldsymbol{\omega}$ is frame-invariant, we can further simplify the problem by defining $\mathbf{D} \equiv \boldsymbol{\Delta}/\|\boldsymbol{\omega}\|_2$, where

$$\mathbf{D} \equiv \begin{bmatrix} u_{\boldsymbol{\omega},1} & 0 & 0 \\ 0 & u_{\boldsymbol{\omega},2} & 0 \\ 0 & 0 & u_{\boldsymbol{\omega},3} \end{bmatrix}, \text{ and } \mathbf{u}_{\boldsymbol{\omega}} \equiv \begin{bmatrix} u_{\boldsymbol{\omega},1} \\ u_{\boldsymbol{\omega},2} \\ u_{\boldsymbol{\omega},3} \end{bmatrix} \equiv \boldsymbol{\omega}/\|\boldsymbol{\omega}\|_2 \tag{C.2}$$

is the unit-vector pointing in the direction of $\boldsymbol{\omega}$. Thus, Eq. (8.3) can be rewritten as

$$4\|\boldsymbol{\omega}\|_2[\mathbf{D}]_{\mathcal{C}}\,[\partial\boldsymbol{\omega}/\partial\mathbf{w}']_{\mathcal{C}} = \mathbf{B} = \mathbf{U}\boldsymbol{\Sigma}\mathbf{V}^T, \tag{C.3}$$

where

$$\mathbf{U} \equiv \begin{bmatrix} 0 & -\sqrt{2/3} & -1/\sqrt{3} \\ -1/\sqrt{2} & 1/\sqrt{6} & -1/\sqrt{3} \\ 1/\sqrt{2} & 1/\sqrt{6} & -1/\sqrt{3} \end{bmatrix}, \quad \mathbf{\Sigma} \equiv \begin{bmatrix} 2 & 0 & 0 \\ 0 & 2 & 0 \\ 0 & 0 & 1 \end{bmatrix},$$
$$\text{and } \mathbf{V} \equiv \begin{bmatrix} 0 & -\sqrt{2/3} & 1/\sqrt{3} \\ -1/\sqrt{2} & 1/\sqrt{6} & 1/\sqrt{3} \\ 1/\sqrt{2} & 1/\sqrt{6} & 1/\sqrt{3} \end{bmatrix},$$

i.e., the rightmost-hand side of eq. (C.3) represents the singular–value decomposition of $\mathbf{B}$. Notice that $\mathbf{\Sigma}$ can be further decomposed into $\mathbf{\Sigma} = (2)\mathbf{1}_{3\times 3} - \mathbf{e}_3\mathbf{e}_3^T$, where $\mathbf{e}_i \in \mathbb{R}^3$ has all its components null except for the i^{th} component, which is 1. We perform the foregoing substitution, solve for the Jacobian matrix and take its Euclidean norm, which yields

$$4\|\boldsymbol{\omega}\|_2 \| \left[\partial\boldsymbol{\omega}/\partial\mathbf{w}'\right]_{\mathcal{C}} \|_2 = \|[\mathbf{D}]_{\mathcal{C}}^{-1}\mathbf{U}(2\mathbf{1}_{3\times 3} - \mathbf{e}_3\mathbf{e}_3^T)\mathbf{V}^T\|_2. \tag{C.4}$$

As the matrix Euclidean norm is invariant under rotations, we can write,

$$\begin{aligned} 4\|\boldsymbol{\omega}\|_2 f_2 &= \|[\mathbf{D}]_{\mathcal{C}}^{-1}\mathbf{U}(2\mathbf{1}_{3\times 3} - \mathbf{e}_3\mathbf{e}_3^T)\mathbf{U}^T\|_2 \\ &= \|[\mathbf{D}]_{\mathcal{C}}^{-1}(2\mathbf{1}_{3\times 3} - \mathbf{u}_3\mathbf{u}_3^T)\|_2, \end{aligned} \tag{C.5}$$

where $\mathbf{u}_3 \equiv -(1/\sqrt{3})[1 \quad 1 \quad 1]^T$ is the third column vector of $\mathbf{U}$. Upon defining the orthogonal projector $\mathbf{P}_{u,3} \equiv \mathbf{1}_{3\times 3} - \mathbf{u}_3\mathbf{u}_3^T$ onto the plane normal to $\mathbf{u}_3$, we obtain

$$4\|\boldsymbol{\omega}\|_2 f_2 = \|[\mathbf{D}]_{\mathcal{C}}^{-1}(\mathbf{1}_{3\times 3} + \mathbf{P}_{u,3})\|_2. \tag{C.6}$$

The strategy is now to define a lower bound for the objective function which, if it is inclusive, will prove to be a global minimum of f_2. Hence, by comparing with Eq. (C.6), one can readily verify that

$$4\|\boldsymbol{\omega}\|_2 f_2 \geq \|[\mathbf{D}]_{\mathcal{C}}^{-1}(2\mathbf{P}_{u,3})\|_2 = 2 \max_{\|\mathbf{x}\|_2=1} \|[\mathbf{D}]_{\mathcal{C}}^{-1}\mathbf{P}_{u,3}\mathbf{x}\|_2. \tag{C.7}$$

The product $\mathbf{P}_{u,3}\mathbf{x}$, for $\mathbf{x}$ subject to the constraint $\|\mathbf{x}\|_2 = 1$, can be viewed as a mapping that takes the unit sphere onto the unit disk $\mathcal{D}$ centred at the origin and lying in the plane $\mathcal{P}$ normal to $\mathbf{u}_3$. Furthermore, the action of the diagonal matrix $[\mathbf{D}]_{\mathcal{C}}$ on $\mathcal{D}$ can be viewed as a scaling along the three orthogonal directions $\{\mathbf{e}_i\}_{i=1}^3$ corresponding to the three diagonal entries of $[\mathbf{D}]_{\mathcal{C}}$, respectively. It is now apparent that a matrix $[\mathbf{D}]_{\mathcal{C}}$ that minimizes the lower-bound is one of the isotropic solutions, that is, $[\mathbf{D}]_{\mathcal{C}}^{-1} = \sqrt{3}\mathbf{1}_{3\times 3}$. Indeed, any attempt to reduce the i^{th} component of $[\mathbf{D}]_{\mathcal{C}}$ results in an augmentation of at least one of the other components through the relation $\|\mathbf{u}_{\boldsymbol{\omega}}\|_2^2 = 1$, thereby increasing the radius of the circle in a direction orthogonal to $\mathbf{e}_i$. Hence, the minimum lower bound is attained when the circle is scaled uniformly in all directions, which corresponds to a lower bound value of $2\sqrt{3}$. On the other hand, upon substituting the foregoing value of $[\mathbf{D}]_{\mathcal{C}}$ into Eq. (C.6), we obtain

$$4\|\boldsymbol{\omega}\|_2 f_2 = \sqrt{3}\|\mathbf{1}_{3\times 3} + \mathbf{P}_{u,3}\|_2 = 2\sqrt{3}, \tag{C.8}$$

which is the same result as for the lower bound. Hence, $[\mathbf{D}]_{\mathcal{C}}^{-1} = \sqrt{3}\mathbf{1}_{3\times 3}$, or, equivalently, $\mathbf{u}_{\boldsymbol{\omega}} = \mathbf{u}_{\boldsymbol{\omega}}^* \equiv (1/\sqrt{3})[1 \quad 1 \quad 1]^T$, corresponds to a global minimum of the objective function f_2. In fact, one can readily verify that any of the vectors

$$\mathbf{u}_{\boldsymbol{\omega}} = (1/\sqrt{3})[\pm 1 \quad \pm 1 \quad \pm 1]^T \tag{C.9}$$

also corresponds to a global minimum of f_2.

C.2.2 Minimizing f_1

Upon choosing $p = 1$ in Eq. (8.4), we obtain

$$f_1 = \left\| \left[\frac{\partial \boldsymbol{\omega}}{\partial \mathbf{w}'} \right]_{\mathcal{C}} \right\|_1 = \frac{\|[\mathbf{D}^{-1}]_{\mathcal{C}}\mathbf{B}\|_1}{4\|\boldsymbol{\omega}\|_2} \quad \rightarrow \quad \min_{\mathcal{C}} f_1. \tag{C.10}$$

Let us rewrite this minimization problem in terms of $\mathbf{u}_{\boldsymbol{\omega}}$ as defined in Eq. (8.5), which requires the addition of a constraint equation. After simplification, this

yields

$$f_1 = \frac{1}{4\|\boldsymbol{\omega}\|_2} \sum_{i=1,2,3} \frac{1}{|u_{\boldsymbol{\omega},i}|} \quad \rightarrow \quad \min_{\mathbf{u}_{\boldsymbol{\omega}}} f_1, \tag{C.11}$$

subject to

$$g(\mathbf{u}_{\boldsymbol{\omega}}) = \|\mathbf{u}_{\boldsymbol{\omega}}\|_2^2 - 1 = 0. \tag{C.12}$$

Let us consider the objective function over the first octant of the Cartesian space only, over which it is continuous. This leads to the optimization problem

$$f_1 = \frac{1}{4\|\boldsymbol{\omega}\|_2} \sum_{i=1,2,3} \frac{1}{u_{\boldsymbol{\omega},i}} \quad \rightarrow \quad \min_{\mathbf{u}_{\boldsymbol{\omega}} > \mathbf{0}_3} f_1, \tag{C.13}$$

subject to

$$g(\mathbf{u}_{\boldsymbol{\omega}}) = \|\mathbf{u}_{\boldsymbol{\omega}}\|_2^2 - 1 = 0, \tag{C.14}$$

which can be solved using the method of Lagrange multipliers. Accordingly, we write

$$\nabla f_1 + \lambda \nabla g = \frac{-1}{4\|\boldsymbol{\omega}\|_2^2} \begin{bmatrix} 1/u_{\boldsymbol{\omega},1}^2 & 1/u_{\boldsymbol{\omega},2}^2 & 1/u_{\boldsymbol{\omega},3}^2 \end{bmatrix}^T + 2\lambda \mathbf{u}_{\boldsymbol{\omega}} = \mathbf{0}_3, \tag{C.15}$$

where λ is the Lagrange multiplier. We thus obtain

$$-1/(4\|\boldsymbol{\omega}\|_2^2 u_{\boldsymbol{\omega},i}^2) + 2\lambda u_{\boldsymbol{\omega},i} = 0, \quad \text{or} \quad u_{\boldsymbol{\omega},i} = 1/(2\sqrt[3]{\lambda}), \quad i = 1,2,3, \tag{C.16}$$

which yields $\lambda = (\sqrt{3}/2)^3$, after substitution of Eq. (C.16) in the constraint equation. The resulting optimum unit vector is $\mathbf{u}_{\boldsymbol{\omega}} = (1/\sqrt{3})[1 \quad 1 \quad 1]^T$. Performing the same analysis over the seven other octants of the cartesian space yields the optima

$$\mathbf{u}_{\boldsymbol{\omega}} = (1/\sqrt{3}) \begin{bmatrix} \pm 1 & \pm 1 & \pm 1 \end{bmatrix}^T, \tag{C.17}$$

which yield, apparently, the global minimum of f_1.

C.2.3 Minimizing f_∞

The objective function obtained from the selection $p = \infty$ is

$$f_\infty = \left\| \left[\frac{\partial \boldsymbol{\omega}}{\partial \mathbf{w}'} \right]_{\mathcal{C}} \right\|_\infty = \frac{\|[\mathbf{D}^{-1}]_{\mathcal{C}} \mathbf{B}\|_\infty}{4\|\boldsymbol{\omega}\|_2} \quad \rightarrow \quad \min_{\mathcal{C}} f_\infty \tag{C.18}$$

and is rewritten in terms of $\mathbf{u}_{\boldsymbol{\omega}}$ as

$$f_\infty = \frac{3}{4\|\boldsymbol{\omega}\|_2} \max_{i=1,2,3} \frac{1}{|u_i|} \quad \rightarrow \quad \min_{\mathbf{u}_{\boldsymbol{\omega}}} f_\infty, \tag{C.19}$$

subject to

$$g(\mathbf{u}_{\boldsymbol{\omega}}) = \|\mathbf{u}_{\boldsymbol{\omega}}\|_2^2 - 1 = 0. \tag{C.20}$$

The solution of this problem by the method of Lagrange multipliers is cumbersome. Indeed, the presence of the maximum function which experiences discontinuities over the planes $u_{\boldsymbol{\omega},i} = \pm u_{\boldsymbol{\omega},j}$, $i, j = 1, 2, 3$, $i \neq j$, forces the partition of the space into 24 pseudopyramids having their apex at the origin and their lateral faces within the planes $u_{\boldsymbol{\omega},i} = 0$, $u_{\boldsymbol{\omega},j} = 0$, $u_{\boldsymbol{\omega},i} = u_{\boldsymbol{\omega},k}$, and $u_{\boldsymbol{\omega},j} = u_{\boldsymbol{\omega},k}$, $i = 1, 2, 3$, $i \neq j \neq k$.

Consider instead the general relation

$$f_\infty \geq f_1, \tag{C.21}$$

which can be verified by inspection of eqs. (C.11) and (C.19). Upon evaluating the two functions at the global minima of f_1 given in eq. (C.17), we obtain

$$f_1(\mathbf{u}_{\boldsymbol{\omega}}) = f_\infty(\mathbf{u}_{\boldsymbol{\omega}}) = (3\sqrt{3})/(4\|\boldsymbol{\omega}\|_2^2). \tag{C.22}$$

Inequality (C.21), eq. (C.22), and the two objective functions being subjected to the same constraint (C.20) imply that the global minimum of f_∞ is attained

at those values of $\mathbf{u}_{\boldsymbol{\omega}}$ yielding the global minimum of f_1, namely

$$\mathbf{u}_{\boldsymbol{\omega}} = (1/\sqrt{3}) \begin{bmatrix} \pm 1 & \pm 1 & \pm 1 \end{bmatrix}^T . \tag{C.23}$$